DISS ETH NO. 15858

Quantitative analysis of the topographic evolution of the Andes of Northern Chile using cosmogenic nuclides

A dissertation submitted to the

SWISS FEDERAL INSTITUTE OF TECHNOLOGY ZÜRICH

for the degree of

DOCTOR OF SCIENCES

presented by

FLORIAN KOBER

Dipl. Geol. TU Bergakademie Freiberg

born April, 24, 1975

Meiningen/Germany

on the recommendation of

Prof. Dr. Philip Allen, ETH-Zürich, examiner

Prof. Dr. Rainer Wieler, ETH-Zürich, co-examiner

Prof. Dr. Fritz Schlunegger, University of Bern, co-examiner

Dr. Samuel Niedermann, GFZ-Potsdam, co-examiner

Dr. Susan Ivy-Ochs, ETH-Zürich, co-examiner

Zürich, December, 2004

Abstract

The evolution of the transient landscape at the Western Escarpment of the central Andes of northern Chile (Arica area) is described for the time interval from ca. 7.5 My ago to present. Base-level lowering with magnitudes of ca. 300-500 m in the Coastal Cordillera and a change in paleoclimate has been modifying a landscape from a geomorphic decay state towards relief growth by incision. Calculated minimum fluvial incision rates increased from ca. 0.2 mm/yr between ca. 7.5 My and 3 My to ca. 0.3 mm/yr thereafter. It is suggested that an incision rate increase was caused by an increase in effective water discharge for drainage systems sourced in the Western Cordillera. During the same time, however, valleys with headwaters in the coastal region lack any evidence of fluvial incision. This implies that the Coastal Cordillera became hyperarid sometime after 7.5 My ago. Furthermore, between 7.5 My and present, the sediment yields have been consistently higher in the catchments with distal sources (ca. 15 m/my) than in the headwaters of rivers with local sources (<7 m/my). The positive correlation between sediment yields and the altitude of the headwaters (distal versus local sources) seems to reflect the effect of orographic precipitation on surface erosion.

A major part of the thesis was dedicated to the study of terrestrial cosmogenic nuclides in quartz (^{10}Be, ^{26}Al and ^{21}Ne) to establish exposure duration and erosion rates of surfaces at the Western Andean Escarpment. Dry areas at lower to medium elevations in the Western Escarpment and the Coastal Cordillera (the northern branches of the Atacama Desert) yielded very low erosion rates (≤100cm/my). In contrast, the upper Western Escarpment and the adjacent Western Cordillera exhibit steadily increasing erosion rates up to ≤4600cm/my. These areas receive the highest rainfall today. These erosion rates have prevailed for timescales back to the late Miocene for the low erosion surfaces, but are only valid for Holocene/late Pleistocene timescales for the high erosion areas. For the low erosion surfaces, steady-state nuclide concentrations are not achieved, likely due to episodic spalling events or by resetting of nuclide concentrations due major removal of rock (in an m-scale). Nevertheless, erosion rates deduced from single nuclides are equal to values determined with nuclide pairs. For sample sites with low erosion, nuclides reach their steady-state concentrations faster than the landscape itself, which may remain in a transient stage shown by preserved stages of knickzone-headward migration of major streams.

In a side-study, we investigated cosmogenic ^{10}Be and ^{21}Ne in sanidine and cosmogenic ^{3}He in Fe-Ti-oxide minerals, coexisting with quartz in the ignimbritic successions of northern Chile. Based on known production rates for quartz, the resulting mean experimental ^{21}Ne production rate for five sanidine samples is 30.4±3.6 atoms*g^{-1}*yr^{-1} compared to a modelled value of 28.3 atoms*g^{-1}*yr^{-1}. Preliminary results also indicate that sanidine is also well suited for ^{10}Be studies. The mean experimental ^{10}Be production rate from two sanidine samples is 4.45±0.38 atoms*g^{-1}*yr^{-1}, very close to the modelled value of 4.55 atoms*g^{-1}*yr^{-1}. For Fe-Ti-oxide minerals, the mean experimental ^{3}He production rate established on five samples is 120±11 atoms*g^{-1}*yr^{-1}, compared to a modelled value of 121 atoms*g^{-1}*yr^{-1}. Model results are provided by I. Leya (University of Bern) and values are based on artificial target experiments and model production rates calculated with new cross sections for ^{3}He-, ^{21}Ne-, and ^{10}Be-production, respectively, from the individual target elements. Sanidine and Fe-Ti-oxide minerals can thus be added to the list of nuclide-isotope pairs useful in terrestrial cosmogenic nuclide studies.

Quantitative studies of trace impurities in quartz and their effect on terrestrial cosmogenic nuclide production revealed that traces of impurities have no effect on the total nuclide production. Such concentrations at a ~100 ppm level were detected in quartz from Chilean ignimbrites in structural bound position and likely also within micro melt-inclusions. The presence of impurities required caution in sample preparation and repeated physical and chemical sample treatment.

Preliminary artificial target experiments on quartz-filled containers, which were exposed during several years at various altitudes and latitudes to constrain existing scaling models of terrestrial cosmogenic nuclides, are presented. The targets contained cosmogenic noble gases, which were, however, compromised by non-cosmogenic (atmospheric, nucleogenic and/or crustal) contributions. These results lead to the development of a new generation of targets at ETH by S. Strasky.

Zusammenfassung

Das Hauptziel der vorliegenden Arbeit bestand in der quantitativen Analyse der Landschaftsentwicklung der Westabdachung Nordchiles im Gebiet um Arica. Die Studie beschränkt sich auf den Zeitraum von ca. 7.5 My bis heute. Hauptursache für die Veränderung der Landschaftsgenese von einem Zustand der geomorphologischen Einnivellierung hin zu einer wachsenden Topografie mit zunehmendem Relief (um 300-500m), waren eine Absenkung des Niveaus der Flusssyteme sowie eine Veränderung des Paläoklimas. Die daraus resultierenden Einschneideraten der Hauptflüsse waren um die 0.2 mm/y im Zeitraum von ca. 7.5-3 My und stiegen danach auf 0.3 mm/y an. Dieser Anstieg wird verursacht durch eine Zunahme des effektiven Wasserdurchflusses verstärkt, was allerdings nur auf Flüsse mit Einzugsgebiet in der Westlichen Kordillere zurifft. Zu der selben Zeit weisen die Gebiete der Unteren Westabdachung und der Küstenkordillere keinerlei Anzeichen von fluvialer Erosion auf. Dies lässt vermuten, dass diese Gebiete ab ca. 7.5Ma ein hyparides Klima hatten.

Weiterhin wurde eine Zunahme der abgeführten Sedimentraten ab ca. 7.5 My festgestellt. Höhere Raten konnten für Einzugsgebiete in den Hochanden (ca. 15 m/my) berechnet werden, verglichen mit lokalen Einzugsgebieten auf der Westabdachung, die geringere Werte aufwiesen (<7 m/my). Diese positive Korrelation von Sedimentabfuhrraten mit zunehmender Höhe lässt vermuten, dass die oberflächlichen Erosionraten eine Funktion der orografisch gesteuerten Niederschlagsmenge sind.

Der Haupteil der Dissertation befasst sich mit der Analyse von kosmogenen Nukliden in Quarz (^{10}Be, ^{26}Al and ^{21}Ne) und der daraus berechneten Oberflächenerosionraten. Diese korrelieren ebenfalls positiv mit einem orografisch gesteuerten Niederschlag. So sind im Bereich der unteren Westabdachung und der Küstenkordillere (was dem nördlichen Teil der Atacama-Wüste entspricht) äusserst geringe Erosionsraten von ≤100 cm/my zu verzeichnen. Diese nehmen zur oberen Westabdachung und der Westlichen Kordilliere hin konstant zu, auf Werte bis ≤4600 cm/my. Diese Oberflächenerosionsraten gelten für unterschiedliche Zeiträume. Während die Aussage von sehr geringen Erosionsraten in der Unteren Westabdachung für Zeiträume bis ins späte Miozän gültig ist, sind die höheren Erosionsraten der Westlichen Kordilliere für Holozäne/Spät-Pleistozäne Zeiträume nachweisbar. Dabei sind die Nuklidkonzentrationen im Bereich der Atacamawüste meist nicht in Sättigung.

Bei der Analyse der Oberflächenersoionsraten wurde weiterhin festgestellt, dass die Zeiträume für ein Sättigungsgleichgewicht der Nuklidekonzentration unterschiedlich sein

können im Vergleich zur Landschaft als Ganzes. Diese befindet sich wahrscheinlich in einem Übergangsstadium, wie die Knickzonen in den Flussläufen beweisen.

In einer Nebenstudie dieser Dissertation wurden kosmogenes ^{3}He, ^{10}Be and ^{21}Ne in den Mineralen Sanidin und Magnetit gemessen. Diese Minerale sind in Paragenese mit Quarzen in den analysierten Ignimbriten aus Nordchile. Basierend auf bekannten ^{21}Ne-Produtionsraten in Quarz wurden gemittelete ^{21}Ne-Produktionsraten in Sanidin von 30.4±3.6 Atome*g^{-1}*yr^{-1} ermittelt, währendessen neu modellierte Produktionsraten einen Wert von 28.3 Atome*g^{-1}*yr^{-1} für Sanidin ergaben. Weiterhin konnte nachgewiesen werden, dass kosmogenes ^{10}Be in Sanidin für die Expositionsdatierung geeignet ist. Dessen vorläufige experimentelle Produktionsrate beträgt 4.45 Atome*g^{-1}*yr^{-1}, bei einer modellierten Produktionsrate von 4.55 Atome*g^{-1}*yr^{-1}. Für ^{3}He in Magnetit wurden eine experimetelle Produktionsraten von 120 Atome*g^{-1}*yr^{-1} ermittelt, die fast identisch verglichen mit der modellierten Produktionsrate von 121 Atome*g^{-1}*yr^{-1} ist. Die modellierten Produtionsraten von I. Leya (Universität Bern) errechneten sich aus der Verwendung neuer Wirkungsquerschnitte für die einzelnen Elemente, welche an künstlichen Targets gewonnen wurden. Aufgrund der ausserordentlich gut übereinstimmenden Werte von experimentellen und modellierten Produktionsraten sind Sanidin und Magnetit verwendbar in terrestrisch-kosmogenen Nuklidanalysen.

Die quantitative Analyse von Verunreinigungen in Quarz zeigen, dass diese einen vernachlässigbaren Einfluss auf die kosmogene Produktionsraten haben. Dies ist deshalb so, weil die meisten Verunreinigungen im Gitter der Quarze in den nordchilenischen Ignimbriten in der Grössenordnung von <100 ppm waren. Zahlreiche Mikro-Schmelzeinschlüsse beinhalten wahrscheinlich ähnliche Mengen an Verunreiningungen. Während der Einfluss der Verunreinigungen auf die totale Nuklidproduktion vernachlässigbar ist, erforderten diese aber zusätzliche Aufbereitungsschritte während der Probenvorbereitung (z.B. Wiederholung physikalischer Trennmethoden und in der chemischen Auflösungsprozedur).

Ergebnisse von ersten Messreihen an exponierten künstlichen Targets zur Verifizierung von Skalierungsmodellen für die Höhen- und Breitenabhängigkeit der kosmogenen Nuklidproduktion werden präsentiert. Die Targets enthielten eine Mischung aus kosmogenen und nichtkosmogenen (atmosphärischen, nukleogenen und/oder krustalen)

Edelgaskomponenten. Die Testexperimente wurden von S. Strasky and der ETH genutzt, um neue Targets zu konzipieren.

Contents

Abstract i
Zusammenfassung iii

Contents vi

1. Introduction 1

1.1 Quantitative geomorphology 1
1.2 The study areas 2
1.3 Terrestrial cosmogenic nuclides in quantitative geomorphology 3
1.4 TCN-systematics 4

2. Surface uplift and climate change: The geomorphic evolution of the Western Escarpment of the Andes of northern Chile between the Miocene and present 8

2.1 Abstract 8
2.2 Introduction 9
2.3 Geological setting 10
2.4 Reconstruction of the geomorphic situation prior to dissection 15
2.5 Headward erosion and changes in relief 18
2.6 Increase in fluvial incision rates 19
2.7 Temporal trends in stream power 21
2.8 Comparative estimates of sediment yields 22
2.9 Discussion 23
2.10 Conclusion 24

3. Denudation rates and a topography-driven precipitation threshold in northern Chile: multiple cosmogenic nuclide data and sediment yield budgets 26

3.1 Abstract 26
3.2 Introduction 27
3.3 Study area 29
3.4 Sampling strategy 32
3.5 Methods, production rates and calculation procedures 34
3.6 Result 36
3.7 Discussion 46
3.8 Conclusion 53

4. Preliminary results on weathering and erosion rates using cosmogenic nuclides in semi-arid regions of the Sierras Pampeanas, Argentina 58

4.1 Abstract 58
4.2 Introduction 59
4.3 Geotectonic setting and climate 59
4.4 Soil profiles 61

4.5 Methods 62
4.6 Result 63
4.7 Discussion 66
4.8 Conclusion 68

5. In situ cosmogenic ^{10}Be and ^{21}Ne in sanidine and in situ cosmogenic ^{3}He in Fe-Ti-oxide minerals 69

5.1 Abstract 69
5.2 Introduction 70
5.3 Mineral aspects 72
5.4 Sample site geology 72
5.5 Sample preparation and measurement techniques 73
5.6 Isotope data and calculation of experimental production rates 75
5.7 Modeling of cosmogenic nuclide production rates on Earth 85
5.8 Comparison of experimental and modelled production rates 87
5.9 Conclusion 91

6. Possible interferences in terrestrial cosmogenic nuclide studies due to trace impurities in quartz grains and quartz separates 93

6.1 Introduction 93
6.2 Bulk chemistry and production rate estimations 95
6.3 Results from LA-ICP-MS 97
6.4 The effect of elevated F and U/Th-concentrations on neon isotopes 98
6.5 Discussion 99
6.6 Appendix 101

7. Artificial targets for production rate scaling systematics in terrestrial cosmogenic nuclide studies 97

7.1 Abstract 102
7.2 Rationale of the experiment 102
7.3 Brief history of artificial target experiments for TCN-production rate systematics 103
7.4 Methodical Concepts 104
7.5 Data/results and interpretation 107
7.6 Discussion and suggestions 116
7.7 Conclusion 117

8. Outlook and conclusions 118

9. References 121

10. Appendix

Curriculum vitae

Acknowledgements

1 Introduction

The progress made in deciphering processes of landscape evolution either by physical or numerical modelling helps to understand the past, present and future shape of the Earth. Modelling of future climate scenarios, tectonic impacts or land use on landscapes requires the knowledge on the fundamentals of how the present day landscape has been formed. Accordingly, this thesis discusses three major topics:

1.) Quantitative analysis of topographies (case study: northern Chile)
2.) Tracing geomorphological process rates on variable temporal and spatial scales
3.) Investigating terrestrial cosmogenic nuclides in quantitative geomorphology and in methodological systematics.

1.1 Quantitative geomorphology

Modelling of quantitative geomorphology and landscape evolution requires knowledge about processes that are governed and interlinked by climate, tectonics and erosion. If these primary forces are coupled, balanced or whether there is a "chicken or egg" identifiable (Molnar, 2003; Molnar and England, 1990) is under debate (e.g., Burbank et al., 2003; Dadson et al., 2003; Molnar and England, 1990; Reiners et al., 2003). One way to resolve such controversies is studying diverse geotectonic settings under similar or equal climate conditions and on variable spatial and temporal scales. In order to obtain quantitative data, we need (i) calibrations of ages of landscapes, (ii) incision rates of rivers, (iii) growth rates of mountain belts, (iv) slip rates of faults and growth rates of folds, (v) rates of weathering and erosion, or (vi) rates of weathering and regolith/soil production rates (see (Allen, 1997; Burbank and Anderson, 2001; Summerfield, 1991). Specifically, methods that allow the quantification and comparison of process rates that cover similar spatial scales but various timescales are needed. For instance, to correlated sediment transport- or precipitation rates recorded on a decadal scale are difficult to connect to geothermochronological data relevant for timescales of millions of years, although such positive correlations are observable (e.g., Reiners et al., 2003). Intermediate timescales are desirable. Furthermore, one technique to quantify a specific process rate does not necessarily measure the ultimate process leading to the (present day) expression of a landscape. It might only quantify a certain process in the evolution towards this landscape. For example, weathering of bare bedrock is controlled by physico-chemical processes but is also governed by the transport capacity of the surrounding landscape (cf., Anderson and Humphrey, 1989; Heimsath et al., 1997). Fortunately, methods

to quantify various process rates are constantly under refinement and new techniques are emerging (cf., Burbank and Anderson, 2001).

A crucial assumption in quantitative landscape studies is the search or the prerequisite of steady state or dynamic equilibrium conditions of e.g., weathering, sediment flux, topography, thermal gradients (e.g., Carson and Kirkby, 1972; Montgomery, 2001; Whipple, 2001; Willet and Brandon, 2002). Using terrestrial cosmogenic isotopes, erosional-isotopic steady state is commonly assumed (e.g., Bierman and Steig, 1996; Lal, 1991; Nishiizumi et al., 1986). This is necessary e.g., to predict landscape evolution scenarios or to run numerical models (e.g., Chase, 1992; Koons, 1989; Tucker and Slingerland, 1994, 1997). Furthermore, simplifications and abstractions have to be made when physical models are tested and compared with real nature evidence (e.g., Hancock and Willgoose, 2002; Swenson and Brown, 2004). However, commonly it is difficult to justify or to prove a steady-state condition, especially on long-term scales (Stark, 1999). Many landscapes are in transient stages of limited duration and evolve towards a state of equilibrium, such as glacial events acting on formerly fluvial landscapes or a slip of a fault, truncating a river-profile and modifying a graded river-profile in two separate segments.

In the recent past much attention has been paid to refining the resolution of temporal and spatial scales and to deciphering the steady/non-steady conditions of the system (e.g., Anderson, 1994; Bierman and Nichols, 2004; Burbank, 2002; Burbank and Anderson, 2001; Kirchner et al., 2001; Pratt-Sitaula et al., 2004). New techniques were employed and resolve intermediate timescales. One of these temporal linking methods is the analysis of terrestrial cosmogenic nuclides, the main technique used in this thesis. Bedrock erosion rates at the western slope of the Central Andes, assumed to be in a (near) steady state, were quantified using multiple terrestrial cosmogenic nuclides in Chapter 3.

1.2 The study areas

1.2.1 Northern Chile

The aim of this thesis is to quantify the topographic evolution of the Western Andes in northern Chile in the Neogene. The region is part of the western slope of the Central Andean orogen. Active tectonics (uplift of the Altiplano) and arid to hyperarid climate (Atacama Desert) characterize the region (Gregory-Wodzicki, 2000; Isacks, 1988; Montgomery et al., 2001; Mortimer, 1980). Topography constantly increases from sea level, to the 4000m high Altiplano and the 6000m peak heights of active volcanoes. Precipitation is orographically

controlled and restricted to elevations higher than ~3500m (Abele, 1990; Hoffman and Grotzinger, 1993; Hoffmann, 1975). The present day rainfall pattern is the result of the intertropical convergence zone (Westerlies), the Humboldt Current and the uplifted Andes (Abele, 1991). This pattern has likely persisted since the middle Miocene but might have shifted spatially (Alpers and Brimhall, 1988; Mortimer, 1980). Other investigations suggested that this rainfall pattern may have been initiated as late as Pliocene times (Hartley, 2003; Hartley and Chong, 2002). However, quantifications of erosion and incision rates in the Central Andes, which are the prime responder to precipitation and an important factor changing landscapes and creating relief, are sparse and were difficult to assess so far (see for a summary in Gregory-Wodzicki, 2000). This is due to the lack of datable material, limited field access, and the temporal resolution of applicable methods or the slow rates of processes. Morphological investigations and bedrock erosion rates on an escarpment scale are reported in Chapter 2 and 3.

1.2.2 Argentina

In a complementary pilot study, preliminary data on the initial landscape shaping process in semiarid climates by the means of terrestrial cosmogenic nuclides and geochemical analysis are reported in Chapter 4. Regolith profiles and adjacent bedrock surfaces of central Argentina (Sierras de Grande and Córdoba) were investigated.

1.3 Terrestrial cosmogenic nuclides in quantitative geomorphology

Analysis of terrestrial cosmogenic nuclides (TCN) developed over the last two decades offers the opportunity to quantify landscape evolution processes, as they allow to estimate erosion rates or exposure ages of a specific surface (see Bierman, 1994; Finkel and Suter, 1993; Lal, 1991; Nishiizumi et al., 1993). If only one nuclide is measured, maximum erosion rates or minimum exposure ages are determined, assuming the nuclide to be in steady state. This is achieved when isotope production (and radioactive decay) is in equilibrium with the erosional state of the surface (Lal, 1991). If two or more nuclides can be measured, non-steady state conditions can be identified and erosion rates and exposure ages can be determined simultaneously.

TCN-applications today range from temporal estimations of glacial events, dating of lava-flows, calculations of river incision rates, catchment-wide and spot soil erosion rates, but also estimations of mountain scale uplift rates and individual fault slip rates (reviews on

principles, methodology and applications are by Bierman and Nichols (2004), Bierman et al., (2002), Cockburn and Summerfield, (2004), Gosse and Phillips, (2001), Morris et al., (2002), Muzikar et al., (2003), Niedermann, (2002), Zreda and Phillips, (2004).

The temporal resolution provided by cosmogenic nuclides depends on the half-life of the nuclide investigated and on the processes governing nuclide accumulation (e.g., production, erosion, shielding). Short-lived nuclides, such as ^{14}C, reach saturation on Holocene/late Pleistocene timescales, whereas longer-lived nuclides reach saturation on Pleistocene to Miocene timescales (^{36}Cl:saturation~1My, ^{26}Al:~2My and ^{10}Be:~4.5My). Additionally, noble gases such as ^{3}He and ^{21}Ne allow a farther extension of the timescale, since these nuclides are stable. On the other hand, the spatial resolution of all these nuclides depends on the geomorphological setting (cf., Cockburn and Summerfield, 2004).

1.4 TCN-systematics

Numerous accounts have dealt with the principles, methodologies, measurements, applications and problems of TCN-systematics (see recent reviews by Bierman and Caffee, (2002), Gosse and Phillips, (2001), Niedermann, (2002) and references therein). In the last two decades, a number of theses at ETH and the University of Bern discussed specific topics, e.g, on the one hand methodical approaches like mass-spectrometer advances (compressor source), sample crushing devices or artificial targets (Aeschbach-Hertig, 1994; Baur, 1980; Oberholzer, 2004; Schäfer, 2000)). On the other hand, applied studies dealt with the sample preparation for radionuclides and noble gases, pre-exposure, and the actual landscape interpretation etc. (Bruno, 1995; Ivy-Ochs, 1996; Oberholzer, 2004; Schäfer, 2000; Schaller, 2001; Tschudi, 2000)). This thesis focuses on sub-topics which were investigated in more detail. Firstly, investigations on the mineral-isotope pairs ^{3}He in Fe-Ti-oxide minerals and ^{10}Be and ^{21}Ne in sanidine were performed (Chapter 5). Secondly, quartz chemistry and specifically the impurities in quartz were quantified in order to estimate a possible effect on TCN production rates using cathodoluminescence, ICP-AES, LA-ICP-MS and nuclear reaction analysis (Chapter 6). Thirdly, artificial target experiments were used to investigate scaling formalisms necessary for applied terrestrial cosmogenic nuclide studies (Chapter 7).

1.4.1 State of the art of available mineral-isotope pairs

While the most common mineral used in geomorphological TCN-studies is quartz (isotopes: ^{10}Be, ^{14}C, ^{21}Ne, ^{26}Al; see for reviews Bierman et al., (2002), Gosse and Phillips, (2001), Lifton et al., (2001), Niedermann, (2002)), not all places of interest comprise lithologies containing abundant quartz. Additionally, ^{3}He - the nuclide with highest production rates and lowest detection limits - is not quantitatively retained in quartz (Trull, et al., 1991; Shuster et al., 2005). In order to apply the TCN-method to geomorphological settings where quartz is not available, other minerals and nuclides are therefore desirable.

In the following, a brief account on presently used and recently explored nuclide-mineral pairs is given. Reliable mineral-nuclide pairs are ^{3}He and ^{21}Ne in pyroxene and olivine, respectively (e.g., Cerling, 1990; Kurz, 1986; Poreda and Cerling, 1992). Currently, ongoing investigations refine these nuclide-isotope pairs (Oberholzer et al., subm.; Williams et al., in press)). (Ivy-Ochs et al., 1998) studied pyroxenes for ^{10}Be but reported difficulties in eliminating meteoric ^{10}Be. In contrast, (Blard et al., 2004) recently reported successful use of ^{10}Be with a new cleaning procedure. Additionally, the use of ^{38}Ar in pyroxenes is currently being investigated, although widely differing production rates are suggested so far (Knight et al., 2003; Niedermann et al., 2004; Renne et al., 2001). Beside ^{3}He and ^{21}Ne in olivine, Nishiizumi et al. (1990) and Seidl et al. (1997) developed techniques to use ^{10}Be and ^{26}Al in this mineral. The latter found meteoric contamination to be a problem.

Carbonates and whole rock (such as basalts) are well suited for ^{36}Cl analysis (e.g., Phillips et al., 1986; Zreda et al., 1991). Braucher et al. (2004) reported additionally production rates of ^{10}Be in carbonates. ^{41}Ca was suggested for TCN-studies in limestone and feldspars (e.g., Fink et al., 1990; Finkel and Suter, 1993; Henning et al., 1987) but is currently limited by low levels of concentrations and requires further advances in measurement techniques. Plagioclase-feldspar has been shown not to retain ^{21}Ne quantitatively (Bogard and Cressy, 1973; Bruno et al., 1997; Poreda and Cerling, 1992) as earlier suggested by Bogard and Cressy (1973), Bruno et al. (1997), or Poreda and Cerling (1992). Preliminary studies of ^{10}Be (and ^{26}Al) in plagioclase suggested a feasibility of this mineral-isotope pair (Graham et al., 1995), but analysis revealed inconsistencies due to compositional variability.

Recently, Gayer et al. (2005) reported the suitability of ^{3}He in garnet, while Bryce and Farley (2002) proposed ^{3}He-production rates in magnetite. Other isotopes currently under investigation are ^{53}Mn in pyroxene (and potentially in biotite, garnet and hornblende; Knie et al. (2002) and ^{15}N in pyroxenes.

Commonly, two nuclides (e.g., ^{10}Be and ^{26}Al) are analysed to reveal exposure ages, erosion rates or the effect of erosion on exposure ages and to identify complex exposure or burial histories (see Bierman et al. (2002), Bierman et al., (1999); Granger and Muzikar, (2001)). Apart from the ^{10}Be/^{26}Al-pair, other multiple isotope approaches have been used, e.g., by Nishiizumi et al. (1990) used additionally ^{3}He to constrain lava-flow exposures, while Seidl et al. (1997) applied ^{36}Cl, ^{3}He, ^{21}Ne, beside ^{10}Be and ^{26}Al to calculate river-knickpoint-migration rates. Shephard et al. (1995) combined measurements of ^{10}Be/^{36}Cl in order to estimate lava-flow ages, erosion rates and desert pavement evolution. Studies by Trull et al. (1995) and Hetzel et al. (2002) combined noble gas (^{3}He, ^{21}Ne) and radionuclide isotopes (^{10}Be, ^{26}Al) for calibrating ages of the abandonment of aggradational surfaces and discussed nuclide specific retention features. Glacial morphologies were investigated by multiple noble gas and radionuclide isotopes (most times due to variable lithologies) to constrain exposure histories of moraines, glacial advances and to quantify the effect of erosion on exposure (e.g., Brook et al., 1993; Ivy-Ochs et al., 2004; Kaplan et al., 2003; Liccardi et al., 2001; Oberholzer et al., 2003; Phillips et al., 1993). The combined use of nuclides with short- (e.g., ^{14}C and ^{36}Cl) and long- (e.g, ^{3}He, ^{10}Be, ^{21}Ne, ^{26}Al) half-lives or of stable nature with time (e.g., Brook et al., 1993; Ivy-Ochs et al., 2004; Kaplan et al., 2003; Liccardi et al., 2001; Oberholzer et al., 2003; Phillips et al., 1993) is not yet well established, not only because of the time-consuming analysis of all of these isotopes but also due to the only recent advancements of some techniques, e.g. ^{14}C, (Lifton et al., 2001).

In this thesis, we show that several so far unexplored mineral-nuclide pairs have a potential in TCN-studies: ^{3}He in Fe-Ti-oxide minerals and ^{10}Be and ^{21}Ne in sanidine (Chapter 5).

1.4.2 Quartz mineralogy and production rates

Due to the stoichiometry of quartz (SiO_2), the production of cosmogenic nuclides is limited to the elements Si and O. However, trace impurities in quartz may occur, either in the crystal structure (e.g., Flem et al., 2002; or in fluid/melt-inclusions, e.g., Peppard et al., 2001). A third source of impurities is insufficient sample cleaning. Problematical may be impurities containing elements such as Na, Al or Mg which have higher elemental production rates, for e.g., ^{21}Ne, than Si (Masarik (2002) and Chapter 5), beside elevated U, Th and F contenets. A quantification of the importance of impurities in quartz will be presented (Chapter 6).

1.4.3 Spatial scaling of TCN-production rates by artificial target experiments

A major uncertainty in TCN-studies is introduced by the scaling formalism required to calculate the production rate for a cosmogenic nuclide at the samples altitude and latitude. Different scaling procedures were proposed by Desilets and Zreda (2001); Dunai, (2000), Lal, (1991) and Stone (2000). Currently, the most widely applied procedure is by Stone (2000). Errors in the range of 10-20% have to be assumed due to scaling (see Gosse and Phillips, 2001; Niedermann, 2002). The refinement of the scaling factors is one effort of the presently starting CRONUS-initiatives (CRONUS-EU and CHRONUS-US) by a network of exposing and measuring artificial targets on various latitudinal/altitudinal transects. Pilot experiments where ^{3}He and ^{21}Ne were measured in artificial targets are in thesis presented in Chapter 7.

2 SURFACE UPLIFT AND CLIMATE CHANGE: THE GEOMORPHIC EVOLUTION OF THE WESTERN ESCARPMENT OF THE ANDES OF NORTHERN CHILE BETWEEN THE MIOCENE AND PRESENT

Florian Kober[a,b], Fritz Schlunegger[c], Gerold Zeilinger[c], Heinz Schneider[c]

[a] *Institute of Geology, ETH Zürich, 8092 Zürich, Switzerland*

[b] *Institute of Isotope Geology, ETH Zürich, 8092 Zürich, Switzerland*

[c] *Institute of Geology, University of Bern, 3012 Bern, Switzerland*

2.1 Abstract

The Western Escarpment of the Andes at 18.30°S (Arica area, northern Chile) is a classical example for a transient state in landscape evolution. This part of the Andes is characterized by the presence of >10,000 km^2 plains that formed between the Miocene and the present, and >1500 m deeply incised valleys. Although processes in these valleys scale the rates of landscape evolution, determinations of ages of incision, and more importantly, interpretations of possible controls on valley formation have been controversial. This paper uses morphometric data and observations, stratigraphic information and estimates of sediment yields for the time interval between ca. 7.5 Ma and present to illustrate that the formation of these valleys was driven by two probably unrelated components. The first component comprises a phase of base-level lowering with magnitudes of ca. 300-500 m in the Coastal Cordillera. This period of base-level change in the Arica area, that started at ca. 7.5 Ma according to stratigraphic data, caused the trunk streams to dissect headwards into the plains. The headward erosion interpretation is based on the presence of well-defined knickzones in stream profiles and the decrease in valley widths from the coast towards these knickzones. The second component comprises a change in paleoclimate. This interpretation is based on (i) the increase in the size of the largest alluvial boulders (from dm to m scale) with distal sources during the last 7.5 Ma, and (ii) the calculated increase in minimum fluvial incision rates of ca. 0.2 mm/yr between ca. 7.5 Ma and 3 Ma to ca. 0.3 mm/yr thereafter.

In press: Willet, S., Hovius, N., Fisher, D., and Brandon, M., eds., Tectonics, Climate and Landscape evolution, GSA - Penrose Special Paper, Chapter 20.

These trends suggest an increase in effective water discharge for systems sourced in the Western Cordillera (distal source). During the same time, however, valleys with headwaters in the coastal region (local source) lack any evidence of fluvial incision. This implies that the Coastal Cordillera became hyperarid sometime after 7.5 Ma. Furthermore, between 7.5 Ma and present, the sediment yields have been consistently higher in the catchments with distal sources (ca. 15 m/my) than in the headwaters of rivers with local sources (<7 m/my). The positive correlation between sediment yields and the altitude of the headwaters (distal versus local sources) seem to reflect the effect of orographic precipitation on surface erosion. It appears that base-level change in the coastal region in combination with an increase in the orographic effect of precipitation controlled the topographic evolution of the northern Chilean Andes.

2.2 Introduction

Understanding controls on spatial and temporal variations of surface erosion has become a major research objective in the last few years. This issue has been discussed in detail by the review paper on bedrock rivers and the geomorphology of active orogens by Whipple (2004). Because of the importance of this problem, many studies have been directed towards analyzing (i) the nature of surface erosion in channels and on hillslopes (e.g., Schumm, 1956; Montgomery and Dietrich, 1992; Montgomery et al., 2003), (ii) possible feedback mechanisms between erosion in channels and on hillslopes (Tucker and Bras, 1998; Harvey, 2001; Schlunegger et al., 2001), (iii) the sensitivity of erosional processes and the resulting sediment flux to climatic and tectonic perturbations (Molnar, 2001; Pratt et al., 2002; Roe et al., 2002), (iv) the nature and the magnitudes of parameters that scale with erosional processes for different temporal and spatial length scales (Tucker and Slingerland, 1996; 1997; Hinderer et al., 2002), and (v) possible controls on limits of relief and surface erosion at the local scale and at that of a whole mountain belt (Burbank et al., 1996; Whipple et al., 1999; Whipple and Tucker, 1999; Schlunegger and Hinderer, 2003). As suggested by Bull (1991), Rosenbloom and Anderson (1994), Pazzaglia et al. (1998) and Wegmann and Pazzaglia (2002), terraced landscapes represent the simplest examples to address these research objectives because initial conditions, present form and ages of different geomorphic elements can possibly be constrained. These landforms represent transient stages towards a steady state between erosional processes and exogenic/endogenic forces. Transient stages of landscape development can be identified by the presence of knickzones in stream profiles. If

digitized, the information extracted from these landscapes can be converted into volumes of eroded rock or depth of local incision per unit time, which, in turn, allows the testing of possible controls and limits on surface erosion (e.g., Whipple et al., 2000; Schlunegger, 2002).

This paper focuses on the landscape evolution of the Arica area, northern Chile, that potentially allows interpreting the tectonic and climatic fingerprints because of the preservation of different steps in the topographic evolution (Mortimer and Saric, 1975; Mortimer, 1980; García, 2002; Wörner et al., 2002). In this region, the landscape is characterized by the presence of flat to gently undulating plains hundreds of km^2 in extent and >1500 m deep valleys that dissect these landscapes (Fig. 1). Previous studies thought that initiation of incision was the result of (i) eustatic sea level fall (Herm, 1969; Paskoff, 1980), (ii) onset of glaciations in the Pleistocene (which is considered to have increased fluvial runoff) (Wörner et al., 2002), (iii) differential tectonic movements (Paskoff, 1980; Mortimer, 1980; Kennan, 2000), (iv) enhanced flow of ground water derived from the Altiplano (Hoke et al., 2002), and (v) the modification of the atmospheric and hydrospheric circulation patterns caused by the rising Andes (Mortimer, 1980; Paskoff, 1980). Our study will use a refined stratigraphic framework to unravel in more detail than presented before the tectonic and the climatic fingerprints and highlight the consequential driving forces.

2.3 Geologic setting

The Western Escarpment of the Andes of northern Chile is divided into three main longitudinal geological-morphological units that comprise from west to east the *Coastal*, the *Western Escarpment*, and the *Western Andean Cordillera* (Fig. 1). The *Coastal Cordillera* is made up of upper Jurassic to Cretaceous tholeiitic arc rocks and marine backarc strata that are partly covered by Oligocene to Miocene alluvial deposits (Wörner et al., 2002) (Fig. 2A, B). In the study area, the Coastal Cordillera forms a steep cliff ca. 500 m high that parallels the Andean strike, and that gently dips towards the east. At Arica, the Coastal Cordillera dips beneath the Peruvian coastal plain (Fig. 1) (Salas et al., 1966; Tosdal et al., 1984). Hanging paleochannels that are incised into the basement of the Coastal Cordillera are in many places cut at the coastal cliff (Fig. 2A, C). To the east of the *Coastal Cordillera* starts the *Western Escarpment* that comprises (from W to E) the *Pampa de Diablo*, the *Oxaya Antiform*, and the *Pampa de Oxaya* (Fig. 1). These pampas form a westward dipping ramp and are the result of multiple erosional and depositional phases during the Miocene (Mortimer and Saric, 1975;

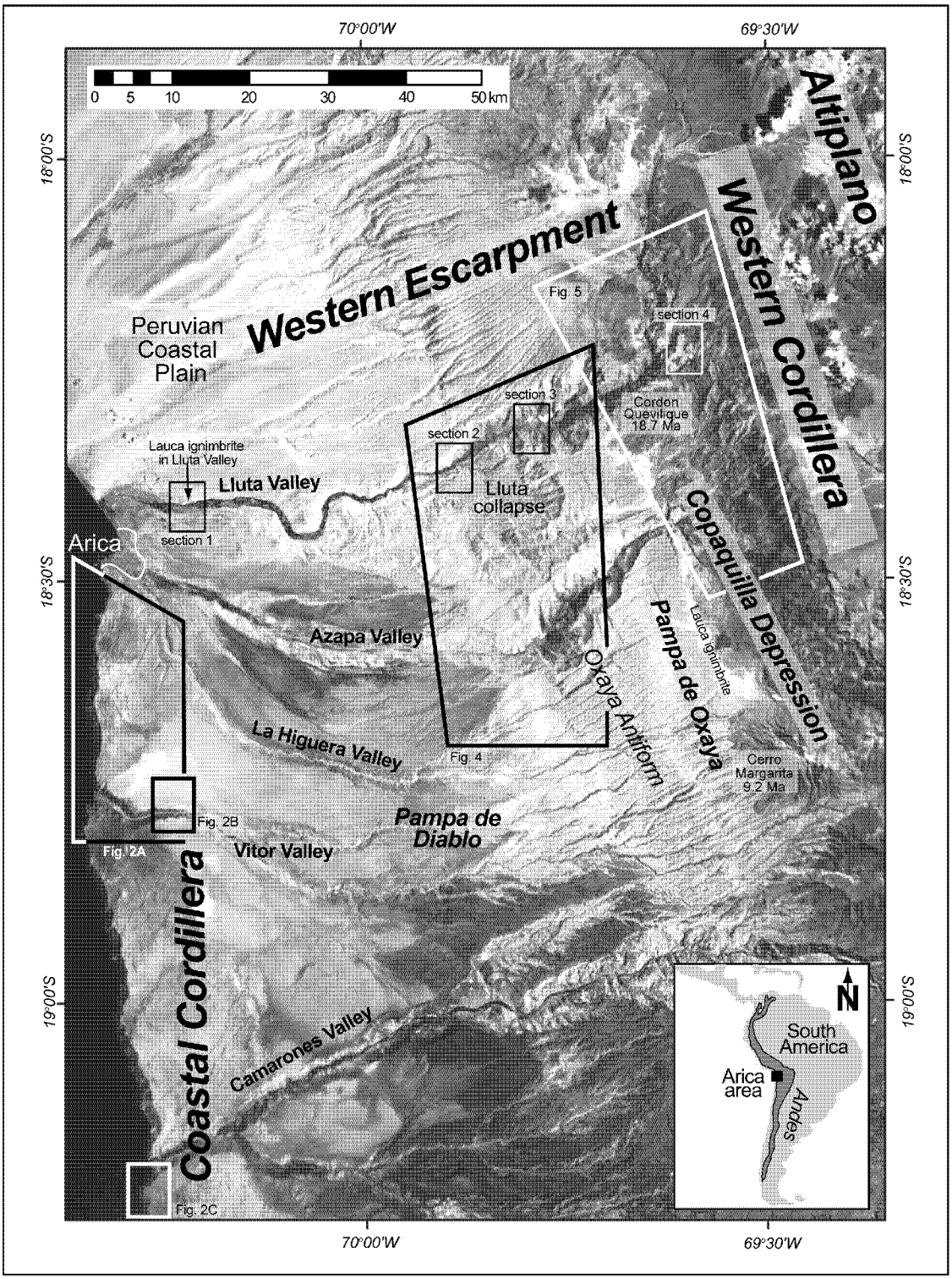

Fig. 1 Landsat image and location of study area of the Western Escarpment of the Andes of northern Chile, showing the most important geomorphic units discussed in the text.

Mortimer, 1980; Wörner et al., 2002). As will be discussed in detail below, we will use the Pampa de Diablo as reference base level prior to the formation of the major valleys. A formation age of 7.5 Ma was assigned to this Pampa according to magnetostratigraphic chronologies of the underlying strata (von Rotz, 2003). In the vicinity of the *Oxaya Antiform*, the Pampa de Oxaya lies at 3000-3600 m above sea level. It dips towards the east, and is characterized by the presence of E-W aligned relict valleys 20-100 m deep separated by ridges with nearly constant curvatures (Figs. 1, 4A). These valleys deepen and widen towards the west indicating a west-directed paleoflow (Wörner et al., 2002). At present, discharge today occurs in the opposite direction (i.e. towards the east, Fig. 4A). The substratum of the pampa (Fig. 3) is the ca. 23-19 Ma-old sequence of ignimbrite sheets and interbedded fluvial sediments that make up the Oxaya Formation (García, 2002). This unit blankets an antecedent mountainous landscape with Mesozoic/Cenozoic plutonic and metasedimentary rocks in its core (east-ward migrating evolving arc - basement on Fig. 4B). The western border of this primary Oligocene landscape was formed by a reverse fault system (Ausipar fault system, Fig. 4A, B) that accommodated crustal shortening (Munoz and Charrier, 1996; Garcia, 2002; Mörner et al. 2002).

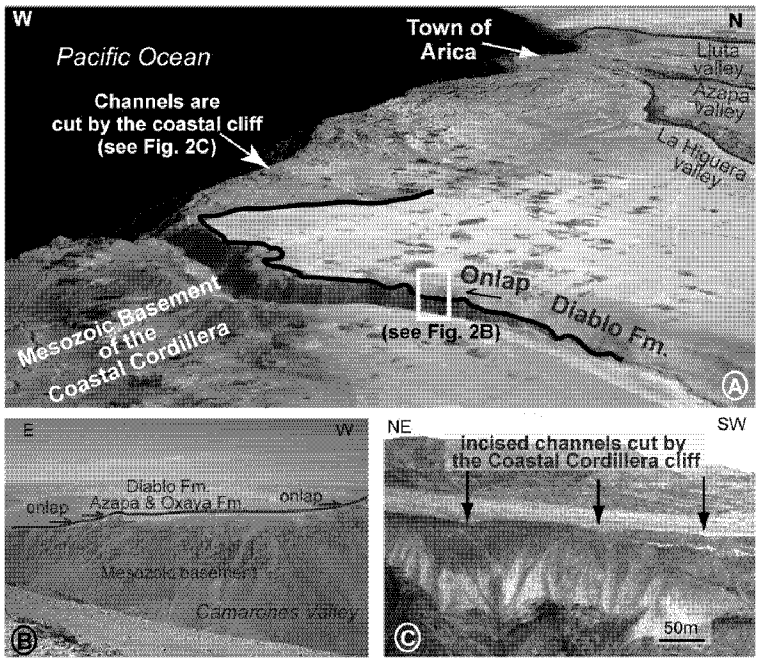

Fig. 2 A) 3-D perspective view of the coastal area and geologic interpretation showing the relationships between the Coastal Cordillera and the overlying deposits. The perspective view which is oriented to the NW was achieved by underlying the landsat image of Fig. 1 with 50 m-resolution DEM. See Fig. 1 for location and scale. Because of accessibility in the field, sub-picture A and B are taken from valleys farther south (Fig. 1). B) Onlap situation similar at the Vitor valley (A), but here in the Camarones valley (Fig.1). C) Detailed situation of cut channels by the Coastal Cordillera similar at the mouth of the Vitor valley (A), but here at the Camarones river mouth.

It appears that uplift along this fault and subsequent erosion resulted in construction of a >400 m-thick sequence of high-concentrated flow deposits (25-23 Ma-old Azapa Formation) adjacent to this fault (García, 2002).

West of the Oxaya Antiform is the *Pampa de Diablo* (Fig. 1). This geomorphic feature forms a gently westward dipping ramp that is cut by valleys with local (e.g., Vitor and Camarones valleys, Fig. 1) and distal sources (e.g. Lluta and Azapa valleys). The Pampa de Diablo is underlain by (in stratigraphic order) the westward thinning Azapa Formation, the Oxaya Formation and the Diablo Formation (Fig. 3). This latter unit, deposited between ca. 19-7.5 Ma according to Rb-Sr ages of interbedded ash layers, covering ignimbrites (García, 2002) and new magnetostratigraphic chronologies (von Rotz, 2003), is made up of a large-scale coarsening- and thickening upward sequence with dm-thick mudflows at its base and fluvial trough cross-bedded m-thick conglomerate beds at its top. In the Arica area where the Coastal Cordillera is stratigraphically and morphological below the Peruvian Coastal Plains (Fig. 1), the dispersal systems of the Diablo Formation discharged into the Pacific Ocean (see below for details). South of Arica, however, the fluvio-lacustrine deposits of the Diablo Formation (and Oxaya Formation) onlap, and partly overlap the crystalline basement of the Coastal Cordillera (Fig. 2B). In the Longitudinal Valley some hundreds of kilometers farther south, however, the dispersal systems of the Diablo Formation have had a closed drainage until present (Hartley and Chong, 2002). The occurrence of andesitic and metasedimentary clasts suggests erosion of the Miocene andesitic volcanoes (e.g. the 18.7 Ma old Cordon Quelvilque, and the 9.2 Ma old Cerro Margarita, Fig. 1) and of basement rocks that are exposed in the Western Andean Cordillera (García, 2002; Wörner et al., 2002).

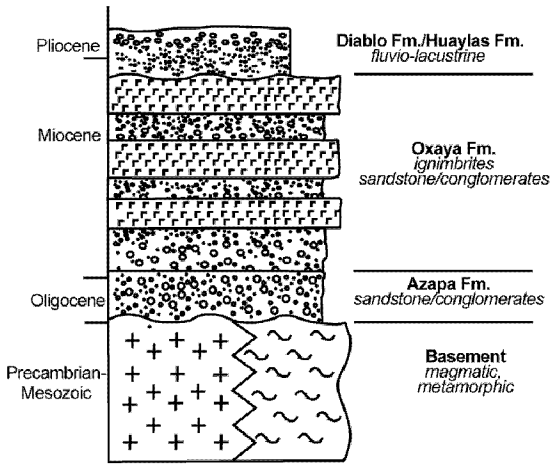

Fig. 3 Stratigraphic scheme of the Western Escarpment of the Andes of northern Chile (simplified after Salas, 1966; Garcia 2002; Wörner et al., 2002).

The *Copaquilla depression* (García, 2002) (Figs. 1, 5) is made up of a >300 m-thick series of fluvio-lacustrine sediments (e.g., Huaylas Formation) that were deposited between ca. 18 and 7 Ma according to K-Ar ages of interbedded ignimbrites and tuffs (García, 2002). The Huaylas deposits were sourced from the Western Andean Cordillera (that is made up of the metamorphic basement, Miocene to modern volcanoes and Miocene to modern fluvio-lacustrine deposits). Locally, the Miocene depositional surface of the Huaylas unit is still well preserved, displaying a fan-shaped surface with a convex curvature. In the Copaquilla depression, the Huaylas Formation is overlain by the 2.7 Ma-old Lauca ignimbrite (Fig. 5, Wörner et al., 2002), with an erosional unconformity between both units.

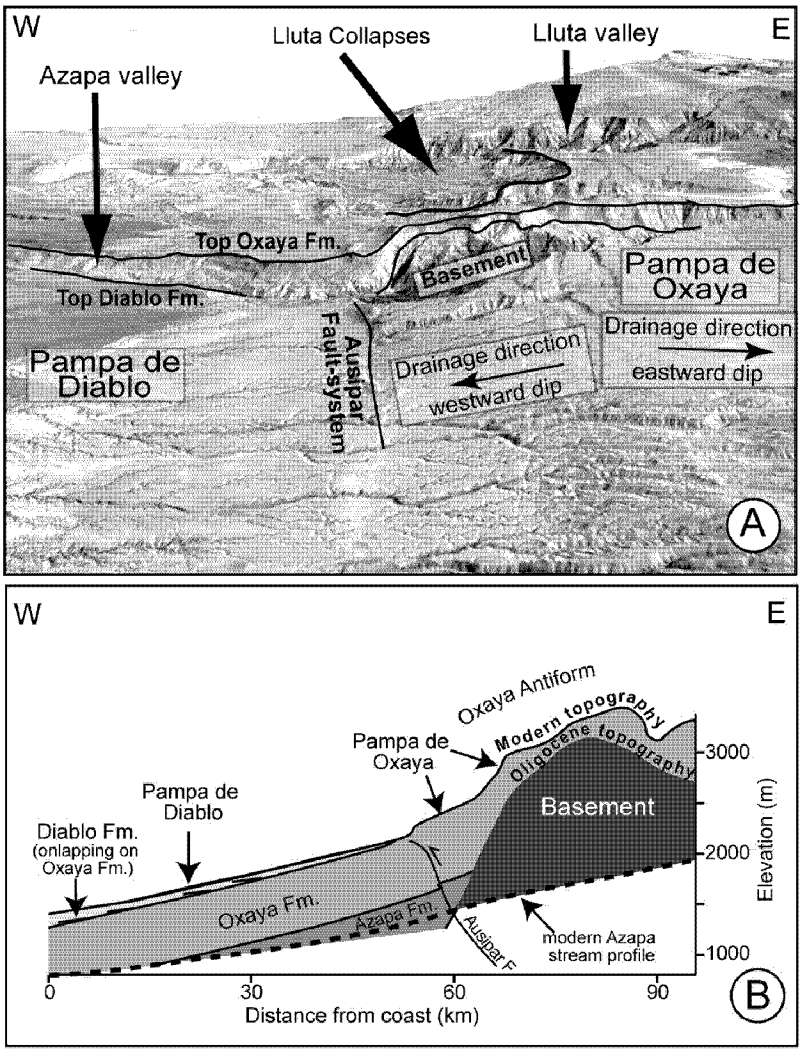

Fig. 4 3-D perspective view of the Pampa de Diablo and the Pampa de Oxaya (A), and geomorphic and geologic interpretation that is presented as a cross-section (B). See note to Fig. 2 for explanation of methodology of 3-D view calculation and scale. The 3D view is oriented to the N. Valleys here cut ca. 1000 m deep.

The *Lluta collapse* (Figs. 1, 6) is a giant landslide that covers an area of ca. 600 km^2, and that displaced ca. 50 km^3 of rocks (Wörner et al., 2002; Strasser, 2003). The basal detachment of the Lluta collapse is the top of the Azapa Formation; the slip plane is well exposed on both sides of the Lluta valley. Because slide blocks are found on both sides of the Lluta valley, Wörner et al. thought that initiation of landsliding predates the formation of the Lluta valley. However, a postdating alternative interpretation was proposed by Strasser (2003). The slide blocks are overlain by conglomerates, sandstones and siltstones that were deposited in a fluvio-lacustrine environment (Strasser, 2003). The clasts and boulders of the Lluta-collapse deposits are Oxaya ignimbrites close to the escarpment, suggesting a local provenance. Farther north in the Lluta valley, these sediments are interbedded with conglomerates that reveal a distal source (low-grade metasedimentary clasts, and clasts from granites and andesites of the Western Andean Cordillera).

Finally, the *Western Cordillera* forms the modern magmatic arc system of the Central Andes with heights up to 6000m. This unit is composed of Miocene to Holocene volcanic and sedimentary rocks that were deposited in interarc sedimentary basins on a Precambrian basement (Wörner et al., 2002). The headwaters of the main rivers (Lluta river, Azapa river) charge their water here.

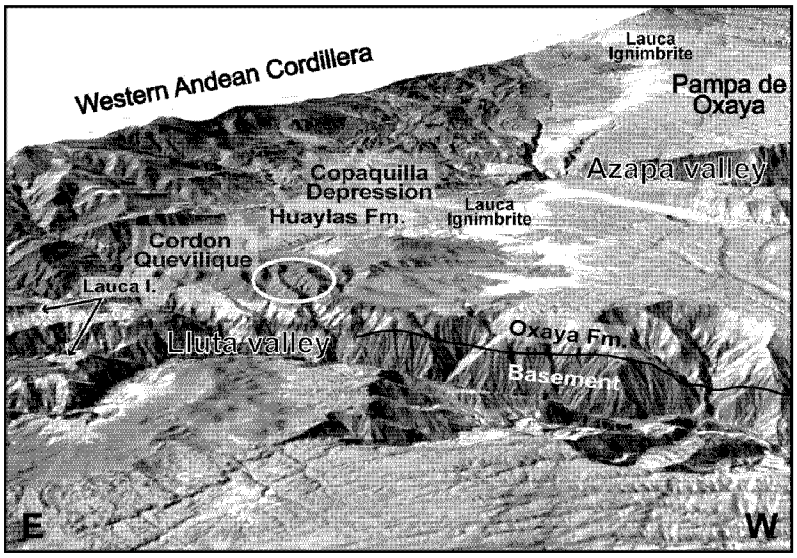

Fig. 5 3-D perspective view of the Pampa de Oxaya, the Copaquilla depression and the Western Cordillera, and geomorphic and geologic interpretations. The view is towards the SE. Here, the Azapa and Lluta valleys are up to 1500 m deep. See note to Fig. 2 for explanation of methodology of 3-D view calculation and scale.

2.4 Reconstruction of the geomorphic situation prior to dissection

In order to define a spatial and temporal datum that is needed here as reference for the situation prior to the major phase of valley formation, the top of the Diablo and Huyalas

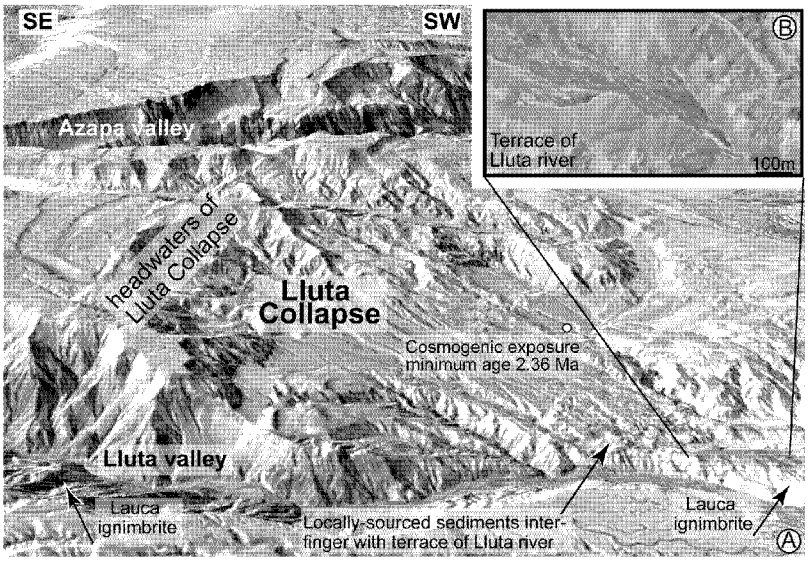

Fig. 6 (A) 3-D perspective view of the Lluta landslide with view to the south. See note to Fig. 2 for explanation of methodology of 3-D view calculation and scale. (B) Detail of parts of the >2.4 Ma old Lluta-river base level showing the pattern of abundant network of channels and bars.

Formations appear the prime target. The Diablo and Huyalas Formations were deposited during the same time interval (Fig. 3). Both units have abundant andesitc clasts which suggest a distal provenance (i.e. the Western Andean Cordillera, e.g., Garcia, 2002). Because of the isochronous relationship between the Diablo and Huyalas Formations and the similar petrographic composition of the deposits, we interpret that both depositional realms were hydrologically linked. This implies that deposition in the Diablo and the Huyalas areas were presumably controlled by an identical regional base level that is assigned to as Diablo base level in this paper. Furthermore, because the youngest deposits of the Diablo Formation was dated with 7.5 Ma according to magnetopolarity stratigraphies (von Rotz, 2003), we tentatively assign this Late Miocene age to the Diablo base level.

In the Arica area, however, the Diablo base level has its current position ca. 350m above the modern sea level ca. 10 km inland. Here, this unit is made up of trough cross-bedded conglomerates without any evidence of lacustrine (or playa) deposits, suggesting deposition on a braidplain (Gracia, 2002). This implies that the system feeding the Diablo Formation was hydrologically open and hence must have discharged into the Pacific. Because the rivers feeding the Diablo Formation were open to the Pacific, base level lowering (possibly either due to surface uplift or due to subsidence of crustal segments; Salas, 1966) must have likely initiated incision of the Lluta, Azapa and all other valleys in the study area. However, this phase of base-level lowering must have terminated at 2.7 Ma at the latest as a

fragment of the Lauca ignimbrite is found in the lower Lluta valley (see also Wörner et al., 2002) (Fig. 1).

The Diablo base level that is currently ca. 350m above sea level appears not only to have controlled aggradation of sediment in the Diablo and Huaylas sedimentary realms, but it probably also affected the large-scale morphometric properties of the Western Andean Cordillera. We observed that in this part of the Andes hillslopes are smooth and covered by a regolith > 1m thick, and that the hillslopes reveal tangential lower contacts to the depositional surfaces of the Huaylas Formation, which in turn was assigned to be part of the Diablo base level above. Because Huaylas and Diablo depositional surfaces are still well preserved (see Mortimer and Saric, 1975; Mortimer, 1980; Wörner et al., 2002), these landscapes record to large extents surface processes during the time of the Diablo base level.

The aggradational nature of the conglomerates of the Diablo and Huaylas Formations and the smooth hillslopes with a m-thick regolith cover and tangential lower surfaces suggest that here, the rates of geomorphic processes have been to a large extent transport limited. Support for this interpretation is given by two sets of results from theoretical models (e.g. Tucker and Slingerland, 1996; Simpson and Schlunegger, 2003). First, a regolith cover and the smooth nature of the hillslopes imply that the dip angles and the curvatures of the hillslopes are controlled by transport rates of regolith (e.g. Tucker and Slingerland, 1997). Second, aggradation of conglomerates in the Diablo and Huaylas depositional realms suggest that the sediment routing systems were at their transport capacity.

The transport-limited stage of sediment flux during deposition of the Diablo and Huaylas Formations implies that at that time, the Western Escarpment of the Andes of northern Chile was presumably in a stage of geomorphic decay. This interpretation is confirmed by theoretical concepts of landscape evolution (e.g. Tucker and Slingerland, 1996; 1997; Whipple et al., 1999). According to these models, geomorphic processes with transport-limited fluxes will result in a decrease in the local and the drainage basin relief, which, in turn, is indicative for the stage of geomorphic decay of a landscape. This situation, however, changed at ca. 7.5 Ma as the lowering of the base-level in the Coastal Cordillera caused dissection and headward erosion of the rivers sourced in the eastern parts of the Western Escarpment and the Western Cordillera, respectively. This new stage of landscape rejuvenation will be explored in more detail in the following sections.

2.5 Headward erosion and changes in relief

The stream profiles especially of the distally sourced systems (i.e. the Azapa valley, and the Lluta River) display two segments separated by well-defined knickzones (Fig. 7A). Below these knickzones, the channel gradients of the streams continuously increase in the upstream direction. Similarly, immediately above the knickzones the channels are flat, and their gradients then continuously increase in the upstream direction. Furthermore, the cross-sectional geometries of the valleys reveal distinct trends in the upstream direction that closely correlate with the valley gradients and the distance from the present-day knickzones. Specifically, in the lower reaches where the gradients are flat, the valleys are wider than the river belts (that are made up of braided channels and longitudinal and transverse gravel bars), resulting in the establishment of large floodplains. Here, the rivers flow on alluvial gravels (alluvial channels, e.g. Tucker and Slingerland, 1996). Towards the knickzones, the valleys become narrower, and the gradients increase. In the uppermost 5 kilometers below the center of the knickzones, the rivers incise into bedrock (bedrock channels, e.g. Tucker and Slingerland, 1996), and the valley flanks are nearly vertical. Above the knickzones, the channel gradients decrease, the valleys widen and alluvial channels are occupying the valley floors.

The presence of knickzones that separate the stream profiles into two segments with distinct differences in stream gradients and valley morphologies is interpreted here to reflect that the fluvial systems accommodated the post 7.5 Ma-old lowering of the base level by headward erosion. According to this interpretation, the knickzones represent the locations of the erosional front, separating an older landscape with morphometric properties that still record the former base level (e.g., the Diablo base level) from a rejuvenated geomorphology that is currently adapting to the modern base level. Note that at present, the knickzones are located in the vicinity of basement-bedrock/Neogene conglomerate transitions (e.g. the Huaylas Fm.), at the interfluves of several tributaries and on abandoned tectonic features (west-vergent-thrust system of Munoz and Charrier, 1996). Therefore, it would be possible to interpret a lithological, tectonic and/or a discharge control on the establishment of a knickzone in these locations. In this case, the change in bedrock lithologies, the specific drainage pattern configuration in the locations of the present-day knickzones or, alternatively, enhanced rates of rock uplift in this location have simply resulted in an overall reduction of headward erosion rates or in a nearly stationary locus of the knickzone itself.

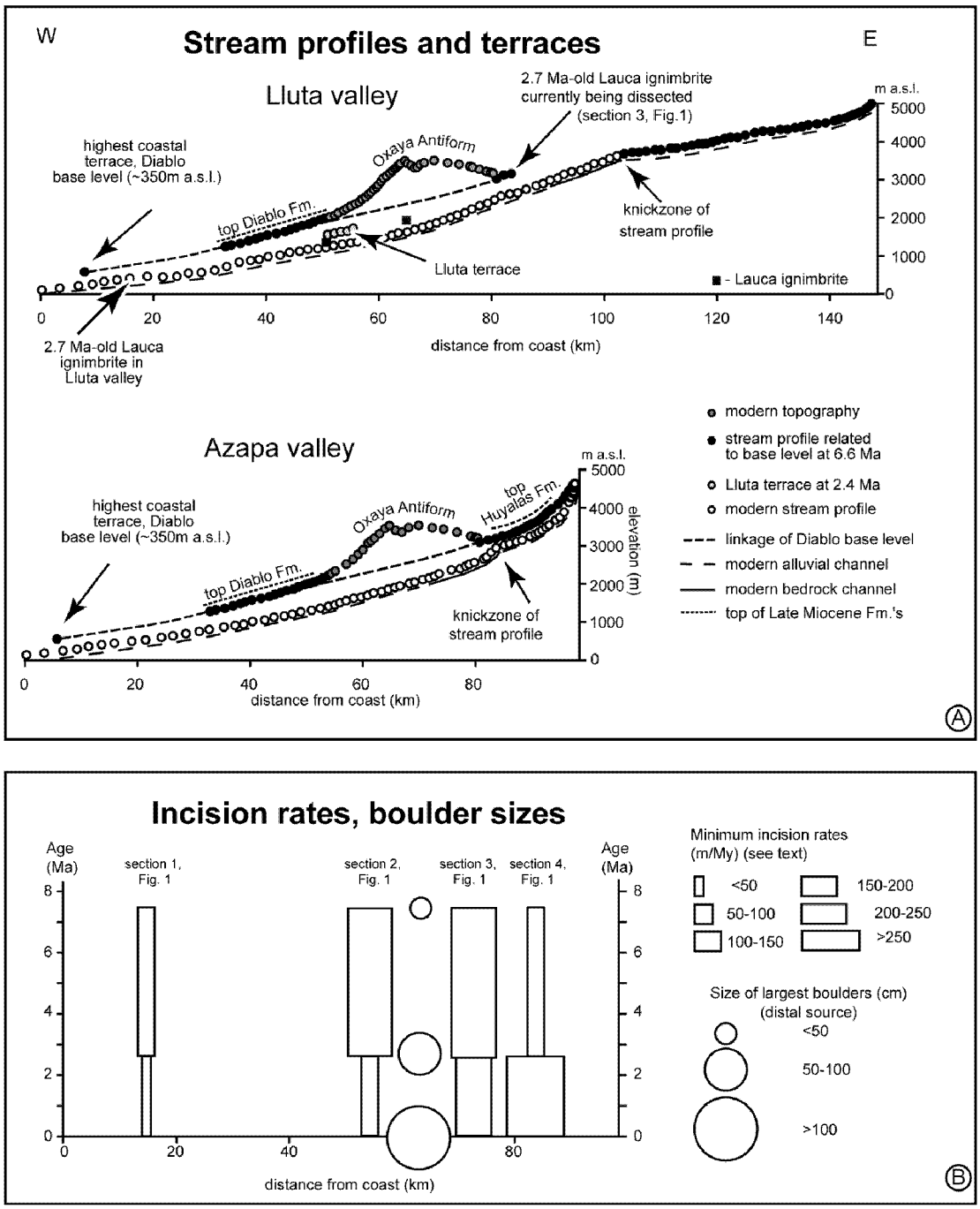

Fig. 7 (A) Morphometric information of Azapa valley, Lluta valley and the Diablo base-level, and (B) trends in incision rates and sizes of maximum clasts of Lluta river. See text for more information on data acquisition.

2.6 Increase in fluvial incision rates

Differences in elevations between fluvial and/or strath terraces of known ages are generally used to calculate fluvial incision rates. However, provided that surface uplift and the associated lowering of the base level is accommodated by headward erosion, then differences

in elevations between terraces of known ages will only yield information about average local incision rates, and they might differ from effective erosion rates. This is the case because during the process of headward erosion, the local incision rates first increase as the erosional front arrives, and then decrease as it passes. This pattern of temporally varying incision rates might not be seen if dated terraces of various elevations are used. Despite these drawbacks in assessing temporal and spatial changes in erosion rates, data are presented here to suggest that minimum local incision rates have increased between ca. 7.5 Ma and present. Wörner et al. (2002) suggested increasing incision rates between ca. 3 Ma and present.

Here, minimum incision rates are estimated for three sectors in the Lluta valley (see Fig.1, 7B). In the lower portion of the Lluta valley, fluvial dissection was initiated after deposition of the Diablo Fm. at < 7.5 Ma (as a result of base-level lowering in the Coastal Cordillera as discussed above). At 2.7 Ma at the latest, the modern base level was reached as indicated by the presence of Lauca ignimbrite fragments in the Lluta valley some tens of kilometers east of Arica (Fig. 1). In this location, the difference in elevation between the top of the Diablo formation and the broad valley floor measures ca. 350 m (Figs. 1, 7B), yielding rates of fluvial incision of ca. 70 m/My between 7.5 and 2.7 Ma. The modern Lluta-river course is presently further ca. 20-30 m lower in that location which results in incision rates towards present of less than 10 m/Ma, likely as a consequence of a more stable sea-base-level, flattest parts of longitudinal river profiles (most distal) and the long time since the erosional front passed.

In the middle sector of the Lluta valley at ca. 60 km distance from the coast (Fig. 1), alluvial terraces of the Lluta river lie 300 m beneath the top of the Diablo Fm., and 350 m above the modern valley floor (Fig. 6, 7A). These deposits dip at an angle of ca. 3.5° in a NNW-direction towards the Lluta valley. Based on a detailed reconstruction of the stratigraphy in this area, Strasser (2003) found that the deposits of the Lluta river terrace (Fig. 6) interfinger with the detritus sourced from the headwaters of the Lluta collapse. We estimated the time when the formation of this terrace system ended using concentrations of cosmogenically produced ^{21}Ne in quartz (see Table 1 for explanation, and Fig. 6A for sample site). This methodology yields a minimum exposure age of 2.36±0.23 Ma for this terrace system. However, in the same location an ignimbrite that overlies distally sourced conglomerates ca. 20m above the present valley floor possibly represents the Lauca-ignimbrite. The same ignimbrite is found 260m above the modern valley floor ca. 15km farther east (Fig. 7A). Using this constraints the resulting incision rates measure ca. 200 m/My between 7.5 and 2.7 Ma, and between 50-100 m/My between 2.7 Ma and present. We

cannot completely exclude the possibility that the formation of the Lluta river terrace is simply the result of a cut-and-fill process that might have been initiated by the Lluta landslide. However, since evidence of lacustrine sediments in the higher portion east of the Lluta landslide is missing, we do not consider that this landslide significantly altered the base level and hence the lowering process of the Lluta river.

Finally, at ca. 85 km distance from the ocean (Fig. 1), the Lluta River has cut into 2.7 Ma-old Lauca ignimbrite deposits (Figs. 1, 5) that lie ca. 300 m beneath the Diablo base level, and ca. 900 m above the modern valley floor. The resulting incision rates are ca. 60 m/My between 7.5 and 2.7 Ma, and >300 m/My between 2.7 Ma and present.

From the stratigraphic evidence we conclude that the locus of enhanced incision shifted from the coast to the Western Andean Cordillera (Fig. 7B), and that the time interval between ca. 2.7 Ma and present is characterized by maximum incision rates especially in the upper catchments (Fig. 7B).

2.7 Temporal trends in stream power

Flume experiments reveal that flowing water exerts a shear stress on the riverbed that is proportional to the product between stream gradient and water discharge if the flow is unconfined (Bagnold, 1966). This shear stress results in erosion and transport of sediment as bedload if a threshold is exceeded. This critical magnitude depends on the sorting of the bed material, the state of the armouring of the bed by a layer of coarse material, and in particular on the particle sizes of the sediment. Specifically, the critical shear stress has to increase to entrain particles with increasing sizes (especially, if stream gradients decrease during the same time interval).

For the Lluta system, temporal changes of maximum shear stress are estimated at 50 km distance from the ocean (i.e. in the location of the earlier described Lluta terrace, section 2, Figs. 1, 7B) using the diameters of the largest clasts that had a distal source (i.e. clasts from andesites and granites). Specifically, for each stratigraphic unit that represents the base levels of Fig. 7B (conglomerates of Diablo Formation, >2.4 Ma-old terrace of Lluta river, and modern Lluta deposits) we selected at least two >100-500 m^2-large areas where we measured the size of ca. 20-50 clasts. From these dataset the maximum diameters of the five largest clasts are presented on Figure 8B. The data reveal a general increase in the maximum clast size from ca. 50 cm for the 7.5 Ma-old deposits (i.e. the top of the Diablo Formation), to 50-100 cm for the >2.4 Ma-old Lluta terrace reference, and to diameters >100 cm for the modern

deposits. In these locations, erosional scours exceeding depths of 1 m are absent and the bars are horizontally stratified, implying that the flow has generally been unconfined. Consequently, the observed general increase in the size of the largest clasts is interpreted here to indicate an augmentation in the magnitudes of maximum discharge events.

Farther west in the Arica area, however, channels that were incised into basement of the Coastal Cordillera are truncated at the coastal steep cliff. Furthermore, they lack any evidence of any re-incision (Fig. 2C). This implies, that in the coastal region precipitation rates fell below the threshold conditions for fluvial incision at 3 Ma at the latest (i.e. at the time when the phase of major base-level lowering was terminated).

2.8 Comparative estimates of sediment yields

The excellent preservation of the relict Late Miocene plain – the Diablo landscape - that formed prior to dissection allows the calculation of sediments yields for systems with various sources. Furthermore, because the erosional systems that drain the Arica area have cut through the same lithological architecture, and since incision was initiated for all analyzed systems at the same time (i.e. 7.5 Ma, see above), the comparison of volumes of eroded rocks allows interpreting possible controls of water discharge on surface erosion rates. Specifically, we aim at identifying whether possible orographic effects of precipitation have had an influence on erosion rates.

Figure 8 illustrates the calculated volumes of rocks that were eroded between 7.5 Ma and present, the present day sizes of the drainage basins for the systems draining the Arica area, and a resulting erosion rate. The resulting sediment yields are ~15 m/My for systems that are sourced in the Western Andean Cordillera (i.e. the rivers flowing through the Lluta and Azapa valleys), and <7 m/My for rivers with sources solely on the Escarpment. Note that these calculations assume no major increase in the size of the headwaters which might be expected because of headward erosion. However, catchments rather compete with the systems that discharge to the east (i.e., Altiplano, Mortimer and Saric, 1975). Because the sediment yields represent volumes of eroded rocks that are normalized to the size of the drainage basins, the differences in yields cannot be explained by the various sizes of the headwaters. It appears that the enhanced erosional efficiencies calculated for the rivers with sources in the Western Andean Cordillera simply reflect the observation that modern precipitation rates significantly increase towards the Western Cordillera. As will be argued in the next section,

the contrasts in precipitation rates between the coastal region and the Western Andean Cordillera have become enhanced at least between 7.5 Ma and present.

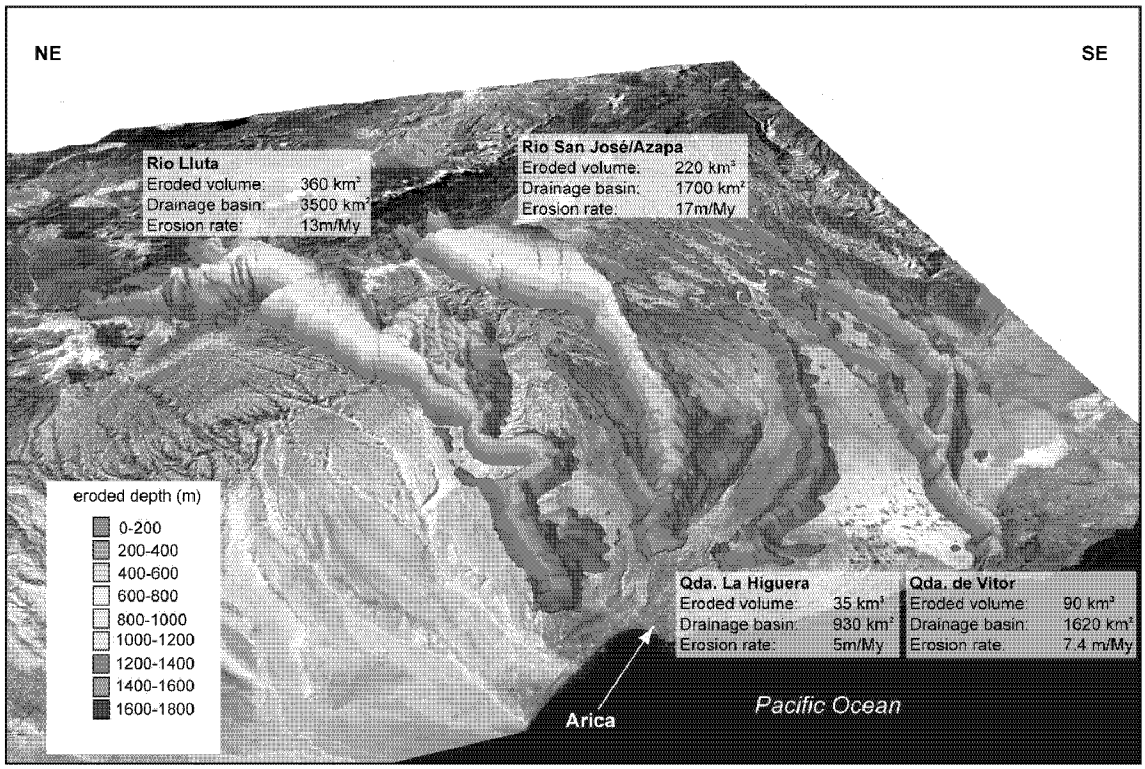

Fig. 8 Comparison between volumes of eroded rocks (differential modelling, see text for obtainment), catchment size, and resulting sediment yields of distally- and locally-sourced rivers. See Fig.1 for scale.

2.9 Discussion

It was outlined before that fluvial dissection and valley formation was initiated at ca. 7.5 Ma as a result of a major base-level change in the coastal area, and that the fluvial processes have adapted to the new base level by headward erosion. The climate component in valley formation was identified in the comparison between sediment yields calculated for systems with distal and local sources, revealing that the larger yields calculated for the distally sourced systems most likely resulted from the effect of orographic precipitation. Here we will argue that the effect of orographic precipitation has become enhanced between the Late Miocene/Pliocene and present. Support for this interpretation is given by the general coarsening trend in the clast size of the conglomerates and the contemporaneous increase in headward erosion rates. These information imply an increase in effective water discharge. However, a tectonic control cannot be ruled out at the moment (e.g., monoclinal surface uplift proposed by Isacks, 1988, which might have the same effect), so the solution appears non-

unique. Nevertheless, if the tectonic component would be the dominant force driving headward erosion, then rates of monoclinal surface uplift needs to have become enhanced at 3 Ma at the time when incision rates increased (as observed in the Aricas area). Existing data, however, do not support such a scenario (Isacks, 1988; Gregory-Wodzicki, 2000). Therefore, the enhanced discharge scenario has to be considered to explain the increase in both the sizes of the largest clasts and incision rates between ca. 3 Ma and present (Fig. 7B), and the overall evolution of the valley systems. This does not mean, however, that the Andes of Chile have become more humid between the Late Miocene and present. Indeed, the presence of valleys that are cut by the coastal cliff implies that in the lower portions of the study area, precipitation rates fell below the threshold conditions for fluvial incision of systems with small catchments. Similarly, theoretical considerations about controls on erosion led Molnar (2001) to conclude that an increase in aridity (and hence a decrease in average precipitation rates) might even result in an increase in erosion rates provided that the frequency and the magnitudes of large flood increase (as supported by the observed increase in the size of the largest clasts), i.e. such an increase might even occur even if average water discharge decreases. The presented data do not allow estimation of whether average precipitation rates decreased. They only indicate a shift towards a more incisive climate, and towards an enhancement of the effect of orographic precipitation as the system evolved.

2.10 Conclusion

The stratigraphic and morphometric data and observation from the Western Escarpment of northern Chile (Arica area) imply that a major phase of valley formation resulted from base-level lowering in the Coastal Cordillera that was initiated at ca. 7.5 Ma, and that was almost completed at 2.7 Ma at the latest. Additional small-scale base-level changes as recorded in several terraces farther to the north (S'-Peru, Ortlieb et al., 1996a) and to the south (e.g., Antofagasta, Ortlieb et al., 1996b) would not result in such prominent incision features. The stratigraphic and geomorphic data also indicate that fluvial incision and valley formation have become enhanced during the last 3 My presumably as a result of enhanced effective water discharge. During the same time interval, however, the Coastal Cordillera and the Atacama Desert became hyperarid (Hartley and Chong, 2002). It appears, therefore, that precipitation became restricted to the higher parts of the Western Escarpment and the Western Cordillera where the major rivers are sourced that deeply cut into the Oxaya and Diablo landscapes. That also highlights the orographic effect on the precipitation pattern

due to the raising Andes. The hyperarid conditions that established in the lower elevations of the northern Andes of Chile caused the Miocene/Pliocene strata to become covered by crusts of salt and anhydrite that even blanket hillslopes and summits especially in the region of the Coastal Cordillera. We interpret that this stabilization of surfaces decreased the sediment discharge from e.g. the Pampa de Diablo and Oxaya to the fluvial transport systems, possibly shifting the rivers into the supply limited stage. In case that the fluvial systems are transport-limited, a decrease in sediment discharge - especially at lower elevations - can result in an increase in incision and headward erosion rates.

Acknowledgements

We thank G. Simpson and G. Hoke for discussions, R. Wieler, H. Baur, S. Ivy-Ochs, and P. Kubik for support while deducing cosmogenic nuclide data. The paper benefited from reviews by B. Horton, C. Duncan and S. Willett. This study was funded by the Swiss National Science Foundation (grant 620-576.663).

APPENDIX

Table 1 Cosmogenic ^{21}Ne-data. All concentrations given and calculated for sampling site. Sample CN8 - boulder on abandoned terrace, CN10 - boulder in the youngest wash (lower side), assuming a geological blank case. Sample preparation following Ivy-Ochs et al. (1996). Ne-data represent cosmogenic-temperature step of 600^0C, higher steps were air. $^{21}Ne_{cosmo}$-concentration calculated as excess over air. Production rates used after Niedermann (2000) and scaled by modified Lal (1991) and Dunai (2000). Density ρ=2.375gcm^{-3}, attenuation length Λ=160gcm^{-2}.Erosion rates are defined by erosion-island-plots of Ne/Be-Be (Kober et al., 2002).

Sample	^{20}Ne	^{21}Ne/^{20}Ne	^{22}Ne/^{20}Ne	$^{21}Ne_{cosmo}$	blank corrected $^{21}Ne_{cosmo}$	age (corrected for 70cm/My erosion)
	[10^9atoms/g]			[10^7atoms/g]	[10^7atoms/g]	[10^6yr]
CN8b	13.729±0.026	0.00635±0.00081	0.1059±0.0035	4.659±0.216	3.874±0.287	2.36±0.23
CN10(blank)	5.622±0.248	0.0043±0.000647	0.104±0.0025			

3 Denudation rates and a topography-driven precipitation threshold in northern Chile: multiple cosmogenic nuclide data and sediment yield budgets [1]

F. Kober[a, b], S. Ivy-Ochs[c,d], F. Schlunegger[e], H. Baur[b], P.W. Kubik[f], R. Wieler[b]

[a] *Institute of Geology, ETH Zurich, CH-8092 Zurich, Switzerland,*

email: kober@erdw.ethz.ch, Tel.: ++41-1-6320361

[b] *Institute of Isotope Geology, ETH Zurich, CH-8092 Zurich, Switzerland,*

[c] *Institute of Particle Physics, ETH Hoenggerberg,CH-8093 Zurich, Switzerland*

[d] *Institute of Geography, University of Zurich-Irchel, CH-8057 Zurich, Switzerland*

[e] *Institute of Geology, University of Bern, CH-3012 Bern, Switzerland*

[f] *PSI/c/o Institute of Particle Physics, ETH Hoenggerberg,CH-8093 Zurich, Switzerland*

3.1 Abstract

The quantification of geomorphic process rates on the outcrop and the orogen scale is important to describe accurately the interaction between the effects of erosion, tectonics and climate. We report erosion rates on hillslope interfluves in the western Central Andes derived from long-lived (^{10}Be, ^{26}Al) and stable (^{21}Ne) cosmogenic nuclides that show a positive correlation with elevation and with present-day precipitation rates. Erosion rates at lower altitudes - the hyperarid *Coastal Cordillera* and the *Western Escarpment* with the northern part of the *Atacama Desert* - are on the order of 10-100 cm/my (nominal exposure ages 1-6 my). These erosion rates have been so low since at least the middle-late Miocene. In contrast, erosion rates at higher altitudes - the semiarid *Western Cordillera* - range up to 4600 cm/my (nominal exposure ages 0.02-0.1 my). These values have persisted since at least the Pleistocene/Holocene. This orographically controlled pattern of precipitation and erosion is also reflected in the pattern of denudation rates derived from sediment yield data. Specifically, denudation rates calculated from sediment flux data are of a similar order of magnitude as those deduced from long-lived nuclides for the *Western Cordillera*.

[1] Submitted to *Geomorphology*.

A sediment input deficiency in the Chile-Peru trench has been postulated to have played a key role in the uplift of the Andes in the Late Cenozoic. This would imply that climate is the main parameter controlling the present geodynamic state of the Central Andes. The low erosion and denudation rates we calculate from our cosmogenic data provide evidence that the supply of sediment from the western Andean slope to the Chile-Peru trench was limited.

The analysis of multiple cosmogenic nuclides allowed the simultaneous determination of erosion rates and exposure ages but also revealed complex exposure histories of non-bedrock samples, such as boulders or amalgamated clast samples. Specifically, this study reveals that saturation of nuclides, usually assumed in studies where only a single nuclide is analyzed, is rather the exception than the rule, as revealed by steady state erosion island plots. Constant erosion that started later than the formation age of the rocks or episodic erosion by spalling can partially explain such non-steady state concentrations. Furthermore, the use of nuclides with different half-lives allowed us to infer that no significant variations in erosion rates over prolonged time periods has occurred and that at the *Western Escarpment* erosion rates have been low and constant during the late Neogene. Nevertheless, the time intervals necessary to reach steady-state concentrations for cosmogenic nuclides can be different from those needed for landscapes to reach steady-state.

Keywords: *cosmogenic nuclides (^{10}Be, ^{26}Al, ^{21}Ne), erosion rates, erosion island plots, orographic precipitation, landscape evolution, northern Chile*

3.2 Introduction

The extent and the scale to which precipitation, and climate in general, influence the nature and the rates of surface erosion, sediment transport and landscape evolution is difficult to evaluate until more quantitative data are available on rates of landscape change. A number of recent studies have been made which measured rates of landscape change by means of cosmogenic nuclides or geothermochronology. A goal of these studies was to quantify the relationships between tectonic, climatic, geochemical or lithological interactions. For instance, von Blanckenburg et al. (2004) concluded that, in the steep tropical highlands of Sri Lanka, erosion rates appear to be independent on climate but are rather responding to tectonic forces. In contrast, Riebe et al. (2004) used cosmogenic radionuclides from diverse climatic regimes all in granitic terrains to illustrate that chemical weathering intensity varies

systematically with climate. Nevertheless, tectonic uplift was suggested to control chemical weathering rates via the generation of relief (Riebe et al., 2004). Reiners et al. (2003) discussed possible links between climate and erosion, suggesting that long term surface erosion (>10^6-10^7 yrs) is strongly coupled with modern precipitation rates in the Washington Cascades. In contrast, erosion and precipitation appear to have been decoupled in the Himalayas (Burbank et al., 2003). For the Taiwan orogen, erosion rates are reported to be coupled with variations in precipitation and seismicity (Dadson et al., 2003).

This paper presents an analysis of the possible interplay between precipitation, surface erosion and the rates at which landscapes change over various temporal and spatial scales. We present erosion rates and denudation rates on hillslope interfluves and high-altitude catchments for the western slope of the Central Andes (northern Chile) based on concentrations of multiple in-situ produced terrestrial cosmogenic nuclides (TCNs - ^{10}Be, ^{21}Ne and ^{26}Al) and sediment yield data. Such data are necessary to distinguish between the various driving forces (erosion, tectonics, and climate) and to determine the timing for the geodynamic evolution of the western Central Andes. Furthermore, they are crucial for the discussion of whether the Andes as morphological barrier led to the present climate conditions or if prevailing climate conditions led to the uplift of the Central Andes (Lamb and Davis, 2003).

Our study focuses on the geomorphic evolution of the western Andes in northern Chile, an area that exhibits broad relict Miocene landscapes indicative of slow rates of landscape modification (Mortimer and Saric, 1975; Mortimer, 1980). However, information on determinations of rates of landscape change are sparse (Gregory-Wodzicki, 2000, and references therein). The Neogene hyperarid climate was suggested to play a prime role controlling the landscape evolution of the Andes that favored the preservation of relict landscapes (Mortimer and Saric, 1975; Mortimer, 1980; Alpers and Brimhall, 1988; Montgomery et al., 2001). The hyperaridity is thought to have been initiated in the Late Cenozoic. While Dunai et al. (2005) suggest the onset of the dry climate occurred somewhere between 25-14My ago, Mortimer (1980) and Alpers and Brimhall (1988) suggested the onset around 15-9My, whereas Hartley (2003) proposed an initiation of hyperarid conditions as late as 4-3My. Late Quaternary climate fluctuations with wetter periods have been documented (e.g. Betancourt et al., 2000; Grosjean et al., 2003). As the time of onset of arid climate conditions and associated sediment flux reduction is suggested to have played a key role in the geodynamic evolution of the Central Andes (Lamb and Davis, 2003) it is critical to improve the knowledge of the change of process rates for this region.

Crucial for the analysis and the modeling of mountain belt evolution is a knowledge of the current equilibrium state of the system, whether it is in a transient state or at steady state (Willet and Brandon, 2002), either on the outcrop or on the mountain belt scale. Hereby, TCN represent a powerful tool to constrain the temporal evolution of various geomorphic landforms (Cockburn and Summerfield, 2004, and references therein). TCN may integrate over more than one climatic cycle that are shaping landscapes. Especially the use of multiple nuclides allows one to distinguish between simple and complex exposure histories (Gosse and Phillips, 2001).

3.3 Study Area

3.3.1 Geologic/geomorphic setting

The western Andes of northern Chile are commonly subdivided into longitudinal-geomorphological units (Fig. 1). From west to east these are the *Coastal Cordillera*, the *Western Escarpment,* the *Western Cordillera* and the *Altiplano*. The different units are the result of the Cenozoic geodynamic evolution of the western Central Andes, dominated by crustal thickening and related uplift of the *Western Cordillera* and the *Altiplano*, and westward tilting of the *Western Escarpment* since the middle Miocene (Isacks, 1988; Gregory-Wodzicki, 2000; Wörner et al., 2002)). The magmatic and tectonic evolution of the *Coastal Cordillera* since the Cenozoic has been decoupled from the evolution of the *Western Escarpment* (Riquelme et al., 2003). At present, these two geomorphic units comprise broad undulating plains >1000km^2 in size that have been deeply incised by rivers (Rio Lluta, Rio Azapa, Rio Vitor) with sources in the eastern portion of the *Western Escarpment* and the *Western Cordillera* (Fig. 1).

The *Coastal Cordillera* is constructed of Upper Jurassic to Cretaceous tholeiitic arc rocks and marine backarc strata that are locally covered by Tertiary alluvial deposits (Wörner et al., 2002; Garcia and Herail, 2005) (Fig. 2). Except for the deep valleys mentioned above, the *Coastal Cordillera* represents a subdued relict landscape. This landscape is characterized by smooth hillslopes ca. 300 m high that display nearly constant curvatures, and by enclosed basins several kilometers wide (Mortimer, 1973; Mortimer, 1980). Adjacent to the *Coastal Cordillera* is the *Western Escarpment* that rises up to ~3600 m above sea level. In the west, this morphological unit forms a gently westward dipping surface (Pampa de Diablo) that is underlain by the fluviolacustrine deposits of the Miocene El Diablo Formation (Fig. 1). Towards the coast, the El Diablo deposits interfinger with the sedimentary cover of the

Coastal Cordillera (Mortimer, 1980; von Rotz et al., 2005.). The El Diablo Formation overlays an Oligo/Miocene series of fluvial, volcanic and volcanoclastic rocks (Azapa and Oxaya Formations) that are exposed in the eastern segment of the *Western Escarpment* (Pampa de Oxaya; Fig. 1). Similar to the topography of the *Coastal Cordillera*, the Pampa de Oxaya is characterized by E-W-aligned valleys with steep slopes separated by broad smooth surfaces. The local relief is subdued and ranges between 50-300 m. (Mortimer et al., 1974; Mortimer, 1980; Tosdal et al., 1984; Wörner et al., 2002) postulated that the Pampas represent a relict landscape that has been preserved since the late Miocene.

The *Western Cordillera* rises up to 4500 m above sea level, with some volcanoes exceeding even 6000 m in altitude. This geomorphic unit is made up of metamorphic, volcanic, volcanoclastic and sedimentary rocks (e.g., Lauca, Oxaya and Zapahuira Formations) that record a geologic history including burial, exhumation and intermittent volcanic activity (Wörner et al., 2000; Wörner et al., 2002). In contrast to the Pampa de Oxaya, the landscape of the *Western Cordillera* has been continuously modified by volcanic activity (Wörner et al., 2000), surface erosion and sediment transport.

East of the Western Cordillera is the *Altiplano*. For this geomorphic unit, sedimentologic and paleontologic data imply maximum surface uplift rates of 0.2-0.3 mm/yr between the late Miocene and the present (Gregory-Wodzicki, 2000). According to Isacks (1988) we interpret these rates to represent maximum estimates for any surface uplift rates on the *Western Escarpment*.

3.3.2 Climate

The regional climate of northern Chile is dominated by the SE-Pacific anticyclone, the cold water Humboldt Current and the orographic barrier effect of the Andes (Abele, 1991; Houston and Hartley, 2003). These effects led to a hyperarid climate in the *Coastal Cordillera* and the *Western Escarpment*, and a semiarid climate in the *Western Cordillera*. At present, rain and snow fall in the periglacial to nival zones (≥ 4500 m) of the *Western Cordillera* and the upper parts of the *Western Escarpment*. The area was only glaciated in the very high altitudes during the Quaternary, largely around the flanks of the volcanic cones (Ammann et al., 2001). At elevations between ~4500-3500 m moderate rainfall occurs between January and March (Bolivian Winter periods) with annual precipitation of <150 mm (Houston and Hartley, 2003) (Fig. 1). Only during times of intense Bolivian Winter and El Niño events, precipitation rates reach as much as 250-300 mm/yr (Walter et al., 1967; Hoffmann, 1975; Vuille, 1999; New et al., 2002; Houston and Hartley, 2003). In contrast, precipitation rates are

1 mm/yr and 10 mm/yr in the *Coastal Cordillera* and in the lower *Western Escarpment*, respectively (Hoffmann, 1975; Abele, 1990). On the coast, humidity is present in the form of coastal fog (Camanchaca).

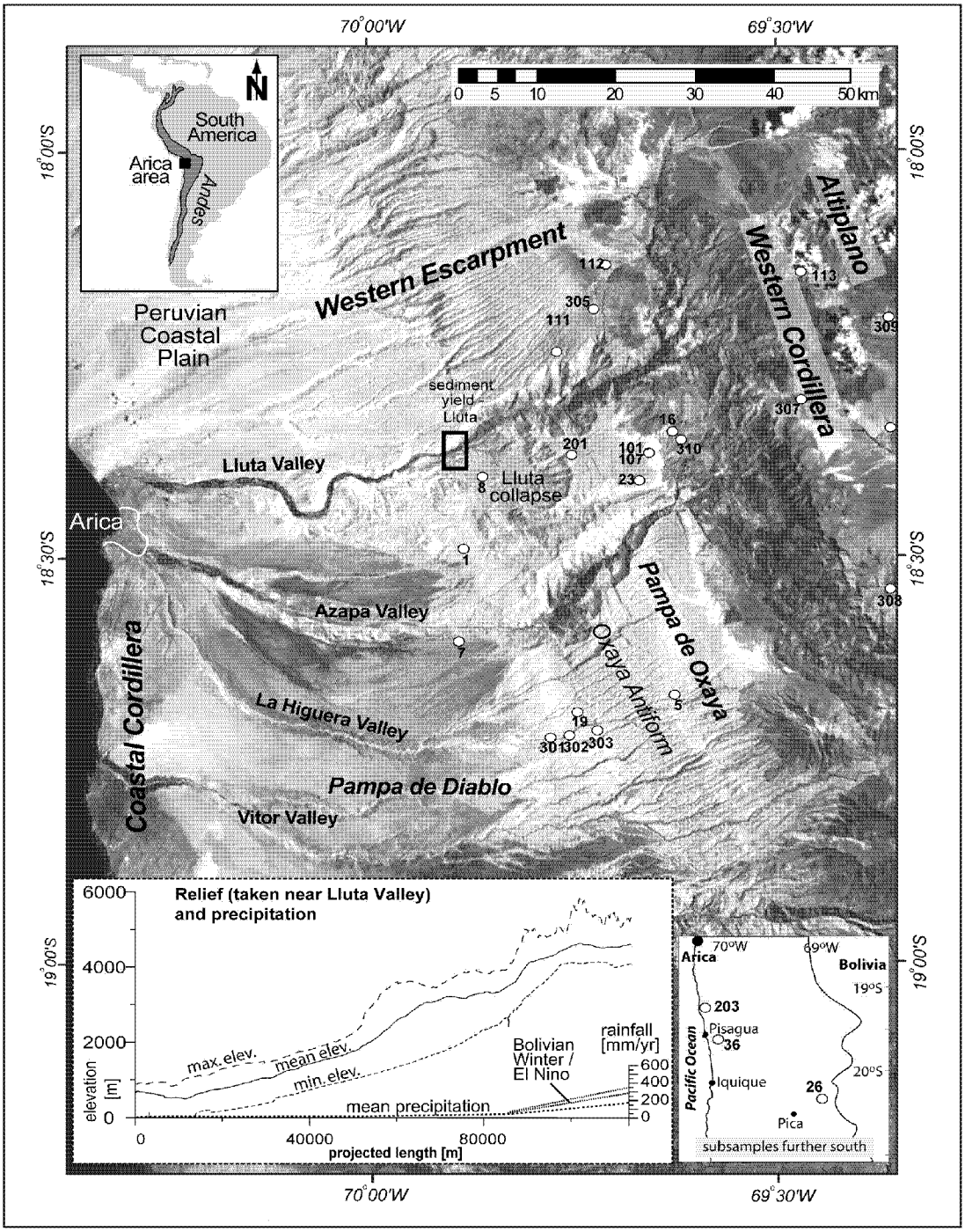

Fig. 1 Field area and sample locations in northern Chile. The lower left inset indicates minimum, mean and maximum elevations obtained north and south of the Lluta Valley. Rainfall data in this inset is from the literature (see text). The lower right inset shows the location of samples taken further south of the main study area.

At present, rain and snow fall occur in the periglacial to nival zones (≥ 4500m) of the *Western Cordillera* and the upper parts of *Western Escarpment*. At elevations between ~4500-3500m moderate rainfall occurs seasonal during November to March (Bolivian Winter periods) with precipitation rates of typically <150 mm/yr [37]. Only occasionally maximum values may exceed these values during severe Bolivian Winter and El Niño times with up to 250-300mm/yr (Walter, 1967; Hoffmann, 1975; New, 2002; Houston, 2003; Vuille, 1999 #907) (Fig. 1). In contrast, precipitation rates are 1-10mm/yr in the *Coastal Cordillera* and at the lower *Western Escarpment*, respectively, and humidity is rather controlled by the coastal fog (camanchaca).

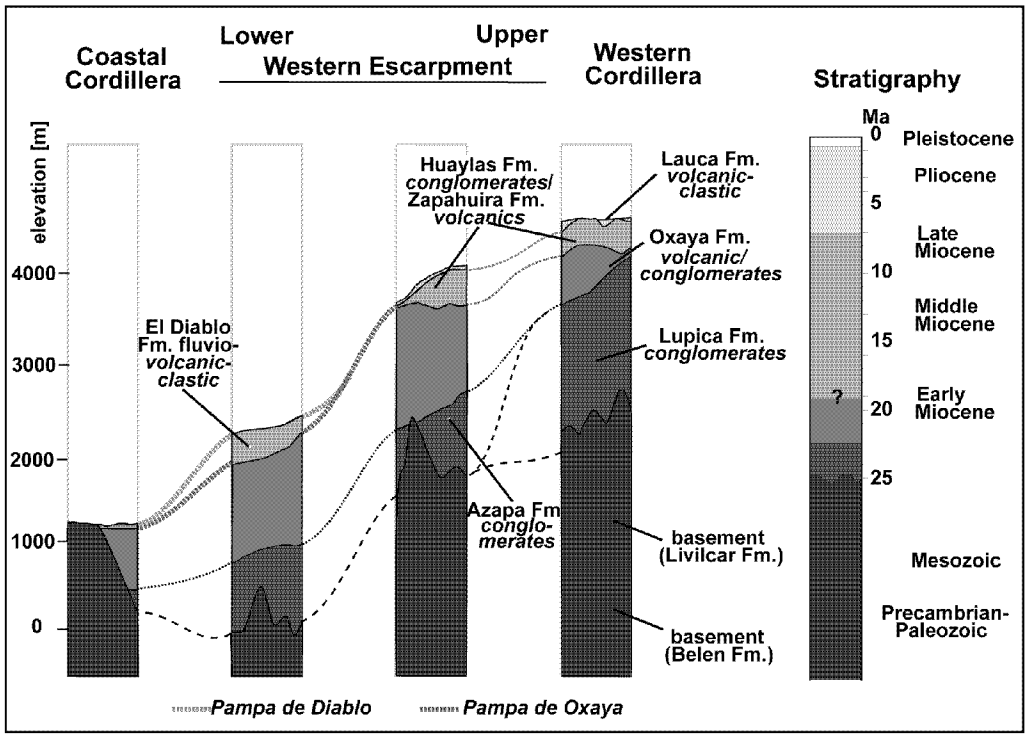

Fig. 2 Stratigraphic columns from the *Coastal Cordillera* into the *Western Cordillera*. Details of lithologies and formation ages are discussed in the text and in Table 1.

3.4 Sampling strategy

We selected sample sites along a transect that covers the entire range of altitudes and precipitation zones of the study area (Fig. 1). In areas that are made up of a variety of lithologies (especially the *Western Cordillera,* see Table 1), we sampled the most frequent lithologies in an effort to detect possible effects of the lithologic properties on surface erosion rates. The samples were collected at the summits of hillslope interfluves

where bedrock is exposed (Fig. 1, 3A,B) and a regolith cover was absent. Therefore, major down-slope advection of material can be neglected. Hence, surface erosion at these sites is anticipated to be in a weathering-limited state. Measured erosion rates thus can be interpreted as in-situ process rates, i.e. directly as a combined function of the local climate and the bedrock lithology. Possible transient effects might be detected by analysing several TCNs. Exceptions from the bedrock sampling strategy are locations that are made up of aggradational sequences. This is especially the case for the *Pampa de Diablo* and for the *Coastal Cordillera*. In these cases, samples from boulders (0.5-2 m in size) or amalgamated clast samples (20 clasts per sample) were taken (Table 1). As will be shown, the formation age of the analysed units is considerably older than the time period recorded by TCN's at these sites. A prerequisite for using TCNs to quantify in-situ process rates is that possible regolith coverage does not substantially modify the TCN-based erosion rates. All bedrock samples were free of regolith at the time of sampling. This condition is tested for the past by analyzing TCN's in a depth profile. For this test we chose a site with a gently sloping surface (~5°) and a ca. 20 cm thick regolith cover (Fig. 3C).

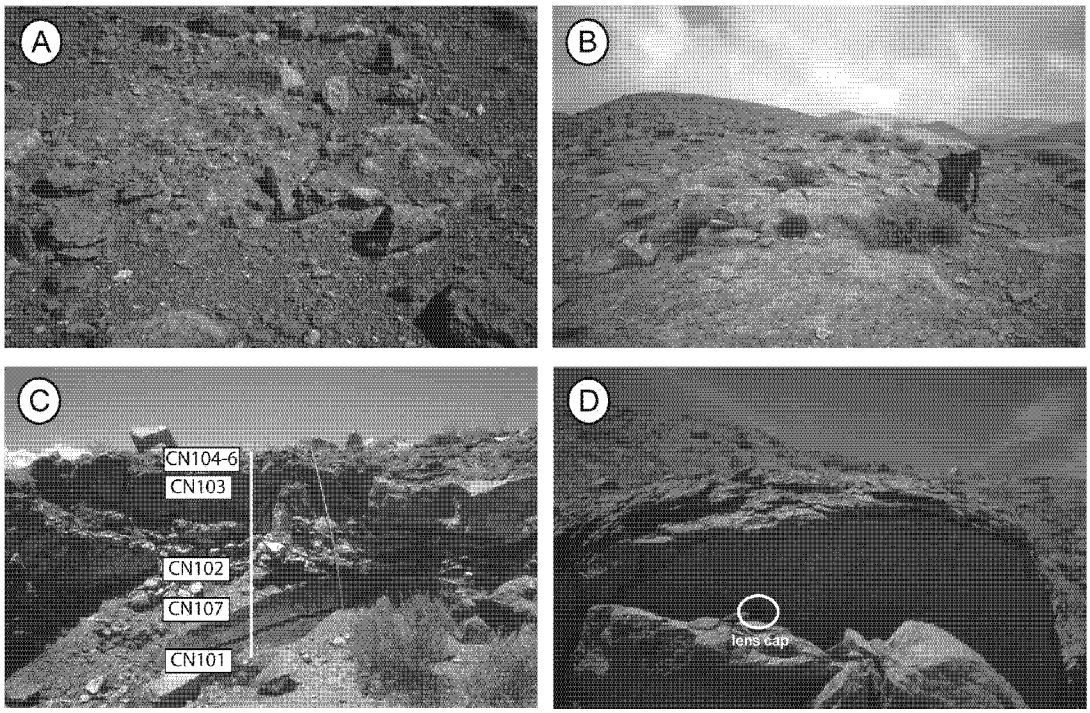

Fig. 3 A) Sample site CN201, B) Sample site CN111, C) Depth profile taken in a recently opened quarry (samples CN101-107), D) cm-scale exfoliation on an Oxaya boulder (onion shell like), lens cap for scale.

A few data on sediment concentrations and water discharge measured in the middle and upper parts of the Lluta river (Fig. 1) are available that record denudation rates of the upper

portions of the *Western Escarpment* and the *Western Cordillera*. These data are used to determine modern sediment yields and thus the flux of coupled hillslope-fluvial processes. This information will then be compared with the TCN-based process rates on hillslope interfluves from the same region in an effort to compare present day rates (deduced by sediment flux) analyses with long-term denudation and erosion rates (based on TCN data).

Table 1 Coordinates and lithological information for samples discussed in the text

sample number	object bedrock (b) boulder (bo) amalgamated (a)	sample location longitude	latitude	altitude [m] (±5m)	lithology Oxaya (O), El Diablo (D), Lauca (L), Huaylas (H), Zapahuira (Z), Altos de Pica (P)	formation age [My] (Wörner et al . 2001; Garcia, 2002; Victor et al. 2004)
Coastal Cordillera						
CN203	bo	70.15W	19.12S	500	granite	Cretaceous
CN36	bo	70.05W	19.33S	1150	granite	Cretaceous
Western Escarpment						
CN7	bo	69.56W	18.37S	1620	andesite-D	~16
CN8b	bo	69.51W	18.25S	1670	ignimbrite-O	19-23
CN1c	bo	69.54W	18.28S	1930	ignimbrite-O	19-23
CN301	b	69.41W	18.44S	2185	ignimbrite-O	19-23
CN302	b	69.39W	18.44S	2590	ignimbrite-O	19-23
CN19	b	69.41W	18.43S	2730	ignimbrite-O	19-23
CN303	b	69.39W	18.43S	3070	ignimbrite-O	19-24
CN310	b	69.37W	18.21S	3220	ignimbrite-L	~2.7
CN104C/P	b	69.40W	18.22S	3235	ignimbrite-O	19-23
CN101-107	b	69.40W	18.22S	3235	ignimbrite-O	19-23
CN5	b	69.37W	18.42S	3260	ignimbrite-O	19-23
CN16	a	69.37W	18.21S	3270	conglomerate-H	19-23
CN23	b	69.40W	18.23S	3280	ignimbrite-O	19-23
CN111F	b	69.49W	18.14S	3435	ignimbrite-O	19-23
CN201	b	69.50W	18.22S	3440	ignimbrite-O	19-23
CN305	b	69.43W	18.11S	3670	ignimbrite-O	19-23
Western Cordillera						
CN112	b	69.41W	18.05S	3920	ignimbrite-L	~2.7
CN308	b	69.17W	18.33S	4150	andesite-Z	11-12
CN26	b	68.55W	20.18S	4205	ignimbrite-P	16-20
CN307	b	69.27W	18.19S	4420	volcanic-Z	11-12
CN309	b	69.09W	18.14S	4510	ignimbrite-L	~2.7
CN113	b	69.30W	18.10S	4560	ignimbrite-L	~2.7

Oxaya ignimbrite: ryolithic, medium to dark pinkish-greyish, welded tuff, fluidal structures, angular xenoliths and phenocrysts of Qtz, San, Bt, Mt, Pl, pumice-fragments in fine grained matrix

Lauca ignimbrite: ryolithic, light pinkish-greyish, high pumice content, Qtz-phenocrysts, porous

Zapahuira-andesite: dense, blackish-greyish basaltic lavas, phenocrysts of Fsp, Ol

Zapahuira-volcanic flow: rhyolithic, devitrified, altered phenocrysts

granite: coarse grained, minerals Qtz-Fsp-Bt

Huyalas conlomerate: coarse grained ryolithic, Oxaya-origin

Altos de Pica ignimbrite: see Oxaya-ignimbrite

3.5 Methods, production rates and calculation procedures

Samples for TCN-analysis were crushed and sieved to a grain size range of 355-1000 µm. Quartz separates for radionuclide and noble gas analysis were prepared by selective

chemical dissolution (Kohl and Nishiizumi, 1992; Ivy-Ochs, 1996). In the case of CN7, CN307, CN308, and for some of the depth profile samples (CN105-107), quartz for ^{21}Ne-analyses was prepared using only physical methods. The influence of the cleaning method (physical 'P' versus chemical 'C') on the measured $^{21}Ne_{cos}$ concentrations was tested for site CN104 (fractions CN104P and CN104C, respectively). $^{21}Ne_{cos}$ concentrations for physically and chemically separated quartz fractions from sample CN104 differs by 3.5% only (see Table 2). We therefore conclude that the preparation method has no influence on the measured $^{21}Ne_{cos}$ concentration of any of our quartz samples. However, the chemically prepared samples in general show lower amounts of atmospheric ^{20}Ne and higher ratios of $^{21}Ne/^{20}Ne$ and $^{22}Ne/^{20}Ne$. Therefore a chemically preparation procedure is to be preferred. Purified quartz and pyroxene separates (see Table 2) were obtained using heavy liquid and magnetic separations followed by handpicking. For ^{21}Ne-analysis quartz and pyroxene separates were crushed to <100 µm and to <355 µm, respectively and cleaned in an ultrasonic bath. Then the fractions in suspension were decanted. Finally, 40-80 mg was wrapped into aluminium foil. Additional detailed information on the noble gas analytical procedure is given in (Kober, 2005, in press-b). For ^{10}Be analyses, the quartz separates were further etched using weak HF to ensure removal of meteoric ^{10}Be. They were then dissolved with concentrated (48%) HF after addition of ^{9}Be carrier. Be and Al were separated and purified using anion and cation exchange and selective pH controlled precipitations (Ivy-Ochs, 1996; Ochs and Ivy-Ochs, 1997). $^{10}Be/^{9}Be$ and $^{26}Al/^{27}Al$ ratios of samples along with appropriate standards and blanks were measured by accelerator mass spectrometry (AMS) at the ETH/PSI tandem facility in Zurich (Synal et al., 1997). Subtracted blanks were $(1\text{-}3)*10^{-14}$ for $^{10}Be/^{9}Be$ and 3-5 x 10^{-15} for $^{26}Al/^{27}Al$, respectively. Stable Al was measured on an aliquot of the dissolved quartz solution by ICP-AES using three standard additions for each sample.

Cosmogenic nuclides average erosion rates over the time a sample resided within about one mean attenuation length of cosmic rays (60-80cm) below the surface (timescale equal to $\Lambda/(\rho*\varepsilon)$; with Λ=absorption mean free path [$cm*g^{-2}$], ρ =density of the rock [$g*cm^{-3}$], ε=erosion rate [cm/my], (Lal, 1991)). If using only a single nuclide the underlying assumption of steady-state nuclide saturation and erosion (Lal, 1991) may not hold for all samples studied in a given area. Therefore, we measured several TCNs within each sample ^{10}Be, ^{21}Ne, ^{26}Al ($t_{1/2}$:^{10}Be=1.51 my, ^{26}Al=0.716 my, ^{21}Ne=stable) in the same sample, except for a few cases where only one or two isotopes were analyzed (pyroxene sample, depth profile). Erosion and exposure histories can be evaluated by the use of so-called 'steady state erosion-island' plots, e.g. $^{26}Al/^{10}Be$ vs. ^{10}Be, (Klein et al., 1986), or $^{21}Ne/^{26}Al$ vs. ^{26}Al, (Graf et al., 1991)). In

principle, such diagrams allow the simultaneous determination of erosion rates and exposure ages (Gosse and Phillips, 2001, and references therein). We used the following total production rates at sea level and high latitude: $P^{10}Be$=5.1±0.3, $P^{21}Ne$=20.3±4.0 [atoms*g^{-1}*yr^{-1}] (Niedermann, 2000; Stone, 2000); and $P^{26}Al$=33.255±2.93 [atoms*g^{-1}*yr^{-1}] based on $^{26}Al/^{10}Be$ =6.52±0.43 (Kubik et al., 1998). Scaling to the coordinates of the sample sites was performed for neutrons following the procedure of (Stone, 2000). Muon contributions (Table 4) were scaled based on (Allkofer, 1975; Boezio et al., 2000; Heisinger et al., 2002). A correction for shielding was not necessary, neither due to outcrop shape, sloping surfaces, vegetation or snow cover. Note that due to the effects of variable production rates caused by variable geomagnetic field intensities (Masarik et al., 2001) our erosion rate and exposure age calculations might represent under- or overestimates (≤10%), since this effect cannot straight forwardly be applied to sites that have experienced erosion. This effect is indeed more pronounced at low latitudes.

3.6 Results

3.6.1 Nuclide concentrations

Neon isotope concentrations and ratios are presented in Table 2. Concentrations of radionuclides ^{10}Be and ^{26}Al are presented in Table 3. Uncertainties stated are 1σ. The ^{21}Ne data include analytical uncertainties as well as sensitivity and mass discrimination errors. Uncertainties due to calibration gas amounts are not included but are <3%. For ^{10}Be and ^{26}Al the uncertainties include statistical errors and the error due to the normalization to the standards and blanks. The uncertainty on the nominal value of the ^{10}Be standard (± 2.5%) is not included in the final AMS uncertainties.

The measured neon isotope ratios are plotted in Fig. 4. The regression line (y=1.18*x+0.098) through the respective points of the ≤600°C steps is close to the mixing line between atmospheric and cosmogenic composition for quartz (y=1.12*x+0.0986) reported by Niedermann (2002), without any detectable amounts of nucleogenic neon (Fig. 4A). Data from high temperature steps (800° and 1750°C) mostly scatter around atmospheric composition (Fig. 4B) and are therefore discarded. Some of the 800°C steps contained >2% of the excess ^{21}Ne in the ≤600°C steps. If the respective data points lie on the atmospheric-cosmogenic-mixing line, then the excess was considered to be cosmogenic and was added to the concentration calculated by the ≤600°C step. The resulting cosmogenic Ne-concentrations are presented in Table 2.

Table 2 Neon data for analyzed samples. Only the 600°C steps were used for calculation of erosion rates and exposure ages, as long as the 800°C steps did contribute <2%. If the ^{21}Ne excess in the 800°C steps was higher than this it is included in the calculation (indicated in bold). For samples with codes >CN300 the excess in the 800°C step is on the order of 30% because the nominal 600°C step presented did not reach excess of ^{21}Ne at this temperature. Data points of the 600oC and 800oC steps are on the cosmogenic-atmospheric mixing line and were therefore included in the calculation

sample	mineral	heating step [temp./time]	^{20}Ne *10^{9} [atoms/g]	^{21}Ne/^{20}Ne *10^{-3}	^{22}Ne/^{20}Ne *10^{-1}	^{21}Ne$_{cosmo}$ *10^{6} [atoms/g]
CN1c	Qtz	**550,20**	4.64 ± 0.19	20.12 ± 0.26	1.246 ± 0.013	79.6 ± 3.9
		800,15	2.77 ± 0.11	4.80 ± 0.19	1.067 ± 0.007	
		1750,15	3.15 ± 0.14	2.97 ± 0.04	1.035 ± 0.007	
CN5	Qtz	**550,20**	4.66 ± 0.19	45.92 ± 0.34	1.549 ± 0.013	200.1 ± 8.9
		800,15	1.85 ± 0.08	3.62 ± 0.05	1.053 ± 0.007	
CN7	Qtz	**550,20**	18.04 ± 1.33	5.93 ± 0.17	1.074 ± 0.019	110.3 ± 16.3
		800,15	32.41 ± 2.45	4.70 ± 0.05	1.039 ± 0.004	
		1750,15	37.85 ± 2.99	3.55 ± 0.04	1.049 ± 0.010	
CN8b	Qtz	**550,20**	13.73 ± 0.49	6.35 ± 0.08	1.060 ± 0.004	46.6 ± 3.4
		800,15	3.68 ± 0.13	3.16 ± 0.03	1.030 ± 0.006	
		1750,15	2.51 ± 0.13	3.02 ± 0.04	1.030 ± 0.006	
CN16	Qtz	**550,20**	18.74 0.66	8.62 0.09	1.083 0.007	144.2 ± 8.5
		800,15	38.31 1.39	3.95 0.03	1.040 0.006	
		1500,15	9.19 0.32	3.30 0.05	1.045 0.008	
CN19	Qtz	**550,20**	4.04 ± 0.13	79.92 ± 0.42	1.990 ± 0.016	320.3 ± 10.8
		800,15	2.15 ± 0.07	7.40 ± 0.17	1.099 ± 0.017	
		1750,15	1.59 ± 0.07	3.36 ± 0.09	1.052 ± 0.015	
CN23	Qtz	**550,20**	6.85 ± 0.23	36.03 ± 0.30	1.452 ± 0.013	226.4 ± 8.5
		1750,15	3.68 ± 0.14	6.62 ± 0.05	1.068 ± 0.018	
CN26	Qtz	**550,20**	4.17 ± 0.15	21.82 ± 0.37	1.280 ± 0.022	78.6 ± 3.6
		1750,15	2.28 ± 0.09	3.43 ± 0.09	1.047 ± 0.010	
CN36	Qtz	**550,20**	9.13 ± 0.33	5.96 ± 0.10	1.051 ± 0.004	43.2 ± 4.9
		800,15	31.28 ± 1.12	3.46 ± 0.01	1.025 ± 0.002	
		1750,15	29.01 ± 1.01	3.09 ± 0.01	1.042 ± 0.003	
CN101	Qtz	**550,30**	1.64 ± 0.07	18.88 ± 0.24	1.187 ± 0.011	26.0 ± 1.3
		800,30	1.28 ± 0.05	3.79 ± 0.14	1.035 ± 0.008	
		1750,15	1.52 ± 0.06	3.58 ± 0.13	1.021 ± 0.013	
CN102	Qtz	**550,30**	1.80 ± 0.07	44.43 ± 0.39	1.532 ± 0.012	74.8 ± 3.2
		800,30	0.80 ± 0.04	3.77 ± 0.12	1.020 ± 0.021	
		1750,15	1.19 ± 0.04	3.47 ± 0.17	1.018 ± 0.012	
CN103	Qtz	**550,30**	2.21 ± 0.08	75.10 ± 0.61	1.875 ± 0.011	159.2 ± 5.9
		800,30	0.98 ± 0.04	3.98 ± 0.14	1.038 ± 0.013	
CN104C	Qtz	**550,30**	1.77 ± 0.05	69.22 ± 0.65	1.766 ± 0.017	117.0 ± 4.5
		800,30	1.08 ± 0.07	4.15 ± 0.16	1.039 ± 0.011	
		1750,15	1.18 ± 0.14	3.17 ± 0.10	0.963 ± 0.009	
CN104P	Qtz	**550,30**	1.33 ± 0.06	88.09 ± 1.06	2.019 ± 0.023	112.8 ± 4.4
		800,30	1.47 ± 0.04	3.94 ± 0.10	1.023 ± 0.014	
		1750,15	3.65 ± 0.04	3.42 ± 0.09	1.010 ± 0.010	
CN105	Qtz	**600,30**	14.14 ± 0.57	8.18 ± 0.04	1.090 ± 0.001	73.8 ± 4.8
		800,30	0.87 ± 0.04	3.26 ± 0.13	1.020 ± 0.006	
		1750,15	0.86 ± 0.04	3.44 ± 0.12	1.022 ± 0.012	
CN106	Qtz	**600,30**	1.77 ± 0.07	70.31 ± 0.46	1.776 ± 0.012	119.0 ± 5.1
		800,30	0.92 ± 0.04	3.55 ± 0.18	0.977 ± 0.012	
		1750,15	1.19 ± 0.05	4.10 ± 0.03	1.018 ± 0.005	

Table 2 Continuous

sample	mineral	heating step [temp./time]	^{20}Ne $*10^{9}$ [atoms/g]	$^{21}Ne/^{20}Ne$ $*10^{3}$	$^{22}Ne/^{20}Ne$ $*10^{1}$	$^{21}Ne_{cosmo}$ $*10^{6}$ [atoms/g]
CN107	Qtz	**600,30**	1.84 ± 0.07	30.21 ± 0.87	1.426 ± 0.011	50.1 ± 2.8
		800,30	0.86 ± 0.04	3.78 ± 0.13	1.000 ± 0.016	
		1750,15	1.01 ± 0.04	3.95 ± 0.07	1.042 ± 0.010	
CN111F	Qtz	**550,20**	1.87 ± 0.08	74.54 ± 1.14	1.872 ± 0.025	134.2 ± 6.6
		800,15	3.77 ± 0.13	3.08 ± 0.03	1.013 ± 0.005	
		1750,15	1.67 ± 0.06	2.91 ± 0.11	1.040 ± 0.013	
CN112	Qtz	**550,20**	3.09 ± 0.11	11.39 ± 0.18	1.123 ± 0.015	26.1 ± 1.4
		800,15	1.97 ± 0.08	3.10 ± 0.05	1.027 ± 0.008	
CN113	Qtz	**550,30**	3.50 ± 0.12	4.19 ± 0.12	1.007 ± 0.007	4.3 ± 0.7
		800,30	2.08 ± 0.08	3.17 ± 0.13	1.009 ± 0.015	
		1750,15	1.27 ± 0.06	2.95 ± 0.10	0.997 ± 0.018	
CN201	Qtz	**600,30**	1.60 ± 0.06	179.91 ± 1.21	3.106 ± 0.024	283.6 ± 11.8
		800,30	4.68 ± 0.19	3.58 ± 0.06	1.002 ± 0.007	
		1750,15	1.20 ± 0.05	3.20 ± 0.09	0.988 ± 0.011	
CN203	Qtz	**600,30**	6.69 ± 0.27	39.30 ± 0.14	1.430 ± 0.009	243.2 ± 10.6
		800,30	3.34 ± 0.14	3.75 ± 0.02	1.029 ± 0.004	
		1750,15	2.20 ± 0.09	13.34 ± 0.13	1.039 ± 0.003	
CN301	Qtz	**600,30**	1.29 ± 0.04	49.94 ± 0.57	1.618 ± 0.011	86.3 ± 2.5
		800,30	0.78 ± 0.03	36.17 ± 0.45	1.438 ± 0.013	
		1750,15	1.23 ± 0.04	3.38 ± 0.16	0.998 ± 0.016	
CN302	Qtz	**600,30**	1.39 ± 0.05	43.00 ± 0.52	1.495 ± 0.021	93.0 ± 2.5
		800,30	0.80 ± 0.03	49.48 ± 0.58	1.560 ± 0.028	
		1750,15	2.10 ± 0.07	3.41 ± 0.04	1.026 ± 0.013	
CN305	Qtz	**600,30**	1.55 ± 0.07	23.42 ± 0.48	1.241 ± 0.018	46.3 ± 2.0
		800,30	1.12 ± 0.05	16.02 ± 0.53	1.142 ± 0.006	
		1750,15	4.96 ± 0.20	3.24 ± 0.12	1.022 ± 0.011	
CN307	Qtz	**600,30**	13.25 ± 0.57	5.64 ± 0.11	1.044 ± 0.006	44.1 ± 4.2
		800,30	9.75 ± 0.42	3.83 ± 0.05	1.029 ± 0.010	
		1750,15	10.51 ± 0.45	3.26 ± 0.06	1.038 ± 0.007	
CN308	Px*	800,45	6.80 ± 0.35	3.18 ± 0.03	1.032 ± 0.004	-
		1750,20	6.22 ± 0.31	6.09 ± 0.12	1.044 ± 0.002	
CN308 corrected ratio for high temperatur to match the atmospheric-cosmogenic mixture line for pyroxenes						
			6.22 ± 0.31	5.34 ± 0.12	1.044 ± 0.002	14.9 2.0
CN309	Qtz	**600,30**	1.10 ± 0.05	11.38 ± 0.23	1.114 ± 0.014	9.3 ± 0.6
		800,30	0.87 ± 0.04	3.08 ± 0.13	0.995 ± 0.024	
		1750,15	0.86 ± 0.04	3.53 ± 0.14	1.023 ± 0.013	
CN310	Qtz	**600,30**	1.04 ± 0.04	12.46 ± 0.18	1.130 ± 0.015	19.2 ± 0.7
		800,30	0.77 ± 0.03	14.97 ± 0.35	1.154 ± 0.016	
		1750,15	1.00 ± 0.03	2.98 ± 0.02	0.987 ± 0.018	

* chemical composition [wt%]: 1-Al_2O_3, 23.5-Fe_2O_3, 35.5-MgO, 39-Si_2O_3, PR according to Chapter 5

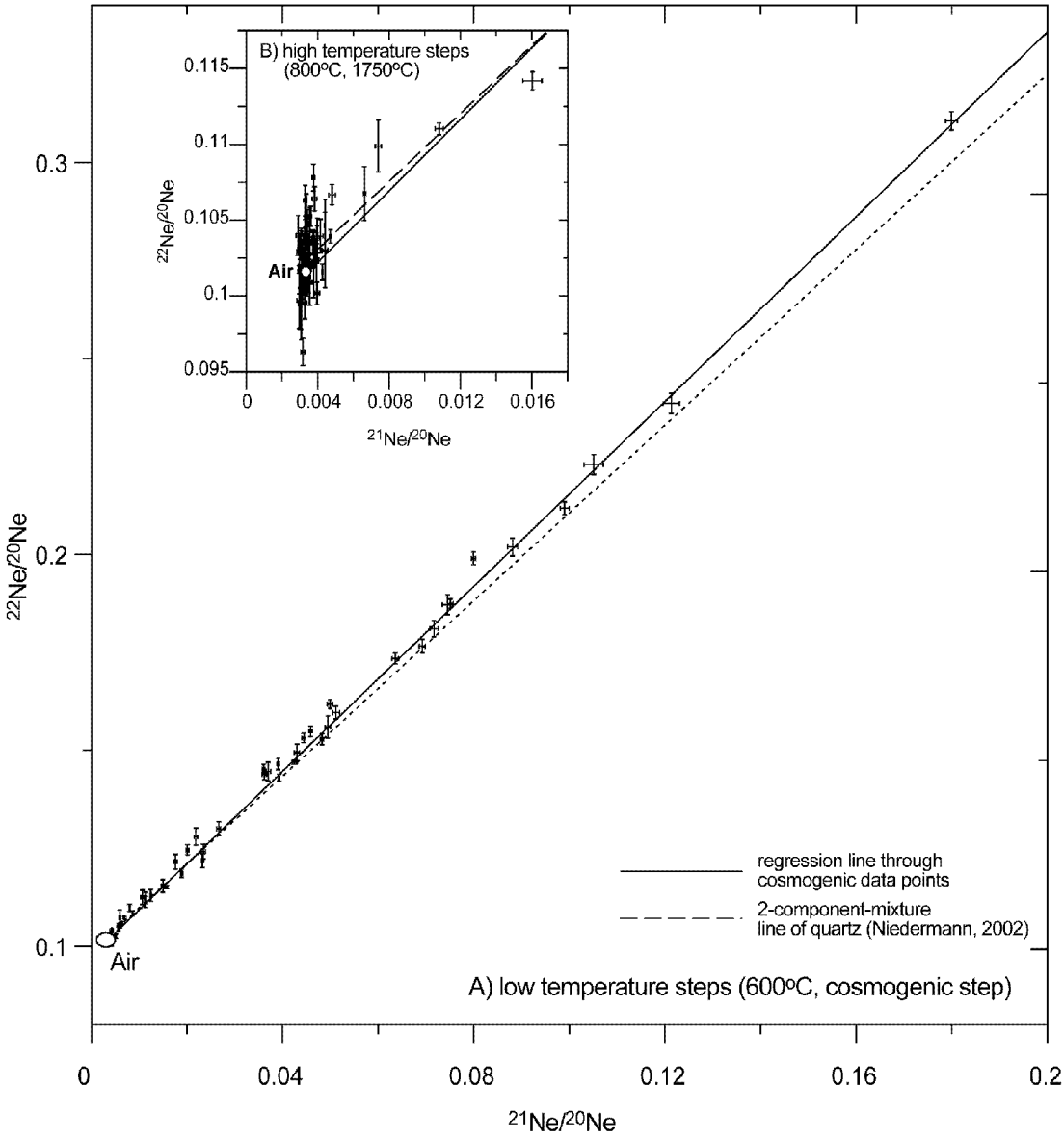

Fig. 4 Neon-three-isotope diagram of samples from northern Chile. A) Low temperature steps, releasing cosmogenic neon, B) high temperature steps. See text for discussion.

Table 3. ^{10}Be- and ^{26}Al nuclide nuclide conetrations and ratios (^{21}Ne see Table 2)

Sample	^{10}Be [atoms/g/yr]	error ^{10}Be [atoms/g/yr]	^{26}Al [atoms/g/yr]	error ^{26}Al [atoms/g/yr]	^{26}Al/^{10}Be	error	^{21}Ne/^{10}Be	error	^{21}Ne/^{26}Al	error
1c	1.33E+07	2.67E+05					5.97	0.24		
5	3.08E+07	9.60E+05	1.42E+08	7.11E+06	4.62	0.27	6.49	0.29	1.406	0.08
7										
8b	7.33E+06	2.86E+05					6.36	0.39		
16	1.85E+07	6.29E+05					7.81	0.49		
19	3.46E+07	8.67E+05	1.25E+08	7.03E+06	3.60	0.22	9.24	0.28	2.569	0.15
23	3.71E+07	5.56E+05	1.21E+08	5.83E+06	3.25	0.16	6.11	0.14	1.879	0.10
26	1.89E+07	5.67E+05	1.15E+08	5.62E+06	6.10	0.35	4.16	0.18	0.683	0.04
36	5.39E+06	2.46E+05	2.07E+07	1.04E+06	3.84	0.26	8.02	0.90	2.089	0.24
101	4.67E+06	1.73E+05								
103	2.66E+07	9.87E+05								
104A	2.20E+07	6.67E+05					5.07	0.20		
111F	2.73E+07	9.32E+05	1.16E+08	5.80E+06	4.24	0.26	4.91	0.25	1.157	0.07
112	6.75E+06	3.11E+05					3.86	0.22		
113	1.19E+06	5.60E+04	7.61E+06	3.95E+05	6.41	0.45	3.63	0.17	0.567	0.03
201	4.16E+07	1.25E+06	2.11E+08	1.35E+07	5.08	0.36	6.82	0.28	1.343	0.09
203	5.93E+06	1.82E+05	3.13E+07	1.60E+06	5.29	0.32	41.02	1.73	7.759	0.46
301	1.47E+07	4.46E+05	7.10E+07	6.58E+06	4.83	0.47	5.87	0.20	1.216	0.11
302	1.66E+07	5.04E+05	5.97E+07	2.89E+06	3.59	0.20	5.59	0.19	1.558	0.08
303	2.33E+07	7.04E+05	9.46E+07	3.94E+06	4.06	0.21				
305	1.08E+07	3.94E+05	5.50E+07	3.68E+06	5.10	0.39	4.29	0.21	0.842	0.06
309	2.13E+06	1.14E+05	1.44E+07	8.79E+05	6.78	0.55	4.39	0.32	0.648	0.05
310	4.66E+06	1.82E+05	2.49E+07	1.02E+06	5.35	0.30	4.12	0.19	0.769	0.04

3.6.2 Erosion island plots

The formulas presented by Schaller et al. (2004) are used to construct erosion island plots for the Ne-Be, Ne-Al and Be-Al systems. However, for the neutron component we used a pure exponential decrease in production with depth (Lal, 1991). Most of the data points plot within the erosion island, bounded by the zero erosion line and the saturation line (Fig. 5a-c). These sampled surfaces probably had a simple exposure history with constant erosion rates, but have not yet reached saturation. A few data points fall outside the erosion island indicating a "complex" or a multiple exposure history (CN8b, CN16, CN36) likely by elevated ^{21}Ne (Fig. 5a,b) and ^{10}Be (Fig. 5c) concentrations from earlier exposures. Notably, the latter data points all represent boulder or amalgamated clast samples (Table 1). Some data points plot left of the apparent intersection between the zero-erosion-line and the saturation line in the erosion island plots (Fig. 5a-c; in reality the two lines are offset if time would be plotted in the third dimension, see APPENDIX B). The crossover of the zero-erosion-line and the saturation line is the result of the increasing importance of muogenic ^{10}Be- or ^{26}Al-production with depth (Heisinger et al., 2002) whereas no ^{21}Ne production by muons has been reported (see Niedermann, 2002).

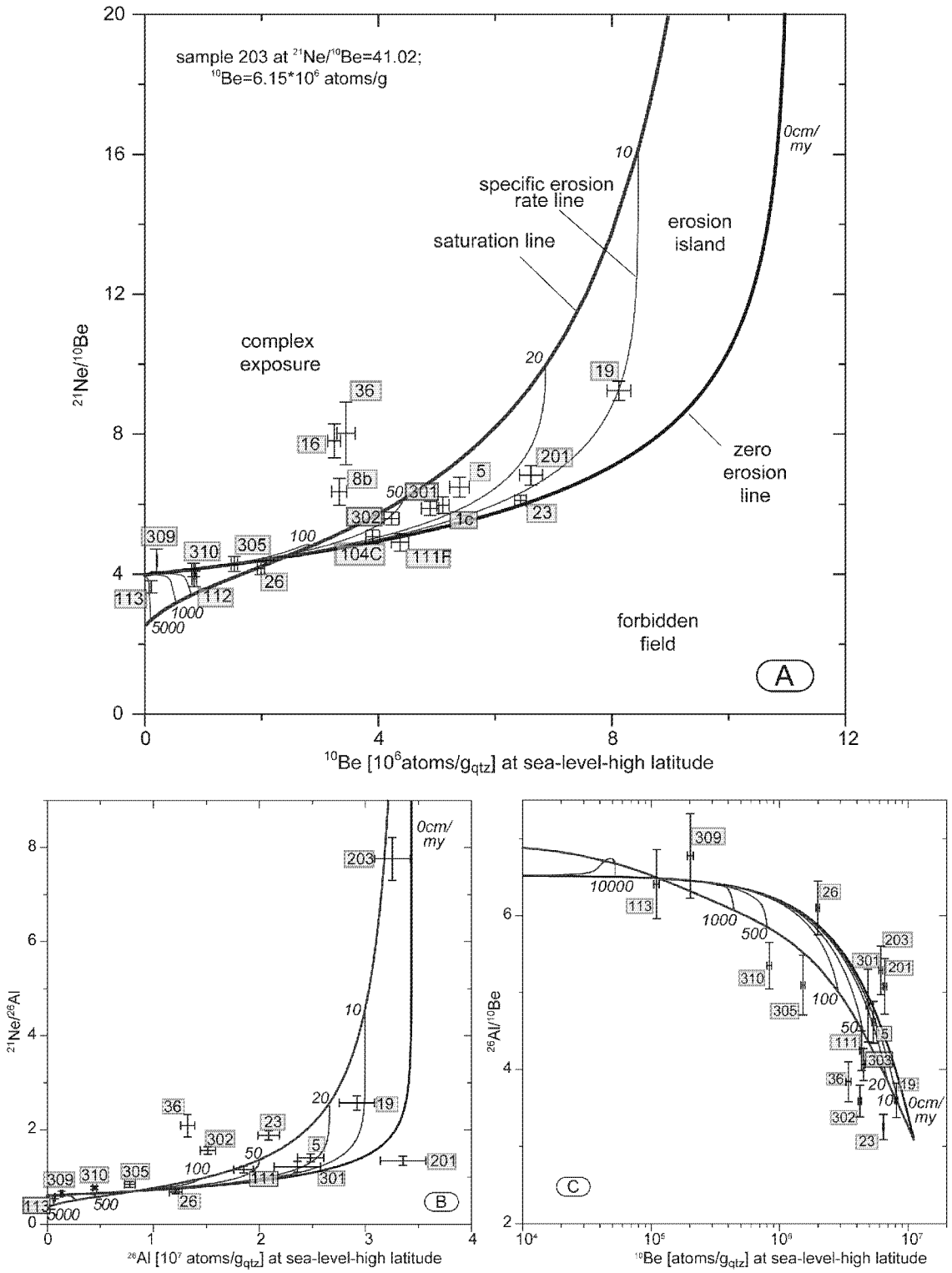

Fig. 5 Various erosion-islands diagrams. Detailed discussion of these figures is provided in the text. A) $^{21}Ne/^{10}Be$-^{10}Be erosion-island plot, B) $^{21}Ne/^{26}Al$ erosion-island plot, B) $^{21}Ne/^{26}Al$-^{26}Al erosion-island plot, C) $^{26}Al/^{10}Be$-^{10}Be erosion-island plot. Error-bars for nuclide ratio are analytical errors only (1σ). Attenuation length Λ=160 g*cm^{-2}, density ρ=2.375 g*cm^{-3}.

Note also that there is a difference in sensitivity in the different erosion island plots (Fig. 5a-c). While in stable nuclide/radionuclide diagrams the nuclide concentration is rather sensitive to erosion rates and exposure ages (Fig. 5a,b), in radionuclide/radionuclide plots the nuclide ratio is the more sensitive parameter (Fig. 5c). This means that stable nuclide/radionuclide diagrams offer a considerably better resolution for the detection of low erosion rates and high exposure ages, since ratios at saturation are reached earlier in radionuclide/radionuclide diagrams. For surfaces exposed for more than several hundreds of thousands years the plots including neon are more sensitive because the erosion island itself becomes broader as one goes to older ages.

For samples whose data points plot within the erosion island erosion rates and exposure ages can in principle be determined simultaneously (Table 4), although this works with good resolution only for erosion rates ≤1m/my. In Table 4 we present erosion rates and exposure ages derived from the Ne-Be erosion island plot (Fig. 5a) since it offers the best resolution. ^{21}Ne-single nuclide estimates are given for comparison in Table 4. Reported uncertainties in erosion rates and exposure ages given in Table 4 are based on analytical uncertainties of the cosmogenic nuclide and assume a single stage exposure history (other scenarios are discussed further down). The Ne-Al and Al-Be diagrams and ^{10}Be and ^{26}Al single nuclide erosion rate and exposure age values are presented in APPENDIX A. For boulder, amalgamated clast and bedrock samples for which only one isotope was analysed we present single nuclide maximum erosion rates and minimum exposure ages in Table 4. In case of samples that indicate complex exposures in Fig. 5a-c the nominal single nuclide erosion rates are minimum values and the exposure ages maximum values.

3.6.3 Erosion rates and exposure ages

Following the same procedure and formulas used to construct the erosion island plots, we iteratively calculated erosion rates and exposure ages using the data provided in Tables 2 and 3. For the *Coastal Cordillera* and the *Western Escarpment* we deduce very low rates between 10-100 cm/my nominal exposure ages 1-6 my; Table 4, APPENDIX A) while for the higher *Western Escarpment* (≥3500 m) and the *Western Cordillera* rates of 100-4600 cm/my are calculated (nominal exposure ages 0.02-0.1 my; Table 4, APPENDIX A). Because no data points fall on the saturation line (Fig. 5a-c), erosion rates calculated with single nuclides always are higher than the values determined from erosion island plots (Table 4, APPENDIX A). From the data a distinct spatial trend in erosion rates increasing from the *Coastal*

Cordillera to the *Western Cordillera* can be observed (Fig. 6). Thus, as a first order trend, erosion rates strongly correlate with altitude and the pattern of present day rainfall (Fig. 6).

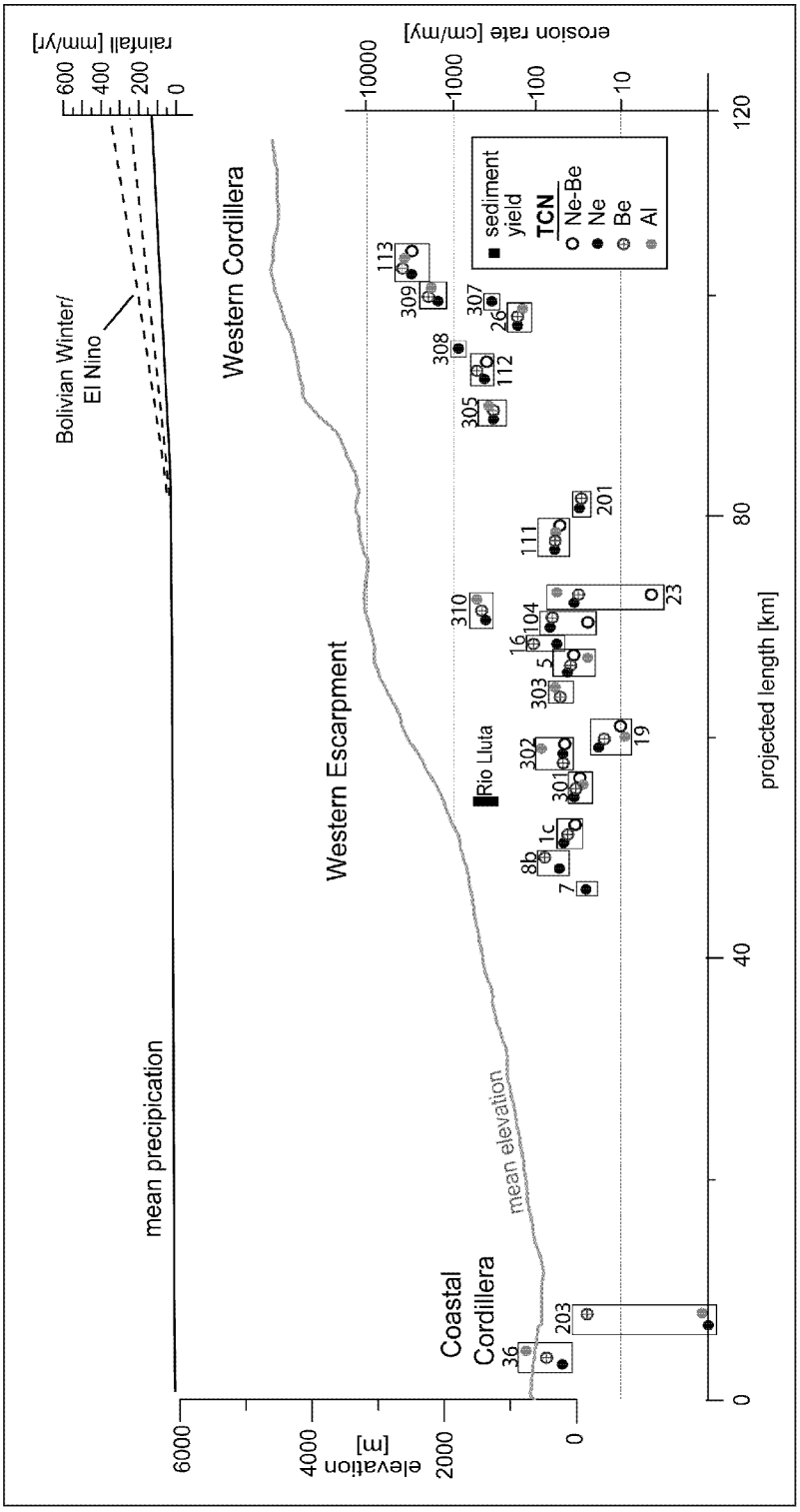

Fig. 6 Composite sketch of mean elevation, rainfall distribution and calculated erosion and denudation rates with respect to the sample localities across a West-East transect in northern Chile indicating a positive correlation of erosion rates, elevation and present day rainfall. Sample CN310, which falls off this trend was used to test the dependency of erosion rates on lithology (see text).

Exposure ages calculated from the Ne-Be erosion island plot are in the range of early to late Pliocene for samples from the *Western Escarpment* (Table 4 and APPENDIX A). For the *Coastal Cordillera* (Table 4) a middle Miocene age was estimated using the Ne-Al erosion island plot. In contrast, samples from the *Western Cordillera* with higher erosion rates, have late Pleistocene to Holocene exposure ages (Table 4).

Table 4 Erosion rates and exposure ages derived from the ^{21}Ne-^{10}Be erosion island diagrams and ^{21}Ne-single nuclide determinations. Otherwise indicate bold. All other data located in Appendix A.

	erosion island plots				**single nuclide**			
sample	erosion rates (cm/myr)		exposure age (Myr)		max. erosion rates infinite time (cm/myr)		min. exposure ages zero eorsion (Myr)	
	Ne/Be	(+/-)	**Ne/Be**	(+/-)	**Ne**	(+/-)	**Ne**	(+/-)
1c	31	(3 / 2)	2.52	(0.10 / 0.08)	45	(2 / 2)	1.50	(0.07 / 0.07)
5	32	(3 / 3)	3.58	(0.28 / 0.3)	39	(1 / 2)	1.70	(0.09 / 0.07)
7					27	(4 / 4)	2.53	(0.38 / 0.38)
8b	cp		cp		65	(5 / 5)	1.04	(0.07 / 0.08)
16	cp		cp		55	(4 / 4)	1.23	(0.07 / 0.08)
19	10	(2 / 2)	5.35	(0.23 / 0.25)	18	(1 / 0)	3.67	(0.12 / 0.12)
23	5	(2 / 2)	2.08	(0.03 / 0.03)	35	(1 / 1)	1.92	(0.09 / 0.08)
26	cp	(fb. / 170, sat.)	cp	(fb. / sat.)	167	(7 / 8)	0.40	(0.02 / 0.02)
36	cp				50	(6 / 6)	1.36	(0.15 / 0.15)
104A	28	(7 / 10)	1.25	(0.05 / 0.10)	70	(3 / 3)	0.96	(0.05 / 0.03)
111F	**50**	**(7 / 9)**	**2.05**	**(0.16 / 0.34)**	65	(3 / 3)	1.05	(0.08 / 0.05)
112	417	(17 / 20)	0.85	(0.08 / 0.08)	423	(22 / 24)	0.16	(0.01 / 0.01)
113	3400	(200 / 160)	0.104	(0.007 / 0.097)	3450	(480 / 680)	0.020	(0.004 / 0.003)
201	15	(3 / 3)	3.05	(0.13 / 0.10)	31	(2 / 1)	2.20	(0.09 / 0.08)
203	**4**	**(2 cp)**	**22.45**	(9.3 cp)	0	(0 / 1)	12.50	(0.5 / 0.5)
301	34	(3 / 4)	2.48	(0.1 / 0.15)	48	(1 / 1)	1.41	(0.04 / 0.04)
302	48	(5 / 5)	2.48	(0.20 / 0.25)	58	(1 / 2)	1.16	(0.03 / 0.03)
303					**49**	**(3 / 3)**	**1.13**	**(0.05 / 0.04)**
305	0		0.32	(0.01 / 0.02)	210	(8 / 12)	0.32	(0.01 / 0.01)
307					318	(27 / 34)	0.21	(0.02 / 0.02)
308					835	(200 / 385)	0.08	(0.03 / 0.03)
309	**390**	**(65 / 290)**	**0.051**	**(0.005 / 0.012)**	1560	(90 / 110)	0.043	(0.003 / 0.002)
310	225	(25 / 35)	0.25	(0.04 / 0.03)	402	(13 / 16)	0.17	(0.06 / 0.06)

bold Ne/Al (Appendix A) **bold Be** (Appendix A)

cp. - complex in erosion islands (Fig.6) in the field of complex exposure, boulder and amalgamted clast samples
fb. - forbidden in erosion islands (Fig.6) in the field of forbidden exposure, see text
sat. - saturated, not resolvable for exposure time, see text

3.6.4 Depth profile

In order to test the effect of a thin regolith cover that may have potentially altered the reconstructed pattern of erosion rates based on our bedrock samples for hillslope interfluves we analysed ^{10}Be and ^{21}Ne in a depth profile within an Oxaya ignimbrite section (CN101-107). The sampled section is made up of a 20 cm thin regolith cover that is characterized by a clast-supported fabric with ignimbrite boulders and a sandy matrix. Beneath 20 cm depth the ignimbrite displays its original stratigraphic sequence (Fig. 3C and 7). The nuclide data are presented in Tables 2 and 3 and Fig. 7.

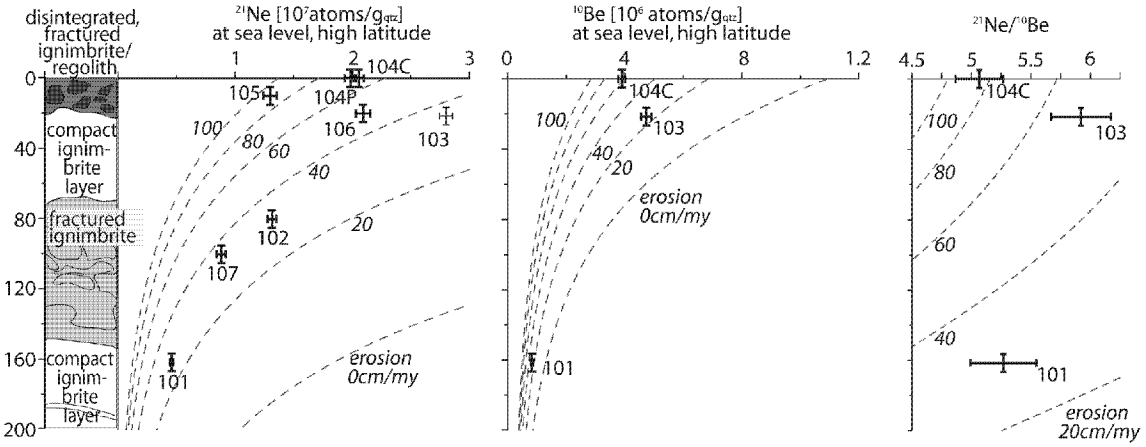

Fig. 7 Depth profile analysed to distinguish weathering vs. transport limited conditions. Concentrations of cosmogenic ^{21}Ne, ^{10}Be and ^{21}Ne/^{10}Be vs. depth.

The ^{10}Be and $^{21}Ne_{cos}$ concentrations reveal a pattern that is consistent with the stratigraphic architecture of the section (Fig. 7). Specifically, samples taken from the regolith cover display an irregular scatter in $^{21}Ne_{cos}$-concentrations and suggest that the uppermost 20 cm of the depth profile represent a mixed (mobile) layer. In this mixed layer, calculated erosion rates vary between 40-100 cm/my (Fig. 7). In the bedrock below, concentrations of ^{21}Ne and ^{10}Be decrease continuously with depth. The maximum concentration is measured for sample CN103 at 25 cm depth, while the lowest concentration is determined for sample CN101 at 160 cm depth. This drop in nuclide concentrations follows an exponential line characteristic for erosion rates of ~30 cm/my. The ^{21}Ne/^{10}Be-ratios suggest erosion rates in good agreement with the single nuclide estimates (Fig. 7). Because erosion rates deduced from bedrock samples at hillslope interfluves and the depth profile are almost identical, we presume that a possible sporadic coverage by a thin regolith will not substantially modify the general pattern of erosion rates reconstructed for the Andes of northern Chile.

3.6.5 Sediment yield

Data about suspended sediment concentration, water discharge, and denudation rates for the Rio Lluta, that drains the northern portion of the study area, are presented in Table 5. The data represent a fragmentary record over the years of 1988-2002. The resulting denudation rates serve only as a first order estimate for the comparison with TCN-derived erosion rates. The pattern of discharge shows strong seasonal variations with maximum values during Bolivian Winter periods (late January to early March). These maxima can be especially pronounced when superimposed by an El Niño period. The data imply that Bolivian Winter periods account for >50% of the sediment concentration.

Since there are no systematic measurements of bedload and solutes we assume a (bedload+solute)/suspended load ratio of 0.7 to calculate the total sediment flux. This ratio is likely a maximum that may cover the range of bedload and solute load contributions measured in natural arid systems (Meybeck, 1987; Summerfield, 1991; Laronne et al., 2002). The catchments that contribute to the sediment yield budget are in the *Western Cordillera* (Kober, 2005, in press-b) whereas the *Western Escarpment* and *Coastal Cordillera* are only transfer zones. To transform sediment yield data (t/(yr*km^2) to denudation rates (m/my) we assume a density of 2.7 tm^{-3}.

Table 5 Sediment yield data for high elevated catchments of Rio Lluta (ρ=2.7g/cm^3)

Lluta River			
		Average (1988-2002)	**ENSO years (1994/2001)**
total sediment quantity	mg/l	408	708
discharge	m^3/s	1.31	1.59
particulate load	(*10^4)t/yr	3.55	1.69
Area	km^2	2550	2550
sediment yield	t/(yr*km^2)	6.61	13.93
average total denudation rate	(*10^{-3})mm/yr=(m/myr)	2.33	4.90

Data from: Ministerio de Obras Publicas Direccion General de Aguas

Calculated short-term total denudation rates for the drainage systems of Rio Lluta are 2.33*10^{-3} mm/y (2.33 m/my). This value increases by a factor of two for El Niño years. Hence, the data clearly illustrate the importance of the episodic (annual and decadal) nature of sediment flux and surface denudation in the study area. Note that because the *Western Cordillera* has been the predominant sediment source, the calculated denudation rates for the Lluta drainage system are only representative for the highest part of the Andes of northern Chile. The short-term denudation rates derived from sediment yield are of the same order of magnitude or perhaps somewhat lower than the long-long erosion rates derived from TCN for the *Western Cordillera* (Fig. 6).

3.7 Discussion

In the following we will first discuss factors possibly influencing TCN-derived erosion rates and apparent exposure ages in the study area, such as climate variability, episodic erosion or lithological effects. This will be followed by a discussion of the potential temporal and spatial scale of erosion rates at the western slope of the Central Andes.

Similarities and differences between erosion rates on hillslope interfluves (TCN) and in the coupled hillslope-channel network system (sediment load) will also be considered.

3.7.1 Climate and erosion rates

The various nuclides reach saturation concentrations after different times, depending on half-life and erosion rate. Therefore, drastic variations in, e.g., climate, that in turn would lead to an increase in erosion rates, of say, orders of magnitude, would lead to different apparent mean TCN-erosion rates and exposure ages for the various nuclides. We do not see such a trend of systematically high or low erosion rates for any of the nuclides studied (Tables 4, APPENDIX A and Fig. 6). This suggests that on the *Western Escarpment* climatic conditions remained approximately constant over 1-5 my. Note that only for the *Western Escarpment* such climate variations can be detected since there the initial erosion rates are very low. In the *Western Cordillera* erosion rates are too high ($\geq$ 1m/my) to detect climate variations with the TCN used here.

3.7.2 Constant versus episodic erosion

So far we have treated the erosion rates as being constant in time, although we have observed situations in the field where spalling of rock slabs (1-10 cm) had occurred (Fig. 3D). Furthermore, in thin sections, we noted a planar texture defined by flattened glass shards that is related to welding and which may enhance slab break-off. We therefore consider here whether the fact that none of our data points fall on the saturation line may be explained because in reality the samples were all eroded episodically by slab detachment rather than by continuous erosion. The influence of episodic spalling on TCN concentrations has been discussed in some detail by Small et al. (1997). Here we model the path of data points in a Ne-Be erosion island diagram (Fig. 8) for samples having suffered regular episodic slab removal (with episode intervals – t_s in y). Various combinations of the interval between two successive spalling events and the thickness of the spalled slabs (L_s; in cm) are shown. The forcing time (i.e., to break off a slab) is considerably shorter than the response time (to recover the nuclide inventory) in these models. Paths described may oscillate considerably around the curve representing continuous erosion with rates equal to the long-term average values for the respective episodic scenario. While a relatively rapid succession of removals of relatively thin slabs (e. g. L_s<10 cm; $t_s=10^5$ yr) leads only to minor oscillations, spalling of relatively thick slabs at longer intervals (e. g. L_s>20 cm; $t_s=10^6$ yr) will lead to considerable offsets from the respective line for continuous erosion. Depending on the time elapsed since

the last spalling event, inferred erosion rates assuming continuous erosion may indeed be considerably higher or lower than the true mean rates for episodic erosion, and in some cases the data path even extends into the field of complex exposure, e.g. right after a spalling event.

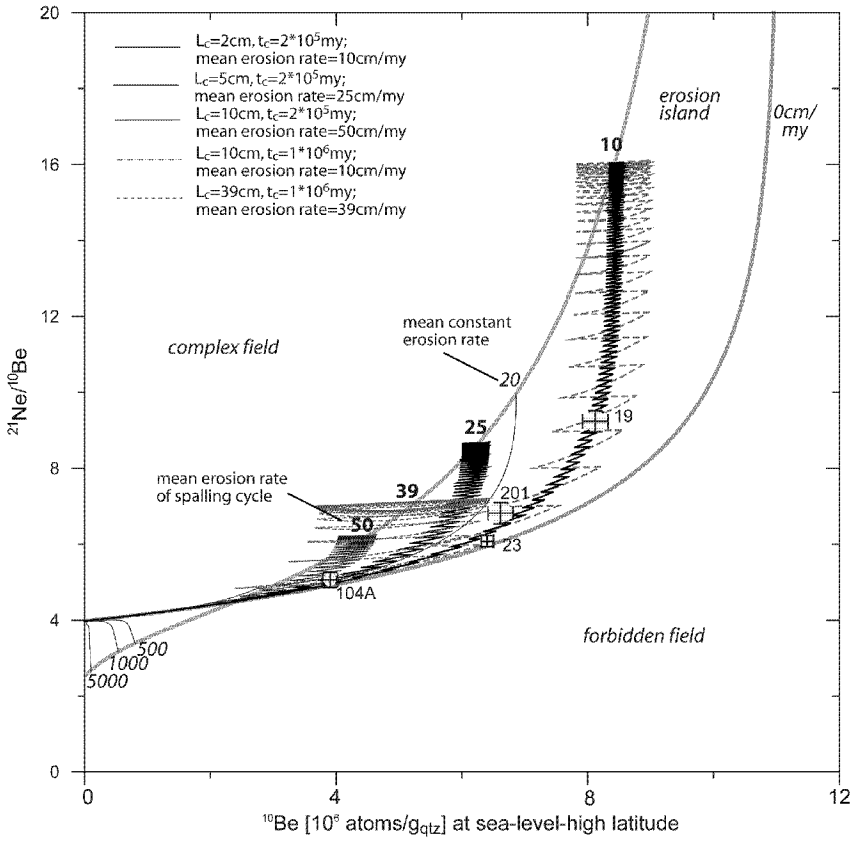

Fig. 8 Evolution of the ^{10}Be and ^{21}Ne concentrations in a rock experiencing episodic erosion by rock spalling. Initial nuclide concentrations are zero. Each curve is calculated by assuming removal of slabs of identical thickness (L_s) at constant intervals of time (t_s). The mean resulting erosion rate is given at the top of each curve, where nuclide saturation is reached. All curves oscillate around the line representing continuous erosion with the rate equal to the mean erosion rate. However, apparent erosion rates based on the continuous erosion assumption may be considerably higher than the true mean rate shortly after the break off event and considerably lower than the true value shortly before the next break off. Some portions of the paths even extend into the complex field of erosion. The data points indicated are discussed as examples in the text. Note that a relatively rapid succession of removals of relatively thin slabs (L_s<10cm, as observed in the field) would lead only to minor oscillation, around the mean erosion rate.

We conclude, however, that the position of those data points with relatively high nuclide concentrations below the saturation line cannot solely be explained by episodic erosion. For example, sample CN19 (with a nominal continuous erosion rate of about 10 cm/my and an exposure age of ~6 My; Table 4), can be explained by various episodic scenarios but all with long term mean erosion rates not too different from 10 cm/my (only a few typical lines shown in Fig. 8). In none of these cases, however, the position of the data point can be explained by assuming an infinite exposure age. All scenarios shown will lead to

exposure ages of CN19 well below the time of ~30 My needed to approach saturation at a mean erosion rate of 10cm/my. Additionally, this time is higher than the age of eruption of the Oxaya ignimbrites from which sample CN19 was taken (19-23 My, Table 1). While no spalling scenario with a mean erosion rate considerably different from the 10 cm/my can explain CN19, the position of other data points of samples such as CN201 (with e.g., L_s=39 cm, t_s=1*10^6 yr instead of continuous erosion of 15 cm/my) or CN104 (with e.g., L_s=10 cm, t_s=2*10^5 yr instead of continuous erosion of 28 cm/my) can be explained by spalling. In these cases, the measured data point and the oscillating spalling curve match when the spalling curve reaches a minimum value of erosion (Fig. 8). However, also here, infinite exposure ages are not reached.

In conclusion, episodic spalling of slabs with thicknesses on the order of decimetres and with recurrence intervals of <1*10^6 may bias our inferred mean erosion rates in Table 4, although hardly by much more than a factor of 2. The number of samples at a given elevation with similar erosion rates (Fig. 6) suggests that the trend of increasing erosion rates with increasing elevation and precipitation is not significantly modified by this factor of 2.

While undersaturation of nuclide concentrations is likely caused neither by episodic spalling nor by burial alone (e.g., a thin regolith cover, see section 'Depth profile') for our samples, it can be due to a relatively short exposure interval by even constant erosion. Shorter exposures histories than the time required to reach saturation can occur by unroofing the sample site instantaneously on the m-scale during events for which we may have no field evidence. Therefore we are only able to constrain our erosion rates for the time intervals given in Table 4 and Appendix A, which are less than the formation ages of the rocks stated in Table 1. Additionally and consequently, the studied surfaces have not been exposed since their initial emplacement with respect to the upper meter of the earth surface. In terms of (regional) landscape evolution, where a few meters likely are negligible, the surfaces sampled may indeed be the 'original' surfaces in place since deposition (see discussion below).

3.7.3 Dependency of TCN-erosion rates on lithology

Erosion rates presented in Table 4 were determined from samples representing different lithologies (Fig. 2). However, we interpret the observed increase in erosion rates with increasing elevation as a climatic signal not biased by lithology. Firstly, inferred erosion rates increase with altitude and precipitation rate irrespective of the sampled lithology. Secondly, similar or identical lithologies from different elevations yielded erosion rates that consistently increase with precipitation rates. This is, for instance, the case for the ignimbrite

samples CN111 (Oxaya ignimbrite) and CN26 farther south (Altos de Pica ignimbrite), or for the Lauca ignimbrite samples CN310 and CN113 (Table 4).

3.7.4 Effects of surface uplift on TCN-derived erosion rates

In our calculations we neglected the effect of surface uplift on TCN-concentrations, which generally would lead to overestimation of erosion rates (Craig and Poreda, 1986; Brown et al., 1991; Lal, 1991; Ivy-Ochs, 1996). In our case, maximum surface uplift rates are 0.2-0.3 mm/yr for the *Altiplano* since the late Miocene (Gregory-Wodzicki, 2000), and must be even less for the *Western Escarpment*, a monoclinal flexure to the west of the Altiplano (Isacks, 1988). Such uplift rates will not significantly alter the relevant nuclide production rates and hence the deduced surface erosion rates (see Lal, 1991).

3.7.5 Temporal variations in surface erosion rates and apparent exposure times

The multiple and single nuclide mean erosion rates for the three nuclide systems - ^{10}Be, ^{26}Al, and ^{21}Ne - are similar to each other (Fig. 6). This highlights the consistency of the dataset and the long-term steadiness of erosion rates (e.g., >2 My for some locations). Complex exposure histories were identified for boulder and amalgamated clast samples by the use of erosion island diagrams.

Erosion rates calculated from the depth-profile data support the general estimates of erosion rates that are based on regolith-free bedrock surface samples. Although we have identified a mixed regolith layer at site CN104, the erosion rates calculated for the depth profile are very similar to those for the bedrock samples. Therefore, even if our bedrock sample sites had been covered for a limited time by regolith due to possible down-slope advection of material, this possible coverage would not significantly modify our general pattern of established erosion rates of the western slope of the Central Andes (Fig. 6).

Interestingly, annual and decadal scale denudation rates determined from modern sediment flux are similar to or slightly smaller than the long-term TCN erosion rates derived for the *Western Cordillera* (Fig. 6). Differences can be explained by sediment storage in the catchment area (although not apparent in the field), an offset between rainfall and runoff extremes (Dickinson and Wall, 1977) or simply reflects the uncertainties of our calculations. Nevertheless, this comparison suggests that the rainfall pattern observed in the *Western Cordillera* today must have prevailed since at least the Pleistocene/Holocene. This argument can be extended to the Pliocene/late Miocene, since rainfall was likely orographically fixed. This is supported by low TCN-erosion rates at the *Western Escarpment* and thus rainfall must have been restricted to the *Western Cordillera*. Hence, the Andean relief, that controls the

position of the orographic rainfall, might have been in place for similar time periods, if not longer.

While (Mortimer, 1980; Alpers and Brimhall, 1988; Dunai et al., 2005) deduced similarly low erosion rates to have prevailed since the Oligocene, but certainly since the middle Miocene, (Hartley, 2003) suggested that in the *Atacama Desert* hyperarid conditions started only around 4 My ago. Our results confirm the reported temporal range of hyperarid climate conditions from the middle to late Miocene onwards, or even earlier (cf. (Kober, 2005, in pres-b).

3.7.6 Spatial variations in surface erosion rates and apparent exposure times

Erosion rates based on ^{10}Be, ^{21}Ne, and ^{26}Al remain nearly constant at ca. 10-100 cm/my between the *Coastal Cordillera* and the *Western Escarpment*, and then increase substantially from 100 to 4600 cm/my between the base of the *upper Western Escarpment/ Western Cordillera* and the *Altiplano* (Fig 5). Thus, landscape shaping processes are suppressed in the *Coastal Cordillera* and the *Western Escarpment* area and restricted to incision by the major rivers (see Kober, 2005, in press-b). Additional evidence for this derives from incised channels described in the *Costal Cordillera* that lack any evidence of fluvial incision and sediment transport after late Miocene times (Allmendinger, 2003;Kober, 2005, in press-b). The findings of increasing erosion rates in the *Western Cordillera* derived from TCN is also corroborated by the sediment yield data. As outlined earlier, the erosion rates correlate positively with the present day pattern of precipitation, which, in turn, is a function of altitude. This implies a topography induced precipitation threshold and control on erosion and denudation rates.

Our erosion rate estimates derived for the *Western Cordillera* are similar to those reported in earlier studies for the region although on different temporal and spatial scales. Based on mineralization analysis and mass-balance calculations (Scholl et al., 1970; Alpers and Brimhall, 1988) derived values of 7-42 m/my for the Oligocene/Miocene to the Pliocene, whereas we report for the *Western Cordillera* up to 46 m/my for the Pleistocene/Holocene. For the core of the Atacama Desert further south, Nishiizumi et al. (1998) and Dunai et al. (2005) determined erosion rates that are as low as or lower than those of the *Coastal Cordillera* and the *Western Escarpment* measured in this study. The constancy of low erosion rates over a north-south transect of over 500 km contrasts markedly with the two to three orders of magnitude increase in erosion rates that occurs over an W-E-altitudinal cross-section

of <50 km. This highlights the dominant influence of orographic rainfall on surface erosion, not only at present, but also for time scales back into the late Miocene.

3.7.7 Implications of low erosion rates for the western Central Andes

For the *Western Cordillera* long-term production rates of transportable sediment deduced from TCNs are similar to sediment yields, and hence, to denudation rates of coupled hillslope-fluvial processes. This indicates that, except for volcanic activity, the landscape has been nearly in steady-state equilibrium for Holocene/Pleistocene time periods. In the lower reaches of the study area that receive no rainfall, TCN based erosion rates are in the range of several tens of cm/my. Low river incision rates (50-100 m/my) were also reported for this part of the Andes (Wörner, 2002; Garcia, 2005; Kober, 2005, in press-b). Although the similarity between hillslope and fluvial erosion rates implies little relief growth in this part of northern Chile and hence near steady-state geomorphic conditions, there is no correspondence between processes in the major valleys and on hillslopes in the dry portions of the study area. Slopes that border active river channels (e.g., Lluta River) are dominated by landslide activity as a means to adjust to critical hillslope angles. The upper hillslopes merge into the adjacent broad plains with a sharp break in slope. This suggests that denudation processes in these near steady-state landscapes occur although a decoupling between hillslope and channel processes is observed.

This near steady-state equilibrium of the topography or landscape, governed by hillslope and channel processes, is in stark contrast to the transient nuclide concentrations. Most of our samples do not exhibit saturation concentrations. This indicates that equilibrium timescales of TCN-accumulation and landscape processes must not necessarily be similar, which has to be taken into account when quantifying or modeling landscapes processes.

Although northern Chile represents an area with a potential for high sediment yield due to high drainage basin relief, sediment flux into the Chile-Peru trench is low (Scholl et al., 1970; Krissek et al., 1980; Thornburg and Kulm, 1986) compared to other active mountain belts (Milliman and Meade, 1983). The arid to hyperarid climate conditions and the limited coverage by glaciers in the past (Ammann et al., 2001) may have reduced sediment production. The low erosion rates compared to the uplift rates led Lamb and Davis (2003) to conclude that the arid climate enhanced the uplift of the Andes and led to a net increase in the elevation of the central Andes since the Miocene. The deficiency of sediment input into the Chile-Peru trench was postulated to have been a result of the low erosion rates, which in turn were caused by a prolonged hyperarid climate. This latter argument was verified recently by

Dunai et al. (2005) for the *Coastal Cordillera*, and we now extend it to the Western Escarpment.

Similarly low erosion rates as those reported here have been obtained by TCN-studies for other hot and cold arid landscapes, such as the passive margin settings of the desert parts of Africa and Australia (e.g., Cockburn et al., 1999; Bierman and Caffee, 2001; Bierman and Caffee, 2002) or Antarctica (e.g., Nishiizumi et al., 1991; Ivy-Ochs et al., 1995). In contrast to these investigations, our study area is part of an active orogen. In contrast, the eastern flank of the Andes that receives more rainfall is characterized by high erosion rates and high tectonic activity (Masek et al., 1994).

3.8 Conclusions

Erosion rates across the *Coastal Cordillera* and *Western Escarpment* (the northern part of the *Atacama Desert*) of northern Chile determined with cosmogenic nuclides are extremely low (<1 m/my; nominal exposure ages 1-6 my), but increase to >10 m/my nominal exposure ages 0.02-0.1 my) towards the *Western Cordillera*. As a result, estimated times of surface exposure vary from the middle-late Miocene in the *Coastal Cordillera* and the *Western Escarpment* (Pampa de Oxaya) to Pleistocene/Holocene times in the *Western Cordillera*. The decreasing exposure ages and increasing erosion rates with altitude are interpreted to be a function of orographic precipitation.

Erosion island plots are a valuable tool for the determination of erosion rates and exposure ages and for the identification of complex exposure histories. Saturation of nuclide concentrations, commonly assumed in single nuclide erosion rate and exposure age studies, is not always recorded, likely due to TCN exposure histories that are younger than the formation age of the studied rocks or perhaps due to some episodic spalling events mimicking constant erosion for some samples. However, the spalling must have occurred in thin flakes, otherwise our data points would more often plot in the complex field of exposure and erosion. Therefore, erosion island plots are a helpful means to evaluate exposure/erosion histories.

Production rates of transportable sediment deduced from cosmogenic nuclides are similar to sediment yields and denudation rates of coupled hillslope-fluvial processes derived from sediment yield data in the *Western Cordillera*. This is the area were present day rainfall occurs. Therefore, in terms of landscape shaping processes the western slope of the Central Andes can be subdivided into an active (*Western Cordillera*) – and inactive (*Coastal Cordillera* and *Western Escarpment*) zone. According to this, topographic steady-state

conditions are suggested to be linked with orographic precipitation. The time intervals necessary to reach steady-state concentrations for cosmogenic nuclides can be quite different from those needed for a landscape to reach steady-state.

Acknowledgments

We appreciate the help of H. Schneider, G. Simpson and G. Zeilinger in the field and for satellite image processing. Discussions with M. Schaller, T. Dunai and G. Hoke are also greatly appreciated. We thank F. Scheifele for help with quartz separation and radionuclide sample preparation. The Zürich AMS facility is jointly operated by the Swiss Federal Institute of Technology, Zürich and the Paul Scherrer Institute, Villigen, Switzerland. This study was funded by Swiss National Science Foundation grant 620-576.663 to F. Schlunegger.

Table 4A comparison erosion rates

sample	single nuclide erosion rates (cm/my), infinite time									minimum ages - single nuclide (my), zero eorsion								
	Be			Al			Ne			Be			Al			Ne		
		(+/-)			(+/-)			(+/-)			(+/-)			(+/-)			(+/-)	
1c	**39**	2	1				**45**	2	2	**1.34**	0.04	0.03				**1.50**	0.07	0.07
5	**35**	2	2	**23**	5	4	**39**	1	2	**1.45**	0.07	0.06	**1.45**	0.17	0.15	**1.70**	0.09	0.07
7							**27**	4	4							**2.53**	0.38	0.38
8b	**80**	5	4				**65**	5	5	**0.78**	0.04	0.04				**1.04**	0.07	0.08
16	**83**	5	4				**55**	4	4	**0.75**	0.04	0.03				**1.23**	0.07	0.08
19	**12**	1	1	**9**	4	5	**18**	1	0	**2.92**	0.13	0.17	**2.25**	0.56	0.38	**3.67**	0.12	0.12
23	**24**	1	1	**40**	5	6	**35**	1	1	**1.90**	0.04	0.05	**1.04**	0.09	0.09	**1.92**	0.09	0.08
26	**162**	6	8	**125**	10	10	**167**	7	8	**0.43**	0.02	0.02	**0.47**	0.03	0.03	**0.40**	0.02	0.02
36	**76**	5	6	**107**	9	9	**50**	6	6	**0.81**	0.04	0.04	**0.53**	0.04	0.03	**1.36**	0.15	0.15
104A	**62**	3	3				**70**	3	3	**0.94**	0.04	0.03				**0.96**	0.05	0.03
111F	**52**	3	3	**55**	6	6	**65**	3	3	**1.09**	0.05	0.05	**0.85**	0.07	0.06	**1.05**	0.08	0.05
112	**470**	25	30				**423**	22	24	**0.17**	0.01	0.01				**0.16**	0.01	0.01
113	**4600**	250	250	**4540**	240	260	**3450**	480	680	**0.020**	0.001	0.001	**0.022**	0.001	0.001	**0.020**	0.004	0.003
201	**22**	2	2	**n.p.**	n.p.	max.3	**31**	2	1	**1.98**	0.1	0.1	**n.p.**	n.p.	min. 3.15	**2.20**	0.09	0.08
203	**26**	1	2	**1**	n.p.	4	**0**	0	1	**1.76**	0.09	0.08	**4.39**	n.p.	1.35	**12.50**	0.50	0.50
301	**42**	2	3	**27**	9	10	**48**	1	1	**1.26**	0.06	0.04	**1.30**	0.28	0.22	**1.41**	0.04	0.04
302	**55**	3	2	**84**	8	8	**58**	1	2	**1.05**	0.04	0.01	**0.63**	0.05	0.04	**1.16**	0.03	0.03
303	**49**	3	3	**56**	5	6				**1.13**	0.05	0.04	**0.84**	0.05	0.05			
305	**230**	10	10	**245**	22	24	**210**	8	12	**0.32**	0.02	0.01	**0.28**	0.02	0.02	**0.32**	0.01	0.01
307							**318**	27	34							**0.21**	0.02	0.02
308							**835**	200	385							**0.08**	0.03	0.03
309	**2400**	150	150	**2130**	130	180	**1560**	90	110	**0.040**	0.002	0.002	**0.044**	0.003	0.003	**0.043**	0.003	0.002
310	**480**	20	20	**512**	25	28	**402**	13	16	**0.17**	0.01	0.01	**0.15**	0.07	0.06	**0.17**	0.06	0.06

n.p. - not possible; max. - maximum; mim - minimum

Table 4B Composite table of erosion rates and exposure ages derived from the Ne/Al, Ne/Be and Al/Be erosion island diagram and calculation procedure, see text

sample	**erosion island plots - erosion rates (cm/my)**									**erosion island plots - age (my)**								
	Ne/Al	(+/-)		Ne/Be	(+/-)		Be/Al	(+/-)		Ne/Al	(+/-)		Ne/Be	(+/-)		Be/Al	(+/-)	
1c				**31**	3	2							**2.52**	0.10	0.08			
5	**23**	5	7	**32**	3	3	**16**	0	sat.	**2.59**	0.22	0.31	**3.58**	0.28	0.30	**1.88**	0.44	sat.
7																		
8b				**cp**									**cp**					
16				**cp**									**cp**					
19	**12**	5	5	**10**	2	2	**12**	cp	6	**6.00**	0.95	2.35	**5.35**	0.23	0.25	**min 6.2**	cp	2.51
23	**cp**			**5**	2	2	**cp**			**cp**			**2.08**	0.03	0.03	**cp**		
26	**fb**			**cp**	cp	(min 170)	**fb**	fb	(85)	**fb**			**fb**		sat.	**fb**	fb	(0.63)
36	**cp**			**cp**			**cp**			**cp**			**cp**			**cp**		
104A				**28**	7	10							**1.25**	0.05	0.10			
111F	**59**	7	8	**<10/cp**			**cp**	cp(50)	cp	**2.94**	0.48	4.61	**<1.25**			**cp**	(min 10)	cp
112				**417**	17	20							**0.85**	0.08	0.08			
113	**3350**	180	150	**3400**	200	160	**cp**	fb (4600)	cp	**0.077**	0.001	0.009	**0.104**	0.007	0.097	**cp**	fb(1.55)	cp
201	**fb**			**15**	3	3	**fb**			**fb**			**3.05**	0.13	0.10	**fb**		
203	**4**	0	cp (1	**cp**			**fb**			**22.45**	9.3	cp(>60)	**cp**			**fb**		
301	**23**	14	15	**34**	3	4	**15**	fb	sat. (42)	**1.93**	0.2	0.4	**2.48**	0.10	0.15	**1.53**	fb	(min 5)
302	**cp**			**48**	5	5	**cp**			**cp**			**2.48**	0.2	0.25	**cp**		
303							**cp**									**cp**		
305	**cp**			**0**			**cp**			**cp**			**0.32**	0.01	0.02	**cp**		
307																		
308																		
309	**cp**			**cp**			**fb**	fb	cp(2400)	**cp**			**cp**			**fb**	fb	cp, (min 3.7)
310	**cp**			**225**	25	35	**cp**			**cp**			**0.25**	0.04	0.03	**cp**		

erosion rate/eposure age calculation: mean values calculated for concentrations and ratios from Tables 2 & 3; error +: using concentration error + for Ne/Be and Ne/Al and ratio error+ for Al/Be (and vice versa for error -); error values are added or subtracted from the mean values, unless in parenthesis, than it is the actual value

cp = sample is in the complex field of complex exposure (Fig. 5) , see text

fb = forbidden - sample is in the forbidden field of exposure (Fig. 5), although largely in the range of analytical uncertanties, see text

sat = saturated, value given for exposure ages is a minimum value

min = minimum value

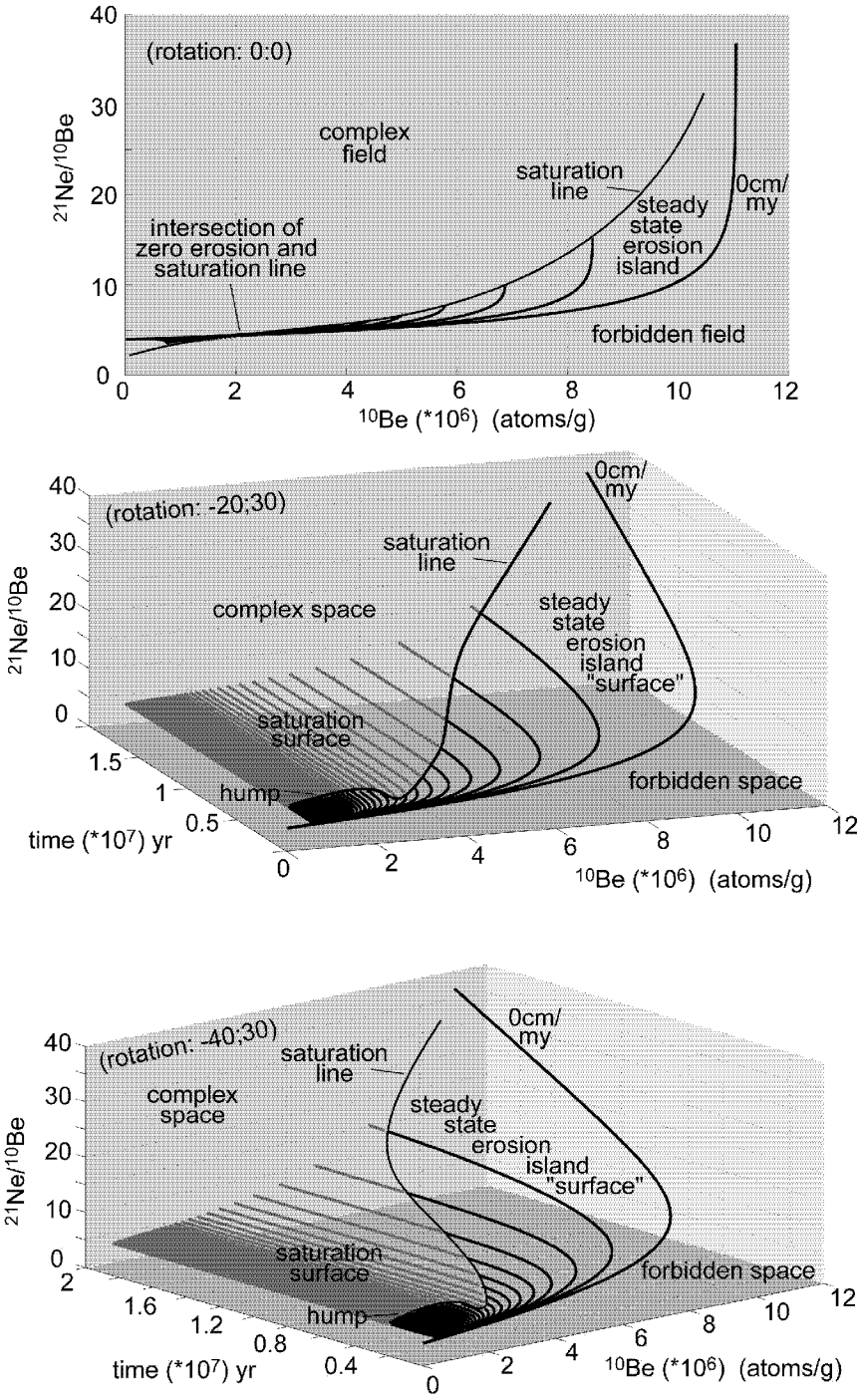

APPENDIX B Visualization of a Ne-Be and Al-Be steady state erosion island plots in 3D, with time as the third dimension, in order to illustrate the relationship between time, nuclide concentration and nuclide ratios. Black lines indicate transient nuclide concentrations (non-saturation), while grey lines indicate steady state nuclide concentrations (saturation). Erosion rate lines increase in steps with 10 cm/my per line for Ne-Be (up to 1000 cm/my) and 50 cm/my for Al-Be (up to 5000 cm/my) and beginning at zero erosion. Starting form an erosion island plot in 2D as shown in Fig. 5 the Ne-Be and the Al-Be are rotated -40:30 and 150:20 (horizontal:vertical), respectively. The rotation of the plot shows the steady state erosion island being a curved and stretched surface in the 3D-space (covering the erosion lines). The apparent saturation line in a 2D erosion island plot is the connection of points that are marked by the transition from black to grey of each line, i.e. the

transition from transient to steady state nuclide concentrations. The hump of saturation for low nuclide concentrations is caused by the dominance of muon production for radionuclides. Note that the intersection of the zero erosion line and the saturation line in Fig. 5 is only an apparent feature since they are offset due to the time dimension, not directly indicated in a 2D erosion island plot (clearly visible in the Ne-Be-3D-diagram). The field of higher muon production being located below the zero erosion line in a 2D erosion island diagram is not visible due to the scale of the 3D diagram (it's the 'hump' region in the last shown rotation step). While the steady state erosion island surface is the only solution(per definition) for a continuous erosion and exposure scenario for a sample, the complex and forbidden field - in 2D - occupying a space in 3D. The saturation field is only visible in a 3D erosion island diagram. All parameters for setting up the 3D erosion island plots are equal to the parameters given in Table 4 and Fig 5. (Code: G. Simpson).

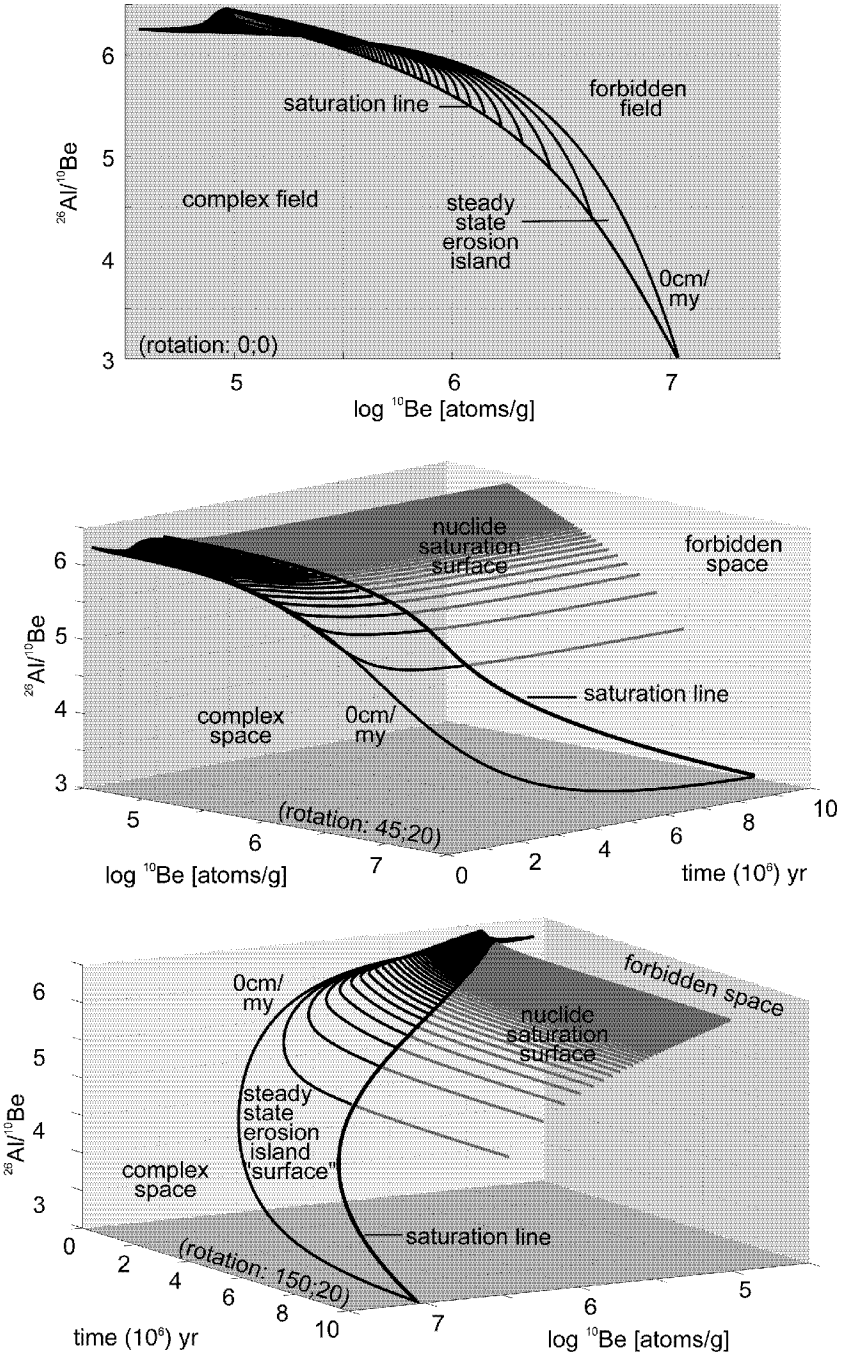

APPENDIX B Continuous

4 Preliminary results on weathering and erosion rates using cosmogenic nuclides in semi-arid regions of the Sierras Pampeanas, Argentina

In collaboration with

A. Kirschbaum[1], E. L. Piovano[2], F. Schlunegger[3], S. Ivy-Ochs[4], P. W. Kubik[5], R. Wieler[6], H. Baur[6]

[1]*Universidad Nacional de Salta, CONICET, Argentina*
[2]*Universidad de Córdoba, Argentina*
[3]*Institute of Geology, University of Bern, Switzerland*
[4]*Particle Physics ETH Zürich/University of Zürich, Switzerland*
[5]*PSI/Particle Physics ETH Zürich, Switzerland*
[6]*Isotope Geology ETH Zürich, Switzerland*

4.1 Abstract

The investigation of exposure ages and erosion rates as a pilot study for the timing of the exposure of granitic bedrock surfaces and the production of soil/regolith profiles of the Sierras Pampeanas in central Argentina is reported. Such calibrations can be used as tracers of Pleistocene climates.

In situ produced cosmogenic ^{21}Ne- and ^{10}Be concentrations in bare bedrock samples of the Sierra Norte de Córdoba and Sierra Grande del Norte yield minimum exposure ages in the range of middle Pleistocene values (110-195ky), which coincides with the penultimate glaciation. In turn, maximum single nuclide erosion rates of those bedrock surfaces are around 0.3-0.7cm/ky.

Initial attempts to place constraints on weathering- and regolith production rates by using cosmogenic nuclide concentrations in soil-depth profiles yielded ambiguous results when using $^{21}Ne_{cosmo}$ in physically cleaned quartz. Large contributions of atmospheric - and most likely also nucleogenic - neon components compromise any cosmogenic nuclide signal. The atmospheric contribution is probably due to an insufficient cleaning. Therefore in future studies, samples will be processed by chemical cleaning. In addition, ^{10}Be measurements will also be performed.

4.2 Introduction

Quantitative and qualitative knowledge is desirable about the mechanics and rates of weathering at denudational settings, and the production of material (by weathering) that can be transported (by erosion) from hillslopes via fluvial transport into depositional areas (i.e., floodplains, lakes and oceans). Climate and precipitation plays a major role in this cycle.

The huge Paleozoic granitic batholiths of central and northern Argentina are such denudating landscapes that exhibit erosional surfaces with multiple stages of development, e.g., Rabassa et al. (1995). Onto these granitic erosional surfaces, soil profiles of up to 30m in thickness have developed during the Quaternary. However, currently data on (i) the timing of the establishment of such surfaces, (ii) the erosion rates acting on those surfaces (iii) as well as the rates of soil/regolith production from the underlying granitic bedrock are lacking. Our goal was to provide such data by the analysis of cosmogenic nuclides.

The study-locations are the Sierra Grande de Córdoba (SG) and the Sierra Norte de Córdoba (Fig. 1). Geochemical and mineralogical investigations by Ross et al. (1998) indicated an initial weathering stage of the analysed soil profiles. Kirschbaum et al. (2004) analysed rock profiles, which were investigated in this study, and interpreted them in an incipient weathering stage.

In order to deduce minimum exposure ages and maximum erosion rates of bare bedrock surfaces and production rates of soil and regolith we used cosmogenic ^{21}Ne and ^{10}Be. The analysis of soil/regolith-depth profiles followed the methods developed by Monaghan et al. (1992); McKean et al. (1993); Brown et al. (1995b); Small and Anderson (1998); Heimsath et al. (1999). We assume for a first approximation that cosmogenic nuclide concentrations in bare bedrock surfaces are saturated and that the accumulation of cosmogenic nuclides within the soil profiles represents an in situ growth process.

If soil/regolith production is balanced by surface erosion the calculated rates represent comparable and convertible values. The geochemical and physical modification of bedrock into soil is investigated in a complementary study by petrological and major element analysis Kirschbaum et al. (2004),

4.3 Geotectonic setting and climate

The Sierras Pampeanas (Fig. 1) are subdivided into mountain ridges, bounded by tectonic valleys, due to tectonic activity during the late Tertiary (10-0My, Jordan and

Allmendinger (1986). Faults predominantly strike N, NNW and NNE. The Palaeozoic Sierra Norte batholith, on which the profiles studied here are located, was regionally eroded in the late Palaeozoic by an unknown thickness (Jordan and Allmendinger, 1986). This resulted in the establishment of erosional surfaces that were formed by multiple events of wide spread erosion (Ruiz Huidobro, 1972, Sayago et al, 1998).

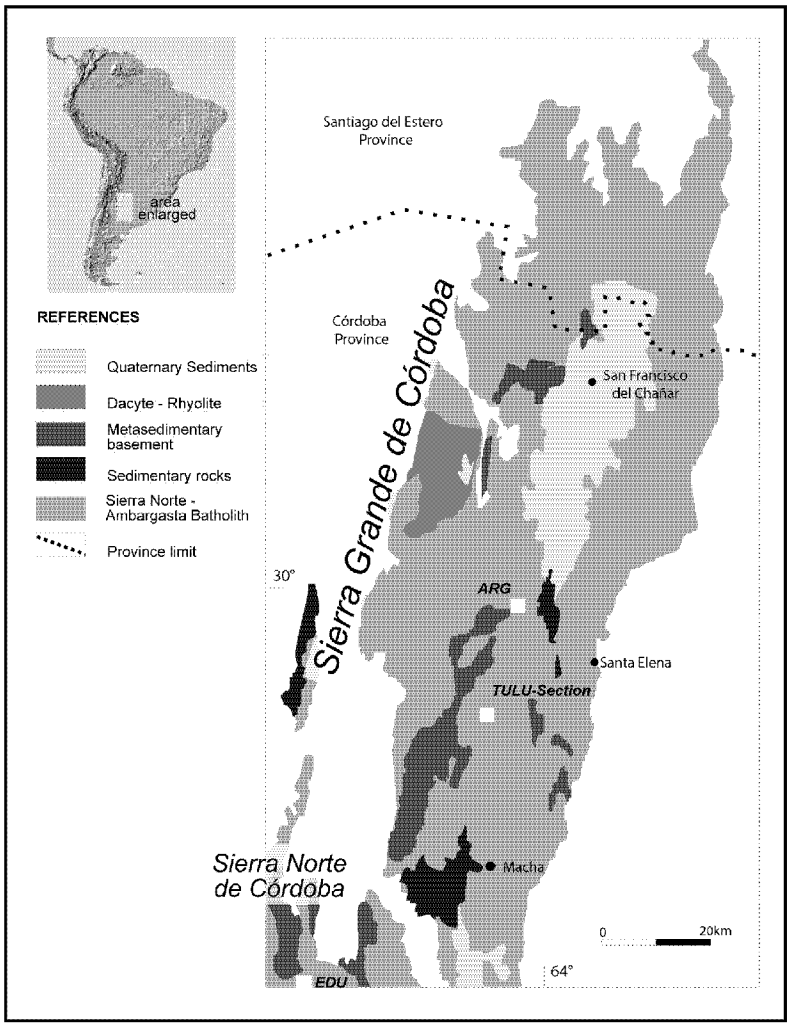

Fig. 1 Simplified map of the Sierras and samples discussed in the text (after Kirschbaum et al. 2004).

The climate during the Quaternary was controlled by the extent of glacial fluctuations (Clapperton, 1983; Carignano, 1999; Zarate et al., 2002; Zarate, 2003). Today, the study area is governed by a semi-arid climate and is located within the cool to warm temperate zones of central Argentina (Clapperton, 1993). Vegetation is characterized by pampas grassland. The Sierra Norte de Córdoba is at ca 2200m asl and is characterized by huge temperature

fluctuations, dry air and frequent strong winds. Average mean temperature is 10°C with minimum values of -10°C.

4.4 Soil profiles

The soil profiles that are investigated are characterized by A, B and C horizons (see Appendix, profile TULU, Fig.1 and 2a). The depth of the granitic basement varies between 3-12m. The A-horizon is usually thin, in the range of <0.5-1m. It superimposes a B-horizon of variable depth. The C-horizons are made of weathered granite of different stages, from fractured into almost intact bedrock. Distinct loess layers, derived from the Andean glacial valleys as typical for northwestern Argentina (e.g., Zinck and Sayago (1999)), are absent in the discussed profiles. Such loess layers are reported to date from middle to late Pleistocene/Holocene (Sayado et al., 2001; Schellenberger et al., 2003).

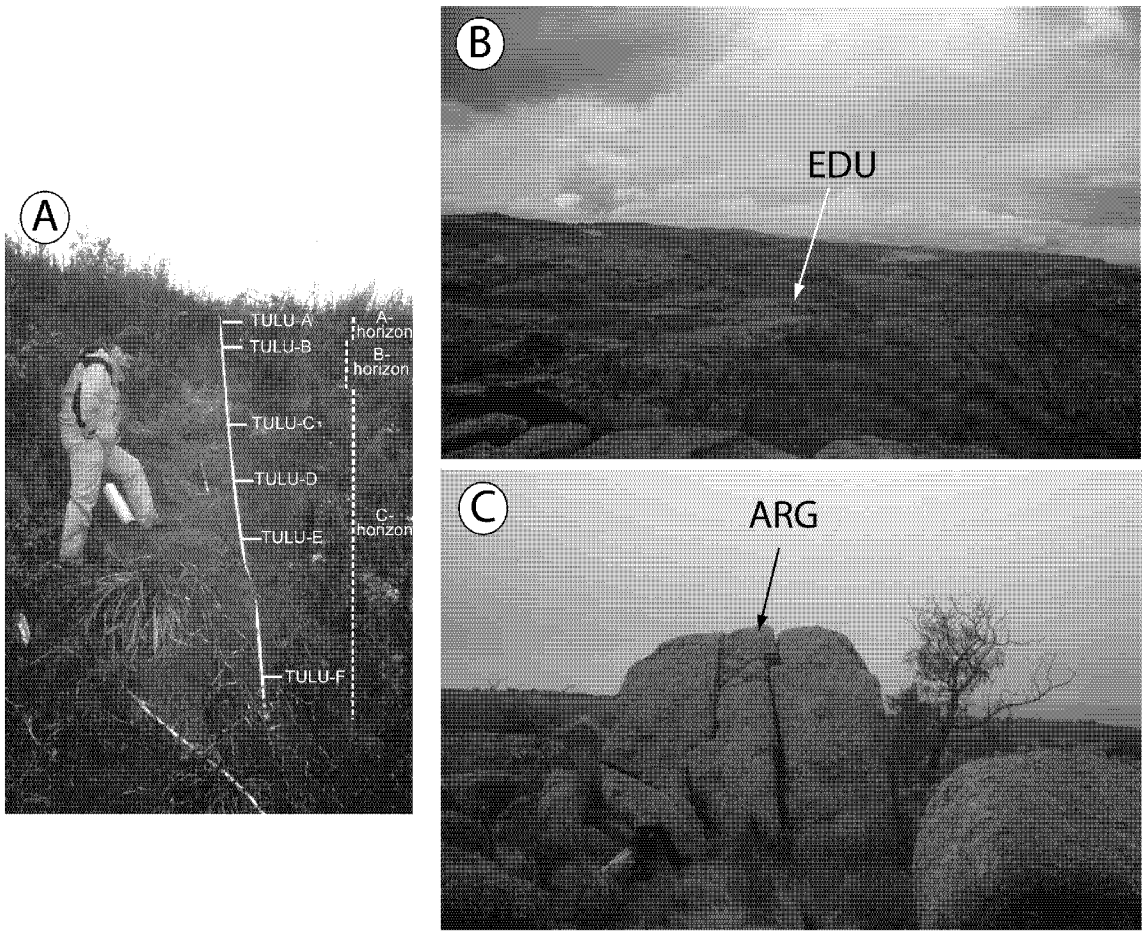

Fig. 2 A) Depth profile TULU, B) sample EDU and C) sample ARG. See text for further sample information

4.5 Methods

Sampling, sample preparation and analytical procedures

At the location Sierra Norte, we took a sample from a granitic boulder (EDU, Fig. 2b) while a piece from a quartz vein was taken in the Sierra Grande (ARG, Fig. 2c). In both instances, the minimum exposure age and the maximum erosion rate were of interest, to determine the maturity of the surfaces of those peneplains (Fig. 2, 3). Sample EDU was separated by physical cleaning methods only to give pure quartz aliquots, while the chemical separation procedure of Ivy-Ochs et al. (1996) was used to separate sample ARG. Detailed methodical information on sample preparation is given in Chapters 3 and 5.

Soil profiles were sampled by identifying specific horizons and taking samples from a fixed depth interval (usually a band of 10cm thickness). Detailed petrographical descriptions of the TULU-profile are given in Kirschbaum et al. (2004). In order to study whether cosmogenic nuclide concentrations indicate significant changes in mobility of fragments and clasts compared to fine-grained particles, we have partitioned the samples in "X" (=fines) and "Xgr" (=clasts) - fractions. Such a difference was suggested by Brown et al. (1995a) and Brown et al. (1998) due to variable transport processes and travel-times of clasts and fines in the soil profile. After washing out the clay and mud fraction, a size separation of >1000µm ("Xgr") and <355µm ("X") was performed. The fraction larger than 1000µm was subsequently crushed and sieved to fractions <1000µm and <355µm, respectively. In a further step both fractions <355µm (X and Xgr) were separated by heavy liquid and magnetic susceptibility methods and handpicking. High concentrations of alterated mica flakes were common for the samples of the A-horizon, suggesting a major grussification and conversion of bedrock into fines from the C- to B-horizon by mica-alteration.

Cosmogenic neon was measured by degassing samples in temperature steps of 600°C, 800°C and 1750°C, assuming the total cosmogenic component to have been released at 600°C (see details for method in Chapters 3 and 5). The 800°C step was used to test this assumption and the total extraction step at 1750°C was performed to release any non-cosmogenic component (Niedermann, 2002). Details of the analytical and technical procedures, data reduction, ^{10}Be-analystics and AMS measurements are reported in Chapters 3 and 5. Production rate scaling followed the procedure by Lal (1991) (Table 2) for the neutron component while muons were scaled based on Allkofer (1975; Heisinger et al. (2002a) and Heisinger et al., (2002b). We use production rates at sea level/high latitude following Niedermann et al. (1994) and Niedermann (2000) for $P^{21}Ne=20.3\pm4.0$ atoms$*g^{-1}*yr^{-1}$ and

Kubik and Ivy-Ochs (2004) for $P^{10}Be$=5.44±0.19 atoms*g^{-1}*yr^{-1}. Density of bedrocks is assumed to be 2.7g*cm^{-3} and for soil 2 g*cm^{-3}.

4.6 Results

4.6.1 Bedrock samples

Neon-nuclide concentrations of samples EDU and ARG are presented in Table 1A and neon isotope ratios are plotted in Fig. 3. Both the 600°C step and the 800°C control step of sample EDU plot on the atmospheric-cosmogenic mixing line with the 600°C step revealing a significantly higher ^{21}Ne excess. Nevertheless, we also include the small excess of the 800°C step in the calculations of a minimum exposure age and maximal erosion rate by following the formulations of Schaller et al. (2004) (Table 1C). A ^{21}Ne minimum age for sample EDU of 125±22ky is obtained, placing the exposure of the sampled surface at the latest into the middle Pleistocene. Instead, assuming an infinite exposure time a maximum erosion rate of 0.6cm/ky can be calculated.

For sample ARG, the ^{21}Ne-excess is calculated by using the 600°C degassing step (Fig. 3). However, this step is contaminated by a nucleogenic component which causes its data point to fall below the atmospheric-cosmogenic mixing line. We correct for this by assuming the total offset from the atmospheric-cosmogenic mixing line to be of nucleogenic origin and subtracting this $^{21}Ne_{nucleo}$ component (Fig. 3). This results in a lowering of the $^{21}Ne_{cosmo}$ concentration by ~50%. We are aware that this approach is oversimplifying the neon-inventory of the studied sample, and treat this concentration as an approximation. The 800°C step is ignored (Fig. 3). Surprisingly, the 1750°C fusion step plots again within uncertainties on the atmospheric-cosmogenic mixing line (Fig. 3). This step is ignored in the calculation as well, as we assume that cosmogenic contributions are released only at low temperatures. The source and nature of this high temperature component mimicking cosmogenic neon is unclear.

From the corrected concentration of the 600°C-temperature step we calculate a ^{21}Ne minimum exposure age of 195±68ky for sample ARG (Table 1C). On this sample ARG we have additionally measured ^{10}Be (Table 1B). The ^{10}Be-concentration corresponds to a minimum exposure age of 110±17ky. In turn, maximum erosion rates are 0.3cm/ky and 0.7cm/ky, for neon and beryllium, respectively. We consider the beryllium values to be more reliable due to the ambiguous neon-data (see above).

Table 1A. Neon-concentration and ratios

Sample Degassing (Temp. °C, time [min])	sample locality	elevation [m]	^{20}Ne $*10^{9}$ atoms/g	total error $*10^{9}$ atoms/g	$^{21}Ne/^{20}Ne$ $*10^{-3}$	total error $*10^{-3}$	$^{22}Ne/^{20}Ne$ $*10^{-1}$	total error $*10^{-1}$	$^{21}Ne_{cosmo}$ $*10^{6}$ atoms/g	total error $*10^{6}$ atoms/g	$^{21}Ne_{cosmo}$ total $*10^{6}$ atoms/g	total error $*10^{6}$ atoms/g
ARG(600,45')	64.07°W,	917	4.88	0.07	5.64	0.03	1.03	0.01	13.07	0.49	13.07	0.49
correction (see text)	*30.04°S*		***4.88***	***0.07***	***4.32***	***0.03***	***1.03***	***0.01***	***6.65***	***0.41***	***6.65***	***0.41***
ARG(800,30')			3.05	0.05	3.26	0.05	1.00	0.01	0.91	0.26		
ARG(1750,20')			1.42	0.02	3.54	0.19	1.03	0.01	0.82	0.29		
EDU(600,30')	64.45°W,	2200	10.18	0.27	3.90	0.04	1.03	0.01	9.54	1.39	**10.93**	**5.96**
EDU(800,30')	31.35°S		5.41	0.15	3.22	0.06	1.02	0.01	1.39	0.73		
EDU(1750,20')			6.33	0.17	3.05	0.02	0.99	0.01	0.55	0.73		

Table 1B. Beryllium concentrations

Sample	^{10}Be $*10^{5}$ [atoms/g]	error $*10^{5}$ [atoms/g]
ARG	9.68	0.50

Table 1C. Calculated minimum exposure ages and maximum erosion rates

sample	minimum age Ne [ky]	error [ky]	minimum age Be [ky]	error [ky]	Ne max. erosion [cm/ky]	Be max. erosion [cm/ky]
ARG	195	68	110	17	0.3	0.7
EDU	126	22			0.6	-

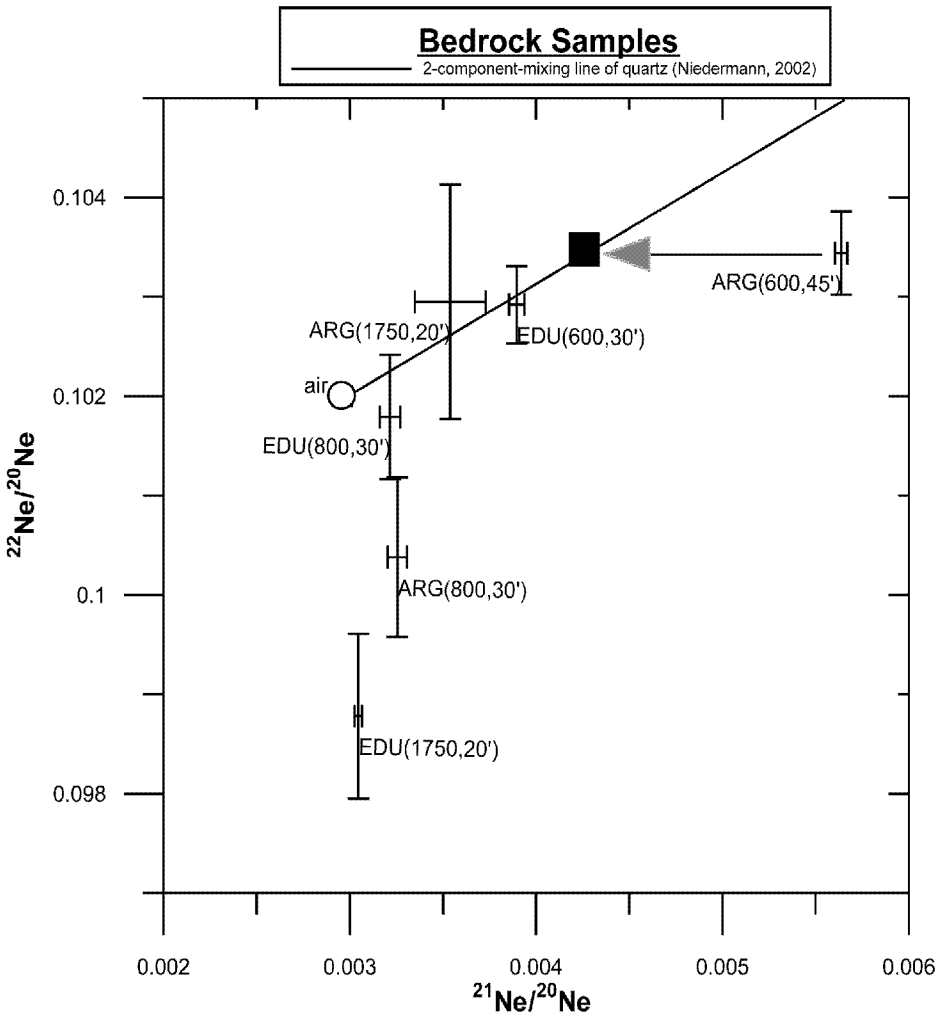

Fig. 3 Neon-three isotope plot for samples EDU and ARG. See text for discussion.

4.6.2 Depth profile

The TULU profile covers a depth of ca. 2m (sample TULU-F not measured, see Appendix A). Neon concentrations are presented in Table 2 and neon isotope ratios are plotted in a three-isotope-diagram in Fig. 4. Three major observations can be drawn from the neon three-isotope-diagram (Fig. 4): (i) Almost all low temperature data points (600°C and 800°C steps) scatter around atmospheric composition, indicating atmospheric and MORB- or nucleogenic neon contributions, (ii) a significant cosmogenic excess as an offset from atmospheric composition on the atmospheric-cosmogenic-mixing line (Niedermann, 2002) is not observed and, (iii) the high temperature steps (1750°C) show a nucleogenic ^{21}Ne source in excess.

The low temperature points that scatter around atmospheric composition indicate insufficient cleaning processes by the physical cleaning procedure. Nucleogenic neon components may be prominent in granitic rocks with elevated U/Th concentrations and an old formation age. High mica contents in the crushed rocks and removed during sample preparation may also be a source of some nucleogenic ^{21}Ne values (see Chapter 6).

Since cosmogenic concentrations are compromised by other neon components, $^{21}Ne_{cosmo}$ is not calculated and a modeling of soil/regolith production rates is not possible.

Table 2. Neon concentrations and ratios for TULU-depth-profile

sample (temperature [°C]/ time [min])	^{20}Ne $*10^{10}$ [atoms/g]	error $*10^{10}$ [atoms/g]	$^{21}Ne/^{20}Ne$ $*10^{-3}$	error $*10^{-3}$	$^{22}Ne/^{20}Ne$ $*10^{-1}$	error $*10^{-1}$	$^{21}Ne_{cosmo}$ $*10^{6}$ [atoms/g]	error $*10^{6}$ [atoms/g]
A(600,30')	1.64	0.05	3.31	0.03	0.96	0.01	5.77	2.08
A(800,20')	1.16	0.03	3.14	0.02	1.00	0.01	2.10	1.40
A(1750,20')	1.43	0.04	4.28	0.04	0.99	0.01	18.97	2.16
Agr(600,30')	0.95	0.03	3.57	0.02	1.01	0.01	5.77	1.17
Agr(800,30')	0.94	0.03	3.18	0.02	1.01	0.01	2.10	1.13
Agr(1750,30')	0.21	0.01	7.14	0.08	1.05	0.01	8.65	0.46
B(600,30')	0.60	0.02	3.44	0.05	1.02	0.01	2.93	0.84
B(800,20')	0.37	0.01	3.12	0.05	1.02	0.01	0.60	0.49
B(1750,20')	0.17	0.01	27.50	0.48	1.17	0.01	41.27	1.67
C(600,45')	1.82	0.03	3.06	0.04	1.03	0.01	1.88	1.42
C(800,30')	0.39	0.01	3.11	0.08	1.02	0.01	0.59	0.44
C(1750,20')	0.12	0.01	7.39	0.31	1.10	0.01	5.31	0.40
D(600,45')	0.78	0.01	3.35	0.03	1.01	0.01	3.08	0.61
D(800,30')	0.34	0.01	2.97	0.08	1.05	0.01	0.05	0.38
D(1750,20')	0.13	0.01	4.28	0.19	1.00	0.02	1.72	0.28
E(600,45')	1.02	0.02	3.16	0.05	1.02	0.01	2.07	0.90
E(800,30')	0.27	0.01	3.08	0.08	1.02	0.01	0.34	0.31
E(1750,20')	0.16	0.01	3.84	0.04	1.02	0.02	1.45	0.22

4.7 Discussion

4.7.1 Bedrock samples

With the limited number of only two minimum ages we can preliminarily place the exposure of the Pampeanean surfaces in the middle to late Pleistocene. This corresponds to the time of the penultimate glaciation in Argentina (Clapperton, 1983). Snow cover and shielding by loess most likely happened, which strongly indicates that true ages are higher. If the discrepancy between neon and beryllium ages is not due to analytical problems in the

neon analysis, it might indicate a complex shielding history by snow or loess (Carignano, 1999; Zarate et al., 2002).

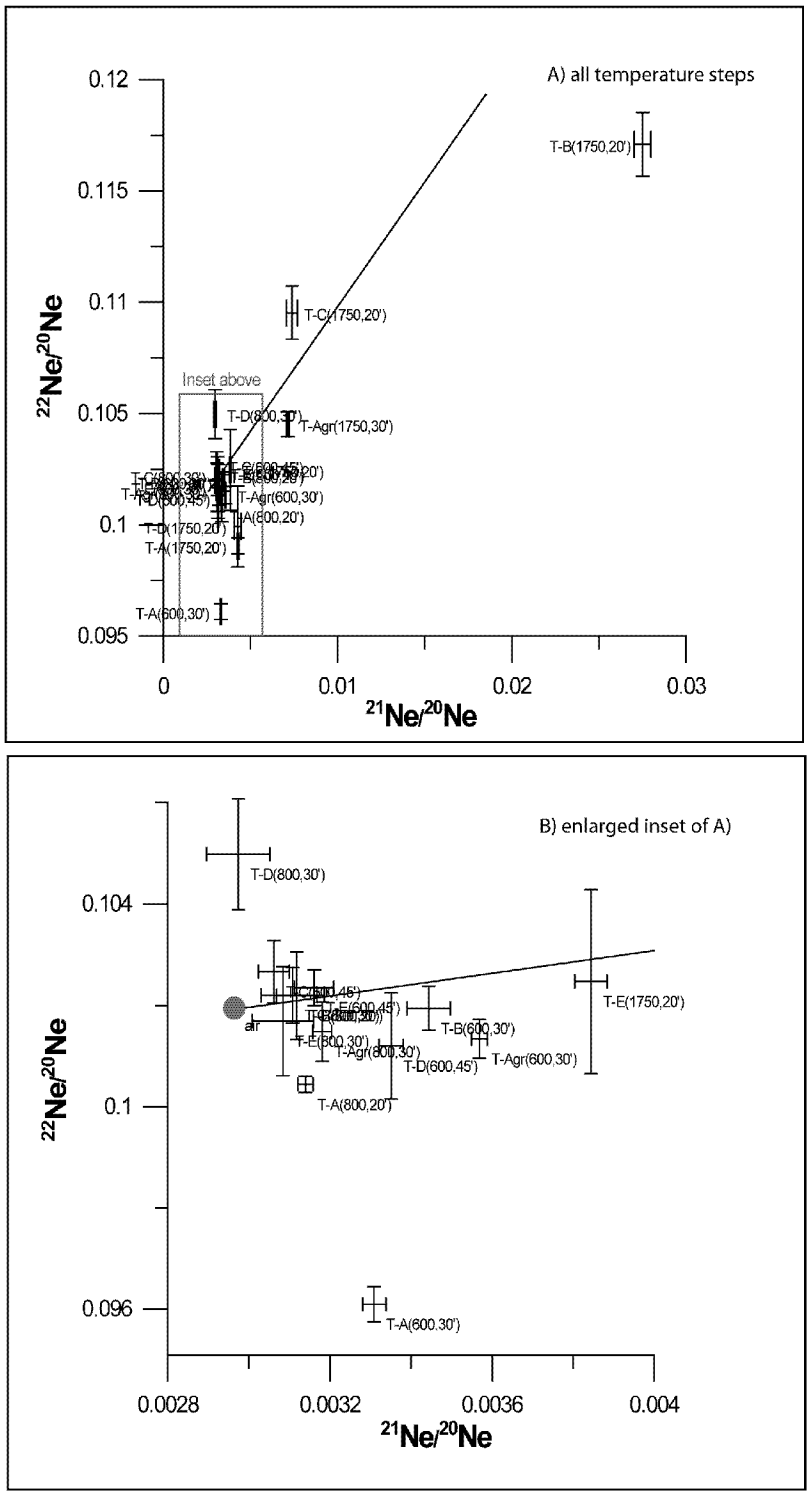

Fig. 4 Neon-three isotope plot for the TULU samples. A) all data points TULU, B) enlargement of subset indicated in A). See text for further discussion

4.7.2 TULU-profile

Further methodological studies on quartz and specifically a switch to a solely chemical etching procedure for quartz are necessary. Therefore, calculations and interpretations of soil production rates and correlations with geochemical parameters of the soil (Kirschbaum et al., 2004) are not yet possible. Neon will also have to be analysed by crushing samples in order to recognize possible nucleogenic components, although only nucleogenic neon from fluid inclusions will be detected by crushing, not crustal neon.

4.8 Conclusions

Preliminary bedrock exposure ages for the Sierra Grande de Córdoba and Sierra Norte de Córdoba revealed middle to late Pleistocene minimum ages, indicating the surfaces to be most likely stable and unaffected by the last glacial events (Carignano, 1999). In turn, erosion rates for bedrock surfaces are less than 0.5cm/ky during the last 100-200ky. Palaeoclimate oscillations as drawn for the late Pleistocene/Holocene as postulated by e.g., Carignano, (1999); Zinck and Sayago (1999); Zinck and Sayado (2001); Zarate et al. (2002) might have had little impact on the modification of the landscapes or were too restricted in magnitude to be recognized by terrestrial cosmogenic nuclides.

Appendix

Profile-TULU-description

- road cut on road from Dean Fuan to San Pedro del Norte near Tulumba

location: S 30°24.747'
W 64°13.294
865m

Sample	Depth	Description
TULU-A	0-10cm	*A-horizon* pebble size 0.5-4cm, high soil content, bad sorting, pebbles more weathered, root remnants, dark-brownish
TULU-B	30-40cm	*B-horizon* pebbles <1cm max, high soil content, bad sorting, root remnants, brownish
TULU-C	90-100	*C-horizon* alterated horizon, weathered granite, bad sorted, max. grain size 3cm, pebble fresh, root remnants, light brown
TULU-D	150-160	weathered granite, good sorting, max. grain size 1.5cm, no roots, high Bt-content, brownish-grayish
TULU-E	195-205	weathered granite, bad sorting, pebble to 5cm, small root remnants, dark brownish
TULU-F	300	weathered granite, bad sorting, pebble max. 4cm, a few roots, grey-brown

5 In situ cosmogenic ^{10}Be and ^{21}Ne in sanidine and in situ cosmogenic ^{3}He in Fe-Ti- oxide minerals [1]

F. Kober[a,b,*], S. Ivy-Ochs[c,d], I. Leya[b,+], H. Baur[b], T. Magna[b], R. Wieler[b], P.W. Kubik[e]

[a] *Institute of Geology, ETH Zurich, CH-8092 Zurich, Switzerland*

[b] *Institute of Isotope Geology, ETH Zurich, CH-8092 Zurich, Switzerland*

[c] *Institute of Particle Physics, ETH Zurich, CH-8093 Zurich, Switzerland*

[d] *Institute of Geography, University of Zurich, CH-8057 Zurich, Switzerland*

[e] *Paul Scherrer Institute, c/o Institute of Particle Physics, ETH Zurich, CH-8093 Zurich, Switzerland*

[+] *present address: Institute of Physics, University of Bern, CH-3012 Bern, Switzerland*

[*] *corresponding author: Tel.: ++41-1-6323637; E-mail: kober@erdw.ethz.ch*

5.1 Abstract

We report concentrations of in situ cosmogenic ^{10}Be and ^{21}Ne from coexisting quartz and sanidine separates and of cosmogenic ^{3}He in coexisting Fe-Ti-oxide minerals from ignimbritic successions of northern Chile (Oxaya and Lauca ignimbrites). New mineral-isotope pairs such as sanidine and Fe-Ti-oxide minerals are helpful in quantitative geomorphology for geological settings where the lithology lacks the commonly used minerals quartz, pyroxene or olivine. Production rates in sanidine and Fe-Ti-oxide minerals were determined by normalizing nuclide concentrations to established production rates in quartz. The experimentally determined production rates are compared to model production rates calculated with new cross sections for ^{3}He, ^{21}Ne, and ^{10}Be production from the individual target elements. The mean experimental ^{21}Ne production rate for five sanidine samples is 30.4±3.7 atoms*g^{-1}*yr^{-1} (30.4±5.4 atoms*g^{-1}*yr^{-1} including the uncertainty of the ^{21}Ne production rate in quartz, $P^{21}Ne_{qtz}$). This is in excellent agreement with the modelled value of 28.3 atoms*g^{-1}*yr^{-1}, which has an estimated uncertainty of 20%. The ^{21}Ne production rate in

[1] In press at *Earth and Planetary Science Letters, Available online 27 June 2005*

sanidine is thus about 50% higher than that in quartz. The cosmogenic neon in sanidine is entirely released in low temperature steps (400-600°C) and no signs of an interfering nucleogenic neon component were observed. This is in stark contrast to quartz and makes sanidine an attractive mineral for terrestrial cosmogenic neon studies. ^{3}He diffuses out of the sanidine structure. Preliminary results also indicate that sanidine is well suited for ^{10}Be studies. The mean experimental ^{10}Be production rate from two sanidine samples is 4.45±0.38 atoms*g^{-1}*yr^{-1} (4.45±0.42 atoms*g^{-1}*yr^{-1} including uncertainty of P^{10}Be$_{qtz}$), very close to the modelled value of 4.55 atoms*g^{-1}*yr^{-1}, which has an estimated uncertainty of 20%. We emphasize that ^{10}Be and ^{21}Ne production in sanidine is composition dependent. Therefore, major element analyses should be carried out and production rates calculated on a sample by sample basis.

Fe-Ti-oxide minerals retain ^{3}He quantitatively. Experimentally derived production rates are in excellent agreement with new values derived from physical modelling. The mean experimental ^{3}He production rate for five Fe-Ti-oxide minerals samples is 120±11 atoms*g^{-1}*yr^{-1} (120±12 atoms*g^{-1}*yr^{-1} including the uncertainties of P^{21}Ne$_{qtz}$), compared to a mean modelled value of 124 atoms*g^{-1}*yr^{-1}, which has an estimated uncertainty of 20%. The variable chemical and structural composition of the solid solution lines of Fe-Ti-oxide minerals has little effect on the total ^{3}He production rate. Cosmogenic ^{21}Ne is not produced in significant quantities in Fe-Ti-oxide minerals due to the absence of suitable target elements.

KEYWORDS: cosmogenic nuclides (^{3}He, ^{10}Be, ^{21}Ne), Fe-Ti-oxide minerals, sanidine, elemental production rates

5.2 Introduction

Terrestrial cosmogenic nuclides (TCN) such as ^{3}He, ^{10}Be, ^{14}C, ^{21}Ne, ^{26}Al and ^{36}Cl are widely used in Quaternary Geology and Geomorphology for exposure dating and erosion rate estimates (e.g., Bierman, 1994; Gosse and Phillips, 2001; Lal, 1991; Niedermann, 2002). The minerals most commonly utilized are quartz (^{10}Be, ^{21}Ne, ^{26}Al), pyroxene and olivine (^{3}He, ^{21}Ne). Several studies have shown that quartz can be cleaned reliably of meteoric ^{10}Be (Brown et al., 1991; Kohl and Nishiizumi, 1992) and retains ^{21}Ne quantitatively (Niedermann, 2002). Both pyroxene and olivine have been shown to retain both ^{3}He and ^{21}Ne (Cerling, 1990; Cerling et al., 1994; Kurz, 1986a, b; Schäfer et al., 1999). ^{36}Cl can be measured in any rock type, as whole rock samples are used and the production rate is calculated individually for

each sample (Gosse and Phillips, 2001; Phillips et al., 1986). In many situations, it would be desirable to rely on other minerals, for example if the lithology does not contain the minerals listed above. The search for the optimal samples from a geomorphological perspective would then not be compromised by the need to collect samples with a suitable mineralogy.

^{3}He is especially attractive because it is easily measured due to its high production rates and low detection limits (Craig and Poreda, 1986; Kurz, 1986b; Schäfer et al., 1999). Unfortunately, the most commonly used target mineral quartz does not retain ^{3}He (Cerling, 1990; Trull et al., 1991). Recently, ^{3}He was investigated in garnet (Gayer et al., 2004), although the high U - Th concentrations in the mineral required a careful assessment of the nucleogenic ^{3}He, i.e. ^{3}He produced via the reaction of ^{6}Li(n,α)^{3}H$\rightarrow$^{3}He. ^{3}He- and ^{4}He-studies in magnetite revealed quantitative retention (Bähr et al., 1994; Bryce and Farley, 2002; Fanale and Kulp, 1962). On the other hand, studies by Bogard and Cressy (1973) and Bruno et al., (1997) indicate that plagioclase retains neither helium nor neon quantitatively.

In this study we explore the usefulness of the mineral sanidine and Fe-Ti-oxide mineral group for exposure dating with cosmogenic noble gases and ^{10}Be. Both minerals can coexist with quartz in silicic volcanic rocks. This allows a reliable cross-calibration, since the production systematics of ^{10}Be, ^{21}Ne and ^{26}Al in quartz are well known (Heisinger et al., 2002a; Heisinger et al., 2002b; Kubik and Ivy-Ochs, 2004; Niedermann, 2000; Niedermann et al., 1994; Nishiizumi et al., 1991; Stone, 2000; Stone et al., 1996). We chose seven samples from the ignimbrites of the Oxaya and Lauca Formations of Northern Chile. These rocks contain phenocrysts of quartz, sanidine and Fe-Ti-oxide minerals and are therefore ideally suited to study multiple nuclides in multiple target minerals. Detailed ^{10}Be and ^{21}Ne analyses in quartz samples in these rocks are reported in (Kober et al., 2003) and summarized in Table A, Background Data Set.

We will show below that ^{3}He in Fe-Ti-oxide minerals ($^{3}He_{Fe\text{-}Ti}$) and ^{10}Be and ^{21}Ne in sanidine ($^{10}Be_{san}$, $^{21}Ne_{san}$) are well suited for TCN studies. Conversely, $^{3}He_{san}$ and $^{21}Ne_{mt}$ are of little use due to poor retention of cosmogenic ^{3}He ($^{3}He_{c}$) in sanidine and low production rates of cosmogenic ^{21}Ne ($^{21}Ne_{c}$) in Fe-Ti-oxide minerals, respectively. The experimental production rates presented here are compared to results from new model calculations for cosmogenic nuclide production. The modelling is based on new cross sections for ^{3}He, ^{21}Ne, and ^{10}Be production from the relevant target elements.

5.3 Mineral aspects

5.3.1 Sanidine

Sanidine is a high-temperature/low-pressure alkali-feldspar found most commonly in rhyolites, dacites, trachytes and phonolites and less frequently in contact metamorphic rocks. Sanidine can occur both as phenocrysts and in the ground mass. Phenocrysts of sanidine coexist with quartz or can be the sole phenocrystic phase. If sanidine would be a mineral suitable for TCN work, isotope studies could be extended to volcanic regions where the rocks lack quartz or pyroxene and where timescales longer than that dictated by ^{36}Cl-saturation are of interest. Compared to plagioclase, alkali-feldspars are more resistant to chemical attack and generally last longer in the sedimentary and soil environment (Blum and Stillings, 1995; Nesbitt et al., 1997; White et al., 2001). As will be discussed below, the sanidine phenocrysts from the studied ignimbrites appear fresh and contain no incipient clay alteration.

Within the sanidine-lattice, Si and Al are disordered which requires charge balance that is most frequently accomplished with K- or Na-cations. Thus, in contrast to quartz, the major element composition of sanidines from different rocks can differ with respect to the main target elements for ^{10}Be and ^{21}Ne production. The concentrations of the target elements important for the production of cosmogenic neon and beryllium in sanidine are given in Table B, Background Data Set. Note that sample CN104 for beryllium analysis is not pure sanidine but likely contained about 20% of quartz. Furthermore, sanidine has been suggested to retain Ar isotopes due to a less complex lattice (Parsons et al., 1988) compared to plagioclase.

5.3.2 Fe-Ti-oxide minerals

Fe-Ti-oxide minerals like the endmembers magnetite and ulvospinel (with the solid solution line of titatnomagnetite) and hematite and ilmenite (titanohematites) are very common accessory minerals in igneous and metamorphic rocks (Frost, 1991; Frost and Lindsley, 1991). The usefulness of Fe-Ti-oxide minerals in TCN studies by studying ^{3}He was suggested by Bryce and Farley (2002) using magnetite and lately by Margerison et al. (2004) using ilmenite, whereas production of ^{21}Ne is expected to be too low (Masarik, 2002).

5.4 Sample site geology

The analysed samples stem from the Western Escarpment of the northern part of the Atacama Desert and the Western Cordillera in northern Chile. This area is characterized by a

hyperarid to arid climate. Active tectonics occurs due to the convergence of the Nazca Plate below the South American continent, leading to uplift of the Andes (Isacks, 1988). The hyperarid climate in the northern branch of the Atacama Desert results in very low erosion rates and hence in very old preserved landscapes (Kober et al., in review; Mortimer, 1980; Nishiizumi et al., 1998; Wörner et al., 2002) similar to ice-free regions in Antarctica (Schäfer et al., 1999). Erosion rates at the northern branch of the Atacama Desert derived from cosmogenic nuclide concentrations in quartz are <100cm/My (Kober et al., 2003). The Western Cordillera in turn receives more rainfall and erosion rates may exceed 1000cm/My (Kober et al., 2003). The samples studied are from resistant ignimbrite (welded tuff) units of the volcano-sedimentary Oxaya Formation (early Miocene, 19-25My) and from the less resistant Lauca Formation (Pliocene, ~2.7My) (García, 2002; Wörner et al., 2000). Nominal exposure ages to cosmic rays (uncorrected for erosion) are in the order of 1-3My in case of the Oxaya ignimbrite samples and 10-100ky for the Lauca ignimbrite samples.

The rocks we studied are made up of 40-50% phenocrysts of sanidine, quartz, plagioclase, biotite, Fe-Ti-oxide minerals and hornblende (in order of abundance) set in a matrix of partially devitrified volcanic glass. Some shards are still visible. Both quartz and sanidine are colourless, crystal clear and up to 3mm in diameter (mean size is about 1-2mm). Such large grain-sizes indicate that diffussional loss of $^{21}Ne_{cos}$ are negligible (Shuster and Farley, 2005; Trull et al., 1991). The quartz phenocrysts are euhedral but strongly resorbed, with embayed margins, and often contain glass inclusions (i.e., melt inclusions). Sanidine phenocrysts are euhedral and blocky with sharp grain boundaries. They lack any turbid areas which would indicate alteration to clays. Plagioclase phenocrysts are invariably zoned with turbid alteration areas concentrated within specific zones or in the cores. Margins are often irregular. Fe-Ti-oxide minerals occur either as octahedral phenocrysts or as aggregates in altered hornblende and biotite (see also below). The maximum size of Fe-Ti-oxide mineral grains is up to 1mm, while the mean grain size is ~ 0.3mm.

5.5 Sample preparation and measurement techniques

Rock samples (Oxaya ignimbrite: CN5, CN19, CN23, CN111, CN201; Lauca ignimbrite: CN112, CN113) were crushed and sieved to a grain size range of 355-1000µm. The crushed rock was then etched several times with weak HF using a shaker table (Ivy-Ochs, 1996; Kohl and Nishiizumi, 1992). This served to dissolve the volcanic groundmass, biotite, hornblende and plagioclase, while quartz, sanidine and Fe-Ti-oxide minerals were enriched.

Fe-Ti-oxide minerals were separated using magnetic susceptibility. Sanidine and quartz were separated and purified using heavy liquids (sanidine is found in the density fraction ≤ 2.62g*cm^{-3}). Fe-Ti-oxide minerals were analysed by thin section examination and primary oxide minerals were predominately magnetite and ilmenite. Primary biotite and hornblende were markedly altered to a mixture of fine-grained Fe-Ti-oxide minerals. Bulk samples of Fe-Ti-oxide minerals were powdered and mineralogically analysed using a Scintag XDS 2000 X-ray diffractometer. Peak comparison indicates a hematite-like composition with a constant offset likely due to Ti-contents. We have also identified single mineral grains of such composition in the magnetic fraction using electron microprobe analysis on carbon coated thin sections.

For the helium and neon measurements in sanidine, pure mineral separates were hand-picked from the enriched fraction which ensured that all grains with adhering phases (e.g., glass) were removed. The sanidine separates were crushed to ≤100µm and aliquots of 40-80mg were wrapped in commercial aluminium foil. The Fe-Ti-oxide mineral separates were degassed without further crushing. Noble gases were extracted in steps by incremental heating between 200-1750°C (details given in data tables) in a molybdenum crucible. Released gases were cleaned in a stainless steel extraction line equipped with Al/Zr-getters (SAES®) and activated charcoal held at the temperature of liquid nitrogen before He and Ne were expanded to a cryogenic pump. Helium and neon were separated by adsorbing neon at 14K on stainless steel frits and analyzing helium first. After the helium measurements, neon was released from the Cryotrap at 50K. Noble gas analyses were performed in a non-commercial, all-metal magnetic sector mass-spectrometer (90°, 210 mm radius) equipped with a modified Baur-Signer ion source whose sensitivity is essentially constant over the pressure range relevant for this work (Baur, 1999). The ion source is equipped with a compressor device that increases the sensitivity compared to a conventional source by factors of 120 and 200 for ^{3}He and ^{21}Ne, respectively (Baur, 1999). Corrections for isobaric interferences for mass 20 have been applied for $^{40}Ar^{++}$ and $H_2{}^{18}O$ but were always less than 2%. No correction for $CO_2{}^{++}$ on ^{22}Ne was necessary. The low corrections factors for doubly charged species were the results of a low electron acceleration voltage of 45V in the ion source. Data reduction followed e.g., (Oberholzer et al., 2003). Helium in the Fe-Ti-oxide minerals was analysed in a small gas fraction only because ^{4}He-concentrations are as high as 10e^{-4}cm^{3}STP*g^{-1}. In addition, some of the Fe-Ti-oxide minerals samples were measured by online crushing in order to constrain possible contributions from mantle derived ^{3}He. Nucleogenic ^{3}He (via the reaction

$^{6}Li(n,\alpha)^{3}H \rightarrow ^{3}He$) has been estimated using geological sample ages and measured Li, U and Th-concentrations.

For the ^{10}Be analyses, the quartz and the sanidine mineral separates were further etched using weak HF to ensure removal of meteoric ^{10}Be. Next, following procedures similar to those used to prepare quartz (Ivy-Ochs, 1996; Kohl and Nishiizumi, 1992), they were dissolved with concentrated HF after addition of ^{9}Be carrier. Be was separated and purified using anion and cation exchange and selective pH controlled precipitations (Child et al., 2000; Ivy-Ochs, 1996). $^{10}Be/^{9}Be$ ratios of the samples along with appropriate standards and blanks were measured by accelerator mass spectrometry at the ETH/PSI tandem facility in Zurich (Synal et al., 1997). Blanks were on the order of $(1\text{-}3)*10^{-14}$ for $^{10}Be/^{9}Be$ and amounted to a subtraction of less than 4% for the samples discussed here.

Chemical analysis of sanidine samples was performed by ICP-AES at Service d'Analyse des Roches et des Minéraux CRPG – CNRS, Vandoeuvre-lès-Nancy - France). Li and other trace elements in Fe-Ti-oxide minerals were measured by a PlasmaQuadrupole-ICP mass spectrometer at the ETH Isotope Lab facilities.

5.6 Isotope data and calculation of experimental production rates

5.6.1 Sanidine

Neon-concentrations of the sanidine samples are summarized in Table 1. Cosmogenic ^{21}Ne was calculated as excess over atmospheric composition ($^{21}Ne/^{20}Ne=0.00296$; $^{22}Ne/^{20}Ne=0.102$; Eberhardt et al., 1965) (Table 1). The neon data are shown in a three-isotope diagram in Fig. 1. Excess $^{21}Ne_c$ was completely released in the 400°C and 600°C temperature steps. The 800°C and total fusion steps showed no significant $^{21}Ne_{excess}$ (Fig. 1B, 2), indicating no significant contributions from nucleogenic or magmatic neon in the high temperature steps. This is in stark contrast to quartz analyses which have shown non-cosmogenic components released in the higher temperature steps (Niedermann, 2002). The 800°C steps always contributed less than 3% of the total $^{21}Ne_{excess}$ signature and are not considered here any further. The data of the low temperature steps in Fig. 1A fall on a well-defined straight line ($y=1.4999+0.098$; $R^2=0.9991$). This indicates that all the excess of ^{21}Ne in the 400 and 600°C steps is entirely cosmogenic. We therefore adopt the sum of the excess ^{21}Ne (over atmospheric composition) in the two low temperature steps as the total cosmogenic ^{21}Ne fraction in the sanidine samples. Note that the regression is almost identical to a mixing

Table 1. Neon concentrations and isotopic ratios in sanidine, production rate calculations and comparisons with modeled production rates.

sample	^{20}Ne	$^{21}Ne/^{20}Ne$	$^{22}Ne/^{20}Ne$	$^{21}Ne_{cosmo-san}$ (400+600°C)	$^{21}Ne_{qtz}$	factor	$P^{21}Ne_{san}$ experimental by	$P^{21}Ne_{san}$ modelled	$P^{21}Ne_{san}$ modelled
	$*10^{-10}$	$*10^{-3}$	$*10^{-1}$	$*10^{7}$	$*10^{7}$	san/qtz	$P^{21}Ne_{qtz}$=20.3	this study	(Masarik, 2002; [34])
(heating step[oC]/ heating time[min])	[ccSTP/g]			[atoms/g]	[atoms/g]		(Niedermann 2000; [23]) [atoms/g/yr]	[atoms/g/yr]	[atoms/g/yr]
CN5S-Ne(400,30')	1.91 ± 0.04	36.79 ± 0.41	1.56 ± 0.01	32.74 ± 0.63	20.01 ± 0.62	1.64 ± 0.06	33.21 ± 3.54	30.15	24.74
CN5S-Ne(600,30')	1.77 ± 0.04	35.26 ± 0.24	1.50 ± 0.01						
CN5S-Ne(800,20')	1.59 ± 0.04	4.93 ± 0.13	1.04 ± 0.01						
CN5S-Ne(1750,20')	4.79 ± 0.11	3.08 ± 0.07	1.03 ± 0.01						
CN19S-Ne(400,30')	1.65 ± 0.04	42.99 ± 0.35	1.65 ± 0.01	39.97 ± 0.67	32.03 ± 0.48	1.25 ± 0.03	25.33 ± 2.60	28.07	23.46
CN19S-Ne(600,30')	2.18 ± 0.04	40.90 ± 0.31	1.60 ± 0.01						
CN19S-Ne(800,20')	1.35 ± 0.03	5.02 ± 0.03	1.08 ± 0.01						
CN19S-Ne(1750,20')	0.73 ± 0.02	3.69 ± 0.03	1.02 ± 0.01						
CN23S-Ne(600,30')	3.93 ± 0.07	38.80 ± 0.25	1.56 ± 0.01	37.80 ± 0.77	22.64 ± 0.42	1.67 ± 0.05	33.89 ± 3.51	29.75	24.38
CN23S-Ne(800,30')	0.81 ± 0.02	5.38 ± 0.06	1.05 ± 0.01						
CN23S-Ne(1750,20')	1.18 ± 0.02	3.32 ± 0.07	1.03 ± 0.01						
CN113S-Ne(200,30')	0.46 ± 0.02	3.10 ± 0.13	1.02 ± 0.02	0.66 ± 0.06	0.48 ± 0.06	1.39 ± 0.23	28.14 ± 5.42	26.44	22.7
CN113S-Ne(400,30')	1.34 ± 0.02	3.77 ± 0.07	1.03 ± 0.01						
CN113S-Ne(600,30')	0.62 ± 0.01	5.04 ± 0.20	1.06 ± 0.01						
CN113S-Ne(800,20')	0.46 ± 0.01	3.08 ± 0.13	1.02 ± 0.02						
CN113S-Ne(1750,15')	0.58 ± 0.01	3.18 ± 0.10	1.02 ± 0.01						
CN201S-Ne(400,30')	1.29 ± 0.02	46.86 ± 0.34	1.67 ± 0.01	43.58 ± 0.74	28.36 ± 0.81	1.54 ± 0.05	31.19 ± 3.29	27.03	22.56
CN201S-Ne(600,30')	0.94 ± 0.02	114.69 ± 0.36	2.69 ± 0.01						
CN201S-Ne(800,20')	0.52 ± 0.01	4.21 ± 0.09	1.04 ± 0.01						
CN201S-Ne(1750,20')	0.47 ± 0.01	3.31 ± 0.03	1.03 ± 0.01						
						Mean production rate	30.35 ± 3.67	28.29	23.56

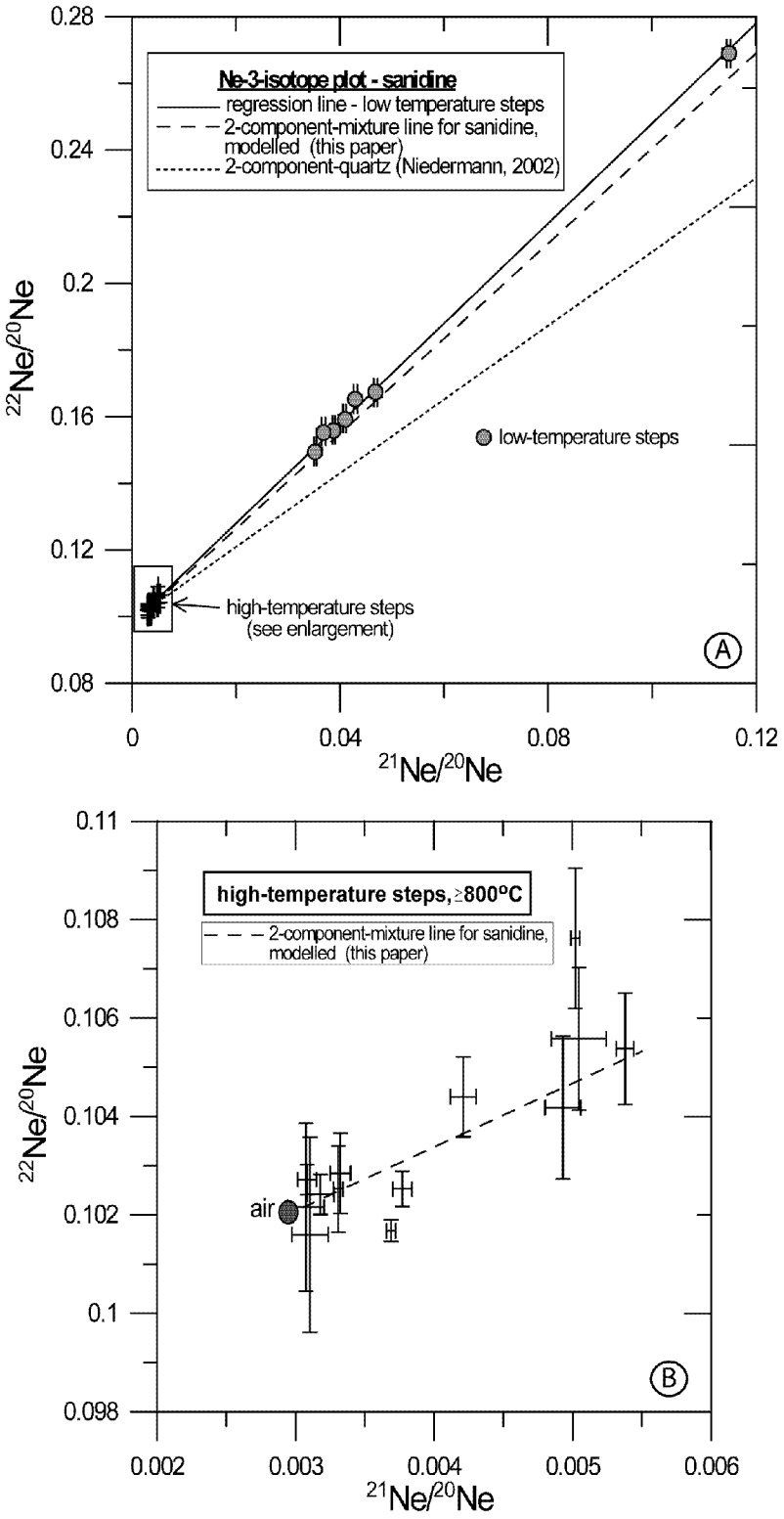

Figure 1: Neon-three-isotope diagram for sanidine samples. A) All data points of all samples fall on a straight line (solid line) which represents a mixture of atmospheric and cosmogenic composition. Only the low temperature steps (≤600°C) plot significantly away from atmospheric composition, indicating substantial release of cosmogenic neon. Modeling of a mean sanidine mixing line (dashed line) with new elemental production rates agrees almost perfectly with the regression line through the data points (see text). For reference, the dotted line is a mixing line for quartz [Niedermann 2000, 2002]. B) Enlargement of the area showing the data of high

temperature steps (800° and 1750°C). These steps contain mostly atmospheric Ne and neither major nucleogenic nor trapped contributions.

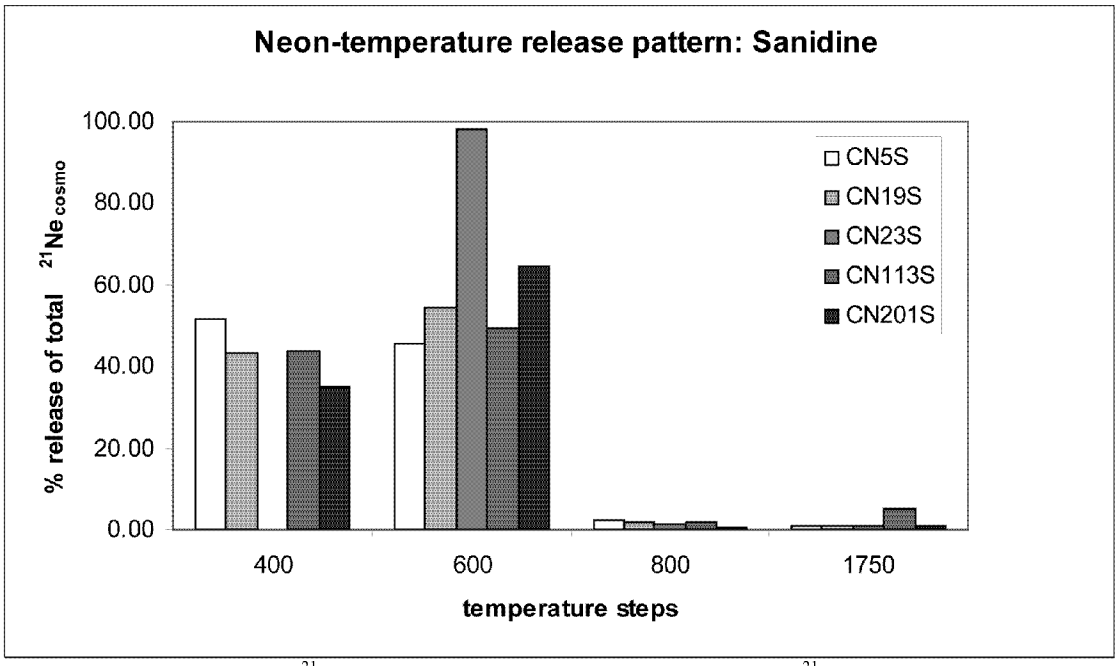

Figure 2: Percent of released $^{21}Ne_{cosmo}$ at each temperature step relative to total $^{21}Ne_{cosmo}$. For sample CN23S no 400°C step has been made. 200°C-step of sample CN113 released 2% and is not shown in graph.

line between atmospheric and cosmogenic neon derived from model calculations, as discussed in more detail below.

The experimentally determined ^{21}Ne production rates for sanidine ($^{21}Ne_{san}$) are presented in Table 1. These values were calculated using the nuclide concentration of ^{21}Ne in quartz ($^{21}Ne_{qtz}$) from the same samples determined earlier (Table A, Background Data Set). In order to derive a production rate of $^{21}Ne_{san}$ ($P^{21}Ne_{san}$) for each sample the ratio of ^{21}Ne concentrations ($^{21}Ne_{san}/^{21}Ne_{qtz}$) was multiplied with the $P^{21}Ne_{qtz}$=20.3±4.0 atoms*g^{-1}*yr^{-1} (Niedermann, 2000; Niedermann et al., 1994) at sea level/high latitude. The $P^{21}Ne_{qtz}$ follows a scaling according to Lal (Lal, 1991) (see Tab. 1 of Niedermann (2000)) . This procedure implicitly assumes that the production rate ratios of ^{21}Ne from various elements are independent of altitude and latitude and that ^{21}Ne has been quantitatively retained in both quartz and sanidine. The model calculations below will verify these assumptions for the latitude range of interest here. The mean empirical production rate for ^{21}Ne in sanidine is 30.4±3.7 atoms*g^{-1}*yr^{-1}. The stated error represents the standard-deviation of the values of the five individual samples and partly the inhomogeneous target element composition (as discussed further down). Including the $P^{21}Ne_{qtz}$ uncertainty (Niedermann, 2000), the empirical ^{21}Ne production rate for sanidine is 30.4±5.6 atoms*g$^{-1}{}_{mt}$*y^{-1}. The production rate in sanidine

is therefore about 50% higher than that in quartz (20.3±4.0 atoms*g^{-1}*yr^{-1} (Niedermann, 2000; Niedermann et al., 1994)).

Concentrations of ^{3}He in sanidine (Table C, Background Data Set) were all close to the blank values with $^{3}He/^{21}Ne_{cosmo}$ ratios below any reasonable production rate ratio. This indicates that sanidine, like quartz, is not quantitatively retentive for cosmogenic ^{3}He (Brook and Kurz, 1993; Niedermann, 2002; Trull et al., 1991).

Concentrations of ^{10}Be for two sanidine samples are presented in Table 2. Again, we use the ratio of ^{10}Be concentrations in sanidine to quartz and the ^{10}Be production rate of 5.44±0.19 atoms*g_{qtz}^{-1}*y^{-1} (Kubik and Ivy-Ochs, 2004) to calculate preliminary ^{10}Be production rates for sanidine. The mean of this value is 4.45±0.38 atoms*g^{-1}*yr^{-1} (4.45±0.42 atoms*g^{-1}*yr^{-1} including the $P^{10}Be_{qtz}$ uncertainty). Here, the stated uncertainty represents the error of the mean value. The ^{10}Be production rate in sanidine is thus about 80 % as efficient as in quartz.

Table A. Neon concentrations and ratios of quartz samples

sample-quartz[1,2] (temperature, heating time) [°C, min]	^{20}Ne *10^{-11} [ccSTP/g]	$^{21}Ne/^{20}Ne$ *10^{-3}	$^{22}Ne/^{20}Ne$ *10^{-1}	$^{21}Ne_{cosmo}$ *10^{6} [atoms/g]
CN5(550,20)	17.34 ± 0.49	45.92 ± 0.34	1.55 ± 0.01	200.12 ± 6.21
CN5(800,15)	6.87 ± 0.20	3.62 ± 0.05	1.05 ± 0.01	
CN19(550,20')	15.03 ± 0.21	79.92 ± 0.42	1.99 ± 0.02	320.32 ± 4.85
CN19(800,15')	8.00 ± 0.13	7.40 ± 0.17	1.10 ± 0.02	
CN19(1750,15')	5.91 ± 0.21	3.36 ± 0.09	1.05 ± 0.02	
CN23(550,20')	25.48 ± 0.37	36.03 ± 0.30	1.45 ± 0.01	226.43 ± 4.16
CN23(1500,15')	13.70 ± 0.32	6.62 ± 0.05	1.07 ± 0.02	
CN111F(550,30')	6.98 ± 0.23	74.54 ± 1.14	1.87 ± 0.03	134.18 ± 5.12
CN111F(800,30')	14.04 ± 0.21	3.08 ± 0.03	1.01 ± 0.01	
CN111F(1750,15')	6.20 ± 0.15	2.91 ± 0.11	1.04 ± 0.01	
CN112(550,30')	11.51 ± 0.23	11.39 ± 0.18	1.12 ± 0.01	26.08 ± 0.91
CN112(800,30')	7.33 ± 0.18	3.10 ± 0.05	1.03 ± 0.01	
CN113A(550,30')	13.02 ± 0.25	4.19 ± 0.12	1.01 ± 0.01	4.76 ± 0.64
CN113A(800,30')	7.74 ± 0.18	3.17 ± 0.13	1.01 ± 0.01	
CN113A(1750,15')	4.73 ± 0.15	2.95 ± 0.10	1.00 ± 0.02	
CN201(600,30')	5.97 ± 0.16	179.91 ± 1.21	3.11 ± 0.02	283.65 ± 8.07
CN201(800,30')	17.40 ± 0.47	3.58 ± 0.06	1.00 ± 0.01	
CN201(1750,15')	4.46 ± 0.12	3.20 ± 0.09	0.99 ± 0.01	

[1] for CN19 and CN113A: 550°C and 800°C $^{21}Ne_{excess}$ over air used for total cosmogenic ^{21}Ne

[2] fusion step of CN5, CN23 and CN112 not analyzed

Table 2. Beryllium-concentrations in quartz and sanidine, production rate calculations and comparisons with modeled production rates.

Sample	Quartz ^{10}Be 10^7atoms/g	Sanidine ^{10}Be 10^7atoms/g	factor $^{10}Be_{qtz}/^{10}Be_{san}$	$P^{10}Be$ using $P^{10}Be_{qtz}$=5.44 (Kubik & Ivy-Ochs, 2004; [28]) atoms/g/yr	$P^{10}Be_{san}$ modeling this study atoms/g/yr	$P^{10}Be_{san}$ modeling (Masarik 2002; [37]) atoms/g/yr
CN19	3.46 ± 0.09	2.68 ± 0.15	0.77 ± 0.05	4.21 ± 0.50	4.50	4.87
CN104	2.22 ± 0.07	1.91 ± 0.13	0.86 ± 0.06	4.69 ± 0.58	4.60	5.08
			mean	4.45 ± 0.38	4.55	4.98

The fact that the ^{10}Be concentrations measured in both sanidines are on the order of 80% of the ^{10}Be concentrations measured in coexisting quartz, gives confidence that the sanidines had been completely cleaned of meteoric ^{10}Be. This is in contrast to several other minerals besides quartz which have been shown to be difficult to be cleaned of meteoric contaminants (Ivy-Ochs et al., 1998; Klein et al., 1986; Kohl and Nishiizumi, 1992; Seidl et al., 1997; Zreda, 1994). In case of the studied ignimbrite samples, the lack of meteoric ^{10}Be may be due to the absence of secondary weathering minerals (clay, plagioclase) in sanidine which can take up meteoric ^{10}Be during formation (Ivy-Ochs et al., 1998).

Table C. Sanidine helium concentrations and ratios, including ratios with neon.

sample-Helium (heating step[°C]/ heating time[min])	^{3}He $*10^{-14}$ ccSTP/g	^{4}He $*10^{-10}$ ccSTP/g	^{3}He/^{4}He $*10^{-6}$	^{3}He -total $*10^8$ atoms/g	^{4}He - total $*10^{11}$ atoms/g	neon-helium ratios total $^{21}Ne_{cosmo}$ $*10^7$ atoms/g	^{3}He/^{21}Ne
CN5S-He(400,30')	12.29 ± 1.88	27.2 ± 4.5	45.2 ± 10.1	14.59 ± 1.01	2.48 ± 1.28	32.74 ± 0.63	0.045
CN5S-He(600,30')	38.94 ± 2.67	50.0 ± 4.6	77.8 ± 8.9				
CN5S-He(800,20')	3.06 ± 1.24	15.3 ± 17.2	20.0 ± 23.9				
CN5S-He(1750,20')	-0.05 ± 1.40	-55.3 ± 43.8					
CN19S-He(400,30')	1.82 ± 0.91	16.6 ± 3.0	11.0 ± 5.8	6.70 ± 0.65	19.52 ± 0.88	39.97 ± 0.67	0.017
CN19S-He(600,30')	8.05 ± 1.30	61.2 ± 3.1	13.2 ± 2.2				
CN19S-He(800,20')	14.08 ± 1.56	413 ± 14	3.41 ± 0.39				
CN19S-He(1750,20')	0.99 ± 0.97	236 ± 29	0.42 ± 0.42				
CN23S-He(600,30')	1.86 ± 0.77	145 ± 3	1.28 ± 0.53	2.18 ± 0.38	24.71 ± 0.73	37.80 ± 0.77	0.006
CN23S-He(800,30')	4.47 ± 0.88	642 ± 14	0.70 ± 0.14				
CN23S-He(1750,20')	1.79 ± 0.80	133 ± 23	1.34 ± 0.64				
CN113S-He(200,30')	2.05 ± 0.60	81.2 ± 1.0	2.52 ± 0.74	3.79 ± 0.49	3.37 ± 0.03	0.66 ± 0.06	0.575
CN113S-He(400,30')	0.18 ± 0.81	36.0 ± 0.5	0.51 ± 2.25				
CN113S-He(600,30')	9.83 ± 0.95	0.49 ± 0.24	2004 ± 1012				
CN113S-He(800,20')	1.91 ± 0.83	5.30 ± 0.28	36.0 ± 15.8				
CN113S-He(1750,15')	0.15 ± 0.87	2.44 ± 0.26	6.12 ± 35.49				
CN201S-He(400,30')	0.96 ± 0.60	3.90 ± 2.26	24.6 ± 21.0	1.28 ± 0.39	16.38 ± 0.69	43.58 ± 0.74	0.003
CN201S-He(600,30')	1.97 ± 0.83	91.3 ± 2.8	2.16 ± 0.91				
CN201S-He(800,20')	1.18 ± 0.70	406 ± 11	0.29 ± 0.17				
CN201S-He(1750,20')	0.67 ± 0.73	108 ± 23	0.62 ± 0.69				

5.6.2 Fe-Ti-oxide minerals

Fe-Ti-oxide minerals were degassed by step-wise heating up to a final temperature of 1750°C (Tables 3, D, Background Data Set). Both, ^{3}He and ^{4}He, were released simultaneously and over a rather broad temperature interval, usually between 800 and 1400°C, with only a small percentage of the gas being released at either lower or higher temperatures. The final temperature steps (1750°C) contained little gas, suggesting complete degassing at ≤1400°C (Fig. A, Background Data Set). ^{3}He in all steps of all samples is assumed to be entirely of cosmogenic origin and is used for production rate calculations. As we will show below non-cosmogenic contributions can be neglected.

Similar to sanidine, ^{3}He production rates for Fe-Ti-oxide minerals were calculated by using the ^{21}Ne concentrations of quartz from the same sample (Table A, Background Data Set) and the procedure delineated above. Resulting ^{3}He production rates are presented in Table 3. The mean of 120±11 atoms*g^{-1}_{mt}*y^{-1} (120±12 atoms*g^{-1}_{mt}*y^{-1} including the $P^{21}Ne_{qtz}$ uncertainty, (Niedermann, 2000)) is considerably higher than a previous value obtained from

Table 3. Helium and neon concentrations and ratios in Fe-Ti-oxide samples. Helium-3-Fe-Ti production rate calculation and comparison with modelled and experimentally established production rates.

sample (heating step [°C]/ heating time [min])	^{3}He *10^{-12} [ccSTP/g]	^{4}He *10^{-6} [ccSTP/g]	$^{3}He/^{4}He$ *10^{-6}	R/Ra	total ^{3}He *10^{9} [atoms/g]	total $^{21}Ne_{cosmo-qtz}$ *10^{7} [atoms/g]	$^{3}He_{Fe-Ti}/^{21}Ne_{qtz}$	$P^{3}He_{Fe-Ti}$ using $P^{21}Ne_{qtz}$=20.3 (Niedermann 2000, [23]) [atoms/g/yr]
CN5Mt(800,30')	11.64 ± 0.72	3.52 ± 0.04	3.31 ± 0.21	2.38	1.137 ± 0.053	20.01 ± 0.62	5.68 ± 0.32	115.31 ± 13.21
CN5Mt(1400,30')	30.68 ± 1.83	4.57 ± 0.05	6.71 ± 0.41	4.83				
CN5Mt(1750,20')	-0.01 ± 0.04	-0.02 ± 0.02						
CN19Mt(600,30')	10.69 ± 0.27	36.11 ± 0.64	0.30 ± 0.01	0.21	1.727 ± 0.054	32.03 ± 0.48	5.39 ± 0.19	109.42 ± 11.58
CN19Mt(1000,30')	20.71 ± 0.53	168.16 ± 3.00	0.12 ± 0.01	0.09				
CN19Mt(1400,30')	32.09 ± 1.91	37.18 ± 0.44	0.86 ± 0.05	0.62				
CN19Mt(1750,20')	0.78 ± 0.09	0.54 ± 0.02	1.44 ± 0.17	1.04				
CN23Mt(600,30')	7.34 ± 0.44	13.17 ± 0.09	0.56 ± 0.03	0.40	1.349 ± 0.045	22.64 ± 0.42	5.96 ± 0.23	120.94 ± 12.94
CN23Mt(800,30')	3.45 ± 0.23	31.28 ± 0.22	0.11 ± 0.01	0.08				
CN23Mt(1000,30')	14.24 ± 0.85	29.87 ± 0.21	0.48 ± 0.03	0.34				
CN23Mt(1200,30')	22.83 ± 1.34	22.61 ± 0.16	1.01 ± 0.06	0.73				
CN23Mt(1400,30')	1.89 ± 0.13	0.84 ± 0.01	2.23 ± 0.15	1.61				
CN23Mt(1750,20')	0.47 ± 0.05	0.18 ± 0.01	2.58 ± 0.27	1.86				
CN111Mt(200,30')	0.04 ± 0.01	0.00 ± 0.01	18.22 ± 2.65	13.11	0.915 ± 0.006	13.42 ± 0.51	6.82 ± 0.26	138.46 ± 14.85
CN111Mt(400,30')	0.03 ± 0.01	0.08 ± 0.01	0.46 ± 0.08	0.33				
CN111Mt(600,30')	1.19 ± 0.03	3.06 ± 0.03	0.39 ± 0.01	0.28				
CN111Mt(800,20')	1.54 ± 0.03	3.72 ± 0.03	0.41 ± 0.01	0.30				
CN111Mt(1000,20')	1.94 ± 0.03	2.97 ± 0.02	0.65 ± 0.01	0.47				
CN111Mt(1200,30')	17.33 ± 0.17	10.55 ± 0.09	1.64 ± 0.02	1.18				
CN111Mt(1400,20')	11.08 ± 0.12	3.28 ± 0.03	3.38 ± 0.05	2.43				
CN111Mt(1600,15')	0.90 ± 0.02	0.19 ± 0.01	4.79 ± 0.13	3.45				
CN112Mt(1000,20')	2.69 ± 0.07	15.25 ± 0.18	0.18 ± 0.01	0.13	0.149 ± 0.002	2.61 ± 0.09	5.71 ± 0.22	115.93 ± 12.42
CN112Mt(1400,20')	2.79 ± 0.06	7.12 ± 0.08	0.39 ± 0.01	0.28				
CN112Mt(1600,15')	0.06 ± 0.01	0.11 ± 0.00	0.55 ± 0.11	0.40				
							mean	120.01 ± 11.09
							$P^{3}He_{Fe-Ti}$, mean modelled, this study	124
							$P^{3}He_{mt}$, experimental (Bryce & Farley 2002; [18])	69-77
							$P^{3}He_{mt}$, modelled (Masarik 2002; [37])	63.5

Table D. Neon and helium concentrations and ratios in Fe-Ti-oxide samples

sample (temperature, heating time) [°C, min]	^{20}Ne $*10^{-10}$ [ccSTP/g]	$^{21}Ne/^{20}Ne$ $*10^{-3}$	$^{21}Ne/^{20}Ne$ $*10^{-1}$	$^{21}Ne_{excess}$ $*10^{5}$ [atoms/g]	^{3}He $*10^{6}$ [atoms/g]	^{4}He $*10^{12}$ [atoms/g]	R/Ra	$^{21}Ne_{nucleo}/^{4}He_{radio}$ $*10^{-7}$	$^{3}He/^{21}Ne_{cosmo}$
CN5Mt(800,30')	4.51 ± 0.08	3.19 ± 0.10	1.03 ± 0.01	28.3 ± 15.8	313 ± 19	94 ± 1	2.434	0.30	110.41
CN5Mt(1400,30')	19.86 ± 0.28	3.35 ± 0.06	1.04 ± 0.01	210 ± 49	824 ± 49	123 ± 1	4.932	1.71	39.29
CN5Mt(1750,20')	1.53 ± 0.04	2.93 ± 0.16	0.98 ± 0.03	-1.14 ± 7.82	-0.15 ± 1.10	-0.47 ± 0.42			
CN19Mt(600,30')	3.17 ± 0.05	3.43 ± 0.06	1.03 ± 0.01	40.1 ± 8.3	287 ± 7	970 ± 17	0.218	0.04	71.59
CN19Mt(1000,30')	6.64 ± 0.12	6.25 ± 0.07	1.04 ± 0.01	587 ± 24	556 ± 14	4518 ± 81	0.091	0.13	9.47
CN19Mt(1400,30')	43.32 ± 0.63	5.24 ± 0.06	1.02 ± 0.01	2651 ± 120	862 ± 51	999 ± 12	0.635	2.65	3.25
CN19Mt(1750,20')	2.76 ± 0.04	3.48 ± 0.14	1.02 ± 0.02	38.9 ± 11.7	20.9 ± 2.4	14.5 ± 0.5	1.060	2.68	5.38
CN23Mt(600,30')	1.87 ± 0.04	3.37 ± 0.04	1.05 ± 0.01	20.7 ± 4.9	197 ± 12	354 ± 2	0.410	0.06	95.24
CN23Mt(800,30')	0.97 ± 0.02	4.95 ± 0.16	1.02 ± 0.01	52.1 ± 5.2	93 ± 6	841 ± 6	0.081	0.06	17.79
CN23Mt(1000,30')	1.93 ± 0.02	6.58 ± 0.15	1.03 ± 0.01	188 ± 9	383 ± 23	803 ± 6	0.350	0.23	20.35
CN23Mt(1200,30')	6.39 ± 0.09	6.91 ± 0.04	1.00 ± 0.01	678 ± 19	613 ± 36	607 ± 4	0.742	1.12	9.05
CN23Mt(1400,30')	5.70 ± 0.07	5.56 ± 0.09	1.01 ± 0.01	398 ± 18	51 ± 3	22.7 ± 0.3	1.643	17.57	1.27
CN23Mt(1750,20')	1.25 ± 0.02	3.29 ± 0.15	1.02 ± 0.02	11.3 ± 5.4	12.7 ± 1.2	4.9 ± 0.2	1.898	2.29	11.28
CN111Mt(200,30')	0.37 ± 0.01	3.50 ± 0.06	0.98 ± 0.01	5.30 ± 0.95	1.19 ± 0.17	0.065 ± 0.001	13.400	80.96	2.25
CN111Mt(400,30')	0.35 ± 0.01	2.98 ± 0.07	1.02 ± 0.01	0.21 ± 0.97	0.94 ± 0.17	2.06 ± 0.02	0.336	0.10	45.18
CN111Mt(600,30')	0.50 ± 0.01	3.55 ± 0.09	1.03 ± 0.01	7.88 ± 1.76	32.0 ± 0.7	82.1 ± 0.7	0.286	0.10	40.58
CN111Mt(800,30')	1.00 ± 0.02	3.79 ± 0.02	1.02 ± 0.01	22.4 ± 2.0	41.5 ± 0.9	100.0 ± 0.8	0.305	0.22	18.53
CN111Mt(1000,20')	1.28 ± 0.02	4.01 ± 0.05	1.00 ± 0.01	36.0 ± 2.8	52.0 ± 0.8	79.7 ± 0.7	0.480	0.45	14.45
CN111Mt(1200,30')	5.70 ± 0.08	3.93 ± 0.03	1.02 ± 0.01	149 ± 12	466 ± 5	283 ± 2	1.208	0.53	31.23
CN111Mt(1400,20')	6.30 ± 0.09	3.82 ± 0.05	1.02 ± 0.01	145 ± 14	298 ± 3	88 ± 1	2.486	1.65	20.53
CN111Mt(1750,20')	0.97 ± 0.01	3.27 ± 0.07	1.00 ± 0.01	8.18 ± 2.36	24.3 ± 0.6	5.06 ± 0.04	3.524	1.62	29.65
CN112Mt(1000,20')	4.36 ± 0.07	3.62 ± 0.03	1.00 ± 0.01	77.0 ± 9.5	72.3 ± 1.8	410 ± 5	0.130	0.19	9.39
CN112Mt(1400,20')	16.16 ± 0.26	3.25 ± 0.02	0.99 ± 0.01	126 ± 32	75.1 ± 1.6	191 ± 2	0.288	0.66	5.95
CN112Mt(1750,20')	1.28 ± 0.02	3.18 ± 0.07	1.02 ± 0.01	7.58 ± 3.45	1.57 ± 0.31	2.85 ± 0.03	0.405	2.66	2.07

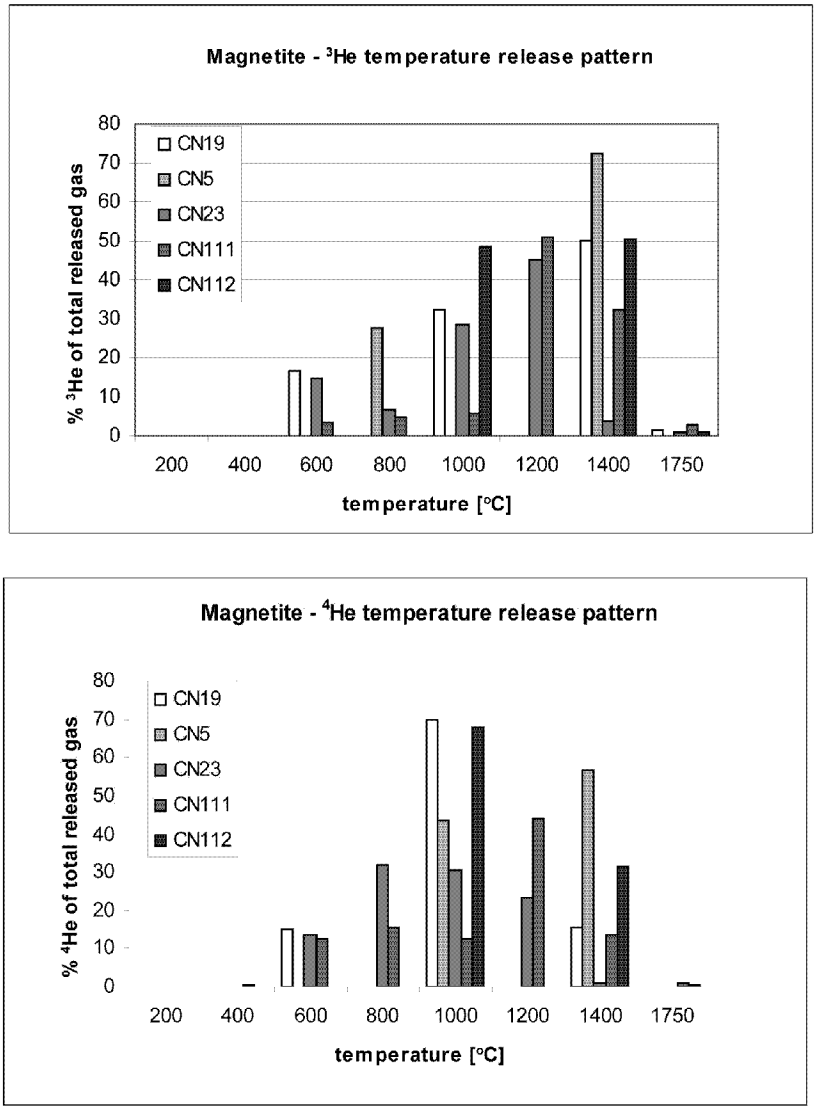

Figure A: Percent of released ^{3}He and ^{4}He from Fe-Ti-oxide samples at each temperature step relative to the total gas amount released. See Table 3 for temperature steps, not all steps were performed for each sample.

numerical simulations of 63 atoms*g^{-1}_{mt}*y^{-1} by Masarik (2002) or the preliminary experimentally determined value of 69-77 atoms*g^{-1}_{mt}*y^{-1} of Bryce and Farley (2002).

The Ne-three-isotope diagram (Figure B, Background Data Set) shows that very few data points lie on a mixing line between atmospheric and cosmogenic neon. Therefore no unambiguous contribution of cosmogenic ^{21}Ne can be detected. Excesses over atmospheric composition are likely due to nucleogenic and/or magmatic contributions. We therefore conclude that ^{21}Ne in Fe-Ti-oxide minerals is not useful for exposure dating. We will show below that this is to be expected based on the low ^{21}Ne production rate from Fe.

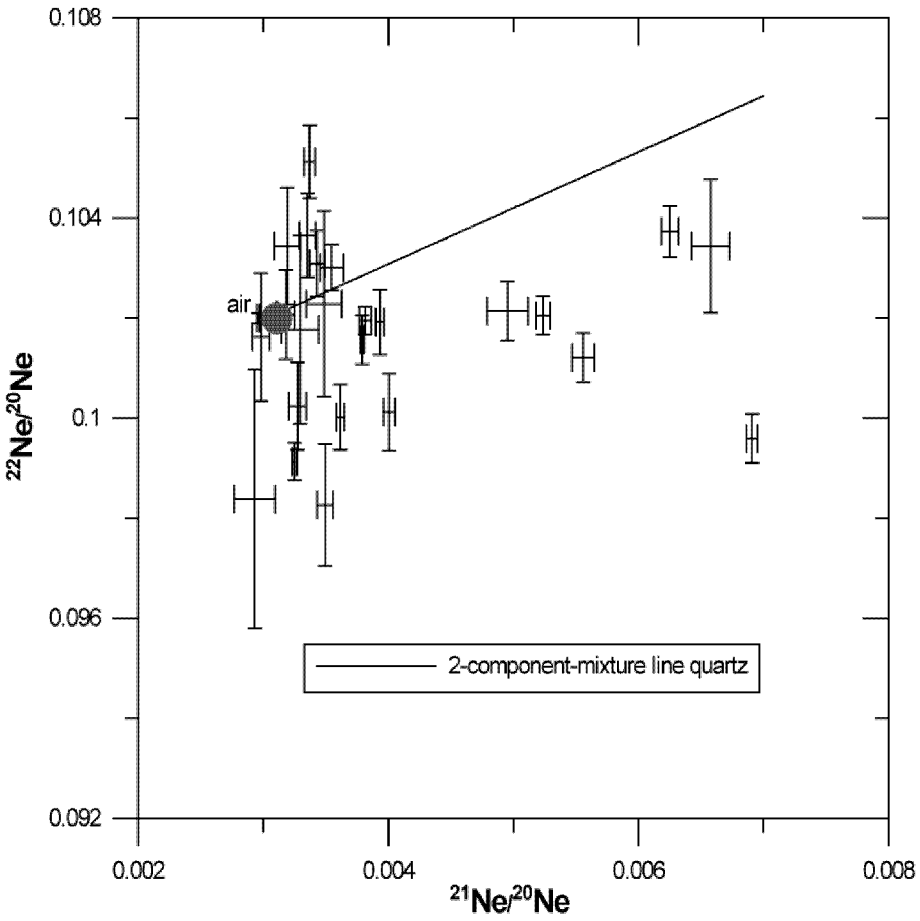

Figure B: Neon-three-isotope diagram for Fe-Ti-oxide samples showing no significant contribution of a cosmogenic component, but rather variable admixtures of trapped and nucleogenic components. A two-component mixing line between atmospheric and cosmogenic neon in quartz is drawn for comparison. A similar line for neon in Fe-Ti-oxides is not well constrained with the presently available data base.

Note that the production rates for Fe-Ti-oxide minerals and sanidine reported here are valid essentially for present-day magnetic field intensities although the exposure ages of the samples are in the order of 10ky to 3My (see above). This is because we have normalized to the production rate for quartz deduced by Niedermann (2000) and Niedermann et al., (1994) based on samples with exposure ages of 13ky only that required no correction for changes in the magnetic field intensity at earlier times. According to Masarik et al. (2001) these corrections would amount to 9% for the low latitudes samples studied here (20°S) and for samples with exposure >50ky. The correction for samples <50ky as established by Dunai, (2001) for low latitude samples is 15%. This means that the reader should perform corrections for paleofield intensity variations if necessary when adopting the production rates for sanidine and Fe-Ti-oxide minerals recommended here.

5.7 Modeling of cosmogenic nuclide production rates on Earth

Here we present new modelled cosmogenic production rates for most of the major target elements relevant for TCN-studies. These modeled values (Tables 4, 5 – uncertainties estimated in Tables 2 and 3) are based on the particle fluxes in the Earth's atmosphere (Masarik and Beer, 1999) and the cross sections for the relevant nuclide reactions. The cross sections were obtained from various irradiation experiments (Leya et al., 2000). The primary model output are elemental production rate ratios relative to Si ([X]/[Si], where [X] denotes O, Mg, Al, Fe and Ni for helium, [X]=Na, Mg, Al, Ca, Fe and Ni for neon, and [X]=O, N, Mg, Al, Ca, Fe, Ni for beryllium. These ratios are essentially constant at all latitudes and altitudes up to 6000m, hence in the following we adopt the values modeled for sea level and high latitude. Note that the [X]/[Si] ratios may change considerably at altitudes above 6000m, but this is hardly relevant in practice. Absolute neon production rates for the specific elements were then obtained by normalizing the model-derived X/[Si]-ratios with the absolute production rate derived by Niedermann (2000) and Niedermann et al. (1994) with quartz samples from the Sierra Nevada ($P^{21}Ne_{Si}$=43.5±8.7 atoms*g^{-1}*y^{-1} at sea level, high latitude). The estimated uncertainties of the specific elemental production rates are 20%. The elemental $P^{21}Ne$ values for Mg and Al in Table 5A are slightly different from those given by Schäfer et al. (1999) due to recently updated cross sections (see above).

Table 4. Elemental production rate calculations for ^3He for this work (bold) and comparison to previously modelled ^3He production rates

Element	O	Mg	Al	Si	Fe	Ni	Ca
$^3He_{element}/^3He_{Si}$	1.482	1.414	1.244	1.000	0.739	0.707	-
modelled ratio $(^3He/^{21}Ne)_{Si}$				2.962			
$P^{21}Ne_{Si}$ [atoms/g/yr] (Niedermann 2000; [23])				43.5			
P^3He_{Si} [atoms/g/yr]				129			
$P^3He_{element}$ [atoms/g/yr]	**191**	**182**	**160**	**129**	**95**	**91**	**-**
$P^3He_{element}$ [atoms/g/yr] (Masarik 2002; [37])	129	111	102	106	39	-	58

Concerning helium, most of the radioactive ^3H ($t_{1/2}$~12.3y) in the artificially irradiated targets studied for cross section measurements (e.g., Leya et al., 2004) had not yet decayed to ^3He by the time the irradiated samples were analysed. Accurate modelling of ^3He production rates therefore requires knowledge of the production rate ratio $P(^3He_{direct})/P(^3H)$. We use here the element specific values determined by (Leya et al., 2004) and earlier by Hintenberger et al. (1967) and Hintenberger and Wänke (1964): 1.73 [O], 3.0 [Fe], 2.22 [Mg], 2.28 [Al], 2.16 [Si], and 3.0 [Ni]. Data for Ti are assumed to be of the Fe value. These values are considerably different from the ratio of 1 assumed by e.g., Masarik (2002), which may

Table 5.

A) Model calculations of ^{21}Ne elemental production rates and comparison to previously established elemental production rates

Element	Na	Mg	Al	Si	Ca	Fe	Ni
$^{21}Ne_{element}/^{21}Ne_{Si}$	4.780	4.340	1.371	1.000	0.381	0.019	0.019
$^{21}Ne_{Si}$ [atoms/g/yr] (Niedermann 2000;[23])				43.5			
$P^{21}Ne_{element}$ [atoms/g/yr]	**208**	**189**	**60**	**44**	**17**	**1**	**1**
Masarik 2002; [37]	102	175	62	42	2	0	-
Schäfer et al. 1999; [68]	-	196	54	45	-	-	-

B) Model calculations of ^{10}Be elemental production rates and comparison to previously established elemental production rates

Element	O	N	Mg	Al	Si	Ca	Fe	Ni
$^{10}Be_{element}/^{10}Be_{Si}$	1.992	7.458	0.588	0.492	1.000	0.340	0.567	0.442
modelled ratio $(^{10}Be/^{21}Ne)_{Si}$					0.075			
$P^{21}Ne_{Si}$ [atoms/g/yr] (Niedermann 2000; [23])					43.5			
absolute $P^{10}Be$ for Si [atoms/g/yr]					3.28			
$P^{10}Be_{element}$ [atoms/g/yr]	**6.54**	**24.49**	**1.93**	**1.61**	**3.28**	**1.12**	**1.86**	**1.45**
Masarik 2002; [37]	9.82	-	1.74	1.03	0.89	-	0.35	-

explain discrepancies between our elemental production rates and values given by (Masarik, 2002) discussed below. In order to establish absolute ^{3}He production rates, first the modelled $^{3}He/^{21}Ne$ elemental production ratio (Table 4) was calculated. By using again the accepted absolute production rate of $P^{21}Ne_{Si}$=43.5±8.7 atoms*g^{-1}*y^{-1} (Niedermann, 2000; Niedermann et al., 1994) the absolute ^{3}He production rate from Si was obtained and the production rates for the other elements of interest were determined via the earlier X/[Si]-ratios.

The mean modelled total ^{21}Ne production rate for sanidine is 28.3 atoms*g^{-1}*y^{-1} (Table 1). This value refers to the mean major element composition of the sanidine samples analyzed here (Table B, Background Data Set). Similarly, the mean modelled total ^{3}He production rate in Fe-Ti-oxide minerals is 124 atoms*g^{-1}*y^{-1} (Table 3) using the end-members ulvospinel (Fe_2TiO_4; 124 atoms*g^{-1}*y^{-1}), ilmenite ($FeTiO_3$; 127 atoms*g^{-1}*y^{-1}), magnetite (Fe_3O_4; 122 atoms*g^{-1}*y^{-1}) and hematite (Fe_2O_3; 124 atoms*g^{-1}*y^{-1}). Hereby it is assumed that the ^{3}He production from titanium and iron does not vary significantly ($P^{3}He_{Ti}$=1.05*$P^{3}He_{Fe}$, determined by interpolation between the elemental production from Fe and Si). Therefore, the ^{3}He production rate of Fe-Ti-oxide minerals is essentially independent of the chemical composition.

The mean modelled production rate for ^{10}Be in sanidine is 4.55 atoms*g^{-1}*y^{-1} (Table 2), including the production by stopped and fast muons following the procedures by Heisinger et al. (2002a); Heisinger et al. (2002b) and Kubik & Ivy-Ochs (2004). The considerable differences in the elemental production rate ratios between our new results and the data published by Masarik are most likely due to the different cross sections used for modeling.

For example, the usual assumption of equal cross sections for proton- and neutron-induced production of

Table B. Chemical composition of sanidine aliquots by ICP-AES

sample	SiO_2 (wt%)	Al_2O_3 (wt%)	Na_2O (wt%)	MgO (wt%)
		^{21}Ne		
CN5S	61.04	23.57	6.66	0.02
CN19S	64.49	20.23	5.55	<0.01
CN23S	63.51	21.3	6.55	0.01
CN113S	67.65	18.11	4.65	<0.01
CN201S	65.21	19.28	4.59	0.01
mean	**64.38**	**20.5**	**5.6**	**0.01**
		^{10}Be		
CN19S	64.49	20.23	5.55	<0.01
CN104S	76.84	12.52	2.97	0.01

Data measured at CRPG-CNRS (www.crpg.cnrs-nancy.fr)

^{10}Be from oxygen is generally not valid (Michel et al., 1998) and can result in production rates too low by up to a factor of 2. While our calculations are based on neutron-induced cross sections adjusted to experimental data from physical model calculations (Leya et al., 2000), the approach by Masarik is mostly based on the assumption of equal cross sections.

5.8 Comparison of experimental and modelled production rates

5.8.1 Sanidine-Neon

The sanidine samples studied here all yield experimentally derived ^{21}Ne production rates between 25-34 atoms*g^{-1}*y^{-1} (Table 1), with a mean of 30.4±3.7 atoms*g^{-1}*y^{-1}. It is suggested that sanidine retains cosmogenic neon quantitatively. This suggestion is corroborated by the fact that for each sample the model-derived production rate based on the actual chemical composition (ranging from 26-30 atoms*g^{-1}*y^{-1}, with a mean of 28.29 atoms*g^{-1}*y^{-1}, Table B, Background Data Set) agrees within uncertainties with the empirically determined value. Hence, the variations of the empirically derived values are to a large extent explainable by variable chemical compositions. The mean production rate for sanidine derived here is considerably higher than the P^{21}Ne value of 20.3±4.0 atoms*g^{-1}*y^{-1} for quartz (Niedermann, 2000; Niedermann et al., 1994). This is to be expected, because Na and Al are major elements in sanidine. ^{21}Ne production rates from these elements are ~1.5 and 5 times higher, respectively, than for Si (Table 5A).

Elemental production rates for ^{21}Ne reported by (Masarik, 2002) would underestimate the total production rate for sanidine by ~20%. Higher elemental production rates for Mg and Al were proposed by Schäfer et al. (1999), while a new Na value is provided in this study.

Based on our model we can also calculate the isotopic composition of cosmogenic neon in sanidine (elemental production rates of $^{20,22}Ne$ in sanidine are not shown in Tables 1, 5A; see Leya et al. (2004). The mixing line between atmospheric and cosmogenic composition in Fig. 1 has been determined using the average chemical composition of the sanidine samples (Table B, Background Data Set) and experimentally determined production rates given in Table 5 by Leya et al. (2004). The modelled line agrees very well with the regression line defined by the data points. This supports the conclusion that apart from atmospheric neon, the bulk of the cosmogenic neon is released in the 400-600°C steps. Note that the regression line defined by the data points and the modelled line for sanidine is steeper in Fig. 1 compared to the mixing line for quartz (Niedermann, 2000; Niedermann et al., 1994). This is due to elevated $^{22}Ne/^{21}Ne$ ratios from both Na and Al compared to Si (Leya et al., 2004).

5.8.2 Sanidine-Beryllium

The measured and modelled ^{10}Be production rates reported here agree very well with each other (4.45±0.38 atoms*g^{-1}*y^{-1} versus 4.55 atoms*g^{-1}*y^{-1}, Tables 2, 5B). Our modelled value is some 11% lower than if calculated by using elemental production rates given by Masarik (2002)(Table 5B). Using our elemental production rates given in Table 5B for the calculation of the production rate of ^{10}Be in quartz yields 5.02 atoms*g^{-1}*y^{-1}(5.65 atoms*g^{-1}*y^{-1} when following the procedure of Masarik (2002). This is a ~10% lower production rate of ^{10}Be-production in sanidine compared to quartz.

5.8.3 Fe-Ti-oxide minerals - Helium

Measured ^{3}He production rates for the Fe-Ti-oxide samples are given in Table 3. Values range between 109-138 atoms*g^{-1}_{mt}*y^{-1}, with a mean of 120±11 atoms*g^{-1}_{mt}*y^{-1}. As it was the case for neon in sanidine, this mean value is very similar to the modelled $P(^{3}He_{Fe\text{-}Ti})$=124 atoms*g^{-1}_{mt}*y^{-1} (see section 'Modeling of terrestrial cosmogenic production rates on Earth'). This excellent agreement strongly suggests that our basic assumption is correct that the measured ^{3}He in all samples is essentially cosmogenic. Nevertheless, before we further discuss this value we will first evaluate the possibility that sizeable fractions of ^{3}He are of

non-cosmogenic origin. The main reasons for this exercise are that one of our samples (CN111) has a ~15% higher measured production rate than both the modelled and the mean measured values and that our recommended value is considerably higher than the recently proposed $P(^3He_{Fe\text{-}Ti})$ values of 69-77 atoms*g^{-1}_{mt}*y^{-1} (Bryce and Farley, 2002).

Li-concentrations in the Fe-Ti-oxide minerals are in the sub-ppm range (Table E). Assuming for the ignimbrites mean U-Th values similar to average granitic crust (Mamani et al., 2004) and using a ^{3}He production rate of $6*10^{-10}$ atoms*g_{mt}^{-1}*s^{-1} for 1ppm of Li (Andrews, 1985; Lal, 1987), we conclude that the nucleogenic ^{3}He concentrations are lower than $2*10^5$ atoms*g^{-1}_{mt} in the Lauca sample (CN112) and lower than $8.2*10^4$-$6*10^5$ atoms*g^{-1}_{mt} for all Oxaya-ignimbrite samples. Sample CN111 in particular does not contain more than $8.2*10^4$ atoms*g_{mt}^{-1} of nucleogenic ^{3}He. Nucleogenic ^{3}He does amount to less than 1% of the total measured ^{3}He in any sample and can therefore be ignored.

Table E. Concentrations of relevant elements besides Fe and O in Fe-Ti-oxide samples (in ppm) measured by PlasmaQuadrupole-ICP.

sample	Li	Ni	Mg	Al	Ca	Na	Ti
CN 5	0.48±0.02	84.2±0.8	3570±68	5975±69	1697±33	142±25	10800±307
CN 19	1.64±0.11	50.3±2.9	6578±295	4292±247	143±22	314±50	21830±355
CN 23	0.41±0.10	27.8±0.8	5260±107	5149±115	260±17	650±31	20770±1046
CN 111	0.23±0.02	69.4±0.1	5747±52	5921±53	434±2	566±32	12060±399
CN 112	4.08±0.26	80.4±1.5	6728±87	3765±49	320±33	410±31	16490±118

^{3}He of magmatic origin cannot a priori be excluded. We therefore thoroughly crushed three of our samples in an online crushing device (Schäfer et al., 2000). After 30 to 45 strokes the average grain size had been reduced to a few tenths of microns. Nevertheless, only ~1% (Table F) of the total ^{3}He found in the aliquots analysed by stepwise-heating had been released by crushing, with the ^{3}He/^{4}He-ratios being similar in crushing and heating experiments. This indicates that Fe-Ti-oxide minerals contain at best negligible amounts of magmatic helium. The experiments show further that by very thorough crushing small fractions of cosmogenic helium might be released. Possibly, friction-induced heating locally resulted in temperatures above the threshold for the release of cosmogenic helium.

Traces of other major elements and Ti contents determined in the Fe-Ti-oxide samples used here are shown in Table E and production rates for these elements are presented in Table 4. The contribution (mostly from Mg and Al) to the total Fe-Ti-oxide minerals production rate is 1 to 3%, which we therefore neglect.

We conclude that neither magmatic nor nucleogenic helium significantly contribute to the total measured helium concentrations in our ignimbrite Fe-Ti-oxide minerals. Therefore cosmogenic ^{3}He in Fe-Ti-oxide minerals is ideally suited for TCN-studies, as long as magmatic or nucleogenic ^{3}He can be excluded or at least accurately corrected for.

Table F. Concentrations and ratios of helium released in crushing steps of selected Fe-Ti-oxide samples
A crushing step consited of a 30sec crushing period followed by a 30sec break

Sample	^{3}He $*10^{-14}$	^{4}He $*10^{-8}$	^{3}He/^{4}He $*10^{-6}$	R/R_a
step crushand break (cycles)	[ccSTP/g]	[ccSTP/g]		
CN19mt-crush1(10,10)	35.7 ± 7.1	173 ± 2	0.21 ± 0.04	0.15
CN19mt-crush2(10,10)	44.8 ± 8.1	109 ± 1	0.41 ± 0.07	0.30
CN19mt-crush3(10,10)	27.8 ± 6.0	87 ± 1	0.32 ± 0.07	0.23
CN23mt-crush1(15,15)	18.9 ± 4.9	59 ± 0	0.32 ± 0.08	0.23
CN23mt-crush2(15,15)	5.07 ± 5.13	78 ± 1	0.06 ± 0.07	0.05
CN111mt-crush1(15,15)	5.81 ± 0.93	4.86 ± 0.03	1.20 ± 0.19	0.86
CN111mt-crush12(15,15)	7.94 ± 1.00	2.66 ± 0.02	2.99 ± 0.38	2.15
CN111mt-crush13(15,15)	9.37 ± 0.79	1.06 ± 0.01	8.80 ± 0.75	6.33

Both measured and modelled ^{3}He production rates in Fe-Ti-oxide minerals presented in this work are considerably higher than recently measured values (Bryce and Farley, 2002; Margerison et al., 2004). Our $P^{3}He_{Fe\text{-}Ti}$ values are also almost twice as high as those calculated with elemental production rates recommended by Masarik (2002). We believe, that our values are to be preferred over previously suggested ones, because of updated cross sections, and in particular, due to the newly evaluated branching ratios $P(^{3}He_{direct})/P(^{3}H)$. All our experimental values are close to each other and the mean measured value is in excellent agreement with the modelled ratio. However, at present we have no clear explanation for the difference between our values and the preliminary measured production rate suggested by Bryce and Farley, (2002) and the ones recently suggested by Margerison et al. (2004). We note that the value by Bryce and Farley (2002) is based on a cross calibration of their magnetite data with $P^{3}He$ data from Antarctic pyroxenes by Schäfer et al. (1999). It has recently been suggested, however, that not all pyroxene varieties retain cosmogenic ^{3}He quantitatively, since $^{3}He_{cos}/^{21}Ne_{cos}$ ratios vary considerably more than can be explained by variable chemical composition of the targets (Oberholzer, 2004). We also note that the poorly constrained ^{3}He production rate from Ti and other elements in trace concentration cannot be the reason for the difference between our production rates and the ones by Bryce and Farley (2002). Even assigning a conservative uncertainty of 20% on the modelled production rates would only lead to an approximation of the two production rates. Clearly, more work is necessary on this topic.

Using the new elemental production rates derived here (Table 3), a production rate of ^{3}He in quartz of 162 atoms*g$^{-1}_{qtz}$*y^{-1} is calculated (compared to 118 atoms*g$^{-1}_{qtz}$*y^{-1} using elemental production rates proposed by Masarik, (2002). This value is of importance for experiments with artificial quartz targets exposed in vacuum containers, e.g. for scaling experiments of terrestrial cosmogenic nuclides with latitude and altitude.

The elemental production rates in Table 4 are also of interest for minerals such as olivine and pyroxene. Table 4 suggests that specific mineral production rates are considerably more variable than previously assumed (e.g., Laughlin et al. (1994)). For various end-members of the pyroxene group, our model and that by Masarik (2002) yield ^{3}He production rates between 135-171 atoms*g^{-1}*y^{-1} and 91-118 atoms*g^{-1}*y^{-1}, respectively. For the olivine end-members fayalite and forsterite the range of modelled values is even wider. Our model predicts P^{3}He between 130 and 175 atoms*g^{-1}*y^{-1}, compared to Masarik's values of 76 and 118 atoms*g^{-1}*y^{-1}.

Even taking into account the quite considerable uncertainties of the model predictions (20% for the model used here), the two models are thus not consistent with each other. Unfortunately, experimentally determined P^{3}He values for pyroxenes and olivines do not allow to prefer one model prediction over the other, since the experimental values of (99-148 atoms*g^{-1}*y^{-1}, (Liccardi et al., 1999; Niedermann, 2002) and references therein) are bracketed by the model predictions. Reasons for the difficulty to assess the model quality are that the chemical composition of the analysed pyroxenes and olivines has rarely been reported in detail, other samples may have been biased by pressure anomalies at the sites (e.g., Ackert et al., 2003).

The olivine (and the few available pyroxene) data do thus not allow to prefer one model prediction over the other. Future cosmogenic nuclide studies on olivines and pyroxenes should report the chemical composition in detail to allow evaluation of this problem.

5.9 Conclusions

We have shown with ignimbrite samples from northern Chile that cosmogenic ^{3}He in Fe-Ti-oxide minerals and ^{21}Ne in sanidine are well retained. We also show the first ^{10}Be data on two sanidine samples, which indicate that meteoric ^{10}Be can quantitatively be removed by a procedure similar to that used for quartz. Therefore, sanidine is also well suited to be analysed for cosmogenic ^{10}Be. With this study, Fe-Ti-oxide minerals and sanidine can thus be added to the list of minerals suitable for terrestrial cosmogenic nuclide studies. We found a

striking agreement between experimentally determined nuclide production rates and values derived from numerical modelling. This confirms that both, experimentally derived production rates and the model calculations are reliable. The helium model calculations here are based on new values for the branching ratios of $P(^3He_{direct})/(P(^3H)$ which for most elements differ considerably from the value of 1 often used in previous studies. The new branching ratios and the improved cross sections thus yield considerably different production rates of cosmogenic ^3He. The calculations also illustrate the importance of knowledge of the major element concentrations for target minerals with more variable composition than quartz. The reason for the discrepancy between our experimental and modelled P^3He compared to previous estimates has not yet been satisfactorily resolved.

In our ignimbrite samples, three mineral phases (quartz, sanidine, Fe-Ti-oxide minerals) and five different nuclides (^3He, ^{10}Be, ^{14}C, ^{21}Ne, ^{26}Al) have been analysed in several rock samples. All these nuclides have different production rates and the radionuclides have different half-lifes, therefore they respond differently to production, accumulation and/or decay of nuclides. Together the different nuclides can deliver basic information on exposure times and erosion rates over a broad range of time scales.

Acknowledgements

This study was funded by Swiss National Science Foundation grant 620-576.663 to F. Schlunegger whose support we acknowledge. J. Masarik and S. Niedermann are thanked for discussion of an earlier draft of this manuscript. G. Wörner is acknowledged for providing U/Th data. P. Meister and E. Reusser supported the X-ray and Electron Microsope analysis. This paper benefited from thorough reviews by D. Shuster and an anonymous reviewer. The Zurich AMS facility is jointly operated by the Swiss Federal Institute of Technology, Zurich and the Paul Scherrer Institute, Villigen, Switzerland.

6 Possible interferences in terrestrial cosmogenic nuclide studies due to trace impurities in quartz grains and in quartz mineral separates

In collaboration with:
S. Ivy-Ochs[1], K. Kunze[2], Th. Pettke[3], R. Wieler[3], M. Döbeli[4], H. Baur[3], T. Magna[3], R.B. Georg[3], P.W. Kubik[4]

[1]*Particle Physics ETH Zürich / Institute of Geography University of Zürich*
[2]*Geological Institute ETH Zürich*
[3]*Institute of Isotope Geology and Mineral Resources, ETH Zürich*
[4]*PSI/Particle Physics ETH Zürich*

6.1 Introduction

In the course of the investigations of quartz from Chilean ignimbrites (see Chapters 3 and 5) we made several observations which led us to further investigate the nature of this quartz.

On the one hand, problems were encountered during the ^{10}Be purification. The quantities of the cations Ca, Al and Fe were rather too high. We attributed this to one or several of the following:

a) impure quartz separates, where a small percentage of impurities would yield significant amounts of these cations
b) possible mineral inclusions in the quartz (e.g., rutile)
c) cations from melt/fluid inclusions as revealed by optical investigations
d) cations in the quartz lattice (structurally bound). Cathodoluminescence (CL) showed an internal zoning with bright luminous rims (Fig. 1).

We noted that, transparent alkali-feldspar grains (sanidine) did not dissolve markedly faster than quartz. After a series of selective chemical dissolution steps (Ivy-Ochs, 1996; Kohl and Nishiizumi, 1992) a mineral separate enriched in both quartz and sanidine was produced. In general, selective chemical dissolution only works because quartz dissolves much slower than most other silicates. Enrichment of cations due to impure quartz or quartz mineral separates may result in a composition of quartz which is different from pure SiO_2. In such a case elevated (trace-)concentrations of e.g., F, Al, Na, Mg, Ca or Fe can be expected. Some of these elements (Na, Mg, Al) in turn have higher elemental production rates for terrestrial

cosmogenic nuclides (i.e., for ^{21}Ne: one to five times compared to Si, (Masarik, 2002) and Chapter 5). Hence, their presence would lead to a production rate different than that based on the production of Si and O alone (Kubik and Ivy-Ochs, 2004; Niedermann, 2000; Niedermann et al., 1994). In addition, the presence of Al, Ca, Fe and Ti can significantly complicate the extraction and purification procedures for Be and Al. Indeed, too high concentrations of ^{27}Al can lead to ^{26}Al/^{27}Al ratios below the AMS detection limit.

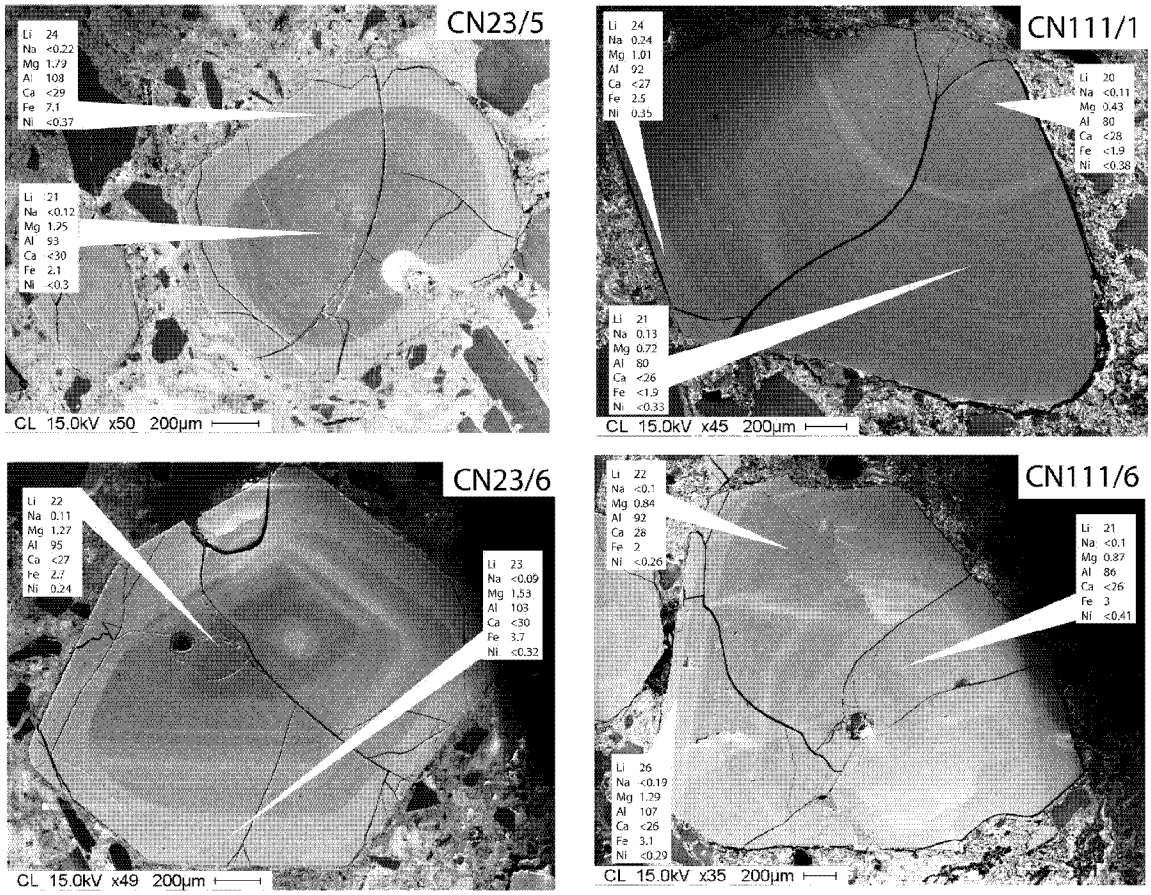

Figure 1 CL-imaging of quartz grains showing broken, abrasive rounded and/or fragmented grains and prominent zoning in quartz grains of either a diffuse or sharp style. However not all quartz grains showed a distinct zoning. Discontinuities in zoning are variable (<20-200µm). Inclusions are melt-inclusions and are of matrix-type composition (CN111/6), or appear opaque (CN23/6). Growth impediments (CN23/5) or embayments are little developed. Grain-matrix boundaries are commonly sharp. Growth nucleation spots are preserved in grain CN23/5,6. Fine oscillatory zoning (~20µm) is obvious in CN23/6 or CN111/1 (see e.g., Müller, 2000) for a complete interpretation of zoning in quartz). Zoning is continuous, periodic and parallel to outer crystal margins and sharp (CN111/1) but also more diffuse, irregular and flame-like (CN111/6). A bright luminescent outer zone (>100µm) is often observable (CN23/5,6 and CN111/6). Resorption structures, cutting pre-existing zoning, are revealed in CN23/6. Inset-boxes represent LA-ICP-MS-element analysis in core, intermediate and rim positions relevant to CL-zoning (data in ppm).

On the other hand, neon-analysis of the Chilean quartz separates indicated slightly elevated ^{22}Ne/^{20}Ne-ratios (Chapter 3), relative to an atmospheric-cosmogenic mixing line

given by (Niedermann, 2002). This can be due to elevated nucleogenic neon produced by elevated F,U/Th-concentrations in the matrix of the quartz hosting rocks or inclusions within the quartz grains (Schäfer et al., 2002).

In order to quantify the effect of impurities in quartz on the production of cosmogenic nuclides (^{10}Be, ^{21}Ne, ^{26}Al), the samples were investigated by the following methods: (1) bulk chemistry analysis was performed after selective chemical dissolution and after selective chemical dissolution in addition with physical separation methods (magnetic separation and heavy liquid methods), (2) zoned quartz grains were investigated by CL/LA-ICP-MS (for all analytical details see the appendix at the end of the chapter) to quantify the amount of trace concentrations of some major elements, and (3) rock-samples were investigated by nuclear reaction-analysis for fluorine content and distribution. Finally, the effect of impurities on sample preparation and production rates was estimated.

6.2 Bulk chemistry and production rate estimations

The chemical data of quartz-aliquots after a selective chemical dissolution procedure and after adding a physical separation step to the selective chemical dissolution procedure are presented in Table 1. Data shown for preparation solely by the selective chemical dissolution procedure indicates that sample CN19Q-1 and CN23Q-1 are not yet cleaned perfectly and contain impurities, mainly of Al, Na and subordinate by Ca and K. In such a case, the calculation of cosmogenic production rates for ^{21}Ne would result in higher production rates that differ by 5 and 18% (Table 1A), respectively, from an assumed 20.3 atoms/g/yr of a stoichiometric quartz-SiO_2 composition (Niedermann, 2000; Niedermann et al., 1994). Here the uncertainties of the production rate itself are neglected. After addition of physical separation steps, the bulk chemical composition of the quartz indicates pure monomineralic quartz aliquots, with impurities at the 100ppm-level (Table 1B). Only a few values are higher than this value. Consequently, calculated production rates of the samples analysed for cosmogenic nuclides are indistinguishable from an assumed 20.3 atoms/g/yr of a pure SiO_2 composition (without uncertainties). Sample CN111Q-2 differs by ~3% largely due to the uncertainty in bulk silicon analysis.

Data for ^{10}Be-production rate estimations are presented in Table 1A and are only available for measurements after the step of selective chemical dissolution, but not after the physical separation steps. From the earlier it is obvious that any production rate due to the variable SiO_2-composition lowers the total ^{10}Be-production rate, due to a lower Si- and O-concentration. Furthermore, the presence of e.g, Fe, Ca and Mg will interfere with the column

separation (see e.g., Ochs and Ivy-Ochs, 1997). As suggested for ^{21}Ne, after the addition of physical separation steps, pure quartz-separates might be achieved and the aliquots are ready for AMS-target preparation and measurements of ^{10}Be- and ^{26}Al, respectively.

In conclusion, the commonly applied physical and chemical cleaning procedures can in most cases sufficiently clean quartz separates. However, if purified quartz aliquots cannot be achieved, even by repeated physical and chemical separation procedures, the samples have to be discarded. Concentrations of impurities observed in our final quartz bulk chemistry analysis are of the order of the measurement uncertainties.

The amount of impurities that can be related to the internal zoning of quartz, revealed by CL and likely corresponding to structurally bound trace impurities (e.g., Flem et al., 2002), was quantified by LA-ICP-MS. Chemical zoning and inclusions in quartz would largely affect the ^{26}Al-sample preparation.

Table 1A. Bulk chemistry analysis and production rate estimations of quartz separates produced by selective chemical dissolution; measurements at CRPG-CNRS

Sample	SiO_2 %	Al_2O_3 %	Na_2O %	MgO %	CaO %	K_2O %	Fe_2O_3 tot %	TiO_2 %
CN19Q-1	90.96	3.83	1.12	0.01	0.26	0.96	0.07	0.01
CN23Q-1	86.73	8.08	2.47	0.01	1.5	0.65	0.01	0.02
CN104Q-1	98.74	0.2	0.04	0.01	<0.01	0.07	0.01	0.01
CN111Q-1	97.27	0.79	0.2	0.01	0.08	0.16	0.01	0.01

Table 1A continued

	^{21}Ne elemental production				^{10}Be elemental production					
Sample	Si at/g	Al + Na at/g	total at/g	% to normal*	Si at/g	O at/g	Al + Na at/g	O at/g	total at/g	% to normal**
CN19Q-1	18.5	2.95	21.45	5.67	1.396	3.168	0.046	0.14	4.75	-12.74
CN23Q-1	17.64	6.37	24.01	18.28	1.331	3.02	0.099	0.29	4.74	-12.87
CN104Q-1	20.08	0.14	20.22	-0.39	1.515	3.439	0.002	0.01	4.96	-8.77
CN111Q-1	19.73	0.57	20.3	0.00	1.493	3.387	0.009	0.03	4.92	-9.61

*normal: 20.3atoms/g/yr (Niedermann 2000)
**normal: 5.44atoms/g/yr (Kubik & Ivy-Ochs, 2004)

Table 1B. Bulk chemistry analysis and production rate estimations after selective chemical dissolution and physical separation steps; ICP-measurements at ETH; isotope-analysis of Mg-24, Ca-44 and Fe-57 suggest no major contribution of this elements to any ^{21}Ne production rate by even low elemental production rates

Sample	SiO_2 wt%	Al $*10^{-4}$ wt%	Na $*10^{-4}$ wt%	Mg-24 ppm	Ca-44 ppm	K ppm	Fe-57 ppm	TiO_2 ppm	Li ppm	Ni ppm
CN19Q-2	98	137	72.8	1.80	13.4	-	14.8	-	20.8	0.10
CN23Q-2	102	121	65.2	6.00	17.3	-	177	-	21.2	0.093
CN111Q-2	99	1836	594	7.9	157.6	-	113.2	-	20.8	0.098

Table 1B, continued

	^{21}Ne elemental production			
Sample	Si* at/g	Al + Na at/g	total at/g	% to normal**
CN19Q-2	19.93	0.08	20.01	-1.43
CN23Q-2	20.3	0.07	20.37	0.34
CN111Q-2	20.13	0.74	20.87	2.81

*uncertainties on quartz are 2%
**normal: 20.3atoms/g/yr (Niedermann 2000)

6.3 Results from LA-ICP-MS

Selected quartz grains (Fig. 1) were investigated by LA-ICP-MS (Table 2). Core, intermediate and rim positions (the latter often as a bright luminous band) of grains revealed minor variations in concentrations of the major elements. Concentrations are around 100ppm for Al as the most abundant impurity. All other elements are in the ≤30ppm range. Commonly Li, Mg, Al and Fe are slightly enriched in bright luminous rims relative to centre positions, while Na, Ca and Ni with very low concentrations have similar concentrations in various parts of the grains. A correlation of bright luminosity can be explained by a variable incorporation of trace elements during cooling (e.g., Landtwing and Pettke, 2005; Müller et al., 2003; Peppard et al., 2001; Perny et al., 1992; Watt et al., 1997). Structurally bound impurities have similar or even smaller concentrations as the range of uncertainties of the bulk chemistry analysis. Overall, such trace impurity concentrations are negligible with respect to TCN-studies (see discussion above).

Kohl and Nishiizumi (1992) suggested that the outer rims of grains are partially erased by a few microns during the chemical quartz isolation process. However, such dissolutions did unlikely erase zones in the range of 100µm - that are enriched by Al - in our quartz grains as observed by CL. However, 100ppm Al will not bias the preparation for AMS (Bierman et al., 2002; Kohl and Nishiizumi, 1992), but indicate that even sufficient etching of quartz grains will not lower possible enriched Al-zones of quartz grains if these are of structurally bound origin. These can be an order of magnitude higher than observed in the Chilean ignimbrite samples (e.g., Bierman et al., 2002; Götze and Lewis, 1994).

Table 2. LA-ICP-MS results (in ppm) from selected quartz grains (see Fig. 1)

Sample, grain, position	Li	Na	Mg	Al	Ca	Fe	Ni
CN23, qtz 5, core1	20.4	<0.08	0.98	87.7	<30	<2.1	<0.298
CN23, qtz 5, core2	21.8	0.12	1.25	92.6	<30	<2.1	<0.278
CN23, qtz 5, rim1	24.2	<0.09	1.51	100.8	<29	4.8	<0.369
CN23, qtz 5, rim2	24.2	0.22	1.79	108.3	<25	7.1	<0.250
CN23, qtz 6, core	22.4	0.11	1.27	94.8	<27	2.7	<0.322
CN23, qtz 6, intermediate	22.5	<0.09	1.22	96.8	<31	3.5	<0.390
CN23, qtz 6, rim	22.9	<0.09	1.53	103.3	<30	3.7	<0.243
CN111 qtz 1, core	19.7	<0.11	0.76	79.9	<28	<1.9	<0.385
CN111 qtz 1, intermediate	21.3	0.13	0.72	80.3	<26	<1.9	<0.328
CN111 qtz 1, rim1	22.8	0.23	0.74	83.2	<26	2.5	<0.277
CN111 qtz 1, rim2	24.0	0.24	1.01	91.9	<27	<1.9	<0.350
CN111 qtz 6, core	21.0	<0.09	0.75	85.6	<26	3.0	<0.411
CN111 qtz 6, intermediate	22.2	<0.10	0.84	92.4	28	2.0	<0.264
CN111 qtz 6, rim	25.7	<0.09	1.28	106.6	<26	3.1	<0.292

6.4 The effect of elevated F and U/Th-concentrations on neon isotopes

Using nuclear reactions analysis (NRA), it turned out that hot-spots of high fluorine-concentrations are micas (Fig. 2). Average F-concentrations are around 1wt% and maximum values reach 1.53wt% (Fig. 2, Table 3). Quartz grains themselves do not have any significant fluorine concentration. Micro-inclusions or micro-accessory minerals (<10µm) are not detected by the nuclear-reaction method. Biotite crystals that are adjacent to quartz grains (and which might have interfered with quartz grains onto the ^{22}Ne-signal likely due to their excitation stage, Flem et al., 2002) were not frequently observed in thin sections.

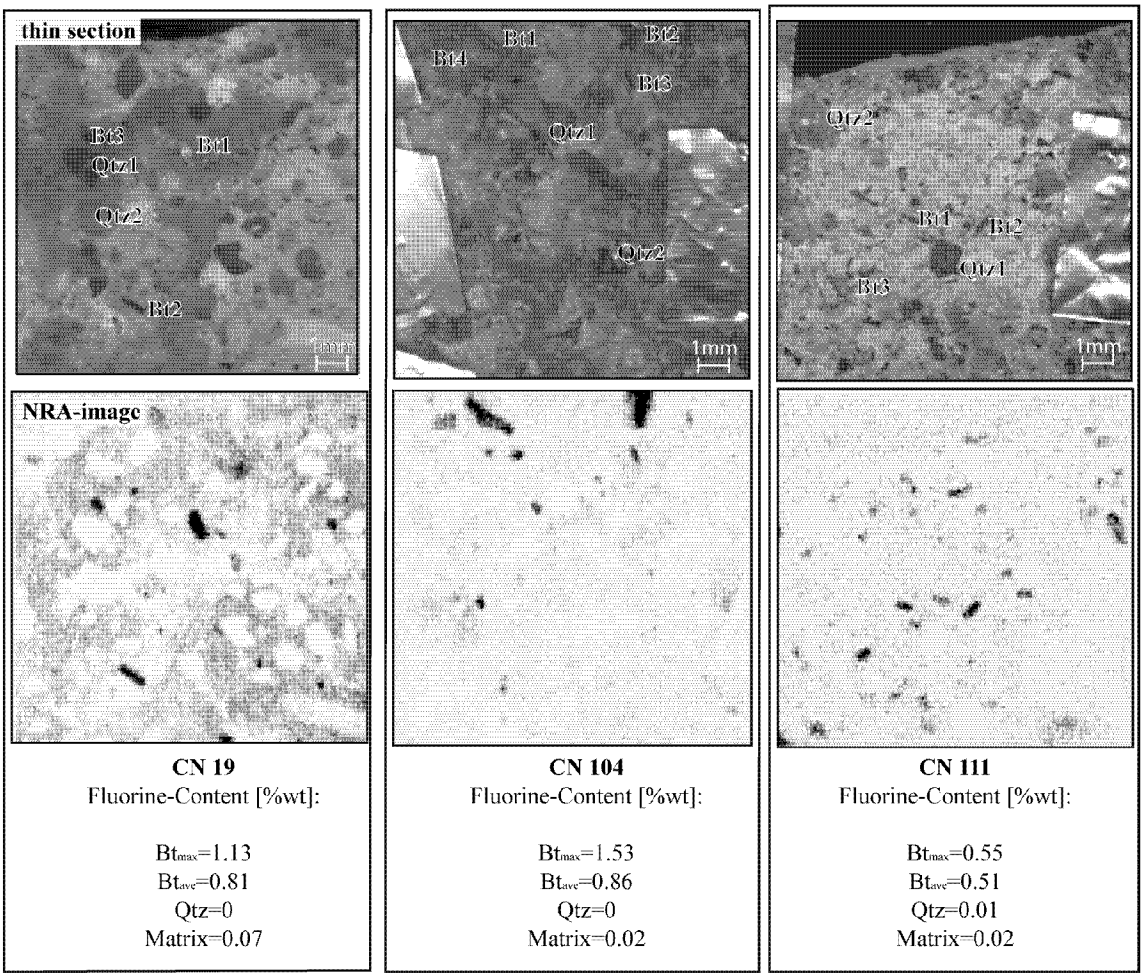

Figure 2 Imaged nuclear reaction analysis. Dark spots in the lower pictures of each column responded to nuclear activation and are identified as micas. Quartz-grains and matrix show no response and are essentially free of fluorine.

We conclude that although F-hotspots are present in the volcanic-ground mass of our ignimbrites and the average U/Th concentrations of the ignimbrites are equal to a granitic crust composition (Mamani et al., 2004), nucleogenic ^{22}Ne production is negligible. This can

be different when the host of elevated F and U/Th concentrations are numerous micro-inclusions in our quartz, undetected by the NRA method. Similarly, interferences for nucleogenic ^{21}Ne-production from Mg may not be expected, since Mg-bearing minerals are of minor abundance and Mg is in the bulk chemical and LA-ICP-MS analysis of the quartz on the analytical limit of measurement.

One might add independent support for a negligence of nucleogenically produced neon components as suggested by Kohl and Nishiizumi (1992) because the chemical etching process may erase some few µm from the outer quartz shell. This would be the relevant α-recoil distance (20-50µm, Kurz, 1986) and would be the zone of enhanced entrapment of nucleogenically produced neon-components. However, some of the quartz grains of the Chilean ignimbrites seem to be very resistant against chemical attack revealed by perfectly sharp edges investigated under microscope after the chemical etching process. The young age of the analysed ignimbrites (≤23Ma) is also in favour for low accumulation rates of nucleogenically produced neon components.

At the moment we do not know, whether the slightly elevated ^{22}Ne/^{20}Ne ratios (see Chapter 3) are specific for the Chilean ignimbrites or are rather on an upper limit of possible ^{22}Ne/^{20}Ne ratios in neon studies (Niedermann, 2002) within relevant measurement uncertainties.

Table 3. Fluorine wt% in whole rock an individual mineral grains by NRA

	Wt% F			
Fluor-	Standard 3.8%(wt) [$Ca_5(PO_4)_3F$]			
sample-file	All-rock	Bt(average)	Bt(max)	Qtz
F-19-1009_xy	0.10	0.83	1.15	0.00
F-104-1008_xy	0.03	0.88	1.56	0.00
F-111-1003_xy	0.03	0.52	0.56	0.01

6.5 Discussion

In the case of our quartz-separates from Chilean ignimbrites this study reveals no influence of trace impurities on TCN-studies. Although impurities in those quartz aliquots and individual quartz grains exist on the order of the uncertainties of measurements (Table 1), they have negligible effects on the total production rates. This is especially the case for structurally bound impurities. In the cases of the presence of minerals other than quartz the chemical dissolution procedure is in many cases sufficient to isolate quartz, but not always.

Additional physical separation methods are commonly required (Bierman et al., 2002; Ivy-Ochs, 1996; Kohl and Nishiizumi, 1992), otherwise such samples have to be discarded. The quartz from the Chilean ignimbrites revealed, however, very small melt-inclusions in the range of 5-50µm (few are 100µm -200µm), which are not easy to separate from the quartz. Even online crushing devices used in noble gas analysis may not break down to such sizes. If they would, further chemical and physical cleaning steps are required to clean up broken grain surfaces. However, bulk chemistry analysis indicated no major contribution that may have derived from melt-inclusions or is lost in the uncertainties. Fluid inclusions may host impurities but they can be eliminated by off- and online crushing if grain sizes smaller than the inclusions can be achieved. Therefore, fluid inclusions are less critical than melt inclusions for noble gas analysis.

If the quartz aliquots are as clean as reported here, variations of <2% of the total production rate due to impurities are negligible compared to uncertainties due to e.g., the analytical procedure, elemental production rate calculations or scaling formalisms (see Gosse and Phillips, 2001; Niedermann, 2002).

In order to illustrate a possible effect when impurity-concentrations become important, an increase of the ^{21}Ne TCN-production rate in quartz by 5% would require either 1wt% Mg, 8wt% Al, or 0.75wt% Na. Such concentrations of Na, Al or Mg impurities in quartz have never been reported, and impurities from structurally bound positions for the most quartz are «1000ppm (D'Lemos et al., 1997; Götze and Lewis, 1994; Götze et al., 2004; Monecke et al., 2002; Müller et al., 2003; Peppard et al., 2001; Watt et al., 1997). On the other hand, melt inclusions may contribute up to ~5wt% of impurities (Peppard et al., 2001). Also, undetected impurities from admixtures of other minerals within an enriched quartz grain-aliquot by e.g., 5% of sanidine, will have only an effect of ~1% (20% admixture an ~4.5% effect) on the total ^{21}Ne elemental production rate. However, such impurity concentrations are too high to permit a Be and/or Al analysis.

We have not measured impurities in quartz from **magmatic** and **metamorphic** rocks, known to raise problems for noble gas analysis (e.g., Hetzel et al., 2002). However, as studies on such lithologies revealed, structurally bound trace elements are in a similar negligible range as observed for the ignimbrites (D'Lemos et al., 1997; Götze and Lewis, 1994; Götze et al., 2004; Monecke et al., 2002; Müller et al., 2003; Peppard et al., 2001; Watt et al., 1997). A most suitable rock for TCN-analysis cannot be defined, since fast cooled magmatic rocks may be free of nucleogenic/trapped neon-components (as observed here) but may incorporate a number of structurally bound impurities (e.g., Dennen, 1964, 1967; Landtwing and Pettke,

2005). However, in the field the geomorphology should be the primary guide for a sampling strategy, and as a second choice, it should be the lithology.

6.6 Appendix

Analytical Methods

Sample preparation to achieve pure quartz aliquots followed the procedures of (Ivy-Ochs, 1996; Kohl and Nishiizumi, 1992). For noble gas analysis, we used a grain-size fraction of >40 to <100µm. This fraction might be suitable to avoid atmospheric trapped neon components but is insufficient to erase melt-inclusions of 5-50µm size (see below and text). Adsorption of gases like CO_2, CH_4 or N_2 cannot be avoided (Barker and Torkelson, 1975) when crushed to smaller grain sizes.

Polished thin sections have been analysed under **polarised transmitted light microscope** for selecting grains and characterizing structure, texture and morphologies of grains and matrix. The matrix of the analysed Chilean ignimbrites consists of a mixture of partially devitrified volcanic glass with sporadic occurrence of biotite/phogopite and magnetite grains, is fine grained and shows concentrical recrystallization spots and fibrous structures. Euhedral quartz and feldspar grains have sizes up to 3mm, but are commonly between 1-2mm, appear mostly as fragments, are angular and transparent. A few quartz-grains come as paramorphosed modification of quartz after high-temperature quartz and occur as hexagonal dipyramids with shortened prismatic planars. Quartz grains show multiple fractures, likely due to the fast cooling and structural α to β-quartz transformation. No internal zoning of quartz is observable under the microscope.

Quartz aliquots were analysed for the minor and major elements producing cosmogenic ^{21}Ne and ^{10}Be by **ICP-AES** and **photospectrometry** (Service d'Analyse des Roches et des Minéraux CRPG – CNRS, Vandoeuvre-lès-Nancy Cedex – France and ETH geochemistry Labs). Analysed samples had a size of ca. 100-300µm.

Backscattered electron imaging (BSE) and **cathodoluminescence** (CL) images were collected after carbon-coating (25nm) of thin sections using a scanning electron microscope (SEM) of type CAMSCAN (CS 44LB) equipped with a CL unit. Beam current was 10nA, accelerating voltage was 15 kV with a 35mm working distance. Magnification ranged between 30x and 80x. Specific descriptions to the facilities used here are reported in (Landtwing and Pettke, 2005). No internal zoning of quartz is observable under BSE-conditions.

The **LA-ICP-MS** measurements were performed with a prototype 193nm ARF Excimer laser system with special homogenized energy profile. Output energy was ~70 mJ, with a laser pulse rate of 10Hz. Dwell time for each isotope was 10ms, within a sweep of 169ms. The ablation volume was ~0.6mm^{-3} by a crater diameter of 100µm and ablation depth of 7.5µm. Further details of LA-ICP-MS setup, technique and data reduction can be found in (Landtwing and Pettke, 2005; Pettke et al., 2004).

Nuclear reaction analyses (NRA) on small sample-pieces have been conducted to estimate the production of nucleogenic ^{22}Ne from high F-concentrations in nearby biotite (F in substitution of OH^-) or of inclusions. Samples were scanned with high spatial resolution and with a beam spot of 100µm (maximum field: 12 by 12 mm), a working current of 10nA and with a 2.7 MeV proton beam. Emitted γ-rays are detected by a NaI-detector. Fluorine concentrations have been calibrated against a fluorapatite-standard by counting rates.

7 Artificial targets for production rate scaling systematics in terrestrial cosmogenic nuclide studies

In collaboration with:
J.M. Schäfer[1], R. Wieler[2], H. Baur[2], Z. Zhou[2]

[1]Lamont-Doherty Earth Observatory, USA
[2]Institute of Isotope Geology ETH Zürich, Switzerland

7.1 Abstract

Reported are data from first experiments using quartz in exposed artificial targets to study scaling systematics of terrestrial cosmogenic nuclide production rates. Stainless steel-containers filled with 4kg of industrial quartz were exposed over 2 to 4 years at altitudes ranging from 500 to 4500m and latitudes between 23° and 73° (northern and southern hemisphere). Initial results of ^{3}He and ^{21}Ne measurements indicate the feasibility of using quartz as artificial target in experimental terrestrial cosmogenic nuclides-scaling studies. Technical and analytical problems, such as low cosmogenic nuclide concentrations, target blanks, or interferences with non-cosmogenic components (radiogenic, nucleogenic) caused difficulties but are expected to be overcome in further studies. Advanced container designs and enhanced pre-treatments of targets are necessary.

7.2 Rationale of the experiment

Production rates of in situ produced terrestrial cosmogenic nuclides (TCN) as used in Quaternary Geology and Quantitative Geomorphology (Bierman, 1994; Cerling and Craig, 1994; Zreda and Phillips, 2000; Gosse and Phillips, 2001; Bierman et al., 2002; Niedermann, 2002) have to be scaled to latitude and altitude for each sample. In the 1990's such a scaling formalism was provided by Lal (1991). It was based on neutron-monitor counting rates and spallation rates deduced from photographic emulsions from the 1960's. Scaling factors were expressed as 3rd-degree polynomials. They were considered to be globally applicable assuming a pure axial symmetric terrestrial dipole magnetic field and global mean constant

temperature and pressure distributions. A ±10% uncertainty due to this scaling-procedure was adopted (Lal, 1991). Later, Dunai (2000), Stone (2000), Desilets and Zreda (2001); Desilets et al, (2003) developed codes addressing especially problems of (i) air-pressure inhomogeneities, (ii) accounting for new and more widespread neutron-monitor surveys with wider energy-spectra, (iii) separate scaling of neutrons and muons, and (iv) applying better known geomagnetic shielding parameters and solar variations. The need for precise scaling models becomes especially obvious e.g., in the dispute of the timing of the last glacial maximum (LGM) - being a world-wide forced climate phenomenon or only of regional extent (Denton et al., 1999; Schäfer et al., 1999).

To evaluate theoretically and physically derived scaling formalisms, direct estimations of scaling parameters are needed. This can be achieved by exposing artificial targets such as water, glass, quartz, etc. at different latitude and altitude transects and over known times, preferably at sites with neutron monitoring. Additionally, the latitude/altitude effects on production rate scaling have to be corrected for geomagnetic field intensity variations, polar wandering (e.g., Lal, 1987; Beer et al., 1988; Beer et al., 1993; Masarik and Beer, 1999; Masarik et al., 2001; Pigati and Lifton, 2004).

In this chapter, the first results of an artificial TCN-target test at ETH Zürich are reported. This experiment was initiated by J. Schäfer and co-workers in 1997 (Schäfer, 2000) using stainless steel containers filled with 4kg degassed industrial quartz exposed over 2 to 4 years at various altitudes and latitudes (see Table 1). We chose quartz since it is a widely used target in TCN-studies.

Table 1. Containers, exposure times, locations and coordinates

container No.	location	start of exposure	Exposure time in [a]	geographic latitude	geomagnetic latitude	altitude [m asl]
1 & 9	Etna	3.10.97	1.6055	38°N	38°N	3000
5 & 6	Chile	20.4.97	2.3315	23°S	10°S	5000
12 & 14	Gornergrat	2.4.98	4.4521	46°N	47.5°N	3000
7 & 13	Greenland	24.6.97	2.0192	72.5°N	80°N	3000
3 & 11	Jungfraujoch	29.7.97	3.9836	46°N	47.5°N	3500
2 & 4	Monte Rosa	13.7.97	5.2219	46°N	47.5°N	4450
8 & 10 & 15	ETH	unexposed				

7.3 Brief history of artificial target experiments for TCN-production rate systematics

Early determinations of nuclide production rates were performed by Lal et al., (1960) for short lived ^{7}Be, ^{32}P, ^{33}P, ^{35}S, and (Yokoyama et al., 1977) for ^{22}Na and ^{24}Na on metal

targets. Reedy et al. (1994) studied ^{7}Be, ^{10}Be, ^{14}C, ^{22}Na, ^{26}Al on Si and SiO_2, while Graf et al. (1996) investigated ^{21}Ne in glass exposed at mountain altitudes.

Direct altitude scaling experiments were performed by Kurz et al. (1990 and unpublished) using ^{3}He in water targets. Similarly, Nishiizumi (1996) and Brown et al. (2000) used water targets for ^{7}Be, ^{10}Be and ^{3}H, ^{3}He, ^{10}Be, respectively.

A combined direct altitude and latitude scaling experiment was performed by Graham et al. (2000) in the southern hemisphere using ^{7}Be in water, from altitudes 0 to 2000m and latitudes 20°-79°S.

All experiments confirmed in principle the trend of Lal's scaling procedure. However, they all suffered from low nuclide concentrations produced over short exposure times and the lack of global sample coverage especially from locations such as Antarctica (Stone, 2000), Iceland (Liccardi and Kurz, 2002), or Patagonia (Ackert et al., 2003) which have permanent pressure anomalies.

The latest approach in addressing the problem of production rate-scaling procedures for TCN-studies is the CRONUS-EARTH/CRONUS-EU-initiative. A comprehensive coverage of the globe by latitude and altitude transects for direct estimations of production rate-scaling algorithms is planned. Further aims are (i) the estimation of absolute production rates by primary calibration sites, (ii) re-checking the half-life of ^{10}Be (iii) testing the temporal variation of production rates through time, (iv) estimation of muon production rates, (v) evaluating, whether the scaling formalism is nuclide specific and, (vi) using neutron-monitoring sites for scaling experiments.

7.4 Methodical Concepts

7.4.1 Artificial targets

The experiment at ETH Zürich was designed for measuring cosmogenically produced helium and neon in degassed industrial quartz (but of natural origin, Fluka, Chemika (84878), purity: 99.9%, grain-size: 149-420µm; loose density: $\rho=1.527 gcm^{-3}$). 4kg of quartz sand were stored in stainless steel containers designed specifically for the experiment. Containers are 14 cm in diameter and quartz fills up inside the containers to 18cm (container height: 45cm). Optimal heating of containers was up to 23cm by an external oven. Filled containers were degassed for 2 weeks in temperature-cycle-steps to 800°C (measured on the exterior of the container). This reduced the pressure from 10^{-5} to 10^{-9} Torr (Schäfer, 2000). The inside

temperature was assumed to be higher than ca. 650°C, as in an earlier experiment aluminum foil placed on top of the sand in a center position got partially melted. Analyses after degassing were performed at temperatures ranging from 400°C to 700°C in 100°C steps for 1h to 3h. Cosmogenic neon is completely released at ≤600°C (Niedermann et al., 1993; Niedermann et al., 1994). Blanks were undetectable for nuclide excesses with ^{3}He and ^{21}Ne $<10^{5}$ atoms and $<3*10^{6}$ atoms, respectively (Schäfer, 2000). The expected excesses of cosmogenic components over atmospheric composition of a degassed container after a planned 18 to 40 month exposure time were estimated to 25-75% (^{21}Ne) and 98-100% (^{3}He). Hereby, no internal increase of blanks during the time of exposure (outgassing of containers, leaking of valves) was assumed. We note, that after exposure of the containers the mass-spectrometer was equipped with a newly designed compressor device (Baur, 1999) that increased the sensitivity compared to a conventional ion-source by a factor of 120 and 200 for ^{3}He and ^{21}Ne, respectively. This increases the precision of isotope ratio and abundance measurements.

The reported diffusion and non-quantitative retention of ^{3}He in quartz at low temperatures (Kurz and Brook, 1994; Trull et al., 1995; Shuster and Farley, 2003; Shuster et al., 2003) can be controlled by analysing a room-temperature step before heating the exposed containers.

Since ^{3}H is simultaneously produced with ^{3}He (^{3}H/^{3}He branching ratio 0.73 for O and 1.16 for Si (Leya et al., 2004)), but decays with a half-life of ca. 12.43yr to ^{3}He, a correction has to be applied, which amounts in our study to 10-12%.

7.4.2 Target (container) exposure strategy and locations

At every location (see Table 1) a plastic box with 2 containers was deposited in order to have a crosscheck possibility. Containers were stored horizontally and quartz was equally distributed by shaking the containers. The height of quartz sand within the container was just a few centimetres and self-shielding can thus be neglected.

Exposure of targets took place between 1997 and 2002 and covered a solar maximum during sun spot cycle 23. Hence the spallogenic production is reduced, which must be corrected for.

7.4.3 Production rates

Production rates of ^{3}He and ^{21}Ne from spallation in quartz are reported as $P^{3}He$=124atoms/g/yr (Masarik, 2002) and $P^{21}Ne$=20.3atoms/g/yr (Lal-scaling, Niedermann, 2000). These values were used for an a priori estimation of cosmogenic nuclide abundances after a certain exposure time. Muogenic production of helium and neon is neglected (see Niedermann, 2002).

7.4.4 Neutron-monitoring

In two cases, container targets were exposed close to neutron monitors. Sample location Jungfraujoch (Switzerland) has been under surveillance for more than 30yrs and produced the most reliable record (monitor-type: NM64 and IGY) already over a number of sun-spot cycles, whereas location Gornergrat has been running since 6yrs (both are operated by the Department of Physics, University of Bern). Stations record secondary neutron energy spectra.

7.4.5 Measurement protocol

After retrieving target containers, one unexposed (10) and two exposed containers (11, 12, see Table 1) were analyzed so far by step-wise heating. The nominal starting time of every heating step was when the outside container temperature reached the nominal temperature, which is not equal to the inside temperature. A simulation test in a non-evacuated container filled with equal amounts of sand yielded a time-lag of 3h between outside and inside temperature at 600°C. A thermocouple placed in the centre of the sand just reached an equilibrium temperature of 570°C. This fact indicates that insufficient heat-transmission control will be a significant source of uncertainty in the experiment unless modifications in the container design are made. Cooling-times of containers were usually equal to the heating-times. Note that in the following, the data are given with the respective temperature as presumed, keeping in mind that the actual temperature in the containers might have been considerably lower.

7.4.6 Mass-spectrometer specifics

Details of mass-spectrometric procedures are reported in Chapter 3 & 5. Except for container 12, a mass-spectrometer with a compressor source (Baur, 1999), internally termed TOM, was used. Container 12 was analysed using a custom-made mass-spectrometer (Supergnom) and a commercial VG5400. Corrections for interferences by doubly charged particles have been applied in both cases for $^{40}Ar^{++}$ and $H_2{}^{18}O^{+}$.

7.5 Data/Results and Interpretation

7.5.1 Industrial quartz-sand - measurements

Loose quartz-sand of the company Fluka was measured by a similar procedure as applied to exposure dating, in order to establish the noble gas inventory of the sand. Non-degassed (pre-treatment) and non-exposed sand separates of 100mg and 200mg were step-wise heated to 600°C and 800°C, respectively, and results are presented in Table 2.

Table 2. Neon and helium measurements of Fluka-sand (untreated)

sample (weight [mg]) (temperature [°C], heating time [min])	^{20}Ne	error	$^{21}Ne/^{20}Ne$	error	$^{22}Ne/^{20}Ne$	error	$^{21}Ne_{cosmo}$	error
	[ccSTP/g]	[ccSTP/g]					[atoms/g]	[atoms/g]
S100-Ne(600,30')	1.84E-09	9.97E-12	3.00E-03	5.15E-06	1.03E-01	1.57E-04	1.91E+06	1.16E+06
S100-Ne(800,30')	2.06E-09	1.29E-11	3.06E-03	1.78E-05	1.04E-01	2.22E-04	5.48E+06	1.77E+06

sample (weight [mg]) (temperature [°C], heating time [min])	^{3}He	error	^{4}He	error	$^{3}He/^{4}He$	error	R/R_a	error
	[atoms/g]	[atoms/g]	[atoms/g]	[atoms/g]				
S100-He(600,30')	8.82E+04	1.37E+04	9.55E+10	9.09E+08	9.24E-07	1.44E-07	0.66	0.10
S100-He(800,30')	1.70E+04	1.44E+04	1.02E+12	5.20E+09	1.66E-08	1.41E-08	0.01	0.01
S200-He(600,30')	9.30E+04	7.83E+03	7.87E+10	2.42E+08	1.18E-06	9.95E-08	0.85	0.07
S200-He(800,30')	-3.51E+03	7.79E+03	4.30E+11	1.17E+09	-8.17E-09	-1.81E-08		

Helium was measured in all fractions while neon was measurable only in the 100mg separate. The 200mg separate yielded too high ^{20}Ne-concentrations to be measured. ^{3}He-concentrations were $(1.7\text{-}9.3)*10^{4}$ atoms/g, while ^{4}He-concentrations ranged between $(7\text{-}102)*10^{10}$ atoms/g. Ratios of $^{3}He/^{4}He$ were below atmospheric composition for the 600°C temperature steps and close to atmospheric composition in the second 600°C step (Table 2). U/Th- concentrations measured by γ-spectroscopy yielded values <1ppm (pers. comm., R. Kipfer, 2002).

Ne-concentrations for the 100mg sample yielded high ^{20}Ne-values of $(1.84\text{-}2.06)*10^{-9}$ ccSTP (Table 2). Excess of ^{21}Ne over atmospheric composition is $(1\text{-}5)*10^{6}$ atoms/g.

However, $^{21}Ne/^{20}Ne$ and $^{22}Ne/^{20}Ne$ ratios plotted above the atmospheric-cosmogenic mixing line (Fig. 1), indicating crustal/trapped components (Niedermann, 2002).

Although the containers are believed to be degassed prior to exposure, an insufficient degassing will likely bias the results of exposed containers by inherited non-cosmogenic components, as observed in this untreated sand-experiment.

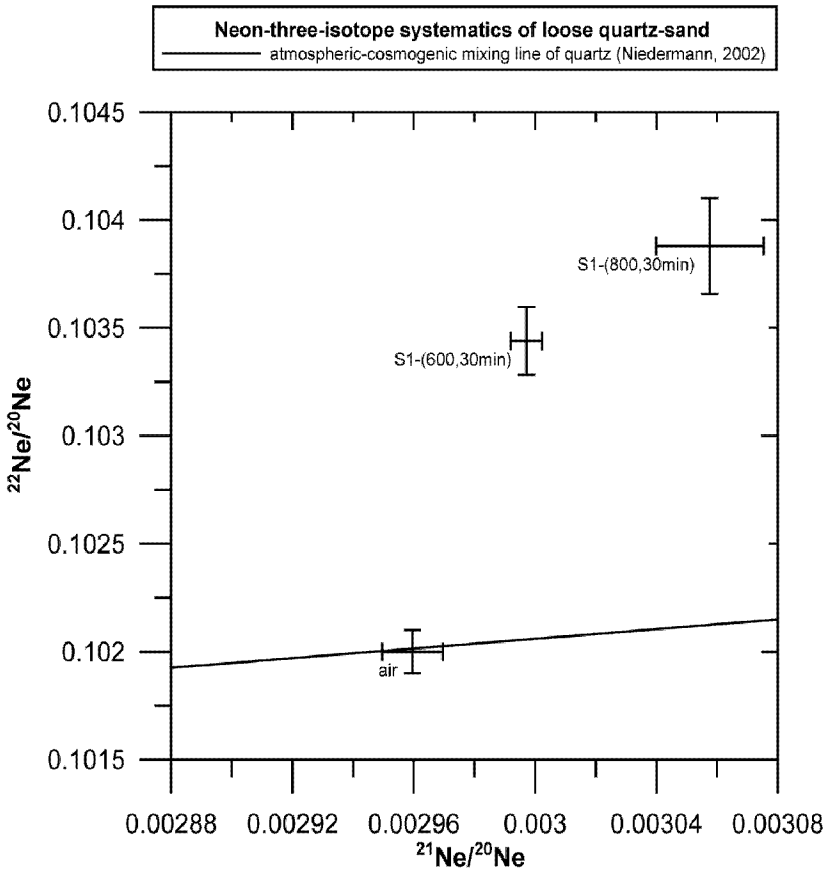

Fig. 1 Neon-three-isotope diagram of loose quartz-sand indicating inherited crustal neon components

7.5.2 Unexposed - Container

A completely shielded container that was stored over 5 years in a basement was used for blank analysis. Any measurable non-cosmogenic nuclide concentration, due to in-growth or diffusion processes during the storage time, can be used to correct data of exposed containers.

Helium

Results are presented in Table 3. At room-temperature and in the first heating step (600°C) almost equal gas amounts of ^{3}He were released. Each of the values is ~2 times higher

than the concentration measured after degassing before storing. The first 800°C step revealed a one order of magnitude higher concentration of ^{3}He. A repeated 600°C step yielded much lower ^{3}He-concentrations, while a second 800°C-step released again increased ^{3}He-concentrations (Table 3).

In summary, ^{3}He-concentrations are much higher than expected from an unexposed container. Whether this is due to diffusion into the container from outside, diffusion from the container walls, or ^{3}He from tritium-decay is difficult to evaluate. The decreased ^{3}He/^{21}Ne ratios with incremental step-heating suggest that only after five heating steps any inherited ^{3}He is completely degassed.

Table 3. Helium concentrations and ratios of unexposed container 10

heating step (°C, min)	^{3}He [atoms/4000g]	error [atoms/4000g]	^{4}He [atoms/4000g]	error [atoms/4000g]	^{3}He/^{4}He	error	R/R_a	^{3}He/^{21}Ne
(20,45')	1.80E+05	2.15E+04	5.52E+11	3.07E+09	3.26E-07	3.91E-08	0.2359	39.64
(600,150')	2.04E+05	2.11E+04	1.97E+11	1.09E+09	1.03E-06	1.07E-07	0.7463	7.26
(800,780')	2.21E+06	1.97E+05	3.93E+14	2.18E+12	5.63E-09	5.03E-10	0.0041	n.d.
(600,210')	9.29E+03	8.77E+03	4.69E+11	3.08E+09	1.98E-08	1.87E-08	0.0143	14.97
(800,300')	1.12E+05	1.97E+04	1.65E+13	9.15E+10	6.79E-09	1.19E-09	0.0049	0.59
total (≤600°C)	**3.93E+05**		**1.22E+12**					
total (all °C)	**2.72E+06**		**4.11E+14**					
concentration after degassing prior to storage	1.00E+05							

Concentrations of ^{4}He indicate similar gas amounts for heating steps ≤600°C, but increased concentrations by 2-3 orders of magnitude at the 800°C steps (Table 3). The majority of ^{4}He was released in the 800°C steps as was observed also in the loose-sand experiments, indicating similar sources (e.g., trapped in inclusions, Niedermann et al., 1993).

The ^{3}He/^{4}He-ratios are all below atmospheric composition. Highest ratios were observed in the room- and 600°C temperature step and were then constantly declining. This suggests two different helium-components where ^{3}He was released at lower temperatures and ^{4}He at higher degassing temperatures.

Neon

Neon concentrations and isotopic ratios are presented in Table 4. A first 800°C step was aborted due to high ^{20}Ne-concentrations. Internal blank corrections of measured data yielded negative values (Table 4). Therefore a closer look at the blanks (the blank of the unexposed container measured after cooling of every temperature step) and measured data

(the temperature steps) is presented in Table 4A-C. Neon-isotope ratios are shown in Fig. 2. In order to evaluate the nature of any ^{21}Ne-excess it needs to be pointed out that the blanks of the unexposed-container are most times offset towards crustal neon-components. Only in one case the blank indicated neon-ratios of atmospheric composition. Neon released at higher temperatures yielded isotope-ratios that plot either towards crustal components due to elevated ^{22}Ne-concentrations or nucleogenic contaminations due to elevated ^{21}Ne-concentrations (Fig. 3). No trend is observable since two repeated 600°C heating steps yielded first crustal and second nucleogenic signatures (note: an 800°C-step was performed in between, but was pumped out for neon analysis). It is obvious that no major excess of ^{21}Ne can be observed to be of cosmogenic origin (as expected from a shielded and unexposed container). However, we probably would have to assume that signatures of crustal or nucleogenic origin would compromise exposed containers as well, unless the quartz sand used could be degassed more efficiently prior to exposure. Such a non-cosmogenic excess is lower than the measured value before storage (<3*10^{6}atoms) but still would make 10-50% of the total concentration after exposure (Table 4C).

Table 4A. Neon concentrations and ratios for un-exposed container 10, corrected with internal blank

Container temperature/time [°C, min]	^{20}Ne ccSTP/4000g	error ccSTP/4000g	^{21}Ne/^{20}Ne	error	^{22}Ne/^{20}Ne	error	^{21}Ne$_{cosmo}$ atoms/4000g	error atoms/4000g
10(20,45')	4.20E-11	3.99E-12	2.95E-03	1.89E-04	9.84E-02	6.75E-03	-1.23E+04	4.96E+05
10(600,150')	4.68E-12	1.80E-12	3.05E-03	1.69E-03	9.80E-02	6.04E-02	1.20E+04	2.96E+05
10(600,210')	1.79E-11	2.37E-12	2.93E-03	4.45E-04	9.74E-02	1.61E-02	-1.55E+04	3.41E+05
10(800,300')	9.29E-13	1.78E-12	9.41E-03	1.91E-02	5.41E-02	2.65E-01	1.61E+05	6.72E+05
total (pos.)							1.73E+05	
expected blank							<3E+06	

Table 4B. Neon concentrations and ratios for the un-exposed container 10, with separate data reduction for blanks

Blank temperature/time [°C, min]	^{20}Ne ccSTP/4000g	error ccSTP/4000g	^{21}Ne/^{20}Ne	error	^{22}Ne/^{20}Ne	error	^{21}Ne$_{cosmo}$ atoms/4000g	error atoms/4000g
Blank(20,45')	1.54E-12	4.17E-13	2.91E-03	5.42E-05	1.02E-01	4.67E-04	-2.09E+03	4.65E+04
Blank(800,45')	6.72E-12	1.82E-12	3.02E-03	2.01E-05	1.07E-01	2.80E-04	1.09E+04	2.07E+05
Blank(0,45')	5.35E-12	1.45E-12	3.20E-03	7.93E-05	1.20E-01	8.69E-04	3.41E+04	1.70E+05
Blank(800,45')	5.60E-12	1.52E-12	3.05E-03	3.25E-05	1.06E-01	3.36E-04	1.41E+04	1.74E+05

Table 4C. Neon concentrations and ratios for the un-exposed container 10, with separate data reduction for each temperature step

Container temperature/time [°C, min]	^{20}Ne ccSTP/4000g	error ccSTP/4000g	^{21}Ne/^{20}Ne	error	^{22}Ne/^{20}Ne	error	^{21}Ne$_{cosmo}$ atoms/4000g	error atoms/4000g	^{3}He/^{21}Ne
10(20,45')	4.68E-11	1.27E-11	2.96E-03	3.23E-05	9.98E-02	1.78E-04	4.55E+03	1.43E+06	39.64
10(600,150')	8.19E-12	2.22E-12	3.09E-03	4.36E-05	1.05E-01	9.71E-04	2.80E+04	2.55E+05	7.26
10(600,210')	2.26E-11	6.14E-12	2.96E-03	9.02E-06	1.00E-01	3.01E-04	6.21E+02	6.91E+05	14.97
10(800,300')	4.54E-12	1.24E-12	4.52E-03	6.88E-05	1.02E-01	7.47E-04	1.91E+05	1.79E+05	0.59
total (pos.)							2.24E+05		
expected blank							<3E+06		

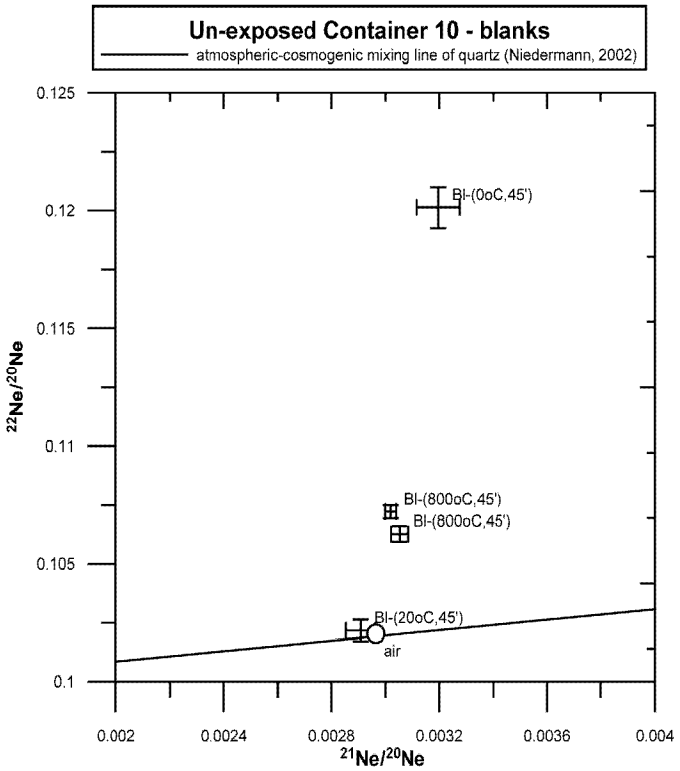

Fig. 2 Neon-three-isotope diagram of the blanks of the unexposed container stored at the Geology department. The blank of the unexposed container was measured after cooling to room-temperature of every temperature step. Crustal neon-components dominate the isotope ratios.

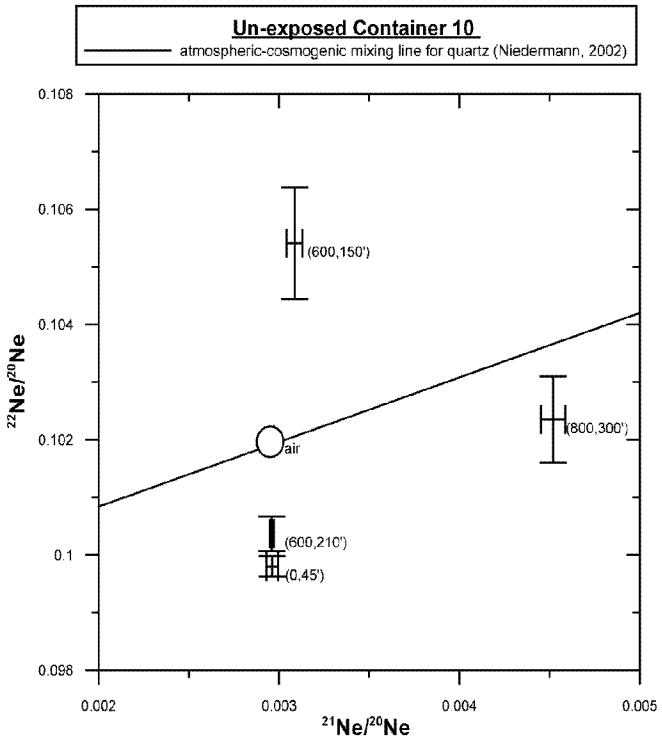

Fig. 3 Neon-three-isotope diagram of the various temperature steps of the unexposed container stored at the Geology department. Crustal and nucleogenic neon-components dominate the isotope ratios.

Summary

In summary, the unexposed container showed an inhomogeneous degassing pattern and yielded nucleogenic and crustal neon-components, while a "cosmogenic" neon-component was not observed. Helium and neon were most likely insufficiently degassed from the quartz before storage or an in-growth of helium and neon over the 5 years of storage occurred. In conclusion, from the first unexposed-container the degassing times for analysis of containers, initially before exposure (to "clean" the container) and after exposure (to release any accumulated component), are likely more than the 10h used so far. Current experiments on newly designed containers (Strasky et al., 2004) with a smaller diameter (6cm instead of 14cm) and filled with synthetic-quartz revealed low blanks of atmospheric composition. Temperature control by thermocouples placed internally of the container allowed additionally the reproduction of step-wise heating protocols. This new design therefore represents a considerable improvement.

7.5.3 Exposed Containers

7.5.3.1 Container 12 - Gornergrat

Since the unexposed container 10 yielded unexpectedly high ^{4}He-concentrations the analysis of the first exposed container 12 (Gornergrat) was made at less sensitive mass-spectrometers (Supergnom and VG5400).

Helium concentrations and isotope ratios are presented in Table 5. Concentrations of ^{4}He released increase with increasing temperature, but the total is less than observed in the unexposed container. However, temperature steps were shorter than those of the unexposed container. Helium-3-concentrations are increasing in the 700°C and decreasing in the 800°C step (Table 5). ^{3}He/^{4}He-ratios are highest in the 700°C-step. The room-temperature step yielded less than 1% of ^{3}He and suggests low rates of helium diffusion out of the quartz. The calculated total ^{3}He is $3.69*10^{8}$ atoms/container. This value is about an order of magnitude higher than that expected from cosmogenic production (including the indirect production of ^{3}He via ^{3}H). At the moment we attribute this discrepancy to poorly developed measuring-systematics of containers at the Supergnom/VG5400 mass-spectrometers. Another source of ^{3}He can be magmatic helium insufficiently degassed prior to exposure of the container.

Table 5. Helium-concentrations, ratios and calculations for Gornergrat-Container (12)

container (temperature, heating time) [°C, min]	^{4}He [ccSTP]	error [ccSTP]	^{3}He/^{4}He	error	R/Ra	^{3}He **atoms/4000g**	error atoms/4000g
12(20, 45)	1.32E-09	3.68E-13	1.66E-05	2.30E-08	11.99	**5.87E+05**	8.32E+02
12(600,240)	5.74E-09	2.91E-13	3.81E-05	6.09E-08	27.54	**5.88E+06**	9.40E+03
12(700,180)	3.22E-08	6.33E-13	4.18E-04	2.22E-07	301.73	**3.61E+08**	1.92E+05
12(800,180)	4.85E-07	8.77E-12	1.46E-07	5.46E-10	0.11	**1.90E+06**	7.11E+03
Total	**5.24E-07**					**3.69E+08**	
expected atoms (no blank)						*2.14E+07*	
expected atoms (including initial blank)						*2.15E+07*	
adding ^{3}He due to ^{3}H decay (^{3}H/^{3}He~1)						*3.02E+06*	
total expected ^{3}He						*2.45E+07*	
subtracting measured blank (container 10) from measured total						*3.67E+08*	
difference between measured total and total expected						*3.42E+08*	

7.5.3.2 Container 11 - Jungfraujoch

Helium

Data from container 11 (Jungfraujoch) are presented in Table 6. The ^{3}He concentration in the room-temperature step was considerable. Lowest gas amounts were released in the 200°C step and highest ones in the 800°C step. Two consecutive steps at 400°C with different heating times gave similar concentrations. Commonly, cosmogenic ^{3}He in quartz is released at much lower temperature than 800°C (Trull et al., 1991). The release of the highest quantities of ^{3}He at this temperature in our experiment probably indicates that in the interior of the container the nominal temperature of the 600°C-step was considerably lower than 600°C due to the low thermal conductivity (see above).

Similar to ^{3}He, the highest amounts of ^{4}He were released at 800°C (Table 6), but the total amounts were lower than those in the unexposed container. Similar to the loose-sand experiment and in container 10 and 12, highest amounts of ^{4}He were released at higher temperatures as it was reported from quartz studies by earlier investigations (Trull et al., 1991; Niedermann et al., 1993).

From all performed steps, an elevated ^{3}He/^{4}He-ratio is observed in the room-temperature step (Table 6, ~9R_a) and suggests some diffusion of ^{3}He already at low temperatures for this specific container. At 400°C, the ^{3}He/^{4}He-ratio is highest and then decreases steadily with increasing temperature, indicating a similar negative correlation as observed by Trull et al. (1991). It was suggested that this is due to a different positioning of the different helium isotopes in the quartz-lattice. However, for this container, any significant amount of ^{4}He was most likely degassed prior to exposure.

Table 6. Helium concentrations, ratios and calculations of Container-11-Jungfraujoch

heating step	^{3}He	error	^{4}He	error	^{3}He/^{4}He	error	R/Ra	^{3}He/^{21}Ne
(°C, min)	[atoms/4000g]	[atoms/4000g]	[atoms/4000g]	[atoms/4000g]				
11(20,45')	4.75E+06	1.40E+05	3.62E+11	1.02E+10	1.31E-05	1.37E-05	9.43	56.55
11(200,240')	2.58E+05	2.01E+04	-4.78E+09	2.34E+08				10.20
11(400,240')	3.77E+06	1.20E+05	5.27E+10	1.50E+09	7.15E-05	7.97E-05	51.46	27.30
11(400,570')	3.53E+06	1.13E+05	8.70E+10	2.46E+09	4.06E-05	4.58E-05	29.24	18.48
11(600,240')	1.85E+06	7.52E+04	4.90E+11	1.38E+10	3.78E-06	5.43E-06	2.72	1.66
11(800,240')	1.42E+07	8.67E+04	4.03E+13	1.14E+12	3.52E-07	7.61E-08	0.25	70.01
	2.83E+07	**Total**						
	2.60E+07	*expected atoms (no blank)*						
	2.61E+07	*expected atoms (including initial blank)*						
	2.99E+06	*adding ^{3}He due to ^{3}H decay (^{3}H/^{3}He~1, see text)*						
	2.81E+07	*total expected ^{3}He*						
	2.57E+07	*subtracting measured blank (container 10) from measured total*						
	-2.33E+06	*difference between measured total and total expected*						

The calculated total ^{3}He concentration is almost equal to the expected concentration when corrected for ^{3}He by the concentrations of the unexposed container and ^{3}He produced by ^{3}H→^{3}He (Table 6). However, since nuclide concentrations of the unexposed and the exposed container are similar and degassing was likely insufficient, any conclusions are difficult to draw. Helium-4 was lower in the Jungfraujoch container, suggesting any pre-exposure ^{3}He-concentration to be lower as well compared to the unexposed container. In turn this suggests that degassing of our unexposed container was incomplete and not reproducible.

Neon

Neon data are presented in Table 7, while neon isotope-ratios are plotted in Fig. 4. The room-temperature data-points plot below atmospheric composition with a nucleogenic/MORB signature. The 200°C and the two consecutive 400°C steps plot above the atmospheric cosmogenic mixing line due to elevated ^{22}Ne-concentrations, indicating a crustal component. The origin of this crustal (e.g., trapped) component is not clear. The 600°C step plots close to the cosmogenic-atmospheric mixture line, suggesting a cosmogenic signature. Only a split of the gas from the 800°C steps was measured due to high ^{20}Ne concentrations. A first 800°C (4h) data point is plotting close to the 25°C point, while a repeated 800°C (9.5h)-step yielded even higher amounts of MORB/nucleogenic neon components (Fig. 4). Such components are degassed at higher temperatures than cosmogenic neon (Niedermann, 2002). Therefore, only the 600°C indicates cosmogenic ^{21}Ne-excess over atmospheric. Any ^{21}Ne-excess of the other temperature steps represents non-cosmogenic components.

Table 7. Neon concentrations, ratios and calculations of Container-11-Jungfraujoch

Container (temperature/time) [°C, min]	^{20}Ne [ccSTP/ 4000g]	error [ccSTP/ 4000g]	^{21}Ne/^{20}Ne	error	^{22}Ne/^{20}Ne	error	^{21}Ne$_{excess}$ [atoms/ 4000g]	error [atoms/ 4000g]
11(25,45')	1.91E-11	2.56E-13	3.12E-03	4.48E-05	1.00E-01	3.70E-04	8.40E+04	3.75E+04
11(200,240')	3.28E-12	5.73E-14	3.25E-03	7.20E-05	1.08E-01	1.13E-03	2.53E+04	9.27E+03
11(400,240')	2.00E-12	4.72E-14	5.53E-03	2.27E-04	1.13E-01	3.28E-03	1.38E+05	1.46E+04
11(400,570')	1.10E-12	4.07E-14	9.43E-03	6.31E-04	1.18E-01	6.84E-03	1.91E+05	2.15E+04
11(600,240')	9.10E-11	1.11E-12	3.41E-03	1.91E-05	1.03E-01	1.83E-04	1.11E+06	1.43E+05
11(800,240')	2.84E-11	4.10E-13	3.22E-03	3.56E-05	1.01E-01	1.20E-04	2.02E+05	5.53E+04
11(800,600')	7.20E-12	1.24E-13	3.15E-03	7.16E-05	9.66E-02	3.34E-04	3.76E+04	2.00E+04
					total cosmogenic from 600°C step		**1.11E+06**	
					expected atoms		*3.98E+06*	
					expected atoms (including blank)		*6.98E+06*	
					difference between total measured and expected		*2.87E+06*	

The calculated cosmogenic ^{21}Ne concentration of the 600°C step is one third of the expected concentration (Table 7). If we subtract the nominal excess of ^{21}Ne of the unexposed container the resulting cosmogenic concentration would even be only 15% of what we expected. Assuming the 400°C-temperature steps to have released cosmogenic ^{21}Ne also (although this temperature is commonly too low for sufficient release of cosmogenic ^{21}Ne; (Niedermann et al., 1993; Niedermann et al., 1994) the total cosmogenic ^{21}Ne would again correspond to 30% of the expected amount. We attribute this low measured cosmogenic concentration to the insufficient degassing of the container as outlined earlier.

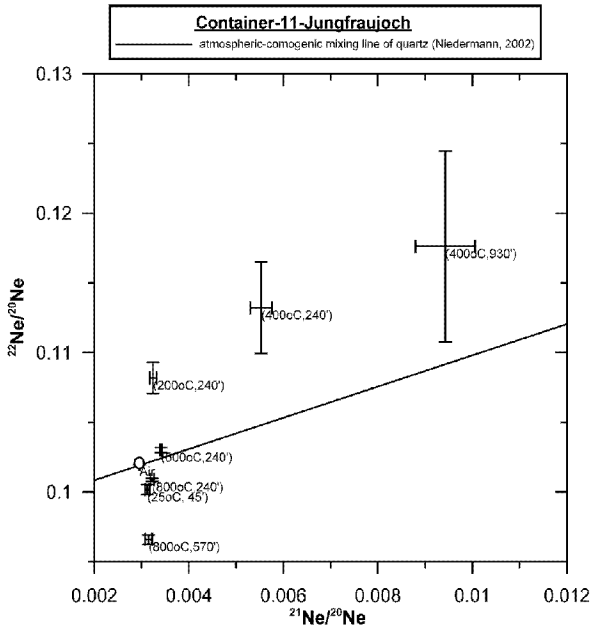

Fig. 4 Neon-three-isotope diagram of container 11 exposed for 4 years at the Jungfraujoch. Crustal neon-components dominate the isotope ratios in the low temperature steps (≤600°C) while nucleogenic/MORB neon-components dominate the isotope ratios in the 800°C steps.

7.5.4 Summary of data

The measurements of artificial quartz targets reveal the following:

a) ^{3}He and ^{21}Ne components in excess over atmospheric composition are detectable in artificial targets and probably largely represent cosmogenic components. Nevertheless, non-cosmogenic/non-atmospheric excesses in these isotopes may compromise the analyses.

b) The degassing of containers prior to exposure was likely insufficient and cannot be assumed to be identical for all-containers. Non-cosmogenic helium or neon components were not completely degassed.

c) As a consequence of these shortcomings, this pilot study has not yet yielded useful results to test and calibrate scaling models for terrestrial cosmogenic nuclides with altitude and latitude. Fortunately, in a follow-up study, Strasky et al. (2004) observed much lower blanks by using synthetically produced quartz and an improved container design, which allows a better control on degassing of containers (see below).

7.6 Discussion and suggestions

In the following, some additional ideas and suggestions are outlined for further studies and experiments and first results thereof are mentioned.

7.6.1 Container design

New designs for containers are currently tested at ETH using smaller tube diameters (Strasky et al., 2004). Temperature control for step-wise heating procedures proofed to be efficient and nominal temperatures were achieved, allowing a better thermal conductivity within the quartz.

7.6.2 Optimal grain size

An optimal grain size would be the generally used grain size in surface exposure dating studies (~50μm<x<100μm) since a well documented degassing behaviour would be guaranteed (Niedermann, 2002). The use of synthetical quartz is preferable (Strasky et al., 2004).

7.6.3 The room-temperature step (diffusion of ^{3}He at low temperatures)

Elevated He-concentrations in the room-temperature step are measurable but were variable. This indicates on the one hand some diffusion of helium out of quartz already at low temperatures as suggested by e.g., Trull et al. (1991). On the other hand the variability of amounts of gas released allows no general rule to conclude. However, the sealed containers retain this component and therefore place no further problems.

7.7 Conclusions

As outlined above, there is a great potential in using quartz in artificial target experiments for scaling terrestrial cosmogenic production rates with latitude and altitude. However, a number of problems have been recognized in this pilot study. Target design and measurement procedures are refined at the moment and give promising results (Strasky et al., 2004).

Acknowledgements

The scientific, technical and financial support of and the stimulating discussions with R. Kipfer (EAWAG), I. Leya (University of Bern), O. Flückiger, (University of Bern), P. Oberholzer (ETH Zürich), Ch. Schlüchter (University of Bern), U. Menet (ETH Zürich) and S. Strasky (ETH Zürich) are acknowledged.

8 Conclusions and Outlook

Three major aspects of the fields of *quantitative geomorphology* and of *terrestrial cosmogenic nuclides* were studied in detailed in this thesis and can be subdivided in:

(i) regional aspects of landscape evolution in northern Chile,

(ii) the quantification of erosion rates in northern Chile using terrestrial cosmogenic nuclides and sediment yield data

(iii) studies of terrestrial cosmogenic nuclide systematics.

(i) Landscape evolution in northern Chile

The landscape evolution of the Andes of northern Chile from the late Miocene to recent was controlled by surface uplift and enhanced effective water discharge. These changes resulted in modification in landscape evolution from a stage of geomorphic decay to a phase of topographic growth and relief formation. Specifically, some time after 7.5Ma, a phase of base-level lowering, probably caused by surface uplift in the Coastal Cordillera, resulted in a phase of headward erosion. This is indicated by knickzones in the longitudinal stream profiles, separating older and younger graded stream segments. Therefore, the landscape is interpreted as being in a transient phase of topographic growth. Since precipitation for the same time interval is suggested to have been restricted to the higher parts of the Western Escarpment and the Western Cordillera, landscape evolution on broad plains in most other parts of the Western Escarpment and the Coastal Cordillera is not controlled by fluvial/erosional processes. These geomorphic units resemble erosional surfaces with relict drainage systems and steep hillslopes, predating the phase of incision. These denudating surfaces are decoupled from active erosion in today's major water-bearing channels and at adjacent hillslopes. Morphometric parameters imply low diffusivities. Only at the higher parts of the Western Escarpment and the Western Cordillera, upstream of the knickzones, can a coupling of processes on hillslopes and erosion in channels be observed. There morphometric parameters imply higher diffusivities. At the moment, it cannot be decided, whether the locations of the knickzones of major rivers are stationary or are shifting towards the headwaters. This is because the areas surrounding the knickzones represent (a) the lowermost regions that receive annual precipitation, (b) they are located near an abandoned fault-system (west-vergent thrust system, Munoz and Charrier, 1996) and (c) the bedrock lithologies vary -

it is possible that further headward migration is unlikely to occur. However, Zeilinger et al. (2005) concluded that incision enhanced localized buckling at the Western Escarpment in the form of the Oxaya Anticline.

On a long-term and an escarpment scale, the system is in a transient stage and still adapts to the modified situation, i.e., the base-level change sometime after 7.5Ma and the enhancement of the orographic effect on precipitation. However, certain smaller scale (hillslope) systems may be already in a topographic and erosional steady state, as suggested by more diffusive landscapes.

(ii) Quantifying erosion rates

Terrestrial cosmogenic nuclide concentrations indicate very low erosion rates at the lower to medium elevations of the Western Escarpment, with ≤100cm/My. These values hold for timescales back into the late Miocene. In turn, for the upper Western Escarpment elevations and the adjacent Western Cordillera, nuclide concentrations are in saturation and erosion rates steadily increase up to ≤3700cm/My. These values must have prevailed for at least the last ~10^5yrs. Morphometric parameters such as hillslope diffusivities also correlate well with increasing precipitation. Erosion rates, therefore, increase with altitude and with increasing precipitation. Such a correlation of orographically controlled precipitation and erosion rates is possible due to a relatively weak tectonic activity of the central Andes on the timescale relevant for TCN-studies. At locations such as the Himalaya or the Southern Alps of New Zealand, where tectonic activity and uplift rates are very high, correlation between precipitation and erosion rates might not be discernible. In contrast, in northern Chile the prevailing tectonic and climate regime allowed the preservation of Miocene formed surfaces, even in an active orogen.

In northern Chile we have determined erosion rates by the analysis of the multiple isotopes ^{10}Be, ^{26}Al and ^{21}Ne. This approach allowed the simultaneous determination of erosion rates and exposure ages and also to recognize complex exposure. On the other hand, this approach also allowed to test whether erosion rates vary with time since the different nuclides have variable half-lifes. Currently, on some of the samples, ^{14}C-measurements are performed and ^{36}Cl-analyses are planned. These two nuclides are much more sensitive to short-term climate variations. Combined analyses will thus help to compare erosion rates on short-term and long-term nuclides as discussed in this thesis. Extending the temporal scale in the other direction towards values above 10Ma by fission-track-analysis, is currently in progress (G. Zeilinger, University of Bern).

Erosion rates determined by terrestrial cosmogenic nuclides and by the limited sediment yield data are in a similar range only in those areas where active erosional processes are governed by the higher rainfall rates, i.e., the Western Cordillera. Nevertheless, such an agreement on widely different timescales is remarkable, especially given the fact, that the short-term sediment yield data are strongly influenced by extreme events. To bridge this gap between decadal and Ma timescales, we sampled river-born quartz sand in order to analyze catchment-wide erosion rates (with ^{10}Be and ^{21}Ne). With this method, erosion rates are averaged over spatial scales of the catchment and on time-scales of 10-100kys (Bierman and Nichols, 2004). However, that method requires that the study area is in erosional equilibrium, which has to be evaluated from place to place.

(iii) Terrestrial cosmogenic nuclide systematics

The feasibility of applying ^{3}He in Fe-Ti-oxide minerals and ^{10}Be and ^{21}Ne in sanidine as terrestrial cosmogenic nuclides has been shown here. Such additional mineral-isotope pairs will broaden the lithologies possible to use in TCN-studies at various geomorphic/geologic sites.

The effect of impurities in quartz on terrestrial cosmogenic nuclide production was quantified in order to make the technique more robust and to highlight eventual complications in sample preparation, nuclide measurements and data interpretation. Although minor amounts of impurities were detected in the analysed quartz samples from the ignimbrites of northern Chile, they have no effect on the data interpretation. However, it cannot a priori be assumed, that quartz from any genetic origin behaves similarly. Therefore, most likely each quartz from a specific lithological domain should be tested during the course of the purification of quartz for impurities.

In a final part of this thesis, it was shown, that artificial target experiments can contribute to constrain existing scaling models of terrestrial cosmogenic nuclides. Although the shortcomings of the pilot study did not allow a direct test of any scaling model, they enabled to improve the target design for future studies.

9 References

Abele, G., 1990, Salzkrusten, Salzbedingte Solifluktion und Steinsalzkarst in der nordchilenisch-peruanischen Wüste: Mainzer Geografische Studien, v. 34, p. 23-46.

—, 1991, The influence of age, climate, and relief on the preservation of volcanic landforms in the North Chilean Andes: Bamberger Geograph. Schriften, v. 11, p. 45-57.

Ackert, R.P., Singer, B., Guillou, H., Kaplan, M.R., and Kurz, M.D., 2003, Long-term cosmogenic ^{3}He production rates from ^{40}Ar/^{39}Ar and K–Ar dated Patagonian lava flows at 47°S: Earth and Planetary Science Letters, v. 210, p. 119-136.

Aeschbach-Hertig, W., 1994, Helium und Tritium als Tracer für physikalische Prozesse in Seen [PhD Nr. 10714 thesis]: Zürich, ETH.

Allen, P.A., 1997, Earth surface processes: Oxford, Blackwell Science, 404 p.

Allkofer, C.O., 1975, Introduction to cosmic radiation, Buchreihe der Atomphysik: München, p. 221.

Allmendinger, R.W., Gonzales, G., Yu, J.S., Isacks, B.L., and Hoke, G.D., 2003, Late Cenozoic tectonics of the Coastal Cordillera of N Chile and implications for paleoclimate and interplate processes, AGU Fall Meeting: San Francisco, EOS Transcations.

Alpers, C.N., and Brimhall, G.H., 1988, Middle Miocene climate change in the Atacama Desert, northern Chile: evidence from supergene mineralization at La Escocndida: GSA Bull., v. 100, p. 1640-1656.

Ammann, C., Jenny, B., Kammer, K., and Messerli, B., 2001, Late Quaternary Glacier response to humidity changes in the arid Andes of Chile (18-29°S): Paleogeography, Paleoclimatology, Paleoecology, v. 172, p. 313-326.

Anderson, R.S., 1994, Evolution of the Santa Cruz Mountains, California, Through tectonic growth and geomorphic decay: J. Geophys. Res., v. 99, p. 20161-20179.

Anderson, R.S., and Humphrey, N.F., 1989, Interaction of weathering and transport processes in the evolution of arid landscapes, *in* Cross, T.A., ed., Quantitative dynamic systems, Prentice Hall, p. 349-361.

Andrews, J.N., 1985, The isotopic composition of radiogenic helium and its use to study groundwater movement in confined aquifers: Chem. Geol., v. 49, p. 339-351.

Bagnold, R.A., 1966, An approach to the sediment transport problem from general physics: Prof. Pap. U.S. Geol. Surv., v. 422-I.

Bähr, R., Lippolt, H.J., and Wernicke, R.S., 1994, Temperature-induced ^{4}He degassing of specularite and botryoidal hematite: A ^{4}He retentivity study: J. Geophys. Res., v. 99, p. 17695.

Barker, C., and Torkelson, B.E., 1975, Gas adsorption on crushed quartz and basalt: Geochim. Cosmochim. Acta, v. 39, p. 212-218.

Baur, H., 1980, Numerische simulation und praktische Erprobung eines rotationssymetrischen Ionenquelle für Gasmassenspektrometer [PhD Nr. 6596 thesis]: Zürich, ETH.

—, 1999, A noble-gas mass spectrometer compressor source with two orders of magnitude improvement in sensitivity, *in* AGU, ed., AGU Fall meeting, Volume 80: San Francisco, EOS Transactions, p. supplement.

Beer, J., Shen, C., Heller, F., Liu, T., Bonani, G., Dietrich, B., Sutter, M., and Kubik, P.W., 1993, ^{10}Be and magnetic susceptibility in Chineses loess: Geophys. Res. Lett., v. 20, p. 57-60.

Beer, J., Siegenthaler, U., Bonani, G., Finkel, R.C., Oeschger, H., Suter, M., and Woelfli, W., 1988, Information on past solar activity and geomagmetism from 10Be in the Camp Century ice core: Nature, v. 331, p. 675-679.

Betancourt, J.L., Latorre, C., Rech, J.A., Quade, J., and Rylander, K.A., 2000, A 22,000-year record of monsoonl precipation from northern Chile's Atacama Desert: Science, v. 289, p. 1542-1546.

Bierman, P., and Caffee, M., 2001, Slow rates of rock surface erosion and sediment production across the Namib Desert and Escarpment, Southern Africa: Am. J. Sci, v. 301, p. 326-358.

—, 2002, Cosmogenic exposure and erosion history of Australian bedrock landforms: GSA Bull., v. 114, p. 787-803.

Bierman, P., and Nichols, K.K., 2004, Rock to sediment - slope to sea with ^{10}Be-rates of landscape change: Annu. Rev. Earth Planet. Sci., v. 32, p. 215-255.

Bierman, P., and Steig, E.J., 1996, Estimating rates of denudation using cosmogenic isotope abundances in sediment: Earth Surface Processes, v. 21, p. 125-139.

Bierman, P.R., 1994, Using in-situ cosmogenic isotopes to estimate rates of landscape evolution: A review from the geomorphologic perspective: Jour. Geophys. Res., v. 48, p. 386-389.

Bierman, P.R., Caffee, M.W., Davis, P.T., Marsella, K., Pavich, M., Colgan, P., Mickelson, D., and Larsen, J., 2002, Rates and timing of earth surface processes from in-situ produced cosmogenic ^{10}Be, *in* Grew, E.,

ed., Beryllium: Mineralogy, Petrology, and Geochemistry, Volume 50, Reviews in Mineralogy and Geochemistry, p. 147-204.

Bierman, P.R., Marsella, K.A., Patterson, C., Davis, P.T., and Caffee, M., 1999, Mid-Pleistocene cosmogenic minimum-age limits for pre-Wisconsian glacial surfaces in southwestern Minnesota and southern Baffin island: a multiple nuclide approach: Geomorphology, v. 27, p. 25-39.

Blard, P.-H., Bourles, D., Braucher, R., Raphael, P., and Jerome, L., 2004, A new determination method for measurement of in situ produced cosmogenic 10-Be in clinopyroxenes, 32IGC: Florence, Italy.

Blum, A.E., and Stillings, L.L., 1995, Feldspar dissolution kinetics, *in* White, A.F., and Brantley, S.L., eds., Chemical Weathering Rates in Silicate Minerals. Reviews in Mineralogy, Volume 31, Min. Soc. America, p. 291-346.

Boezio, M., Carlson, P., Francke, T., Weber, N., Suffert, M., Hof, M., Menn, W., Simon, M., Stephens, S.A., Bellotti, R., Cafagna, F., Circella, M., De Marzo, C., Finetti, N., Papini, P., Piccardi, S., Spillantini, P., Ricci, M., Casolino, M., De Pascale, M.P., Morselli, A., Picozza, P., Sparvoli, R., Barbiellini, G., Schiavon, P., Vacchi, A., Zampa, N., Grimani, C., Mitchell, J.W., Ormes, J.F., Streitmatter, R.E., Bravar, U., Golden, R.L., and Stochaj, S.J., 2000, Measurement of the flux of atmospheric muons with the CAPRICE94 apparatus: Physical Review D, v. 62, p. art. no.-032007.

Bogard, D.D., and Cressy, P.J., 1973, Spallation production of ^{3}He, ^{21}Ne and ^{38}Ar from target elements in the Bruderheim chondrite: Geochim. Cosmochim. Acta, v. 37, p. 527-546.

Braucher, R., Benedetti, L., and Bourles, D., 2004, In situ production rate of 10-Be in carbonates, 32IGC: Florence, Italy.

Brook, E.J., and Kurz, M.D., 1993, Surface-exposure chronology using in-situ cosmogenic 3He in Antarctic quartz sandstone boulders: Quat. Res., v. 39, p. 1-10.

Brook, E.J., Kurz, M.D., Ackert, R.P., Denton, G.J., Brown, E.T., Raisbeck, G.M., and Yiou, F., 1993, Chronology of Taylor Glacier advances in Arena Valley Antarctica, using in-situ cosmogenic 3He and 10Be: Quat. Res., v. 39.

Brown, E.T., Bourles, D.L., Burchfiel, B.C., Qidong, D., Jun, L., Molnae, P., Raisbeck, G.M., and Yiou, F., 1998, Estimation of slip rates in the southern Tien Shan using cosmic ray exposure dates of abandoned alluvial fans: GSA Bull., v. 110, p. 377-386.

Brown, E.T., Bourles, D.L., Colin, F., Raisbeck, G.M., Yiou, F., and Desgarceaux, S., 1995a, Evidence for muon-induced production of 10Be in near-surface rocks from the Congo: Geoph. Res. Lett., v. 22, p. 703-706.

Brown, E.T., Edmond, J.M., Raisbeck, G., Yiou, F., Kurz, M.D., and Brook, E.J., 1991a, Examination of surface exposure ages of Antarctic moraines using ^{10}Be and ^{26}Al: Geochim. Cosmochim. Acta, v. 55, p. 2269-2283.

Brown, E.T., Edmond, J.M., Raisbeck, G.M., Yiou, F., Kurz, M.D., and Brook, E.J., 1991b, Examination of surface expsoure ages in Antarctic moraines using in-situ produced 10Be and 26Al: Geochim. Cosmochim. Acta, v. 55, p. 2269-2283.

Brown, E.T., Stallard, R.F., Larsen, M.C., Bourles, D.L., Raisbeck, G., and Yiou, F., 1995b, Denudation rates determined from the accumulation of in-situ produced ^{10}Be in the Luquillo Fortes, Puerto Rico: Earth and Planetary Science Letters, v. 129, p. 695-702.

Brown, E.T., Trull, T.W., Jean-Baptiste, P., Raisbeck, G., Bourles, D.L., Yiou, F., and Marty, B., 2000, Determintation of cosmogenic production rates of ^{10}Be, ^{3}He and ^{3}H in water: Nucl. Instr. Meth. in Phys. Res., v. B172, p. 873-883.

Bruno, L.A., 1995, Datierung von Moränen und glazial überprägten Oberflächen in der Antarktis mit in situ produzierten kosmogenen Edelgasen [PhD Diss. No. 11256 thesis]: Zürich, ETH Zürich.

Bruno, L.A., Baur, H., Graf, T., Schlüchter, C., Signer, P., and Wieler, R., 1997, Dating of Sirius Group tillites in the Antarctic Dry Valleys with cosmogenic ^{3}He and ^{21}Ne: Earth Planet. Sci. Lett., v. 147, p. 37-54.

Bryce, J.G., and Farley, K.A., 2002, ^{3}He exposure dating of magnetite, *in* Podosek, F.A., ed., Goldschmidt Conference, Volume 66(15A): Davos, Switzerland, Geochim. Cosmochim. Acta, p. A108.

Bull, W.B., 1991, Geomorphic responses to climate change: New York, Oxford University Press, 326 p.

Burbank, D.W., 2002, Rates of erosion and their implications for exhumation: Mineralogical Magazine, v. 66, p. 25-52.

Burbank, D.W., and Anderson, R.S., 2001, Tectonic Geomorphology, Blackwell Science, 274 p.

Burbank, D.W., Blythe, A.E., Putkonen, J., Pratt-Sitaula, B., Gabet, E., Oskin, M., Barros, A., and Ojha, T.P., 2003, Decoupling of erosion and precipitation in the Himalayas: Nature, v. 426, p. 652-655.

Burbank, D.W., Leland, J., Fielding, E., Anderson, R.S., Brozovic, N., Reid, M.R., and Duncan, C., 1996, Bedrock incision, rock uplift and threshold hillslopes in the northwestern Himalayas: Nature, v. 379, p. 505-510.

Carignano, C.A., 1999, Late Pleistocene to recent climate change in Córdoba Province, Argentina: Geomorphological evidence: Quaternary International, p. 117-134.

Carson, M.A., and Kirkby, M.J., 1972, Dating Hillslope forms and processes, Cambridge Univ. Press, 475 p.
Cerling, T.E., 1990, Dating geomorphologic surfaces using cosmogenic ^{3}He: Quat. Res., v. 33, p. 148-156.
Cerling, T.E., and Craig, H., 1994, Geomorphology and in-situ cosmogenic isotopes: Annu. Rev. Earth Planet. Sci., v. 22, p. 273-317.
Cerling, T.E., Poreda, R.J., and Rathburn, S.L., 1994, Cosmogenic 3He and 21Ne age of the Big Lost River flood, Snake River plain, Idaho: Geology, v. 22, p. 227-230.
Chase, C.G., 1992, Fluvial landsculpting and the fractal dimension of topography: Geomorphology, v. 43, p. 55-76.
Child, D., Elliot, G., Mifsud, C., Smith, A.M., and Fink, D., 2000, Sample processing for earth science studies at ANTARES: Nucl. Instr. Meth. in Phys. Res. B, v. 172, p. 856-860.
Clapperton, C.M., 1983, The glaciation of the Andes: Quat. Sci. Rev., v. 2, p. 83-155.
—, 1993, Qurternary Geology and geomorphology of South America: Amsterdam, Elsevier, 779 p.
Cockburn, H.A.P., Seidl, M.A., and Summerfield, M.A., 1999, Quantifying denudation rates on inselbergs in the central Namib Desert using in situ produced cosmogenic 10Be and 26Al: Geology, v. 27, p. 399-402.
Cockburn, H.A.P., and Summerfield, M.A., 2004, Geomorphological applications of cosmogenic isotope analysis: Progress in Physical Geography, v. 28, p. 1-42.
Craig, H., and Poreda, R.J., 1986, Cosmogenic ^{3} He in Terrestrial Rocks: The Summit Lavas of Maui: Proceedings of the National Academy of Sciences of the United States of America, v. 83, p. 1970-1974.
Dadson, S.J., Hovius, N., Chen, H., Dade, W.B., Hsieh, M.-L., Willet, S.D., Hu, J.-C., Horng, M.-J., Chen, M.-C., Stark, C.P., Lague, D., and Lin, J.-C., 2003, Links between erosion, runoff variability and seismicity in the Taiwan orogen: Nature, v. 426, p. 648-651.
Dennen, W.H., 1964, Impurities in quartz: GSA Bull., v. 75, p. 241-246.
—, 1967, Trace elements in quartz as indicators for provenance: GSA Bull., v. 78, p. 125-130.
Desilets, D., and Zreda, M., 2001, On scaling cosmogenic nuclide production rates for altitude and latitude using cosmogenic-ray measurements: Earth Planet. Sci. Lett., v. 193, p. 213-225.
Desilets, D.Z., M., 2003, Spatial and temporal distribution of secondary cosmic-ray nucleon intensities and application to in situ cosmogenic data: Earth Planet. Sci. Lett., v. 206, p. 21-42.
Dickinson, W.T., and Wall, G.J., 1977, The relationship between source-area erosion and sediment yield: Hydrological Sciences Bulletin, v. XXII, p. 527-530.
D'Lemos, R.S., Kearsley, A.T., Pembroke, J.W., Watt, G.R., and Wright, P., 1997, Complex quartz growth histories in granite revealed by scanning cathodoluminescence techniques: Geol. Mag., v. 134, p. 549-552.
Dunai, T.J., 2000, Scaling factors for production rates of in situ produced cosmogenic nuclides: a critical re-evaluation: Earth Planet. Sci. Lett., v. 176, p. 157-169.
—, 2001, Influence of secular variation of the geomagnetic field on production rates of in siyu produced cosmogenic nuclides: Earth Planet. Sci. Lett., v. 193, p. 197-212.
Dunai, T.J., Gonzales Lopez, G.A., and Juez-Larre, J., 2005, Oligocene–Miocene age of aridity in the Atacama Desert revealed by exposure dating of erosion-sensitive landforms: Geology, v. 33, p. 321-324.
Eberhardt, P., Eugster, O., and Marti, K., 1965, A redetermination of the isotopic composition of atmospheric neon: Zeitschrift f. Naturforschung, v. 20a, p. 623-624.
Fanale, F.P., and Kulp, J.L., 1962, The helium method and the age of the Cornwall, Pennsylania magnetite ore: Econ. Geol., v. 57, p. 735-746.
Fink, D., Klein, J., and Middleton, R., 1990, 41Ca: past, present and future: Nucl. Instr. Meth. in Phys. Res., v. B52, p. 572-582.
Finkel, R., C., and Suter, M., 1993, AMS in the Earth Sciences: Advances in Analytical Geochemistry, v. 1, p. 1-114.
Flem, B., Larsen, R.B., Grimstvedt, A., and Mansfeld, J., 2002, In situ analysis of trace elements in quartz by using laser ablation inductively coupled plasma mass spectrometry: Chem. Geol., v. 182, p. 237-247.
Frost, B.R., 1991, Stability of oxide minerals in metamorphic rocks, *in* Lindsley, D.H., ed., Oxide minerals: petrologic and magnetic significance, Volume 25, Mineralogical Society of America, p. 469-488.
Frost, B.R., and Lindsley, D.H., 1991, Occurence of iron-titanium oxides in igneous rocks, *in* Lindsley, D.H., ed., Oxide minerals: petrologic and magnetic significance, Volume 25, Mineralogical Society of America, p. 433-468.
García, M., 2002, Evolution Oligo-Miocène de l'Altiplano occidental (arc et avant-arc du nord du Chili, Arica): Tectonique, volcansime, sédimentation, géomorphologie et bilan érosion-sédimentation, Géologie Alpine, Mémoire H.S., Volume 40.
Garcia, M., and Herail, G., 2005, Fault-related folding, drainage network evolution and valley incision during the Neogene in the Andean Precordillera of Northern Chile: Geomorphology, v. 65, p. 279-300.
Garcia, M., Herail, G., Charrier, R., Mascle, G., Fornari, M., and Perez de Arce, C., 2002, Olidocene-Neogene evolution of the Altiplano of Northern Chile (18-19 S), 5th ISAG: Toulouse, p. 359-362.

Gayer, E., Pik, R., Lave, J., France-Lanord, C., Bourles, D.L., and Marty, B., 2004, Cosmogenic ^{3}He in Himalayan garnets indicating an altitude dependence of the ^{3}He/^{10}Be production ratio: Earth and Planetary Science Letters, v. 229, p. 91-104.

Gosse, J.C., and Phillips, F.M., 2001, Terrestrial in situ cosmogenic nuclides: theory and application: Quat. Sci. Rev., v. 20, p. 1475-1560.

Götze, J., and Lewis, R., 1994, Distribution of REE and trace elements in size and mineral fractions of high-purity quartz sands: Chem. Geol., v. 114, p. 43.

Götze, J., Plötze, M., Graupner, T., Hallbauer, D.K., and Bray, C.J., 2004, Trace element incorporation into quartz: A combined study of ICP-MS, electron spin resonance, cathodoluminescence, capillary ion analysis, and gas chromatography: Geochim. Cosmochim. Acta, v. 68, p. 3741-3759.

Graf, T., Kohl, C.P., Marti, K., and Nishiizumi, K., 1991, Cosmic ray produced neon in Antarctic rocks: Geophys. Res. Lett., v. 18, p. 203-206.

Graf, T., Marti, K., and Wiens, R.C., 1996, The ^{21}Ne production rate in a Si target at mountain altitudes: Radiocarbon, v. 38, p. 155-156.

Graham, I.J., Barry, B.J., Ditchburn, R.G., and Whitehead, N.E., 2000, Validation of cosmogenic nuclide production rate scaling factors through direct measurement: Nucl. Instr. Meth. in Phys. Res., v. B 172, p. 802-805.

Graham, R.F., Elmore, D., Sharma, P., Vogt, S., and Harwood, D.M., 1995, Development of plagioclase as a target for in-situ Be-10 studies, National Meeting of the American Chemical Society, Volume 209, 13-Nucl Part 2: Anaheim, American Chemical Society.

Granger, D.E., and Muzikar, P.F., 2001, Dating sediment burial with in situ-produced cosmogenic nuclides: theory, techniques, and limitations: Earth Planet. Sci. Lett., v. 188, p. 269-281.

Gregory-Wodzicki, K.M., 2000, Uplift history of the Central and Northern Andes: A review: GSA Bull., v. 112, p. 1091-1105.

Grosjean, M., Cartajena, I.M., Geyh, M.A., and Nuñez, L., 2003, From proxy data to paleoclimate interpretation: the mid-Holocene paradox of the Atacama Desert, northern Chile: Palaeogeography, Palaeoclimatology, Palaeoecology, v. 194, p. 247-258.

Hancock, G.S., and Willgoose, G., 2002, The use of a landscape simulator in the validation of the SIBERIA landscape evolution model: transient landforms: Earth Surf. Proc. Landf., v. 27, p. 1321-1334.

Hartley, A.J., 2003, Andean uplift and climate change: Jour. Geol. Soc. Lond., v. 160, p. 7-10.

Hartley, A.J., and Chong, G., 2002, Late Pliocene age for the Atacama Desert: Implications for the desertification of western South America: Geology, v. 30, p. 43-46.

Harvey, A.M., 2001, Coupling between hillslopes and channels in upland fluvial systems: implications for landscape sensitivity, illustrated from the Howgill Fells, northwest England: Catena, v. 42, p. 225-250.

Heimsath, A.M., Dietrich, W.E., Nishiizumi, K., and Finkel, R., C., 1997, The soil production rate function and landscape equilibrium: Nature, v. 388, p. 358-361.

Heimsath, A.M., Dietrich, W.E., Nishiizumi, K., and Finkel, R.C., 1999, Cosmogenic nuclides, topography, and the spatial variation of soil depth: Geomorphology, v. 27, p. 151-172.

Heisinger, B., Lal, D., Jull, A.J., Ivy-Ochs, S., Neumaier, S., Knie, K., Lazarev, V., and Nolte, E., 2002a, Production of selected cosmogenic radionuclides by muons: 1. Fast Muons: Earth and Planetary Science Letters, v. 200, p. 345-355.

Heisinger, B., Lal, D., Jull, A.J., Kubik, P.W., Ivy-Ochs, S., Knie, K., and Nolte, E., 2002b, Production of selected cosmogenic radionuclides by muons: 1. Capture of negative muons: Earth and Planetary Science Letters, v. 200, p. 357-369.

Henning, W., Bell, W.A., Billquist, P.J., Glagola, B.G., Kutschera, W., Liu, Z., Lucas, H.F., Paul, M., Rehm, K.E., and Yntema, J.L., 1987, Calcium-41 Concentration in Terrestrial Materials: Prospects for Dating of Pleistocene Samples: Science, v. 236, p. 725-727.

Herm, D., 1969, Marines Pliozän und Pleistozän in Nord- und Mittelchile unter besonderer Berücksichtigung der Entwicklung der Mollusken-Faunen: Zitteliana, v. 2, p. 159.

Hetzel, R., Niedermann, S., Ivy-Ochs, S., Kubik, P.W., Tao, M., and B., G., 2002, ^{21}Ne verus ^{10}Be and ^{26}Al exposure ages of fluvial terraces: the influence of crustal Ne in quartz: Earth Planet. Sci. Lett., v. 201, p. 575-591.

Hinderer, M., Schäuble, H., and Süss, M.S., 2002, Denudation processes at various scales - towards a new GIS-based global mode: Zentralblatt für Geologie und Paläontologie,, v. 3/4, p. 377-397.

Hintenberger, H., Schultz, L., Wänke, H., and Weber, H., 1967, Helium- und Neonisotope in Eisenmeteoriten und der Tritiumverlust in Hexaedriten: Zeitschrift f. Naturforschung, v. 22, p. 780-787.

Hintenberger, H., and Wänke, H., 1964, Helium - und Neonisotope in Eisenmeteoriten: Zeitschrift f. Naturforschung, v. 19, p. 210-218.

Hoffman, P.F., and Grotzinger, J.P., 1993, Orographic precipitation, erosional unloading, and tectonic style: Geology, v. 21, p. 195-198.

Hoffmann, J.A.J., 1975, Atlas climatico de America del Sur: Budapest, Paris, UNESCO.

Hoke, G.D., Jordan, T.E., and Isacks, B.L., 2003, A groundwater genesis for the giant quebradas of the Atacama Desert, Northern Chile, 5th ISAG: Toulouse, p. 307-310.

Hoke, G.D., Isacks, B.L., Jordan, T.E., and Yu, J.S., 2004, Groundwater-sapping origin for the giant quebradas of northern Chile: Geology, v. 32, p. 605-608.

Houston, J., and Hartley, A.J., 2003, The central Andean west-slope rainshadow and its potential contribution to the origin of hyper-aridity in the Atacama Desert: International Journal of Climatology, v. 23, p. 1453-1464.

Isacks, B.L., 1988, Uplift of the Central Andean Plateau and bending of the Bolivian Orocline: Jour. Geophys. Res., v. 93, p. 3211-3231.

Ivy-Ochs, S., 1996, The dating of rock surface using in situ produced ^{10}Be, ^{26}Al and ^{36}Cl, with examples from Antarctica and the Swiss Alps [PhD,11763 thesis]: Zürich, ETH-Zürich.

Ivy-Ochs, S., Kubik, P.W., Masarik, J., Wieler, R., Bruno, L., and Schlüchter, C., 1998, Preliminary results on the use of pyroxene for ^{10}Be surface exposure dating: Schweiz. Mineral. Petrogr. Mitt., v. 78, p. 375-382.

Ivy-Ochs, S., Schäfer, J.M., Kubik, P.W., Synal, H.-A., and Schlüchter, C., 2004, Timing of deglaciation of the northern Alpine Foreland (Switzerland): Eclogae Geol. Helv., v. 97, p. 47-55.

Ivy-Ochs, S., Schlüchter, C., Kubik, P.W., Dittrich-Hannen, B., and Beer, J., 1995, Minimum ^{10}Be exposure ages of early Pliocene for the Table Moutain plateau and the Sirius Group at Mount Fleming, Dry Valley, Antarctica: Geology, v. 23, p. 1007-1010.

Ivy-Ochs, S., Schlüchter, C., Kubik, P.W., Synal, H.-A., Beer, J., and Kerschner, H., 1996, The exposure age of an Egesen moraine at Julier Pass, Switzerland, measured with the cosmogenic radionuclides ^{10}Be, ^{26}Al and ^{36}Cl: Eclogae Geol. Helv., v. 89, p. 1049-1063.

Jordan, T.E., and Allmendinger, R.W., 1986, Slope The Sierras Pampeanas of Argentina: A modern analogue of the Rocky Mountain Foreland deformation: Am. Jour. Sci., v. 286, p. 737-764.

Kaplan, M.R., Ackert, R.P., Singer, B., Douglass, D.C., and Kurz, M.D., 2003, Indistinguishable O-isotope stage 2 ice ages in mid-latitude South America and the Northern Hemisphere: GSA Bull., v. 116, p. 308-321.

Kennan, L., 2000, Large-scale geomorphology of the Andes: interrelationships of tectonics, magmatism and climate, *in* Summerfield, M.A., ed., Geomorphology and Global Tectonics: Chichester, Wiley, p. 167-199.

Kirchner, J.W., Finkel, R.C., Riebe, C.S., Granger, D.E., Clayton, J.L., King, J.G., and Megahan, W.F., 2001, Mountain erosion over 10 yr, 10k.y. and 10 m.y. time scales: Geology, v. 29, p. 591-594.

Kirschbaum, A.M., Martinez, E., Pettinari, G., and Herrero, S., 2004, Weathering Profiles in Granites. Sierra Norte (Córdoba, Argentina): Journal of South American Earth Sciences.

Klein, J., Giegengack, R., Middleton, R., Sharma, P., Underwood, J., and Weeks, R.A., 1986, Revealing histories of exposure using in situ produced ^{26}Al and ^{10}Be in Lybian Desert Glass: Radiocarbon, v. 28, p. 547-555.

Knie, K., Schäfer, J.M., Arazi, A., Faestermann, T., Herzog, G.F., Korschinek, G., Ma, P., Rugel, G., Wallner, A., and Wieler, R., 2002, Surface Exposure Dating with 53Mn: First Experimental Results: Munich, Maier-Leibnitz-Laboratorium, University of Munich.

Knight, K.B., Renne, P.R., and Farley, K.A., 2003, Preliminary estimate of production rates for terrestrial cosmogenic ^{38}Ar from calcium, AGU Fall Meeting: San Francisco, EOS Trans., p. 84(46).

Kober, F., Ivy-Ochs, S., Leya, I., Wieler, R., Baur, H., and Magna, T., in press-a, In situ cosmogenic ^{10}Be and ^{21}Ne in sanidine and in situ cosmogenic ^{3}He in Fe-Ti-oxide minerals: Earth and Planetary Science Letters.

Kober, F., Schlunegger, F., Ivy-Ochs, S., Baur, H., Wieler, R., Kubik, P.W., and Schneider, H., 2003, Cosmogenic nuclide studies and geomorphological implications in the hyperarid central Western Andes, Northern Chile, AGU Fall Meeting 2003: San Francisco, AGU, EOS Transactions.

Kober, F., Schlunegger, F., Zeilinger, G., and Schneider, H., in press-b, Surface uplift and climate change: The geomorphic evolution of at the Western Escarpment of the Andes of northern Chile between the Miocene and present, *in* Willet, S., Hovius, N., Fisher, D., and Brandon, M., eds., Tectonics, Climate and Landscape evolution, GSA - Penrose Special Paper.

Kohl, C.P., and Nishiizumi, K., 1992, Chemical isolation of quartz for measurement of in-situ-produced cosmogenic nuclides: Geochim. Cosmochim. Acta, v. 56, p. 3583-3587.

Koons, P.O., 1989, The topographic evolution of collisional mountain belts: A numerical look on the Southern Alps, New Zealand: Am. J. Sci, v. 289, p. 1041-1069.

Krissek, L.A., Scheidegger, K.F., and Kulm, L.D., 1980, Surface sediments of the Peru-Chile continental margin and the Nazca plate: GSA Bull., v. 91, p. 321-331.

Kubik, P.W., and Ivy-Ochs, S., 2004, A re-evaluation of the 0-10ky ^{10}Be production rate for exposure dating obtained from the Köfels (Austria) landslide: Nucl. Instr. Meth. in Phys. Res., v. B223-224, p. 618-622.

Kubik, P.W., Ivy-Ochs, S., Masarik, J., Frank., M., and Schlüchter, C., 1998, ^{10}Be and ^{26}Al production rates deduced from an instantaneous event within the dendro-calibration curve, the landslide of Köfels, Ötz Valley, Austria: Earth Planet. Sci. Lett., v. 161, p. 231-241.

Kurz, M.D., 1986a, Cosmogenic helium in a terrestrial rock: Nature, v. 320, p. 435-439.

—, 1986b, In-situ production of terrestrial cosmogenic helium and some applications to geochronology: Geochim. Cosmochim. Acta, v. 50, p. 2855-2862.

Kurz, M.D., and Brook, E.J., 1994, Surface exposure dating with cosmogenic radionuclides, *in* Beck, S., ed., Dating in exposed and surface contexts: University of New Mexico Press, p. 139-159.

Lal, D., 1987, Production of ^{3}He in terrestrial rocks: Chem. Geol., v. 66, p. 89-98.

—, 1991, Cosmic ray labelling of erosion surfaces: in-situ nuclide production rates and erosion models: Earth Planet. Sci. Lett., v. 104, p. 424-439.

Lal, D., Arnold, J.R., and Honda, M., 1960, Cosmic ray production rates of ^{7}Be in oxygen, and ^{32}P, ^{33}P, ^{35}S in argon at mountain altitudes: Physical Review, v. 118, p. 1626-1632.

Lamb, S., and Davis, P., 2003, Cenozoic climate change as possible cause of the rise of the Andes: Nature, v. 425, p. 792-797.

Landtwing, M.R., and Pettke, T., 2005, Relationships between SEM-cathodoluminescence response and trace element composition of hydrothermal vein quartz: American Mineralogist, v. 90, p. 122-131.

Laronne, J.B., Lekach, J., Cohen, H., and Gray, J., 2002, Experimental drainage basins in Israel, AGU Fall Meeting 2002: San Francisco, EOS.

Laughlin, A.W., Poths, J., Healey, H.A., Reneau, S.L., and WoldeGabriel, D., 1994, Dating of Quaternary basalts using the cosmogenic ^{3}He and ^{14}C methods with implications for excess ^{40}Ar: Geology, v. 22, p. 135-138.

Leya, I., Begemann, F., Weber, H.W., Wieler, R., and Michel, R., 2004, Simulation of the interaction of galatic cosmic ray protons with meteoroids - On the production of ^{3}H and light noble gas isotopes in isotropically irradiated thick gabbro and iron tragets: Meteoritics & Planetary Science, v. 39, p. 367-386.

Leya, I., Lange, H.-J., Neumann, S., Wieler, R., and Michel, R., 2000, The production of cosmogenic nuclides in stony meteoroids by galatic cosmic ray particles: Meteoritics & Planetary Science, v. 35, p. 259-287.

Liccardi, J.M., Clark, P., Brook, E.J., Pierce, K.L., and Kurz, M.D., 2001, Cosmogenic ^{3}He and ^{10}Be chronologies of the late Pinedale northern Yellowstone ice cap, Montana, US: Geology, v. 29, p. 1095-1098.

Liccardi, J.M., and Kurz, M.D., 2002, Calibration of cosmogenic ^{3}He production rates from postglacial lava flows in Iceland: Geochim. Cosmochim. Acta, v. 66, p. A456.

Liccardi, J.M., Kurz, M.D., Clark, P.U., and Brook, E.J., 1999, Calibration of cosmogenic ^{3}He production rates from Holocene lava flows in Oregon, USA, and effects of the Earth' magnetic field: Earth Planet. Sci. Lett., v. 172, p. 261-271.

Lifton, N.A., Jull, A.J., and Quade, J., 2001, A new extraction technique and production rate estimate for in situ cosmogenic 14C in quartz: Geochim. Cosmochim. Acta, v. 65, p. 1935-1969.

Mamani, M., Wörner, G., Ruprecht, P., Hartmann, G., and Simon, K., 2004, Sources of Central Andean Magmatism in time and space: implications from geochemical data from Quaternary to Miocene volcanism in S. Peru and N Chile., IAVCEI: Pucon Chile.

Margerison, H.R., Phillips, W.M., Stuart, F.M., and Sudgen, G.E., 2004, Cosmogenic ^{3}He concentrations in ancient f lood deposits from the Coombs Hills, northern Dry Valleys, East Antarctica: interpreting exposure ages and erosion rates: Earth and Planetary Science Letters.

Masarik, J., 2002, Numerical simulation of in-situ production of cosmogenic nuclides: Geochimica Cosmochimica Acta, v. 66, p. A491.

Masarik, J., and Beer, J., 1999, Simulation of particle fluxes and cosmogenic nuclide production in the Earth's atmosphere: J. Geophys. Res., v. 104, p. 12099-12111.

Masarik, J., Frank, M., Schaefer, J.M., and Wieler, R., 2001, Correction of in-situ cosmogenic nuclide production rates for geomagnetic field intensity variations during the past 800,000 years: Geochim. Cosmochim. Acta, v. 65, p. 2995-3003.

Masek, J.G., Isacks, B.L., Gubbels, T.L., and Fielding , E.J., 1994, Erosion and tectonics at the margin of continental plateaus: Jour. Geophys. Res., v. 99, p. 13941-13956.

McKean, J.A., Dietrich, W.E., Finkel, R., C., Southon, J.R., and Caffee, M.W., 1993, Quantification of soil production and downslope creep rates from cosmogenic 10Be accumulations on a hillslope profile: Geology, v. 21, p. 343-346.

Meybeck, M., 1987, Global chemical weathering rates of superficial rocks estimated from river dissloved loads: Amer. Jour. of Science, v. 287, p. 401-428.

Michel, R., Gloris, M., Neumann, S., and Leya, I., 1998, Neutron cross sections for physical model calculations of cosmogenic nuclide production rates: Meteoritics & Planetary Science, v. 33, p. A108.

Milliman, J.D., and Meade, R., 1983, World-wide delivery of river sediment to the oceans: Jour. Geol. Soc. Lond., v. 91, p. 1-21.

Molnar, P., 2001, Climate change, flooding in arid environments, and erosion rates: Geology, v. 29, p. 1071-1074.

—, 2003, Nature, nurture and landscape: Nature, v. 426, p. 612-614.

Molnar, P., and England, P., 1990, Late Cenozoic uplift of mountain ranges and global climate change: chicken or eggs: Nature, v. 346, p. 29-34.

Monaghan, M.C., McKean, J.A., Dietrich, W.E., and Klein, J., 1992, ^{10}Be chronometry of bedrock-to-soil conversion rates: Earth Planet. Sci. Lett., v. 111, p. 483-492.

Monecke, T., Kempe, U., and Götze, 2002, Genetic significance of the trace elements content in metamorphic and hydrothermal quartz: a reconnaissance study: Earth and Planetary Science Letters, v. 202, p. 709-724.

Montgomery, D.R., 2001, Slope distributions, threshold hillslopes, and steady-state topography: Am. Jour. Sci., v. 301, p. 432-454.

Montgomery, D.R., Balco, G., and Willett, S.D., 2001, Climate, tectonics, and the morphology of the Andes: Geology, v. 29, p. 579-582.

Montgomery, D.R., and Dietrich, W.E., 1992, Channel initiation and the problem of landscape scale: Science, v. 255, p. 826-830.

Montgomery, D.R., Massong, T.W., and Hawley, S.C.S., 2003, Influence of debris flows and log jams on the location of pools and alluvial channel reaches, Oregon Coast Range: GSA Bull., v. 115, p. 78-88.

Morris, J.D., Gosse, J.C., Brachfield, S., and Tera, F., 2002, Cosmogenic Be-10 and the Solid Earth: Studies in Geomagnetism, subduction zone processes, and active tectonics, *in* Grew, E., ed., Beryllium: Mineralogy, Petrology, and Geochemistry, Volume 50, Reviews in Mineralogy and Geochemistry, p. 207-270.

Mortimer, C., 1973, Cenozoic history of the southern Atacama desert, Chile: Jour. Geol. Soc. Lond., v. 129, p. 505-526.

—, 1980, Drainage evolution in the Atacama Desert of northernmost Chile: Rev. Geol. Chile, v. 11, p. 3-28.

Mortimer, C., Farrar, E., and Saric, N., 1974, K-Ar ages from Tertiary lavas of the northernmost Chilean Andes: Geol. Rund., v. 63, p. 484-490.

Mortimer, C., and Saric, N., 1975, Cenozoic studies in northernmost Chile: Geol. Rund., v. 64, p. 395-420.

Müller, A., 2000, Application of cathodoluminescence to magmatic quartz in a tin granite - case study from the Schellerhau Granite Complex, Eastern Erzgebirge, Germany: Mineralium Deposita, v. 35, p. 169-189.

Müller, A., Wiedenbeck, M., Van-Den-Kerkhof, A.M., Kronz, A., and Simon, K., 2003, Trace elements in quartz - A combined electron microprobe, secondary ion mass spectrometry, laser-ablation ICP-MS, and cathodoluminescene study: Eur. J. Mineral., v. 15, p. 747-763.

Munoz, N., and Charrier, R., 1996, Uplift of the western border of the Altiplano on a west-vergent thrust system, Northern Chile: Jour. of South American Earth Sciences, v. 9, p. 171-181.

Muzikar, P., Elmore, D., and Granger, D.E., 2003, Accelerator mass spectrometry in geologic research: Geological Society of America Bulletin, v. 115, p. 643-654.

Nesbitt, H.W., Fedo, C.M., and Young, G.M., 1997, Quartz and Feldspar Stability, Steady and Non-steady-State Weathering, and Petrogenesis of Siliciclastic Sands and Muds: Journal of Geology, v. 105, p. 173-191.

New, M., Lister, D., Hulme, M., and Makin, I., 2002, A high-resolution data set of surface climate over global land areas: Climate Research, v. 21, p. 1-25.

Niedermann, S., 2000, The ^{21}Ne production rate in quartz revisited: Earth Planet. Sci. Lett., v. 183, p. 361-364.

—, 2002, Cosmic-ray-produced noble gases in terrestrial rocks: Dating tools for surface processes, *in* Porcelli, D., Ballentine, C.J., and Wieler, R., eds., Noble Gases in Geochemistry and Cosmochemistry: Rev. Mineral. Geochem. 47, p. 731-784.

Niedermann, S., Graf, T., Kim, J.S., Kohl, K., and Nishiizumi, K., 1994, Cosmic-ray-produced ^{21}Ne in terrestrial quartz: the neon inventory of Sierra Nevada quartz separates: Earth Planet. Sci. Lett., v. 125, p. 341-355.

Niedermann, S., Graf, T., and Marti, K., 1993, Mass spectrometric identification of cosmic-ray-produced neon in terrestrial rocks with multiple neon components: Earth Planet. Sci. Lett., v. 118, p. 65-73.

Niedermann, S., Schäfer, J.M., and Wieler, R., 2004, The production rate of cosmogenic argon in an Antarctic pyroxene, *in* IGC, ed., 32-IGC: Florence, Italy.

Nishiizumi, K., 1996, Production rate of ^{10}Be and ^{26}Al on the surface of the earth and underground: Radiocarbon, v. 38, p. 164-165.

Nishiizumi, K., Finkel, R., Brimhall, G., Mote, T., Mueller, G., and Tidy, E., 1998, Ancient exposure ages of alluvial fan surfaces compared with incised stream beds and bedrock in the Atacama Desert of North Chile, GSA Annual Meeting: Toronto, p. 11402.

Nishiizumi, K., Klein, J., Middleton, R., and Craig, H., 1990, Cosmogenic ^{10}Be, ^{26}Al and ^{3}He in olivine from Maui lavas: Earth and Planetary Science Letters, v. 98, p. 263-266.

Nishiizumi, K., Kohl, J.R., Arnold, J.R., Klein, J., Dorn, R., Fink, D., Middleton, R., and Lal, D., 1993, Role of in situ cosmogenic nuclides 10Be and 26Al in the study of diverse geomorphic processes: Earth Surface Processes, v. 18, p. 407-425.

Nishiizumi, K., Kohl, J.R., Arnold, J.R., Klein, J., Fink, D., and Middleton, R., 1991, Cosmic ray produced ^{10}Be and ^{26}Al in Antarctic rocks: exposure and erosion history: Earth Planet. Sci. Lett., v. 104.

Nishiizumi, K., Lal, D., Klein, J., Middleton, R., and Arnold, J.R., 1986, Production of ^{10}Be and ^{26}Al by cosmic rays in terrestrial quartz in situ and implications for erosion rates: Nature, v. 319, p. 134-136.

Oberholzer, P., 2004, Reconstructing paleoclimate and landscape history in Antarctica and Tibet with cosmogenic nuclides [PhD 15472 thesis]: Zurich, ETH.

Oberholzer, P., Baroni, C., Salvatore, M.C., Baur, H., and Wieler, R., subm., Cosmogenic noble gases in pyroxenes used for dating Late-Cenozoic erosional surfaces in Victoria Land, Antarctica: Journal of Quaternary Science.

Oberholzer, P., Baroni, C., Schäfer, J.M., Orombelli, J., Ivy-Ochs, S., Kubik, P.W., Baur, H., and Wieler, R., 2003, Limited Pliocene/Pleistocene glaciation in Deep Freeze Range, northern Victoria Land, derived from in-situ cosmogenic nuclides: Antarctic Science, v. 15, p. 493-502.

Ochs, M., and Ivy-Ochs, S., 1997, The chemical behaviour of Be, Al, Fe, Ca and Mg during AMS target preparation from terrestrial silicates modeled with chemical speciation calculations: Nucl. Instr. Meth. Phys. Res, v. B 123, p. 235-240.

Ortlieb, L., Zazo, C., Goy, J.L., Dabrio, C., and Machare, J., 1996a, Pampa del Palo: an anomalous composite marine terrace on the uprising coast of southern Peru: Jour. South Am. Earth Sci., v. 9, p. 367-379.

Ortlieb, L., Zazo, C., Goy, J.L., Hillaire-Marcel, C., Ghaleb, B., and Cournoyer, L., 1996b, Coastel deformation and sea-level changes in the northern Chile subduction area (23 S) during the last 330 ky: Quat. Sci. Rev., v. 15, p. 819-831.

Parsons, I., Rex, D.C., Guise, P., and Halliday, A.N., 1988, Argon-loss by alkali feldspars: Geochim. Cosmochim. Acta, v. 52, p. 1097-1112.

Paskoff, R.P., 1980, Late Cenozoic crustal movements and sea level variations in the coastal area of Northern Chile, *in* Mörner, N.A., ed., Earth Rheology, Isostasy, and Eustasy, p. 487-495.

Pazzaglia, F.J., Gardner, T.W., and Merritts, D.J., 1998, Bedrock fluvial incision and longuitudinal profile development over geologic time scales determined by fluvial terraces, *in* Tinkler, K.J., and Wohl, E.E., eds., Rivers over rock, fluvial processes in bedrock channels, Volume 107, Geophys. Monograph, p. 207-235.

Peppard, B.T., Steele, I.M., Davis, A.M., Wallace, P.J., and Anderson, A.T., 2001, Zoned quartz phenocrysts from the rhyolitic Bishop Tuff: American Mineralogist, v. 86, p. 1034-1052.

Perny, B., Eberhardt, P., Ramseyer, K., Mullis, J., and Pankrath, R., 1992, Microdistribution of Al, Li, and Na in α quartz: Possible causes and correlation with short-lived cathodoluminescence: Amer. Mineralogist, v. 77, p. 534-544.

Pettke, T., Halter, W.E., Webster, J.D., Aigner-Torres, A., and Heinrich, C.A., 2004, Accurate quantification of melt inclusion chemistry by LA-ICPMS: A comparison with EMP and SIMS and advantages and possible limitations of either method: Lithos, v. 78, p. 333-361.

Phillips, F.M., Leavy, B.D., Jannik, N.O., Elmore, D., and Kubik, P.W., 1986, The accumulation of cosmogenic chlorine-36 in rocks: A method for surface exposure dating: Science, v. 231, p. 41-43.

Phillips, F.M., Zreda, M.G., Ku, T.-L., Luo, S., Huang, Q., Elmore, D., Kubik, P.W., and Sharma, P., 1993, Cosmogenic ^{36}Cl and ^{10}Be ages of Quaternary glacial and fluvial deposits of the Wind River Range, Wyoming: GSA Bull., v. 109, p. 1453-1463.

Pigati, J.S., and Lifton, N.A., 2004, Geomagnetic effects on time-integrated cosmogenic nuclide production with emphasis on in situ 14C and 10Be: Earth and Planetary Science Letters, p. in press.

Poreda, R.J., and Cerling, T.E., 1992, Cosmogenic neon in recent lavas from the Western United States: Geoph. Res. Letters, v. 18, p. 1863-1866.

Pratt, B., Burbank, D.W., Heimsath, A., and Ojha, T., 2002, Impulsive alleviation during early Holocene strengthened monsoons, central Nepal Himalaya: Geology, v. 30, p. 911-914.

Pratt-Sitaula, B., Burbank, D.W., Heimsath, A., and Ojha, T., 2004, Landscape disequilibrium on 1000-10,000 year scales Marsyandi River, Nepal, central Himalaya: Geomorphology, v. 58, p. 233-241.

Rabassa, J., Zarate, M.A., Cioccale, M., Carignano, C.A., Partiridge, T., and Maud, R., 1995, Paisajes relictuales Gondwanicos (Cretacico-Paleoceno) en areas cratonicas de Argentina., Congreso del Paleogeno de America del Sur: La Pampa.

Reedy, R.C., Nishiizumi, K., Lal, D., Arnold, J.R., Englert, P.A.J., Klein, J., Middleton, R., Jull, A.J., and Donahue, D.J., 1994, Simulations of in situ cosmogenic nuclide production: Nucl. Instr. Meth. in Phys. Res., v. B92, p. 297-300.

Reiners, P.W., Ehlers, T.A., Mitchell, S.G., and Montgomery, D.R., 2003, Coupled spatial variations in precipitation and long-term erosion rates across the Washington Cascades: Nature, v. 426, p. 645-647.

Renne, P.R., Farley, K.A., Becker, T.A., and Sharp, W.D., 2001, Terrestrial cosmogenic argon: Earth Planet. Sci. Lett., v. 188, p. 435-440.

Riebe, C.S., Kirchner, J.W., and Finkel, R., C., 2004, Erosional and climate effects on long-term chemical weathering rates in granite landscapes spanning diverse climate regimes: Earth and Planetary Science Letters, v. 224, p. 547-562.

Riquelme, R., Martinod, J., Herail, G., Darrozes, J., and Charrier, R., 2003, A geomorphological approach to determining the Neogene to Recent tectonic deformation in the Coastal Cordillera of northern Chile (Atacama): Tectonophysics, v. 361, p. 255-275.

Roe, G.H., Montgomery, D.R., and Hallet, B., 2002, Effects of orographic precipitation variations on the concavity of steady-state river profiles: Geology, v. 30, p. 143-146.

Rosenbloom, N.A., and Anderson, R.S., 1994, Hillslope and channel evolution in a marine terraced landscape, Santa Cruz, California: Jour. Geophys. Res., v. 99, p. 14013-14029.

Ross, R., Kirschbaum, A.M., Ribeiro, S.G., and Arribere, M.A., 1998, Procesos de meteorización en el granito de Achala, Sierra Grande de Córdoba: cambios químicos y mineralógicos: Revista de la Asociación Geológica Argentina, v. 53, p. 480-488.

Salas, R.O., Kast, R.F., Montecinos, F.P., and Salas, I.Y., 1966, Geologica y recursos minerales del departemento de Arica, Instituto de Investigaciones Geologicas Chile.

Sayado, J.M., Collantes, M.M., Karlson, A., and Sanabria, J., 2001, Genesis and distribution of the Late Pleistocene and Holocene loess of Argentina: a regional approximation: Quat. Int., v. 76/77, p. 247-257.

Schäfer, J.M., 2000, Reconstruction of landscape evolution and continental paleoglaciations using in-situ cosmogenic nuclides. Examples from Antarctica and the Tibetan Plateau [PhD, 13542 thesis]: Zürich, ETH-Zürich.

Schäfer, J.M., Baur, H., Denton, G.H., Ivy-Ochs, S., Marchant, D.R., Schlüchter, C., and Wieler, R., 2000, The oldest ice on Earth in Beacon Valley, Antarctica: New evidence from surface exposure dating: Earth Planet. Sci. Lett., v. 179, p. 91-99.

Schäfer, J.M., Ivy-Ochs, S., Wieler, R., Leya, I., Baur, H., Denton, G.H., and Schlüchter, C., 1999, Cosmogenic noble gas studies in the oldest landscape on earth: surface exposure ages of the Dry Valleys, Antarctica: Earth Planet. Sci. Lett., v. 167, p. 215-226.

Schäfer, J.M., Tschudi, S., Zhao, Z., Wu, X., Ivy-Ochs, S., Wieler, R., Baur, H., Kubik, P.W., and Schlüchter, C., 2002, The limited influence of glaciations in Tibet on global climate over the past 170 000yr: Earth and Planetary Science Letters, v. 194, p. 287-297.

Schaller, M., 2001, Variations of middle European erosion in space and time from in situ-produced cosmogenic nuclides in river sediment [PhD thesis]: Bern, University of Bern.

Schaller, M., von Blanckenburg, F., Hovius, N., Veldkamp, A., van den Berg, M.W., and Kubik, P.W., 2004, Paleoerosion rates from cosmogenic ^{10}Be in a 1.3 Ma terrace sequence: Response of the River Meuse to changes in climate and rock uplift: Journal of Geology, v. 112, p. 127-144.

Schellenberger, A., Heller, F., and Veit, H., 2003, Magnetostratigraphy and magnetic susceptibility of the Las Carreras loess-paleosol sequence in Valle de Tafi, Tucuman, NW-Argentina: Quat. Int., v. 106-107, p. 159-167.

Schlunegger, F., Detzner, K., and Olsson, D., 2001, The evolution towards steady state erosion in a soil-mantled drainage basin: semi-quantitative data from a transient landscape in the Swiss Alps: Geomorphology., v. 43, p. 55-76.

—, 2002, The evolution towards steady state erosion in a soil-mantled drainage basin: semi-quantitative data from a transient landscape in the Swiss Alps: Geomorphology, v. 43, p. 55-76.

Schlunegger, F., Kober, F., and Schneider, H., 2003, Climate change and valley formation in the Andes of Northern Chile, EGS-AGU-EUG Joint Assembly, Volume 5: Nice, France, European Geophysical Society, p. 01926.

Scholl, D.W., Christensen, M.N., von Huene, R., and Marlow, M.S., 1970, Peru-Chile trench sediments and sea-floor spreading: GSA Bull., v. 81, p. 1339-1360.

Schumm, S.A., 1956, The role of creep and rainwash on the retreat of badland slopes: American Journal of Science, v. 254., p. 693-706.

Seidl, M.A., Finkel, R.C., Caffee, M.W., Hudson, G.B., and Dietrich, W.E., 1997, Cosmogenic isotope analysis applied to river longitudinal profile evolution: Problems and interpretations: Earth Surface Processes and Landforms, v. 22, p. 195-209.

Shephard, M.K., Arvidson, R.E., Caffee, M., Finkel, R., C., and Harris, L., 1995, Cosmogenic exposure ages of basalt flows: Lunar crater field, Nevada: Geology, v. 23, p. 21-24.

Shuster, D.L., and Farley, K.A., 2003, ^{4}He/^{3}He thermochronomerty: Earth and Planetary Science Letters, v. 217, p. 1-17.

Shuster, D.L., Farley, K.A., Sisterson, J.M., and Burnett, D.S., 2003, Quantifying the diffusion kinetics and spatial distributions of radiogenic ^{4}He in minerals containing proton-induced ^{3}He: Earth and Planetary Science Letters, v. 217, p. 19-32.

Simpson, G., and Schlunegger, F., 2003, Topographic evolution and morphology of surfaces evolving in response to coupled fluvial and hillslope sediment transport: Jour. Geophys. Res., v. 108.

Small, E.E., and Anderson, R.S., 1998, Pleistocene relief production in Laramide mountain range, western United States: Geology, v. 26, p. 123-126.

Small, E.E., Anderson, R.S., Repka, J.L., and R., F., 1997, Erosion rates of alpine bedrock summit surfaces deduced from in situ ^{10}Be and ^{26}Al: Earth Planet. Sci. Lett., v. 150, p. 413-425.

Stark, C.P., 1999, Time and length scales in steady-state orogens, GSA1999 annual meeting, Volume 31, Abstracts with Programs - Geological Society of America., p. 297.

Stone, J., 2000, Air pressure and cosmogenic isotope production: Jour. Geoph. Res., v. 105, p. 23753-23759.

Stone, J.O., Allan, G.L., Fifield, L.K., and Cresswell, R.G., 1996, Cosmogenic chlorine-36 from calcium spallation: Geochim. Cosmochim. Acta, v. 60, p. 555-561.

Strasky, S., Baur, H., Kober, F., Schlchter, C., and Wieler, R., 2004, Refinement of scaling factors for surface exposure dating using artificial targets, DEUQUA: Nijmegen, The Netherlands, Vrije Universiteit (VU) in Amsterdam.

Strasser, M., 2003, Erosion processes and geomorphologic landscape evolution in arid climatic settings: Lluta-Structure, Northern Chile [Diploma thesis]: Zurich, ETH.

Summerfield, M.A., 1991, Global Geomorphology: New York, Longman, 641 p.

Swenson, J.B., and Brown, E.T., 2004, The interplay between landscape response to tectonic or climatic perturbations and cosmogenic nuclide concentrations: theoretical implications for calculating basin-scale erosion rates, 32IGC: Florence, IGC, p. 920-921.

Synal, H.-A., Bonani, G., Doebeli, M., Ender, R.M., Gartenmann, P., Kubik, P.W., Schnabel, C., and Suter, M., 1997, Status report of the PSI/ETH AMS facility: Nuclear Instruments and Methods in Physics, p. 62-68.

Thornburg, T.M., and Kulm, L.D., 1986, Sedimentation in the Chile trench: petrofacies and provenance: Jour. of. Sed. Petrol., v. 54, p. 55-74.

Tosdal, R.M., Farra, A.E., and Clark, A.H., 1984, Cenozoic polyphase landscape and tectonic evolution ot the Cordillera Occidental, southernmost Peru: GSA Bull., v. 95, p. 1318-1332.

Trull, T.W., Brown, E.T., Marty, B., Raisbeck, G.M., and Yiou, F., 1995, Cosmogenic ^{10}Be and ^{3}He accumulation in Pleistocene beach terraces in Death Valley, California, USA.: Implications for cosmic-ray exposure dating of young surfaces in hot climates: Chemical Geology, v. 119, p. 191-207.

Trull, T.W., Kurz, M.D., and Jenkins, W.J., 1991, Diffusion of cosmogenic ^{3}He in olivine and quartz: Implications for surface exposure dating: Earth Planet. Sci. Lett., v. 103, p. 241-256.

Tschudi, S., 2000, Surface exposure dating: A geologist's view. With examples from both hemispheres [PhD-thesis thesis], Bern.

Tucker, G.E., and Bras, R.L., 1998, Hillslope processes, drainage density, and landscape morphology: Water Resour. Res., v. 34, p. 2751-2764.

Tucker, G.E., and Slingerland, R., 1994, Erosion dynamics, flexuaral isostacy, and long-lived escarpments: A numerical modeling study: Jour. Geoph. Res., v. 99, p. 12229-12243.

—, 1996, Predicting sediment flux from fold and thrust belts: Basin Res., v. 8, p. 329-349.

—, 1997, Drainage basin response to climate change: Water Resour. Res., v. 33, p. 2031-2047.

von Blanckenburg, F., Hewawasam, T., and Kubik, P.W., 2004, Cosmogenic nuclide evidence for low weathering and denudation in the wet, tropical highlands of Sri Lanka,: J. Geophys. Res., v. 109F, p. 03008, doi:10.1029/2003JF000049.

von Rotz, R., 2003, Magnetostratigraphie und fazielle Entwicklung der Westabdachung der Anden, Tarapaca-Region, Nord-Chile [Diploma thesis]: Zurich, ETH Zurich.

von Rotz, R., Schlunegger, F., and Heller, F., 2005., Assessing the age of relief growth in the Andes of Northern Chile: magneto-polarity chronologies from Neogene continental sections: Terra Nova, v. in press.

Vuille, M., 1999, Atmospheric circulation over the Bolivian Altiplano during dry and wet periods and extreme phases of the Southern Oscillation: International Journal of Climatology, v. 19, p. 1579-1600.

Walter, H., Lieth, H., Rehder, H., and Harnickell, E., 1967, Klimadiagramm - Weltaltas: Jena, Gustav Fischer Verlag.

Watt, G.R., Wright, P., Galloway, S., and McLean, C., 1997, Cathodoluminescence and trace element zoning in quartz phenocrysts and xenocrysts: Geochim. Cosmochim. Acta, v. 61, p. 4337-4348.

Wegmann, K.W., and Pazzaglia, F.J., 2002, Holocene strath terraces, climate change, and active tectonics: The Clearwater River basin, Olympic Peninsula, Washington State: Geological Society of America Bulletin, v. 114, p. 731-744.

Whipple, K.X., 2001, Fluvial landscape response time: how plausible is steady-state denudation?: Am. Jour. Sci., v. 301, p. 313-325.

—, 2004, Bedrock rivers and the geomorphology of active orogens: Annual Reviews of Earth and Planetary Science Letters, v. 32, p. 151-185.

Whipple, K.X., Hirby, E., and Brocklehurst, S.H., 1999, Geomorphic limits to climate-induced increases in topographic relief: Nature, v. 401, p. 39-43.

Whipple, K.X., and Tucker, G.E., 1999, Dynamics of the stream-power river incision model: Implication for height limits of mountain ranges, landscape response timescales and research needs: Jour. Geophys. Res., v. 104, p. 17661-17674.

White, A.F., Bullen, T.D., Schulz, M.S., Blum, A.E., Huntington, T.G., and Peters, N.E., 2001, Differential rates of feldspar weathering in granitic regoliths: Geochim. Cosmochim. Acta, v. 65, p. 847-869.

Willet, S., and Brandon, M.T., 2002, On steady states in mountain belts: Geology, v. 30, p. 175-178.

Williams, A.J., Stuart, F.M., Day, S.J., and Phillips, W.M., in press, Using pyroxene microphenocrysts to determine cosmogenic ^{3}He concentrations in old volcanic rocks: an example of landscape development in central Gran Canaria: Quaternary Science Reviews.

Wörner, G., Hammerschmidt, K., Henjes-Kunst, F., Lezaun, J., and Wilke, H., 2000, Geochronology (40Ar/39Ar, K-Ar and He-exposure ages) of Cenozoic magmatic rocks from northern Chile (18-22°S): implications for magmatism and tectonic evolution of the Central Andes: Revista Geologica de Chile, v. 27, p. 205-240.

Wörner, G., Uhlig, D., Kohler, I., and Seyfried, H., 2002, Evolution of the Western Andean Escarpment at 18° S (N. Chile) during during the last 25 Ma: uplift, erosion, and collapse through time: Tectonophysics, v. 345, p. 183-198.

Yokoyama, Y., Reyss, J., and Guichard, F., 1977, Production of radionuclides by cosmic rays at mountain altitudes: Earth Planet. Sci. Lett., v. 36, p. 44-50.

Zarate, M.A., 2003, Loess of southern South America: Quat. Sci. Rev., v. 22, p. 1987-2006.

Zarate, M.A., Kemp, R.A., and Blasi, A.M., 2002, Identification and differentiation of Pleistocene paleosols in the northern Pampas of Buenos Aires, Argentina: Jour. of South Am. Earth Scienes, v. 15, p. 303-313.

Zeilinger, G., Schlunegger, F., and Simpson, G., 2005, in press, The Oxaya Anticline (northern Chile): A buckle enhanced by river incision?: Terra Nova.

Zinck, J.A., and Sayado, J.M., 2001, Climatic periodicity during the late Pleistocene from the loess-paleosol sequence in northwest Argentina: Quat. Int., v. 78, p. 11-16.

Zinck, J.A., and Sayago, J.M., 1999, Loess-paleosol sequence of La Mesada in Tucuman province, northwest Argentina, charaterization abd paleoenvironemntal interpretation: Jour. of South Am. Earth Scienes, v. 12, p. 293-310.

Zreda, M., 1994, Development and calibration of the ^{36}Cl surface expsoure dating method and its application to the chronology of Late Quaternary glaciations [PhD thesis]: Soccorro, USA, New Mexico Institute of Mining and Technology.

Zreda, M., Phillips, F.M., Elmore, D., Kubik, P.W., Sharma, P., and Dorn, R.I., 1991, Cosmogenic chlorine-36 production rates in terrestrial rocks: Earth and Planetary Science Letters, v. 105, p. 94-109.

Zreda, M.G., and Phillips, F.M., 2000, Cosmogenic nuclide buildup in surficial materials, *in* Noller, J.S., Sowers, J.M., and Lettis, W.R., eds., Quaternary Geochronology: Methods and Applications, Volume 14, AGU reference Shelf, p. 61-76.

10 Appendix

Additional samples

Neon

(uncertainties stated are only analytical uncertainties; stat. Error ≤3%, sast. Error ≤3%)

LabCode	Sample	20Ne [atoms/g]	error [atoms/g]	$^{21}Ne/^{20}Ne$	error	$^{22}Ne/^{20}Ne$	error
Chile, Arica							
PO,6,38	FK-CN10 (550,20')	5.62E+09	2.48E+08	4.30E-03	6.47E-05	1.04E-01	2.56E-04
PO,6,39	FK-CN10 (800, 15')	4.90E+09	1.28E+08	3.02E-03	2.51E-05	9.92E-02	1.29E-03
PO,6,40	FK-CN10 (1500,15')	3.68E+09	7.26E+07	3.11E-03	1.31E-05	1.03E-01	3.16E-04
PO,6,21	FK-CN28 (550,20')	4.72E+09	6.90E+07	3.03E-03	6.57E-05	1.02E-01	7.05E-04
PO,6,22	FK-CN28 (800,15)	2.90E+09	5.92E+07	2.97E-03	2.63E-05	1.02E-01	1.52E-03
FK,2,1	FK-CN1/1(550,20')	5.81E+09	1.14E+08	1.57E-02	2.05E-04	1.15E-01	4.55E-04
FK,2,2	FK-CN1/1(800,15')	4.78E+09	9.72E+07	3.46E-03	3.11E-05	1.03E-01	6.87E-04
FK,2,3	FK-CN1/1(1500,15')	4.21E+09	8.41E+07	3.03E-03	1.77E-05	1.04E-01	4.02E-04
FK,2,4	FK-CN1b(550,20')	4.96E+09	9.90E+07	1.76E-02	3.51E-04	1.22E-01	1.87E-03
FK,2,5	FK-CN1b(800,15')	4.35E+09	1.20E+08	3.56E-03	1.49E-04	1.04E-01	3.98E-04
FK,2,6	FK-CN1b(1500,15')	3.15E+09	1.04E+08	3.34E-03	3.56E-05	1.03E-01	5.30E-04
FK,2,16	FK-CN8b(550,20')	1.37E+10	2.65E+08	6.35E-03	8.10E-05	1.06E-01	3.51E-04
FK,2,17	FK-CN8b(800,15')	3.68E+09	7.48E+07	3.16E-03	3.00E-05	1.03E-01	5.68E-04
FK,2,18	FK-CN8b(1500,15')	2.51E+09	1.01E+08	3.02E-03	3.70E-05	1.03E-01	5.84E-04
FK,2,19	FK-CN8c(550,20')	2.64E+09	4.27E+07	1.07E-02	3.11E-04	1.13E-01	1.82E-03
FK,2,20	FK-CN8c(800,15')	3.89E+09	5.99E+07	1.08E-02	2.24E-04	1.11E-01	3.85E-04
FK,2,21	FK-CN8c(1500,15')	6.89E+09	1.01E+08	3.28E-03	1.81E-05	1.03E-01	1.95E-04
FK,2,22	FK-CN36/1(550,20')	9.13E+09	1.87E+08	5.96E-03	1.05E-04	1.05E-01	3.56E-04
FK,2,23	FK-CN36/1(800,15')	3.13E+10	6.15E+08	3.46E-03	1.34E-05	1.02E-01	1.74E-04
FK,2,24	FK-CN36/1(1500,15')	2.90E+10	5.09E+08	3.09E-03	1.45E-05	1.04E-01	2.70E-04
FK,7,4	FK-111G(550,30')	2.28E+09	3.74E+07	6.36E-02	6.80E-04	1.73E-01	1.35E-03
FK,7,5	FK-111G(800,30')	2.46E+09	5.40E+07	3.82E-03	1.26E-04	1.06E-01	7.99E-04
FK,7,6	FK-111G(1750,15')	1.75E+09	5.12E+07	2.98E-03	1.49E-04	1.03E-01	1.20E-03
FK,7,17	FK-24(550,30')	2.92E+09	7.96E+07	7.17E-02	8.61E-04	1.81E-01	2.07E-03
FK,7,18	FK-24(800,30')	3.44E+09	9.62E+07	3.50E-03	1.11E-04	1.01E-01	1.02E-03
FK,7,19	FK-241(1750,15')	3.50E+09	6.02E+07	3.03E-03	5.37E-05	9.92E-02	1.39E-03
FK,8,16	FK-111A(400,15')	2.28E+09	5.14E+07	3.91E-02	2.92E-04	1.47E-01	1.44E-03
FK,8,17	FK-111A(550,30')	1.36E+09	2.46E+07	5.12E-02	7.18E-04	1.60E-01	1.61E-03
FK,8,18	FK-111A(800,30')	1.34E+09	3.48E+07	3.22E-03	1.04E-04	1.02E-01	1.60E-03
FK,8,19	FK-111A(1750,15')	2.91E+09	5.28E+07	3.96E-03	1.26E-04	1.00E-01	7.47E-04
FK,8,20	FK-111B(400,15')	1.34E+09	2.87E+07	4.25E-02	5.45E-04	1.47E-01	4.72E-04
FK,8,21	FK-111B(550,30')	2.27E+09	4.80E+07	4.83E-02	3.19E-04	1.53E-01	1.41E-03
FK,8,22	FK-111B(800,30')	1.17E+09	4.21E+07	3.54E-03	1.42E-04	1.01E-01	1.49E-03
FK,8,23	FK-111B(1750,15')	1.26E+09	2.84E+07	3.27E-03	1.07E-04	9.96E-02	1.07E-03
FK,8,24	FK-111C(400,30')	1.05E+09	3.18E+07	3.70E-02	4.66E-04	1.45E-01	2.39E-03
FK,8,25	FK-111C(550,30')	1.09E+09	3.14E+07	1.05E-01	2.05E-03	2.23E-01	2.50E-03
FK,8,26	FK-111C(800,20')	1.03E+09	1.74E+07	3.73E-03	9.49E-05	1.04E-01	7.70E-04
FK,8,27	FK-111C(1750,15')	1.06E+09	3.08E+07	3.34E-03	6.44E-05	1.02E-01	1.15E-03
FK,8,28	FK-111D(400,30')	1.18E+09	2.51E+07	2.66E-02	4.17E-04	1.30E-01	1.75E-03
FK,8,29	FK-111D(550,30')	9.83E+08	2.13E+07	1.21E-01	1.73E-03	2.39E-01	2.60E-03
FK,8,30	FK-111D(800,20')	1.23E+09	1.85E+07	4.40E-03	3.67E-05	1.05E-01	1.69E-03
FK,8,31	FK-111D(1750,15')	1.45E+09	2.02E+07	3.28E-03	8.93E-05	1.06E-01	1.02E-03
FK,8,32	FK-111E(400,30')	1.11E+09	3.32E+07	2.33E-02	2.54E-04	1.22E-01	1.79E-03
FK,8,33	FK-111E(550,30')	1.33E+09	2.30E+07	9.90E-02	9.06E-04	2.12E-01	1.57E-03
FK,8,34	FK-111E(800,20')	1.48E+09	2.98E+07	4.25E-03	3.24E-05	1.02E-01	5.40E-04
FK,8,35	FK-111E(1750,15')	1.48E+09	2.94E+07	3.24E-03	1.11E-04	1.02E-01	8.75E-04
FK,8,49	FK-T3-Ne(800,45')	3.11E+09	4.48E+07	4.17E-03	1.24E-04	1.03E-01	9.40E-04
FK,8,50	FK-T3-Ne(1500,15')	1.10E+09	2.15E+07	1.70E-02	2.97E-04	1.18E-01	1.75E-03
FK,8,51	FK-T3-Ne(1750,15')	1.01E+09	1.85E+07	3.00E-03	1.04E-04	1.02E-01	2.35E-03
fk,18,04	FK-306-Ne(600,45')	3.90E+09	1.19E+08	5.11E-03	8.50E-05	1.03E-01	5.32E-04
fk,18,05	FK-306-Ne(800,20')	2.98E+10	9.11E+08	3.35E-03	4.17E-05	1.02E-01	3.09E-04
fk,18,06	FK-306-Ne(1750,20')	5.59E+09	1.95E+08	3.27E-03	4.89E-05	1.01E-01	7.39E-04

Continued

LabCode	Sample	20Ne [atoms/g]	error [atoms/g]	$^{21}Ne/^{20}Ne$	error	$^{22}Ne/^{20}Ne$	error
fk,18,25	FK-115-Ne(600,45')	1.59E+09	4.50E+07	5.82E-03	9.81E-05	1.06E-01	2.70E-04
fk,18,26	FK-115-Ne(800,20')	1.24E+09	3.61E+07	4.40E-03	1.74E-04	1.03E-01	2.49E-03
fk,18,27	FK-115-Ne(1750,20')	3.04E+09	8.86E+07	3.17E-03	1.19E-04	1.01E-01	1.35E-03
fk,18,22	FK-116-Ne(600,45')	2.07E+09	7.23E+07	4.35E-03	1.86E-04	9.94E-02	2.04E-03
fk,18,23	FK-116-Ne(800,20')	1.33E+09	3.71E+07	4.31E-03	1.43E-04	1.03E-01	2.31E-03
fk,18,24	FK-116-Ne(1750,20')	5.96E+09	1.78E+08	3.21E-03	4.57E-05	1.02E-01	2.53E-04
fk,18,19	FK-117-Ne(600,45')	1.01E+09	3.56E+07	3.21E-03	8.37E-05	1.01E-01	5.63E-04
fk,18,20	FK-117-Ne(800,20')	7.51E+08	2.60E+07	2.85E-03	2.30E-04	1.04E-01	2.07E-03
fk,18,21	FK-117-Ne(1750,20')	8.79E+08	4.47E+07	3.02E-03	1.06E-04	1.01E-01	1.30E-03
fk,18,16	FK-118-Ne(600,45')	2.69E+09	7.01E+07	5.34E-03	9.50E-05	1.04E-01	1.18E-03
fk,18,17	FK-118-Ne(800,20')	4.49E+09	1.26E+08	3.11E-03	4.23E-05	1.02E-01	3.76E-04
fk,18,18	FK-118-Ne(1750,20')	1.92E+09	5.10E+07	3.26E-03	8.68E-05	1.04E-01	1.20E-03
fk,18,13	FK-119-Ne(600,45')	1.41E+09	3.68E+07	5.79E-03	1.53E-04	1.03E-01	9.82E-04
fk,18,14	FK-119-Ne(800,20')	5.74E+09	1.60E+08	3.74E-03	7.02E-05	1.02E-01	5.41E-04
fk,18,15	FK-119-Ne(1750,20')	2.25E+09	6.30E+07	3.12E-03	1.14E-04	1.00E-01	7.87E-04
Chile - biotite							
fk,13,44	FK-CN19Bt-Ne(850,45')	2.60E+10	7.92E+08	2.08E-02	2.13E-04	1.25E-01	9.03E-04
fk,13,46	FK-CN19Bt-Ne(1750,20')	8.34E+09	2.58E+08	8.48E-03	1.70E-04	1.05E-01	1.35E-03
fk,13,48	FK-CN104Bt-Ne(850,45')	1.41E+10	2.31E+08	1.38E-02	7.97E-05	1.24E-01	4.47E-04
fk,13,50	FK-CN104Bt-Ne(1750,20')	2.09E+09	3.51E+07	5.06E-06	4.56E-06	1.02E-01	1.26E-03
fk,13,52	FK-CN111Bt-Ne(850,45')	2.86E+10	5.50E+08	9.72E-03	5.97E-05	1.11E-01	5.96E-04
fk,13,54	FK-CN111Bt-Ne(1750,20')	3.67E+09	7.36E+07	1.15E-02	2.18E-04	1.11E-01	5.71E-04
Antarctica, Frontier Mountain (L. Folco, K Nishiizumi)							
fk,11,07	T772(600,45')	1.96E+09	2.57E+07	2.58E-02	2.43E-04	1.25E-01	5.30E-04
fk,11,08	T772(800,20')	3.65E+09	5.34E+07	4.90E-03	6.77E-05	1.05E-01	7.01E-04
fk,11,09	T772(1750,20')	1.89E+09	2.72E+07	5.62E-03	1.03E-04	1.04E-01	5.23E-04
fk,11,01	T773(600,30')	1.61E+09	2.67E+07	5.22E-02	5.17E-04	1.55E-01	8.86E-04
fk,11,02	T773(800,20')	1.07E+09	1.53E+07	3.88E-03	6.66E-05	1.03E-01	1.02E-03
fk,11,03	T773(1750,20')	1.29E+09	1.57E+07	3.42E-03	7.06E-05	1.02E-01	1.89E-03
fk,11,13	T775(600,45')	1.64E+09	2.31E+07	5.25E-02	5.37E-04	1.46E-01	9.85E-04
fk,11,14	T775(800,20')	8.14E+08	1.24E+07	4.27E-03	2.33E-04	1.03E-01	1.62E-03
fk,11,15	T775(1750,20')	9.21E+08	3.22E+07	6.05E-03	1.93E-04	1.00E-01	2.55E-03
fk,11,10	T778(600,45')	4.54E+09	6.61E+07	1.06E-01	8.77E-04	2.21E-01	1.13E-03
fk,11,11	T778(800,20')	9.66E+08	1.47E+07	4.24E-03	1.29E-04	1.03E-01	1.67E-03
fk,11,12	T778(1750,20')	1.23E+09	1.59E+07	9.16E-03	1.74E-04	1.04E-01	1.09E-03
fk,11,04	T781(600,45')	7.02E+09	6.60E+07	8.84E-02	2.20E-04	1.97E-01	1.03E-03
fk,11,05	T781(800,20')	2.67E+09	2.68E+07	3.50E-03	6.57E-05	1.02E-01	7.33E-04
fk,11,06	T781(1750,20')	8.63E+09	8.15E+07	3.43E-03	1.50E-05	1.01E-01	1.45E-04
USA/Death Valley (M. Dühnforth)							
fk,14,01	FK-90303-2-Ne(600,45')	2.02E+10	2.31E+08	3.56E-03	2.13E-05	1.02E-01	4.63E-04
fk,14,02	FK-90303-2-Ne(800,20')	3.11E+10	3.57E+08	3.05E-03	2.25E-05	1.02E-01	3.80E-04
fk,14,03	FK-90303-2-Ne(1750,20')	4.67E+09	6.53E+07	5.40E-03	7.93E-05	1.06E-01	1.04E-03
fk,14,06	FK-190303-1-Ne(600,45')	1.56E+10	1.71E+08	4.29E-03	4.66E-05	1.03E-01	6.09E-04
fk,14,07	FK-190303-1-Ne(800,20')	1.23E+10	1.47E+08	3.15E-03	2.21E-05	1.03E-01	5.12E-04
fk,14,08	FK-190303-1-Ne(1750,20')	3.43E+09	3.98E+07	6.66E-03	7.20E-05	1.03E-01	8.72E-04
fk,14,09	FK-10303-1-Ne(600,45')	2.26E+10	2.65E+08	3.81E-03	3.62E-05	1.03E-01	4.46E-04
fk,14,10	FK-10303-1-Ne(800,20')	2.72E+10	3.22E+08	3.08E-03	3.24E-05	1.02E-01	3.99E-04
fk,14,11	FK-10303-1-Ne(1750,20')	4.54E+09	6.55E+07	1.06E-02	1.12E-04	1.06E-01	1.05E-03
Chile, Atacama Desert (J. Owen, K Nishiizumi)							
fk,14,12	A2-Ne(600,45')	9.82E-10	1.68E-11	1.40E-02	1.18E-04	1.15E-01	5.07E-04
fk,14,13	A2-Ne(800,20')	1.05E-09	1.79E-11	3.85E-03	3.71E-05	1.03E-01	5.74E-04
fk,14,14	A2-Ne(1750,20')	2.89E-10	5.28E-12	4.24E-03	2.43E-05	1.02E-01	7.27E-04
Chile, Lago Argentina (N. Glasser)							
fk,19,06	FK-CFG2-Ne(850,45')	2.22E+09	1.72E+07	3.01E-03	8.40E-05	1.01E-01	8.45E-04
fk,19,08	FK-CFG2-Ne(1750,20')	1.69E+09	1.36E+07	3.53E-03	7.08E-05	1.04E-01	9.37E-04

Additional samples

Helium

(uncertainties stated are only analytical uncertainties; stat. error ≤3%)

LabCode	Sample	^{3}He [ccSTP/g]	error [ccSTP/g]	^{4}He [ccSTP/g]	error [ccSTP/g]	^{3}He/^{4}He	error	R/Ra
Chile, Arica, Pyroxene								
fk,19,01	FK-308-He(850,45')	4.39E-13	3.82E-14	1.28E-08	4.94E-10	3.44E-05	3.28E-06	24.77
fk,19,02	FK-308-He(1750,20')	1.74E-12	1.06E-13	1.48E-08	5.66E-10	1.18E-04	8.47E-06	84.66
Chile, Arica, Biotite								
fk,13,43	FK-CN19Bt-He(850,45')	8.76E-12	3.36E-13	7.21E-06	2.23E-07	1.21E-06	5.99E-08	0.87
fk,13,45	FK-CN19Bt-He(1750,20')	1.65E-12	8.00E-14	2.57E-06	8.00E-08	6.40E-07	3.69E-08	0.46
fk,13,47	FK-CN104Bt-He(850,45')	1.12E-12	4.33E-14	5.61E-06	9.88E-08	2.00E-07	8.49E-09	0.14
fk,13,49	FK-CN104Bt-He(1750,20')	6.51E-13	3.01E-14	1.92E-06	3.38E-08	3.40E-07	1.68E-08	0.24
fk,13,51	FK-CN111Bt-He(850,45')	7.67E-12	2.17E-13	2.86E-06	5.77E-08	2.68E-06	9.32E-08	1.93
fk,13,53	FK-CN111Bt-He(1750,20')	3.15E-13	2.07E-14	6.19E-08	3.54E-09	5.08E-06	4.43E-07	3.65
Tibet (E. Gayer)								
fk,12,01	GA98Aclean (850,45')	2.73E-13	2.44E-14	4.90E-07	6.91E-09	5.57E-07	5.04E-08	0.40
fk,12,02	GA98Aclean (1750,20')	1.81E-14	1.05E-14	4.80E-08	6.82E-10	3.78E-07	2.18E-07	0.27
Chile, Lago Argentina (N. Glasser)								
fk,19,05	FK-CFG2-He(850,45')	8.68E-13	3.05E-14	1.77E-07	1.11E-09	4.91E-06	1.75E-07	*3.53*
fk,19,07	FK-CFG2-He(1750,20')	2.41E-11	1.09E-12	4.78E-06	1.77E-07	5.04E-06	2.95E-07	*3.62*

Curriculum Vitae

Florian Kober

Date and Place of Birth: 24th April 1975, Erfurt, Germany
Nationality: German

Academics

Since Jan 2005	PostDoc at the Geological Institute, ETH Zürich, Swizterland, Physical Sedimentary Systems Group of Prof. Ph. Allen
2000 – 2004	PhD-student at the Geological Institute, ETH Zürich, Swizterland Supervisors: Prof. Ph. Allen (ETH Zürich) Prof. F. Schlunegger (University of Bern) Prof. R. Wielder (ETH Zürich) Dr. Samuel Niedermann (GFZ Potsdam) Dr. S. Ivy-Ochs (ETH Zürich)
2000	Diploma at the Institute of Geology, Technical University of Mining and Engineering, Freiberg, Germany
1999	Postgraduate Diploma of Science in Geology at the Institute of Geology, University of Otago, Dunedin, New Zealand
1994 - 1998	Diploma student at the Institute of Geology, Technical University of Mining and Engineering, Freiberg, Germany

---

1993 - 1994	Civil Service at the Administrative Council of Meiningen, Germany, Department of Environment

Schools:

1991 - 1993	Henfling Gymnasium, Meiningen, Germany
1981 - 1991	Polytechnische Oberschule Friedrich Schiller, Meiningen, Germany

Thanks to: Fritz Schlunegger*** Rainer Wieler *** Susan Ivy-Ochs *** Heiri Baur ** Philip Allen ** Samuel Niedermann * Peter Oberholzer*Peter W. Kubik*Ingo Leya*Nat Lifton***Max Döbeli*Guy Simpson*Karsten Kunze*Tomas Magna***Zheng Zhou**Thomas Pettke* Christian Schlüchter** Eric Reusser***Gerold Zeilinger*** Heinz Schneider***Alex Densmore*** Jörg Schäfer***Stefan Strasky* Miriam Schaller*Miriam Dühforth***Patrick Meister***Uli Heimhofer**** Nele Meckler***Kathrin Monecke*** Michi Schnellmann***Miriam Andres*Michi Strasser**Rudi von Rotz***Adi Gilli**Moritz Lehman*Flavio Amsselmetti**Martin Wipf Uli Exner***Möx Maxelon***Ingo Blechschmidt** Veronika Heber**Jörg Bollmann* Frank Schiebel***Anne Reuther*** Maura von Moos*Ivonne Zyst*** Yvonne van Lith***Urs Menet*** Roki Kipfer* *Brit Meyer Maja Reichenbach***Regula Schächli***RaulSalas**Eduardo Piovano** Alicia Kirschbaum**Gerhard Wörner* Greg Hoke* Andrew Tomlinson ***** Tim Jull**Kuni Nishiizumi***Dan Farber* Alberto Ayzama*** Marcelo Garcia*** Erwin Flückiger** Evgenii Kalashnikov**ETH Bibo Geo-Bibo*** Peter Stammbach & Unterburg 7–9 *** Ines & Wim TOM*NO H35* **CLA 34.4*** SBB***VBZ*** VBG*Mensa*** Clausiusbar*** BQM*Lan Chile* Hotel Pyramid** Hotel Madrid* Iberia*American Airlines** Andrea & Co.* SNF***NSF** Apple & Dell** IONIC*Final* Wincalc*Microsoft***Google* Adobe***Lomo Completo*Pisco Sour*NZZ**** und alle diejenigen, die ich an dieser Stelle sollte vergessen haben**** **********

And Telejob on the 17th of April 2000: Landscape evolution, geomorphology, surface exposure dating. The Department of Earth Sciences at ETH invites applications for a doctoral position for four years to determine exposure ages and erosion rates in northern Chile. The PhD. student will collect samples in northern Chile, analyze them for noble gases, and carry out chemical separation of.....